UNIVERSIDAD DE CHILE
FACULTAD DE CIENCIAS FÍSICAS Y MATEMÁTICAS
DEPARTAMENTO DE GEOLOGÍA

EVOLUCIÓN Y FERTILIDAD DE MAGMAS ASOCIADOS CON DEPÓSITOS DE ÓXIDOS DE HIERRO-APATITO: UNA PERSPECTIVA DESDE EL DISTRITO EL ALGARROBO, NORTE DE CHILE

TESIS PARA OPTAR AL GRADO DE MAGÍSTER EN CIENCIAS, MENCIÓN GEOLOGÍA

MEMORIA PARA OPTAR AL TITULO DE GEÓLOGO

ANDRÉS JAVIER OJEDA SEPÚLVEDA

PROFESOR GUÍA:
Fernando Barra Pantoja

MIEMBROS DE LA COMSIÓN:
Martin Reich Morales
Santiago Tassara

Este trabajo es financiado por el proyecto FONDECYT-1190105 y el Núcleo Milenio Trazadores de Metales en Zonas de Subducción NC130065

SANTIAGO DE CHILE

2023

RESUMEN DE LA TESIS PARA OPTAR AL TITULO DE: Geólogo y grado de Magíster en Ciencias, Mención Geología.
POR: Andrés Javier Ojeda Sepúlveda
FECHA: 2023
PROFESOR GUÍA: Fernando Barra Pantoja

EVOLUCIÓN Y FERTILIDAD DE MAGMAS ASOCIADOS CON DEPÓSITOS DE ÓXIDOS DE HIERRO-APATITO: UNA PERSPECTIVA DESDE EL DISTRITO EL ALGARROBO, NORTE DE CHILE

Los depósitos de tipo óxidos de hierro-apatito (*iron oxide-apatite–IOA*) de la Cordillera de la Costa del norte de Chile se encuentran espacialmente asociados a intrusivos de edad Jurásica Tardía a Cretácica Temprana sugiriendo una conexión genética entre las intrusiones y los cuerpos de Fe. En este trabajo, por medio del estudio de la petrocronología del circón con LA-ICP-MS, se reportan las características geoquímicas de intrusiones relacionadas a depósitos IOA en el distrito El Algarrobo y se compara con intrusivos relacionados a pórfidos Cretácicos presentes en el mismo distrito con el fin de comprender la evolución magmática y encontrar indicadores de fertilidad de magmas para la formación de yacimientos tipo IOA.

Los resultados más relevantes muestran que el periodo de formación de depósitos tipo IOA (~128–123 Ma) está marcado por intrusivos con un contenido de agua relativamente bajo, evidenciado por una razón de Eu/Eu*<3, y condiciones redox reducidas (ΔFMQ<+1). En contraste, en el periodo asociado a pórfidos de Cu-Mo±Au, se produce un marcado aumento del contenido de agua en los magmas (Eu/Eu* hasta 0.7) y de la fugacidad de oxígeno (ΔFMQ hasta +2.3), permitiendo un incremento en el contenido de azufre de los intrusivos resultantes. Estas diferencias en la geoquímica de los intrusivos se interpretan como reflejo de un cambio en las condiciones tectónicas desde un ambiente extensional a uno compresivo, que conlleva a mayores tiempos de residencia de los magmas en zonas profundas de la corteza, incrementando los contenidos de H_2O por acumulación y reposición multicílica.

Finalmente, se proponen condiciones magmáticas fértiles para la formación de yacimientos IOA, marcadas por intrusivos pobres en agua y relativamente reducidos representados por un $(Eu/Eu^*/(Dy/Yb)_N$ <3 y ΔFMQ<+1 (incluso < 0). Las condiciones de fugacidad de oxígeno reducidas en intrusivos asociados a depósitos IOA (ΔFMQ <0), son consideradas poco comunes en ambientes de arco y pueden tener un rol crucial en la fertilidad. Se plantean tres posibles orígenes, considerando (i) asimilación de rocas grafíticas, (ii) fuente del manto reducida y (iii), reducción por cristalización y segregación de altas cantidades de magnetita, siendo esta última, la opción más favorecida por la relación existente entre los cuerpos de hierro y los magmas. Este estudio aporta información relevante para determinar magmas parentales con condiciones óptimas para la acumulación de magnetita masiva y deben ser probadas en otros distritos IOA Andinos y de otras partes del mundo.

Para mi familia

Mi mamá

Mi papá

Mi hermano

Y mis abuelas

AGRADECIMIENTOS

Quisiera agradecer en primer lugar a los tres integrantes de la comisión evaluadora del presente trabajo: Dr. Fernando Barra, Dr. Martin Reich y Dr. Santiago Tassara. Punto especial para destacar en mis agradecimientos es para mí profesor guía, el Dr. Fernando Barra, a quien agradezco la confianza para incluirme en este trabajo, la preocupación día a día en todos los aspectos y todo lo que he aprendido de el en estos años. También para el Dr. Martin Reich, a quien agradezco su disposición para ayudar en la discusión del trabajo y sus valiosos puntos de vista en los problemas científicos que se abordaron. Ambos profesores inculcan una pasión por las ciencias y ganas de seguir aprendiendo y creciendo siempre. Agradecimientos especiales para el Dr. Santiago Tassara por la gentileza de aceptar ser parte de la comisión desde una institución externa y poder enriquecer aún más este trabajo.

Este trabajo fue financiado por los proyectos FONDECYT-1190105: "Source and Metal Fertility of Magmas from the Early Jurassic to Late Cretaceous Continental Magmatic Arc, Coastal Cordillera of Northern Chile (26° to 30°S)" y por la Iniciativa Científica Milenio a través del Núcleo Milenio Trazadores de Metales en Zonas de Subducción, NC130065.

Agradezco a la Compañía Minera del Pacífico, en especial a Makarina Orellana, por facilitarnos el acceso a las dependencias del distrito El Algarrobo y a la mina El Algarrobo.

De igual forma quiero agradecer a mis padres y familia por todo el apoyo que siempre me han dado en cada cosa nueva que hago, por darme todo para poder tener una etapa universitaria inmejorable y por todas las enseñanzas que me dan para ser siempre alguien mejor. Agradezco a mi madre por todo lo que me ha entregado, por preocuparse que tenga todo y más de lo que necesito, por el amor incondicional y ser la persona que siempre cree en mí. Agradezco a mi padre por impulsarme siempre a crecer, a aventurarme en nuevos desafíos y por su apoyo incondicional en cada paso que dé. Agradezco también a mis dos abuelas, siempre deseándome lo mejor y dando una energía extra cada vez que las veo, sean eternas.

Infinitos agradecimientos a todos mis amigos que son pilar fundamental en mi día a día. Punto aparte va para mis grandes amigos desde el inicio de la universidad: Bruno, Chris, Ignacio y Piero. Son lo mejor que me pudo haber dado la universidad y una inspiración diaria. Agradecer también a todos los amigos de geología que conocí en el camino, son un grupo increíble y esas tardes en el patio de los naranjos son algo que quedará para toda la vida. No puedo olvidar a Matías y Gianfri, amigos del colegio y Limache que siempre estuvieron y estarán para cualquier cosa. Por último, agradecer a los amigos del núcleo milenio que hicieron que estos años extra de universidad sean de la mejor forma, con buenos cafés, conversaciones, juntas y ayuda en el trabajo, en especial Diego, Mary, Rurik y Salo.

Finalmente agradecer a todos los funcionarios del Departamento de Geología, sin duda que ayudan a tener días amenos en la universidad y poder estudiar de la mejor forma.

Tabla de Contenido

Índice de Tablas

Índice de Figuras

Capítulo 1

Introducción

Los depósitos *Iron Oxide-Apatite (IOA)* representan una de las principales fuentes de hierro y potencialmente de elementos críticos como tierras raras (REE), U, F, P, Co, Bi y Nb (Hitzman, 2000; Barton, 2013; Reich et al., 2022; Skirrow, 2022). Estos yacimientos tienen una distribución mundial y son comúnmente encontrados en provincias volcánicas y/o plutónicas con edades que van desde el Paleoproterozoico (Ej. Kiruna, Suecia) al Pleistoceno (Reich et al., 2022). Dada su complejidad geológica, han sido materia de debate en cuanto a su origen, ambiente tectónico, fuente de metales y fluidos mineralizantes (Williams et al., 2005; Barton 2013; Reich et al., 2022).

En Chile, los depósitos IOA, en conjunto con los Iron-Oxide-Copper-Gold (IOCG), son reconocidos ampliamente en una restringida franja en la Cordillera de la Costa del norte de Chile entre los 21° y 31° S. Están asociados espacialmente a intrusivos de edades del Jurásico Tardío al Cretácico Temprano y al Sistema de Falla Atacama (Grocott y Taylor, 2002; Sillitoe, 2003; Barra et al., 2017), una estructura que se extiende por más de 1000 km por la Cordillera de la Costa (Scheuber y Andriessen, 1990; Cembrano et al., 2005). La Cordillera de la Costa también alberga otros tipos de depósitos, incluyendo los estratoligados de Cu-Ag (Maksaev y Zentilli, 2002) y pequeños pórfidos Cretácicos de Cu-Mo±Au (Maksaev et al., 2010). Estos, en conjunto con los IOA e IOCG, constituyen una importante provincia metalogénica.

Las investigaciones realizadas para los yacimientos IOA e IOCG andinos en la última década han demostrado que la formación de estos depósitos se debe a un proceso de origen magmático-hidrotermal, relacionado con la formación y emplazamiento de rocas intrusivas del Mesozoico (Barra et al., 2017; Rojas et al., 2018). Sin embargo, el origen de los depósitos IOA aún es materia de debate, donde modelos magmáticos-hidrotermales y ortomagmáticos han sido propuestos (Naslund et al., 2002; Knipping et al., 2015a,b; Velasco et al., 2016; Simon et al., 2018; Lledo et al., 2020; Reich et al., 2022). Estudios recientes realizados en yacimientos del tipo IOA andinos, permiten postular un nuevo modelo magmático-hidrotermal que permite explicar su origen por medio de la flotación de magnetita primaria de origen ígneo a la cual se adosan burbujas de fluido hipersalino, que permite que estos granos de magnetita asciendan y se acumulen. Adicionalmente, el fluido puede incorporar Fe y otros metales del magma para después ascender en la corteza por medio de estructuras y precipitar la carga metálica formando los depósitos tipo IOA (Knipping et al.,2015a,b; Simon et al., 2018; Salazar et al., 2019; Palma et al., 2020).

Este modelo es consistente con la observación de escasa presencia de sulfuros, principalmente pirita y menor calcopirita (Reich et al., 2016), y la presencia de una mineralización

tipo IOA (magnetita masiva + actinolita + apatito) en profundidad o espacialmente relacionada con los cuerpos de mena de Cu-Fe en yacimientos tipo IOCG (Benavides et al., 2016; Rieger et al., 2010; Barra et al., 2017; del Real et al., 2018).

Por otro lado, la relación espacial y temporal de los IOA con intrusiones de composición intermedia ha llevado a algunos autores a postular una conexión genética entre los yacimientos de hierro y el magmatismo (Espinoza et al., 1996; Sillitoe, 2003; Rojas et al., 2018; Reich et al., 2022). No obstante, existe escasa información sobre las características geoquímicas de las unidades plutónicas relacionadas a los depósitos tipo IOA. Es por esto, que comprender las condiciones magmáticas de las intrusiones relacionadas a estos cuerpos de hierro es de gran importancia para entender los procesos metalogénicos asociados a la formación de estos yacimientos y como herramienta de exploración.

El circón ($ZrSiO_4$) es un mineral que ha sido ampliamente usado en petrocronología debido a que se considera un mineral robusto geoquímicamente por ser altamente resistente a alteraciones hidrotermales e interacción con fluidos (Cherniak y Watson, 2003). Además, el circón provee un registro químico del ambiente en donde cristaliza debido al fraccionamiento de distintos elementos traza que pueden incorporarse en su estructura, incluyendo las REE, Y, Ti, Hf, Th y U (Hoskin y Schaltegger, 2003). Por otro lado, este mineral es comúnmente utilizado para dataciones U-Pb, lo que permite determinar cambios geoquímicos entre episodios magmáticos dentro de un sistema orogénico y también eventos magmático-hidrotermales formadores de yacimientos (Ballard et al., 2002; Davis et al., 2003; Dilles et al., 2015; Balica et al 2020).

En los últimos años, la petrocronología del circón ha sido utilizada para determinar la "fertilidad de metales" de fases intrusivas asociadas a depósitos minerales, especialmente en yacimientos de tipo pórfidos de Cu-Mo. La determinación y análisis de elementos traza en circones permiten obtener información del contenido de agua, estado de oxidación y fuente magmática, lo que ha sido usado para establecer condiciones de fertilidad metálica de intrusivos y su potencial para generar un depósito tipo pórfido (Lu et al., 2016; Loader et al., 2017; Lee et al., 2017,2021). Otros estudios, también han utilizado técnicas similares para determinar condiciones de evolución de arcos magmáticos, identificando factores como espesor cortical, naturaleza de fluidos y enriquecimiento de la fuente magmática (Grimes et al., 2015; Balica et al., 2020; Jara et al., 2021a,b). Por lo tanto, las concentraciones de elementos traza en circones pueden ser usadas para evaluar el potencial de un intrusivo de generar mineralizaciones asociadas, entregando ventajas para la exploración para distinguir intrusiones que pueden ser fértiles de aquellas estériles.

En este estudio, se busca determinar las signaturas geoquímicas de intrusivos asociados espacialmente a depósitos IOA de la Cordillera de la Costa en el norte de Chile. Para esto, se realizó un estudio geocronológico y de elementos traza en circones con el fin de identificar procesos, características y posibles identificadores de fertilidad para estos yacimientos en el magma parental.

El distrito El Algarrobo, situado al SW de la ciudad de Vallenar, en la región de Atacama, Chile, se presenta como un lugar ideal para este estudio debido a la presencia de numerosos depósitos IOA, incluyendo el yacimiento El Algarrobo (142 Mt @ 46% de Fe (Compañía Minera del Pacífico, 2021) y otros depósitos pequeños tipo IOA (Ojos de Agua) e IOCG (Alcaparra D). Estos depósitos están situados inmediatamente al lado de grandes intrusivos de edad Cretácica Temprana, los cuales se disponen en formas alargadas con una orientación N-S, situándose los más antiguos hacia el oeste y progresivamente más jóvenes hacia el este. Además, al este del mismo distrito y a menos de 10 km, se presentan intrusivos con edades de finales del Cretácico Temprano (~95 Ma) con mineralización tipo pórfido (Arévalo et al., 2009). De esta manera, el área de estudio permite realizar un muestreo a lo largo de una transecta E-W que abarca intrusivos desde los ~135 Ma hasta los ~95 Ma, los cuales están relacionados a depósitos tipo IOA y pórfidos de Cu.

Este estudio presenta el análisis de nuevos datos de elementos traza y dataciones U-Pb obtenidos mediante ablación laser acoplado a un espectrómetro de masas de inducción de plasma (LA-ICP-MS) de circones (n=381) provenientes de un set de quince muestras de intrusivos, en conjunto a seis muestras previamente reportadas (Jara et al., 2021a). Las muestras analizadas corresponden a cuatro complejos plutónicos (Infiernillo, Retamilla, La Higuera y Camarones, Figura 3) en el distrito El Algarrobo (28–29°S) y representan la evolución magmática en un rango de 40 Ma dentro del distrito. Utilizando distintos parámetros geoquímicos basados en la petrocronología del circón se pudo identificar condiciones de contenido de agua, estado de oxidación e inferir procesos tectono-magmáticos asociados para un mejor entendimiento de las condiciones magmáticas durante el Cretácico Temprano y que llevaron a la formación de yacimientos del tipo IOA y la transición a una nueva etapa en donde se desarrollan los pórfidos cupríferos hacia finales del Cretácico Temprano.

1.1 Objetivos

1.1.1 Objetivo General

El objetivo general del presente estudio consiste en determinar la evolución magmática de cuerpos intrusivos asociados a yacimientos IOA, así como obtener indicadores de fertilidad magmática para dichos yacimientos mediante el análisis de la geoquímica y geocronología de los circones presentes en plutones del distrito minero El Algarrobo.

1.1.2 Objetivos específicos

- Determinar la geocronología de los intrusivos presentes en el distrito El Algarrobo mediante el método U-Pb en circones, con el fin de establecer una secuencia temporal de la evolución magmática en el área de estudio.

- Realizar una caracterización química detallada de elementos traza en circones de los intrusivos del distrito El Algarrobo, con el propósito de identificar los procesos magmáticos que dieron lugar a su formación.

- Analizar las características y variaciones geoquímicas de los intrusivos del distrito El Algarrobo, con el objetivo de comprender la evolución magmática durante el Cretácico y su relación con la formación de yacimientos minerales.

- Establecer indicadores de fertilidad magmática para yacimientos IOA mediante la comparación con intrusivos estériles y pórfidos Cretácicos.

- Elaborar un modelo metalogenético para el Cretácico Temprano con el propósito de establecer un marco de referencia conceptual útil para la exploración de depósitos tipo IOA.

1.2 Hipótesis

Se plantea que los yacimientos tipo óxidos de hierro con apatito (IOA) son el resultado de condiciones magmáticas particulares y que difieren de aquellas relacionadas a la formación de depósitos tipo pórfido de Cu-Mo, es decir, los intrusivos asociados a IOA tienen características distintas de contenido de agua, fugacidad de oxígeno, espesor de corteza y profundidad a la cual ocurre la diferenciación magmática.

Las concentraciones y razones elementales en circones proporcionan información fundamental de las características fisicoquímicas de los magmas parentales y los procesos magmáticos que participan en la génesis de dichos depósitos, de tal manera que es posible identificar indicadores de fertilidad magmática para yacimientos IOA de la misma manera que se han determinado para depósitos tipo pórfido.

1.3 Ubicación y vías de acceso

El distrito El Algarrobo se ubica en la Región de Atacama, a 21 kilómetros al sur oeste de la ciudad de Vallenar, al sur del río Huasco en un valle NNE comprendido entre las sierras Maitencillo y Retamilla por el oeste y las sierras Estancilla y Cruz de Cana por el este. Las coordenadas 28°44'20"S y 70°57'51"O corresponden al punto central del distrito.

El acceso se realiza por la ruta C-486 la cual se interna por el valle hasta llegar al campamento minero El Algarrobo cruzando el distrito o alternativamente desde la localidad de Maitencillo por la ruta C-472, la cual empalma con la ruta C-486 mencionada anteriormente.

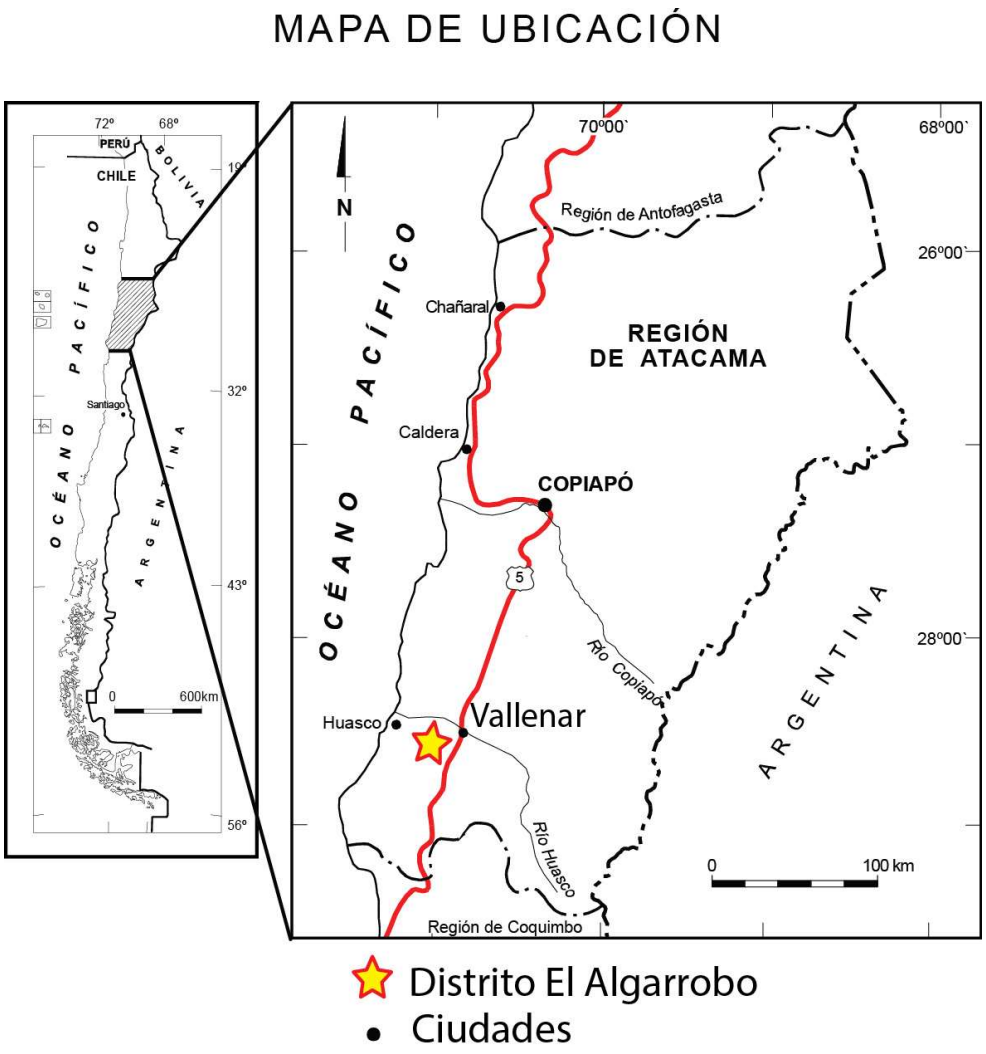

Figura 1: Ubicación del distrito El Algarrobo

Capítulo 2

Marco geológico

2.2 Generalidades

La zona de estudio se encuentra en el dominio geomorfológico de la Cordillera de la Costa, la cual está compuesta principalmente de rocas volcánicas o volcanoclásticas Jurásicas a Cretácicas Tempranas que son intruidas por rocas intrusivas intermedias a félsicas de edad Cretácica Temprana (Moscoso et al., 1982) y que alberga varios tipos de depósitos incluyendo IOA, IOCG, pórfidos de Cu-Mo y estratoligados de Cu-Ag (Espinoza et al., 1996; Maksaev & Zentilli, 2002; Sillitoe, 2003; Richards et al., 2017). Dentro de este dominio se encuentra la denominada Franja Ferrífera Chilena (Figura 2), franja de 600 km con depósitos de hierro que ocurre en el flanco este de la Cordillera de la Costa entre los 21 y 31°S (Espinoza, 1990).

La mineralización IOA se encuentra alojada generalmente en rocas del Cretácico Temprano y Jurásico Tardío de la Formación Punta del Cobre y La Negra (Sillitoe, 2003) y se dispone en cuerpos macizos de magnetita, brechas y stockworks con cantidades variables de minerales de ganga, los cuales incluyen actinolita, apatito y menor albita, epidota y escapolita (Naslund et al., 2002; Sillitoe, 2003; Williams et al., 2005).

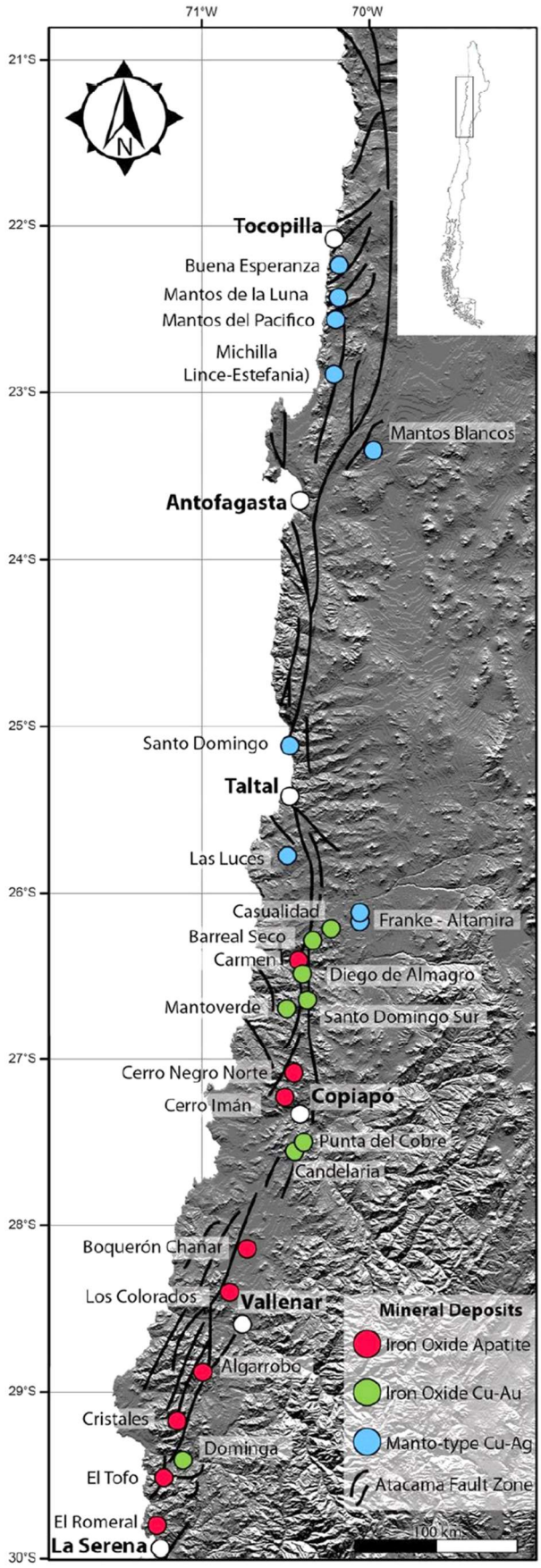

Figura 2: Mapa de la Franja Ferrífera Chilena mostrando los principales yacimientos IOA, IOCG y estratoligados de Cu-(Ag). También se muestra la traza del Sistema de Falla Atacama. Tomado de Barra et al. (2017)

El contexto tectono-magmático en el cual se formó la Franja Ferrífera Chilena y los yacimientos del clan IOCG, es un periodo generalmente considerado como un periodo extensional en respuesta al roll-back del slab. Este periodo es reconocido desde el Jurásico Medio hasta el Cretácico Temprano. Las condiciones de extensión dieron como resultado la formación de un arco magmático paralelo a la fosa y la formación de cuencas sedimentarias-marinas de tras arco (Mpodozis and Ramos, 1989; Grocott and Taylor, 2002). Estas condiciones extensionales terminan en finales del Cretácico Temprano (~125-98 Ma) para empezar un nuevo periodo de compresión y subducción tipo "Chilena", provocando inversión de las cuencas, engrosamiento cortical, migración al este del arco y exhumación del arco del Cretácico Temprano (Dallmeyer et al., 1996; Scheuber and Gonzalez, 1999; Arancibia, 2004; Maksaev et al., 2009; Seymour et al., 2020). Este cambio probablemente se produce debido a cambios en las tasas de convergencia y subducción (Mpodozis & Ramos, 1989; Charrier et al., 2007).

El régimen tectónico extensional en el Jurásico Tardío a Cretácico Temprano produce adelgazamiento cortical, rifting, intenso magmatismo de arco y un volcanismo generalizado caracterizado por grandes secuencias de lavas calco-alcalinas a shoshoníticas. La geoquímica isotópica de estas lavas indica poca o nula contaminación cortical y las signaturas isotópicas de Sr-Nd indican fuentes del manto empobrecido (Morata and Aguirre, 2003; Lucassen et al., 2006; Parada et al., 2007; Girardi, 2014). El emplazamiento de los cuerpos intrusivos tiene directa relación con el Sistema de Falla Atacama (Figura 2), conjunto de fallas NS de más de 1000 km de largo que se forma en respuesta a una subducción oblicua. Este sistema registra movimientos normales tempranos y siniestrales transtensionales tardíos (Brown et al., 1993; Scheuber and Gonzalez, 1999; Grocott and Taylor, 2002).

La zona de estudio está constituida por rocas intrusivas Cretácicas del Complejo Plutónico Retamilla y el Complejo Plutónico La Higuera, las cuales intruyen a rocas volcánicas y sedimentarias de la Formación Punta del Cobre y son cubiertas por las Gravas de Atacama y depósitos aluviales y fluviales no consolidados. Esta zona se emplaza en un bloque estructural con orientación N30°E, el cual está delimitado al oeste por la Faja Plegada y Corrida Los Colorados y al este por la Zona de Cizalle Algarrobo asociadas a la Zona de Falla Atacama (Grocott and Taylor, 2002). En conjunto con esta zona, se estudiará también por el oeste el Complejo Plutónico Infiernillo y por el este el Complejo Plutónico Camarones. Así se abarca el bloque desde el límite oeste delimitado por la Zona de Cizalle Infiernillo hasta el límite este indicado por el borde este del Complejo Plutónico Camarones (Arévalo et al., 2009) (Figura 3).

En el bloque central, al este del Complejo Plutónico Retamilla se presentan distintas mineralizaciones del clan IOCG, reconocidos desde norte a sur como Imán, Alcaparra D, Alcaparra A, Ojos de Agua, Penoso y El Algarrobo (Figura 3), todas albergadas por rocas volcánicas o sedimentarias-metamórficas de la Formación Punta del Cobre y asociadas a fallas regionales que forman parte del Sistema de Falla Atacama (Fortin, 2013; Compañía Minera del Pacífico, 2021). Estas mineralizaciones consisten principalmente en depósitos de tipo IOA, a excepción de

Alcaparra D que debido a la mayor cantidad de sulfuros presentes se ha considerado como un IOCG (Fredes, 2017). Los recursos actuales reportados para este distrito consisten en 148 Mt con 44.7% de Fe en el yacimiento El Algarrobo, mientras que 1120 Mt con 30.3% de Fe para el resto del distrito (Compañía Minera del Pacífico, 2021). En el mismo bloque, pero al norte del área de estudio se presentan también los yacimientos Sosita, Huantemé y Filipinas (Figura 3), los cuales de igual forma que en el distrito El Algarrobo se encuentran en las proximidades del Complejo Plutónico Retamilla (Arévalo & Welkner, 2008).

Al este del Complejo Plutónico La Higuera se desarrolla otra franja de depósitos tipo IOA, constituidos de norte a sur por La Japonesa, Mariposa y La Negrita (Figura 3) (Arévalo et al., 2009). La relación espacial de estas franjas de yacimientos de hierro con los complejos plutónicos Retamilla y La Higuera sugiere una relación genética entre los cuerpos de mena y el magmatismo Cretácico de la zona.

En la parte más oriental de la zona de estudio y en las cercanías del Complejo Plutónico Camarones, se reportan los yacimientos de tipo pórfido de Cu-Mo±Au Productora, Alicia y Cortadera (Figura 3), agrupados en el proyecto Costa Fuego que reporta recursos indicados de 725 Mt con ley 0.47% CuEq (cobre equivalente) conteniendo 2.8 Mt de Cu y 2.6 Moz de Au, 10.4 Moz de Ag y 67 kt de Mo (Hot Chilli limited, 2022). Estos depósitos han sido catalogados como pórfidos, aunque para el caso de Productora, se ha debatido entre depósito tipo IOCG o pórfido (Escolme et al., 2020).

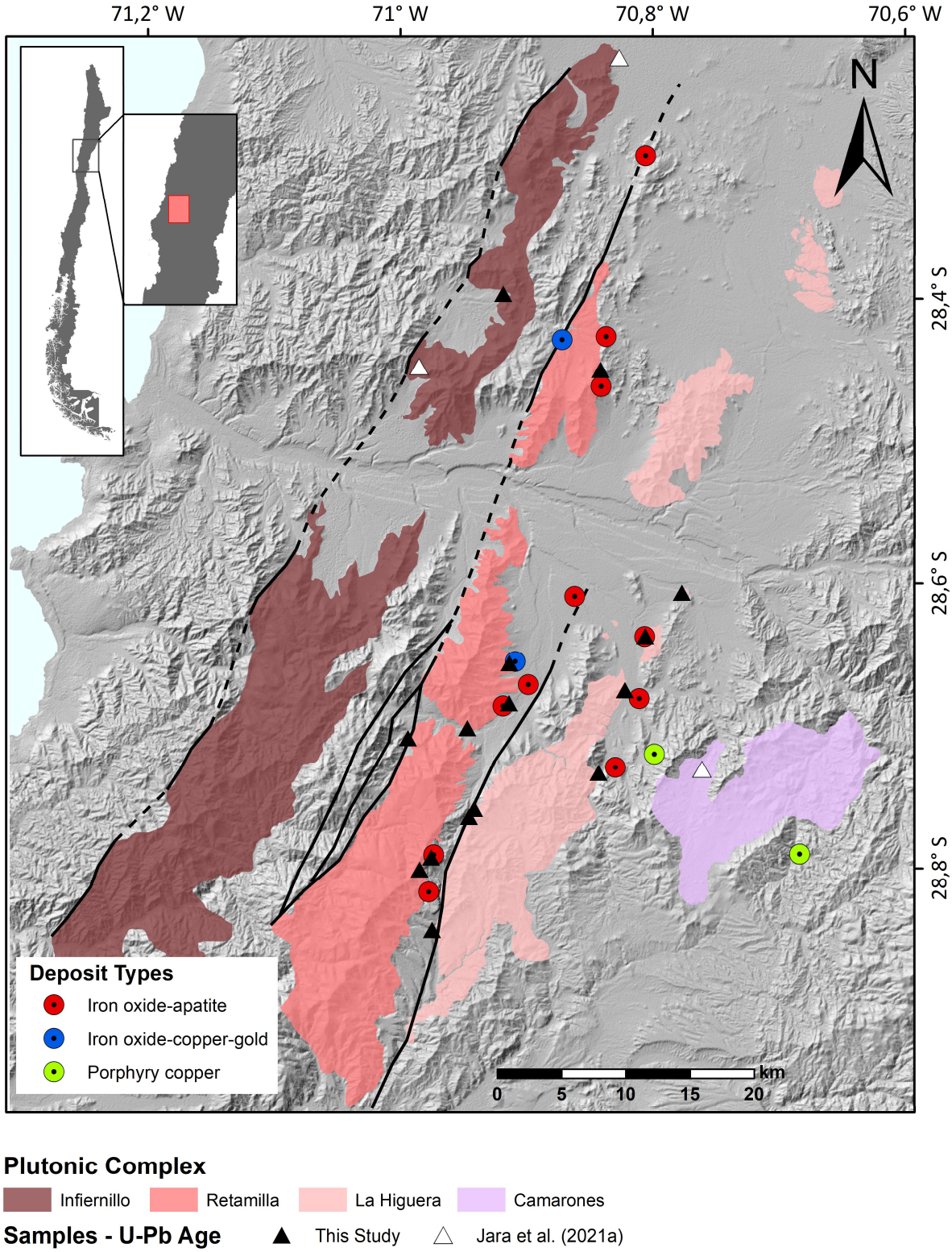

Figura 3: Ubicación de complejos plutónicos y depósitos minerales principales en el área de estudio. Se ilustran, además, las estructuras principales de la zona.

2.3 Rocas intrusivas

2.3.1. Complejo Plutónico Infiernillo

Este complejo aflora en la parte más occidental de la zona de estudio. Se reconoce como una alargada franja NNE que se extiende por más de 60 km. En relación a sus contactos, por el este, subyace a la Formación Punta del Cobre mientras que por el oeste intruye a lavas de la Formación La Negra en contacto por falla (Zona de Cizalle Infiernillo) que incluye una franja milonítica. La Zona de Cizalle Infiernillo representa la rama más occidental del Sistema de Falla Atacama en estas latitudes (Arévalo and Welkner, 2008).

La litología del Complejo Plutónico Infiernillo se divide en dos unidades, una superior correspondiente a dioritas verdosas de piroxeno y anfíboles, con algunas zonas menores de dioritas cuarcíferas y una alteración de clorita y actinolita. La unidad inferior, se presenta como una granodiorita rosada con biotita, anfíbola y ocasional piroxeno como minerales ferromagnesianos principales. En ciertas zonas la litología varía localmente a tonalitas y granitos. En la zona proximal a la Zona de Cizalle Infiernillo, se desarrolla una foliación magmática vertical (Arévalo and Welkner, 2008; Arévalo et al., 2009). Basado en su geometría, unidades y zonas foliadas, se ha interpretado que se habría emplazado por una acreción sucesiva, en donde las capas de intrusivo se desarrollan desde arriba hacia abajo, facilitadas por el espacio creado por el descenso del piso plutónico en una falla normal presente al borde del complejo (Arévalo and Welkner, 2008; Grocott et al., 2009).

Edades radiométricas de U-Pb en circón para este complejo muestran para la unidad granodiorítica edades de 128.4 ± 1.1 Ma, 128.7 ± 0.2 Ma, 129.0 ± 0.2 Ma y 136.3 ± 0.7 Ma. La unidad diorítica por su parte tiene una edad de 131.4 ± 0.2 Ma (Cruden et al., 2004; Jara et al., 2021a). Otras dataciones mediante el método $^{40}Ar/^{39}Ar$ coinciden con las de U-Pb dentro del rango de error (Valenzuela, 2002; Gipson et al., 2003).

2.3.2. Complejo Plutónico Retamilla

Este Complejo Plutónico se localiza en el centro-oeste de la zona de estudio, en una franja alargada NNE que abarca cerca de 67 km de largo. Intruye a la Formación Punta del Cobre en su lado este y en contacto por falla con las unidades inferiores de la misma formación por su lado oeste (Arévalo et al., 2009).

Su litología consta de 3 fases dispuestas en laminas que, de abajo hacia arriba, consisten en: (1) Granodioritas y tonalitas con anfíbola, piroxeno y biotita como ferromagnesianos

principales y con alteración de albita y clorita-epidota, (2) Dioritas y dioritas cuarcíferas de anfíbola y biotita y (3) una unidad microgranítica que no aflora en la zona de estudio (Arévalo et al., 2009).

De igual forma que para el Complejo Plutónico Infiernillo, y por las semejanzas a este mismo, se ha interpretado que este intrusivo se emplaza por el apilamiento vertical de láminas magmáticas subhorizontales favorecidas por los espacios generados por fallas normales adyacentes contemporáneas al emplazamiento (Arévalo et al., 2009).

Edades radiométricas disponibles para este intrusivo corresponden sólo a dataciones $Ar^{40}/^{39}Ar$ y K-Ar, las cuales representan un rango acotado entre 126 y 127 Ma (Valenzuela, 2002; Arévalo and Welkner, 2008; Arévalo et al., 2009).

2.3.3. Complejo Plutónico La Higuera

Corresponde a un intrusivo que de igual forma que los anteriores, se dispone en una franja alargada NNE que se extiende por 53 km. Intruye a rocas de la Formación Punta del Cobre por el este, mientras que por su lado oeste está delimitado por una franja de rocas miloníticas con mineralogía de bajo grado correspondiente a la Zona de Cizalle Algarrobo (Arévalo et al., 2009).

La litología de este complejo consta de dos unidades laminares subhorizontales, en donde la superior corresponde a dioritas y dioritas cuarcíferas de piroxeno y anfiboles, mientras que la inferior se expone como granodioritas y tonalitas de anfiboles, biotita y piroxenos (Arévalo et al., 2009). De la misma forma que para el Complejo Plutónico Infiernillo y Retamilla, se interpreta el crecimiento de esta unidad favorecida por fallas normales construyéndose en laminas subhorizontales de arriba abajo.

Edades $Ar^{40}/^{39}Ar$ para la unidad inferior indican una edad de 122-124 Ma (Valenzuela, 2002; Arévalo and Welkner, 2008; Arévalo et al., 2009), mientras que la unidad superior tiene una edad de 123.7 ± 0.9 Ma (Gipson et al., 2003).

2.3.4. Complejo Plutónico Camarones

Este Complejo Plutónico corresponde a el más oriental de los estudiados en este trabajo. Se dispone como un cuerpo irregular con una superficie de exposición de cerca de 8 km^2, emplazado entre rocas de la Formación Punta del Cobre, Nantoco y Totoralillo (Arévalo et al., 2009).

Este intrusivo se compone principalmente de granodioritas de biotita y anfíbol, aunque en algunas zonas se presenta otra fase diorítica porfídica y microporfídica de anfíbola, piroxeno y con biotita secundaria (Arévalo et al., 2009). Dataciones U-Pb en circón muestran para la unidad diorítica edades de 96.1 ± 0.2 Ma y 97.3 ± 0.7 Ma (Fox, 2000; Jara et al., 2021a), mientras que para la unidad granodiorítica edades de 97.3 ± 0.5 Ma, 96.2 ± 1.7 Ma, 95.1 ± 0.4 Ma y 94.8 ± 1.2 Ma (Jara et al., 2021a).

Las principales características de los intrusivos estudiados se resumen en la Tabla 1.

Tabla 1: Ubicación geográfica (punto central), edades reportadas anteriormente y principales características de los complejos plutónicos estudiados.

Complejo Plutónico	Coordenadas UTM		Composición	Descripción General	Edades Reportadas Previamente (Ma)	Referencias
	N	E				
Infiernillo	6851856	307138	Diorita (Px - Amp) Granodiorita (Bt - Amp - Px)	Cuerpo elongado y tabular que se extiende por más de 60 km en una dirección NNE. Al oeste es delimitado por la Zona de Cizalle Infiernillo y al este intruye a la Fm. Punta del Cobre	128-136	(Valenzuela, 2002; Gipson et al., 2003; Cruden et al., 2004; Jara, et al., 2021a)
Retamilla	6828919	309203	Diorita - Cuarzo Diorita (Amp - Bt) Granodiorita - Tonalita (Px - Bt)	Un cuerpo alargado y compuesto de dirección NNE de más de 70 km de largo. Sus fases se presentan como cuerpos planares y tabulares. Intruye a la Fm. Punta del Cobre y en su borde oeste es delimitado por la falla Los Colorados	126-127	(Valenzuela, 2002; Arévalo and Welkner, 2008; Arévalo et al., 2009)
La Higuera	6819887	312836	Diorita - Cuarzo Diorita (Px - Amp) Granodiorita - Tonalita (Amp - Bt - Px)	Cuerpo subhorizontal compuesto de más de 70 km. Intruye a la Fm. Punta del Cobre y por el límite oeste se presenta la zona de Cizalle Algarrobo	122-124	(Valenzuela, 2002; Gipson et al., 2003; Arévalo and Welkner, 2008; Arévalo et al., 2009)
Camarones	6816996	329104	Granodiorita (Bt - Amp)	También se conoce como "Ruta 5". Se presenta como un cuerpo irregular que intruye a las formaciones Punta del Cobre, Nantoco y Totoralillo. Aflora como un cuerpo irregular de menos de 8 km2 de superficie. En algunas zonas periféricas se presentan composiciones porfíricas y micropofíricas dioríticas.	93-97	(Fox, 2000; Arévalo et al., 2009; Jara et al., 2021a)

2.4 Estructuras

La zona de estudio está incluida en el dominio de Cordillera de la Costa, en el cual en borde oriental se presenta un sistema de fallas con orientación NS-NNE, correspondiente a la Zona de Falla Atacama (ZFA). Esta zona de falla se reconoce desde el sur de Iquique (~20° S) hasta las cercanías de El Romeral en la Región de Coquimbo (~30° S), donde los grandes depósitos de hierro de la Franja Ferrífera Chilena (El Tofo, Los Colorados, El Algarrobo, El Romeral) han sido asociados a ella (Moscoso et al., 1982). La ZFA consiste en una serie de ramas marcadas por zonas de cizalle dúctiles y fallas frágiles de orientación NNW, N y NNE. Los movimientos de estas fallas han sido descritos por varios autores como normales tempranos, seguido por siniestral transtensional y finalmente dextral-inverso como resultado de distintas configuraciones de la placa oblicua convergente (Scheuber et al., 1994; Scheuber and Gonzalez, 1999; Grocott and Taylor, 2002).

La zona de estudio se corresponde con el segmento más austral de la Zona de Falla Atacama, denominado el segmento "El Soldado" (Brown et al., 1993). En esta zona se pueden reconocer importantes rasgos estructurales, los cuales de oeste a este son: La Zona de Cizalle Infiernillo (ZCI), la Faja Plegada y Corrida Los Colorados (FPCLC) y la Zona de Cizalle Algarrobo (ZCA) (Figura 4). La ZCI representa la rama más occidental de la ZFA y corresponde a una banda de milonitas y migmatitas sinplutónicas de orientación NE a NNE, en donde las rocas dúctiles presentan una mineralogía de facies de anfibolita a esquistos verdes. La FPCLC comprende una serie de fallas y pliegues en una franja NNE de 3 km de ancho máximo, la cual se extiende por 80 km desde la mina Los Colorados hasta más al sur de la Quebrada Chañaral. Se compone de una estructura occidental y otra oriental, donde la oriental corresponde a la Falla Los Colorados y coincide con el margen occidental del Complejo Plutónico Retamilla (Arévalo and Welkner, 2008). Por último, la ZCA se expone como una franja milonítica subvertical, la cual se sitúa en el margen occidental del Complejo Plutónico La Higuera y presenta metamorfismo de bajo grado y deformación transpresiva con dirección N30°E (Arévalo et al., 2009). Estas estructuras definen bloques estructurales que presentan desplazamientos relativos verticales y horizontales y que controlarían la distribución espacial de los cuerpos mineralizados y las diferencias en geometría de la zona (Fortin, 2013).

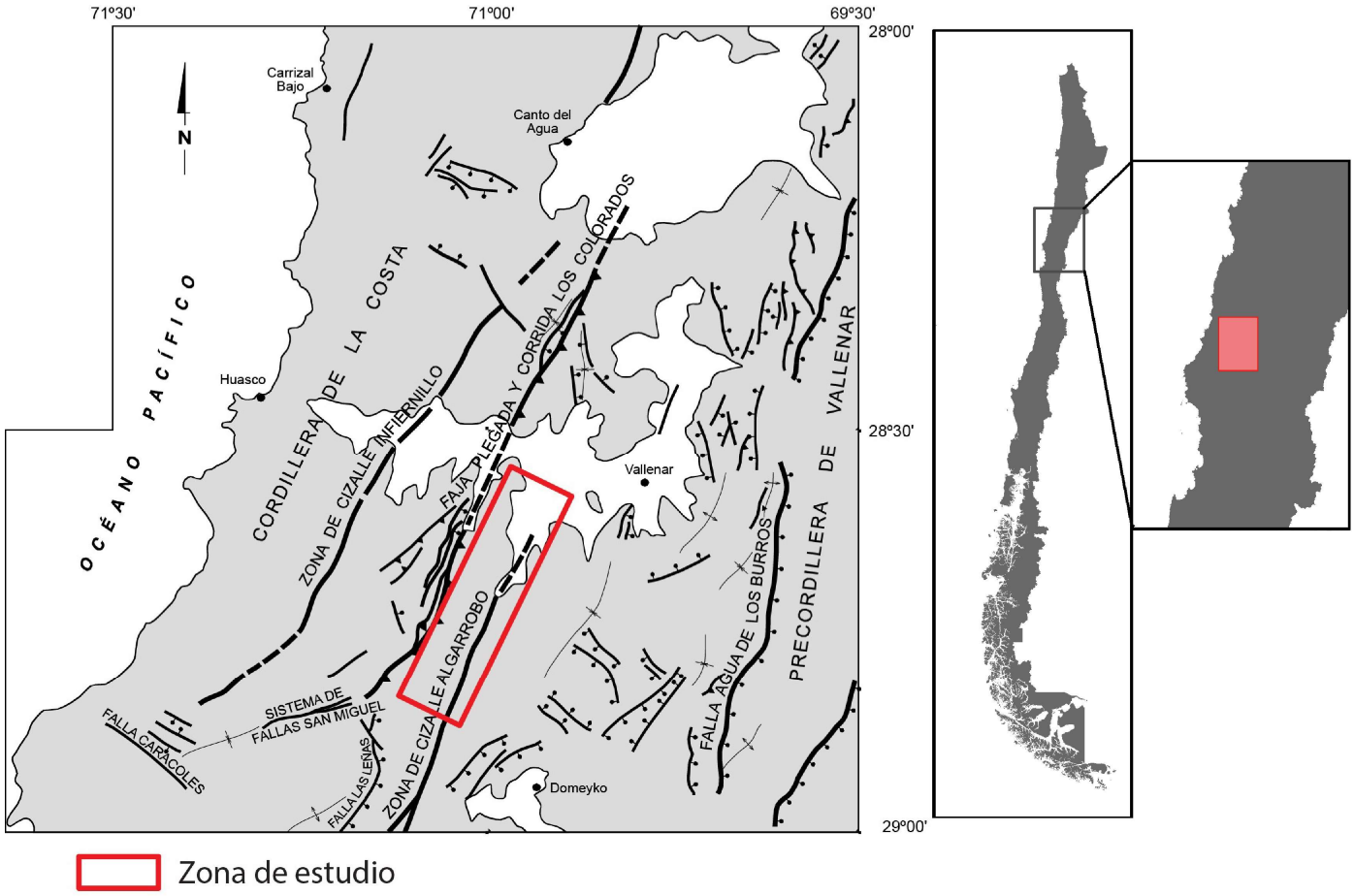

Figura 4: Contexto estructural de la zona de estudio. Modificado de Arévalo et al., 2009

Capítulo 3

Metodología

3.1 Recolección de muestras y láminas delgadas

Veinte muestras de rocas intrusivas fueron recolectadas en dos campañas de terreno. Las zonas de muestreo fueron seleccionadas con el fin de cubrir toda el área del distrito, obtener una representatividad de las distintas litologías dentro de los intrusivos y considerando el grado de alteración de estos. Además, se recolectaron muestras en las inmediaciones del rajo Algarrobo, con el fin de identificar si existiese alguna anomalía local relacionada al yacimiento.

Se recolectaron muestras de los complejos plutónicos Infiernillo, Retamilla y La Higuera. De estas muestras, se seleccionaron las más representativas de cada litología y ubicación para realizar láminas delgadas y caracterizarlos bajo microscopio de luz polarizada, determinando su composición y alteración. Los cortes transparentes y pulidos se confeccionaron en el laboratorio comercial Vancouver Petrographics (VanPetro), Langley, British Columbia, Canadá.

De estas muestras, quince fueron seleccionadas para la separación de circones. La ubicación geográfica de estas se ilustra en la Figure 6 y sus características se resumen en la Table 2.

3.2 Separación y montaje de circones

La separación mineral de circones se realizó en el laboratorio Zirchron LLC, Tucson, Arizona, Estados Unidos. Se enviaron aproximadamente 3 a 5 kg de roca por cada muestra. En este laboratorio, la separación se realizó según los procedimientos clásicos que siguen: Molienda por trituradoras de mandíbula o prensa hidráulica, separación de fracción pesada por mesa de agua Gemini, separación de minerales por separador magnético Frantz en distintos pasos de 0.4, 0.7, 1.0 y >1.0 amperes y por líquidos pesados.

Aproximadamente 100 circones por muestra fueron seleccionados y montados a mano en resina epoxy bajo lupa binocular. Estos montajes fueron pulidos para obtener una exposición del circón óptima y limpiados con ultrasonido para ser posteriormente analizados.

3.3 Imágenes de catodoluminescencia

A los circones montados se les tomó imágenes de catodoluminescencia (CL) para identificar posibles inclusiones minerales, texturas internas y seleccionar el mejor sitio para la ablación laser. Las imágenes fueron obtenidas con un microscopio electrónico de barrido (SEM) FEI Quanta 250 acoplado a un sensor Centaurus en la Universidad de Chile. Se tomaron imágenes individuales las cuales se unieron para formar un mosaico y tener la vista completa del montaje disponible para la siguiente etapa (Fig. 5).

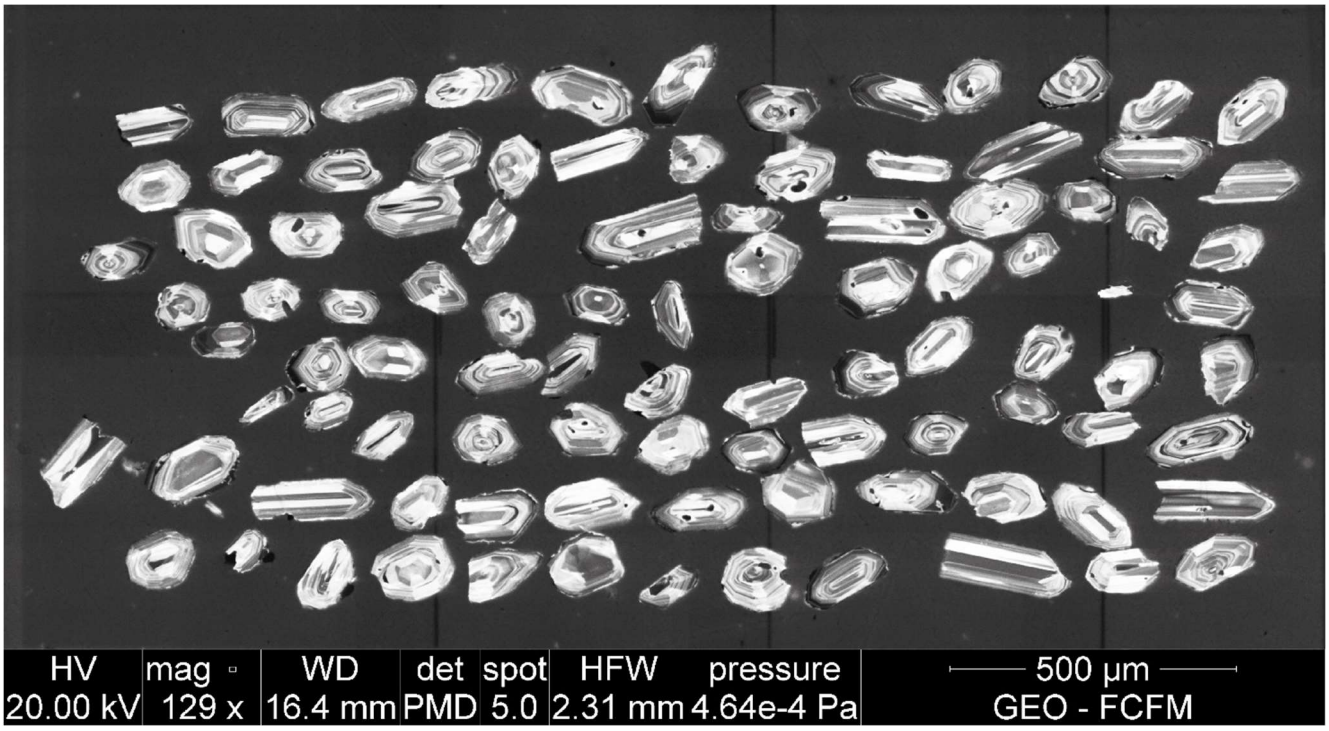

Figura 5: Ejemplo de imagen de catodoluminescencia tomada con el microscopio electrónico de barrido. La imagen corresponde a la muestra RRJP-01.

3.4 Dataciones U-Pb y determinación de concentraciones de elementos traza en circón

Las dataciones U-Pb y la determinación de elementos traza en circones se realizó simultáneamente en el laboratorio de espectrometría de masas (LEM) de la Universidad de Chile. Los análisis son efectuados ocupando con un espectrómetro de masas por inducción de plasma tipo cuadrupolo acoplado a un sistema de ablación por láser (LA-ICP-MS). El espectrómetro de masas tipo cuadrupolo corresponde a un iCAP-Q quadrupole ICP-MS (Thermo Scientific). En cuanto al sistema de ablación laser, se ocupó un equipo Photon Machines Analyte G2, el cual cuenta con un láser excímero de ArF de 193 nm que realiza la ablación en una atmosfera de He.

Para las mediciones se ocupó un haz de 50 micrones y se incluyeron como estándar primario el Plešovice (Sláma et al., 2008) y secundario el Zircon 91500 (Wiedenbeck et al., 2004) para las dataciones, mientras que para las mediciones de elementos traza se utilizó el estándar USGS NIST 610 (Jochum et al., 2011). El análisis se efectuó realizando una secuencia de mediciones de (1) dos NIST 610, dos Plešovice y dos Zircon 91500, (2) cinco circones (3) dos Plešovice y un 91500 (4) cinco circones (5) un Plešovice y un 91500 y (6) cinco circones. Esta secuencia se repite hasta obtener el número de análisis de circones deseado.

La selección e integración de señales, correcciones y calibraciones se realizaron ocupando Iolite (Paton et al., 2011) y la construcción de diagramas de concordia y promedios ponderados fueron construidos usando Isoplot 4.15 (Ludwig, 2010).

Por último, para los análisis de elementos traza en circón y para evitar el efecto de posibles inclusiones no identificadas en las imágenes CL, fueron excluidas muestras con >6 ppm de La (Grimes et al., 2015) y/o muestras en que el P, Ti, Fe, La y Ce superen el promedio más 3 desviaciones estándar dentro de cada muestra.

Capítulo 4

Evolution and fertility of magmas associated with iron oxide-apatite (IOA) deposits, El Algarrobo District, Northern Chile: A zircon petrochronology perspective

Andrés Ojeda[1,*], Fernando Barra[1], Martin Reich[1], Rurik Romero[1], María José Tapia[1]

[1]*Department of Geology and Millennium Nucleus for Metal Tracing Along Subduction, Facultad de Ciencias Físicas y Matemáticas (FCFM), Universidad de Chile, Santiago, Plaza Ercilla 803, Chile*

To be submitted to - - -

July, 2023

*Corresponding author: Andrés Ojeda

Mail: andres.ojeda.s@ug.uchile.cl

Abstract

Iron oxide-apatite (IOA) deposits in the Coastal Cordillera of northern Chile are spatially associated with Late Jurassic to Early Cretaceous intermediate granitoids. To constrain the magmatic conditions and identify possible ore fertility indicators, we used simultaneous LA-ICP-MS U-Pb dating and trace element determination in zircon crystals from intrusions related to IOA deposits in the El Algarrobo district. These data were contrasted against the geochemistry of zircon grains from felsic granitoids spatially related to Cretaceous porphyry Cu–Mo±Au east of the Algarrobo district mineralization to identify possible differences in the geochemistry of magmas leading to IOA and porphyry-type mineralization. Our data show that granitoids related to IOA deposits in the Algarrobo district formed during a ~5 Myr period (128–123 Ma) and were associated with water-poor (Eu/Eu* <0.3) and reduced (ΔFMQ from –1.5 to +1.1) intrusions, which could explain the sulfur-poor nature of IOA deposits. In contrast, felsic intrusive rocks associated with porphyry-type mineralization east of Algarrobo formed between 97 and 95 Ma and exhibit higher water content (Eu/Eu* up to 0.7) and oxidizing conditions (ΔFMQ from 0.0 to +2.2). We interpret these contrasting signatures as reflecting a change in the geodynamic setting at ~123–122 Ma— from extensional to compressional conditions— that led to progressively higher residence times of magmas at deep crustal levels, resulting in an increase in their H_2O content through episodic magma (and volatile) replenishment. Based on our zircon data, we propose potential IOA fertility indicators characterized by $(Eu/Eu^*)/(Dy/Yb)_N$ ratios <3 and relatively reduced conditions, i.e., ΔFMQ <+1. It is worth noting that anomalously reduced conditions (ΔFMQ < 0) may be a distinguishing fertility indicator. This reduced nature may result from several possible factors, but the relation with IOA deposits supports the hypothesis that it be the result of the crystallization of large amounts of igneous magnetite related to ore genesis. Reduced magmas

in arc settings are uncommon, and hence, the proposed IOA fertility indicators are a promising exploration tool that needs further testing in other Andean IOA–IOCG districts and elsewhere.

1. Introduction

Iron oxide–apatite (IOA) deposits are an important source of iron and have significant amounts of critical elements, including rare earth elements (REE), U, F, P, Co, Bi, and Nb (Hitzman, 2000; Barton, 2013; Reich et al., 2022; Skirrow, 2022). These deposits are globally distributed and are usually found in volcano-plutonic provinces of Palaeoproterozoic (e.g., Kiruna, Sweden) to Pleistocene age (e.g., El Laco, Chile) (Reich et al., 2022). Despite their importance, and mainly due to their complex geological characteristics —some of which are also common to iron oxide–copper–gold (IOCG) systems— their origin, tectonic environment, and the source of magmas, metals, and ore fluids are still a matter of debate (Naslund et al., 2002; Williams et al., 2005; Groves et al., 2010; Barton, 2013; Knipping et al., 2015a, b; Velasco et al., 2016; Hou et al., 2018; Rojas et al., 2018a; Simon et al., 2018; Salazar et al., 2019; Xie et al., 2019; Lledo et al., 2020; Tornos et al., 2021; Reich et al., 2022).

A large number of IOA deposits are distributed along the Coastal Cordillera of northern Chile (21°–31°S), in what is locally known as the Cretaceous Iron Belt (CIB). These deposits are spatially associated with Late Jurassic to Early Cretaceous intrusions of intermediate composition (Sillitoe, 2003; Grocott and Taylor, 2002; Sillitoe, 2003; Benavides et al., 2007; Barton, 2013; Barra et al., 2017; Richards et al., 2017; Simon et al., 2018; Reich et al., 2022) and the Atacama Fault System; a structural feature that extends for more than 1000 km along the Coastal Cordillera of northern Chile (Scheuber and Andriessen, 1990; Brown et al., 1993; Cembrano et al., 2005; Ruthven et al., 2020). Besides IOA deposits, the Coastal Cordillera hosts a variety of other ore deposit types including IOCG, stratabound Cu–(Ag) and porphyry Cu–Mo±Au systems of Cretaceous age, which collectively configure an important metallogenic province with world-class

IOCG deposits such as Candelaria and Mantoverde (Marschik and Fontboté, 2001; Benavides et al., 2007; Rieger et al., 2012; del Real et al., 2018).

Research conducted on IOA (and IOCG) systems in the Andean Cordillera has shown that the formation of these deposits associated with magmatic-hydrothermal processes related to the emplacement of Mesozoic plutons of intermediate composition (Sillitoe, 2003; Benavides et al., 2007; Barton, 2013; Barra et al., 2017; Richards et al., 2017; Simon et al., 2018; Reich et al., 2022). However, the origin of IOA deposits is still subject of debate, and both magmatic-hydrothermal and orthomagmatic models have been proposed (Ménard et al., 1995; Naslund et al., 2002; Knipping et al., 2015a, b; Velasco et al., 2016; Hou et al., 2018; Rojas et al., 2018a; Salazar et al., 2019; Simon et al., 2018; Xie et al., 2019; Lledo et al., 2020; Tornos et al., 2021; Reich et al., 2022). Several studies conducted on Andean IOA deposits show that they often contain low to moderate amounts of sulfides, mainly pyrite and minor chalcopyrite and that some IOCG deposits are characterized by early IOA-type mineralization assemblages, i.e., abundant magnetite + actinolite + apatite, spatially related to Cu-Fe ore bodies (Benavides et al., 2007; Rieger et al., 2010; Reich et al., 2016; Barra et al., 2017; del Real et al., 2018). In addition, the spatial and temporal relationship between IOA and granitoids of intermediate composition has led some authors to propose a genetic link between the Fe ore and magmatism (Espinoza et al., 1996; Sillitoe, 2003; Knipping et al., 2015a,b; Rojas et al., 2018b; Simon et al., 2018; Reich et al., 2022). Despite these efforts, very few studies have explored the tectono-magmatic controls and geochemistry of intrusive rocks related to IOA mineralization (e.g., Richards et al., 2017).

Zircon ($ZrSiO_4$) is an accessory mineral widely used in petrochronology studies because it is highly resistant to hydrothermal alteration (Cherniak and Watson, 2003). Because zircon crystals incorporate several trace elements within their structure, including rare earth elements (REE), Y,

Ti, Hf, Th, and U, they also serve as archives of the geochemistry of their parental magma (Hoskin and Schaltegger, 2003; Nazir et al., 2022). For instance, zircon trace element chemistry can be used to place constraints on the water content and oxidation state of magmas, as well as on source processes (Dilles et al., 2015; Lu et al., 2016; Lee et al., 2017, 2021; Loucks et al., 2020; Nathwani et al., 2021). Thus, zircon is commonly used for U–Pb dating, which, coupled with trace element studies, allows to determine the geochemical changes of magmatic episodes within orogenic systems and their relation to magmatic-hydrothermal deposits and thus may be used to discriminate between fertile and barren intrusions (Ballard et al., 2002; Davis et al., 2003; Dilles et al., 2015; Balica et al.; 2020). Several authors have used the trace element concentrations of zircon crystals to trace the evolution of continental arcs, identifying geochemical tracers for parameters such as crustal thickness, nature of fluids, and fertilization of the magmatic source (Grimes et al., 2015; Balica et al., 2020; Jara, et al., 2021a,b). In recent years, zircon petrochronology has been used to determine the ore fertility of plutonic suites associated with mineral deposits, particularly porphyry Cu–Mo systems (Lu et al., 2016; Loader et al., 2017; Lee et al., 2021).

In this study, we present a combined U–Pb crystallization ages and trace element database of zircon grains from intrusive rocks associated with IOA and IOCG deposits in the El Algarrobo district, located southwest of the town of Vallenar, in the Atacama region of northern Chile (Fig. 6). This area was selected due to the presence of numerous deposits including the large El Algarrobo IOA deposit (142 Mt @ 46% Fe; CAP, 2021), and smaller IOA (Ojos de Agua) and IOCG (Alcaparra D) prospects. These deposits are located close to large plutonic complexes of Early Cretaceous age arranged in elongated NS belts that become progressively younger to the east (Fig. 6). In addition, the Late Cretaceous (~95 Ma) Camarones Plutonic Complex east of the El Algarrobo district is coeval to the formation of porphyry Cu–Mo±Au deposits at this region

(Arévalo et al., 2009; Richards et al., 2017). Therefore, the study area comprises plutonic complexes related to different ore deposit types with ages ranging from ~135 to ~95 Ma that provides a unique opportunity to unravel the magmatic evolution and fertility signatures of intrusive rocks related to different types of magmatic-hydrothermal deposits.

2. Geological Background

2.1. Geological setting and study area

The Coastal Cordillera of northern Chile hosts several ore deposit types, including IOA, IOCG, porphyry Cu–Mo±Au, and stratabound Cu-(Ag) deposits (Espinoza et al., 1996; Maksaev and Zentilli, 2002; Sillitoe, 2003; Maksaev et al., 2006, 2010; Richards et al., 2017). The Coastal Cordillera comprises Late Jurassic to Early Cretaceous volcanic and volcano-clastic units intruded by Early Cretaceous intermediate to felsic plutons (Moscoso et al., 1982). Within the Coastal Cordillera domain, Fe-rich deposits are grouped in what is locally known as the Cretaceous Iron Belt (CIB), which extends for more than 600 km between 21° and 31°S and contains over thirty IOA and IOCG deposits (Espinoza, 1990; Sillitoe, 2003; Barra et al., 2017). The IOA mineralization comprises massive magnetite tabular bodies, breccias, and stockworks with variable amounts of gangue minerals, including actinolite, apatite, and lesser albite, epidote, and scapolite (Naslund et al., 2002; Sillitoe, 2003; Reich et al., 2022). These iron deposits are hosted mainly in andesitic volcanic rocks from the Early Cretaceous Punta del Cobre and Late Jurassic La Negra formations (Sillitoe, 2003).

The tectono-magmatic setting during the Middle Jurassic to Early Cretaceous is characterized by extensional conditions generated in response to the slab roll-back (Mpodozis and Ramos, 1989; Grocott and Taylor, 2002; Charrier et al., 2007). This regime prevailed during the

Early Cretaceous (~125–98 Ma) and resulted in crustal thinning, rifting, intense arc magmatism, and widespread volcanic activity represented by thick sequences of calc-alkaline to shoshonitic basalt and andesite lavas (Morata and Aguirre, 2003, Parada et al., 2007). The isotopic geochemistry of these lavas indicates a depleted mantle source with little or no crustal contamination (Morata and Aguirre, 2003; Lucassen et al., 2006; Girardi, 2014; Tornos et al., 2021). Emplacement of plutonic bodies was controlled by the Atacama Fault System, a set of NS faults extending over 1000 km formed in response to oblique subduction. This system recorded early normal and later transtensional sinistral displacements (Brown et al., 1993; Scheuber and Gonzalez, 1999; Grocott and Taylor, 2002; Cembrano et al., 2005; Ruthven et al., 2020). Following the extensional period and probably due to changes in the plate convergence vector and subduction rates (Mpodozis and Ramos, 1989; Charrier et al., 2007), a compressional regime at the end of the Early Cretaceous or beginning of Late Cretaceous was established with a Chilean-type subduction causing crustal thickening, basin inversion, exhumation of the Early Cretaceous arc, and eastward arc migration (Dallmeyer et al., 1996; Scheuber and Gonzalez, 1999; Arancibia, 2004; Maksaev et al., 2009; Seymour et al., 2020).

The study area comprises four Cretaceous plutonic complexes—from west to east Infiernillo, Retamilla, La Higuera, and Camarones (Fig. 6)—which intruded the volcanic and sedimentary rocks of the Punta del Cobre Formation. The central area is located within a structural block with a N30°E orientation limited to the west by the Los Colorados fold and thrust belt and to the east by the Algarrobo Shear Zone associated with the Atacama Fault System (Grocott and Taylor, 2002; Arévalo et al., 2009). Several Fe deposits occur in the central block, including Sosita, Huantemé, Filipinas, Imán, Alcaparra D, Alcaparra A, Ojos de Agua, Penoso and El Algarrobo (Fig. 6). These are IOA-type deposits, excepting the Alcaparra D IOCG deposit (Fredes, 2017).

East of the central block and La Higuera Plutonic Complex, minor IOA prospects have also been recognized, including—from north to south—La Japonesa, Mariposa, and La Negrita (Fig. 6; Arévalo et al., 2009). Further east and close to the Camarones Plutonic Complex, recent exploration efforts have identified the occurrence of porphyry Cu-Mo±Au systems, i.e., Productora, Alice and Cortadera (Fig. 6; Escolme et al., 2020). Indicated resources reported by Hot Chili Ltd. are 725 Mt grading 0.47% CuEq (copper equivalent), containing 2.9 Mt Cu, 2.7 Moz Au, 9.8 Moz Ag, and 64 kt Mo (https://www.hotchili.net.au/projects/costa-fuego-copper-project/).

2.2 Plutonic rocks

Infiernillo Plutonic Complex

The Infiernillo Plutonic Complex (IPC) is located at the westernmost part of the study area and displays a NNE orientation extending for more than 60 km (Fig. 6). It is delimited to the west by the Infiernillo Shear Zone, which represents the westernmost branch of the Atacama Fault System in the area (Arévalo and Welkner, 2008). The IPC was segmented vertically into an upper unit composed of a pyroxene and amphibole diorite with minor quartz-diorite rocks partially altered to chlorite and actinolite, and a lower that comprises pink granodiorite with biotite, amphibole, and minor pyroxene. Locally, tonalite and granite compositions also have been reported (Arévalo and Welkner, 2008; Arévalo et al., 2009). Zircon U–Pb ages for the granodiorite unit are 136.3 ± 0.7 Ma, 129.0 ± 0.2 Ma, 128.7 ± 0.2 Ma, 128.4 ± 1.1 Ma, whereas the diorite phase has been dated at 131.4 ± 0.2 Ma (Table 2; Cruden et al., 2004; Jara et al., 2021a). Biotite and amphibole $^{40}Ar/^{39}Ar$ ages range from 129 to 130 Ma for the granodiorite (Table 2; Valenzuela, 2002; Gipson et al., 2003), and agree with more recent zircon U–Pb ages.

Retamilla Plutonic Complex

The Retamilla Plutonic Complex (RPC) is located at the west-central part of the study area parallels the orientation of the Infiernillo Plutonic Complex (Fig. 6). It outcrops for ~67 km intruding the Punta del Cobre Formation on its eastern side, and is in fault contact with the lower units of the same formation on its western margin (Arévalo et al., 2009). The RPC comprises albitized granodiorite to diorite compositions with amphibole, pyroxene, and biotite (Arévalo et al., 2009). Limited radiometric age data are available for the RPC, showing that this complex was emplaced at ca. 126–127 Ma ($^{40}Ar/^{39}Ar$ and K-Ar, Table 2; Valenzuela, 2002; Arévalo and Welkner, 2008; Arévalo et al., 2009).

La Higuera Plutonic Complex

This complex also has an NNE orientation and extends for about 53 km (Fig. 6). It intrudes the Punta del Cobre Formation at its eastern margin and is limited by mylonitic rocks corresponding to the Algarrobo Shear Zone at its western margin (Arévalo et al., 2009). The La Higuera Plutonic Complex (HPC) has been subdivided in an upper unit composed of diorite and quartz diorite of pyroxene and amphibole (123.7 ± 0.9 Ma; Gipson et al., 2003), and a lower granodiorite to tonalite unit with amphibole, biotite, and pyroxene (122–124 Ma; Valenzuela, 2002; Arévalo and Welkner, 2008; Arévalo et al., 2009).

Camarones Plutonic Complex

The Camarones Plutonic Complex (CPC) is an irregular shape stock with an exposed surface of about 8 km^2, which intrudes rocks of the Punta del Cobre, Nantoco, and Totoralillo formations (Arévalo et al., 2009) (Fig. 6). The CPC comprises a biotite and amphibole granodiorite, although porphyritic and microporphyritic dioritic rocks have been locally described (Arévalo et

al., 2009). Zircon U–Pb ages of 96.1 ± 0.2 Ma and 97.3 ± 0.7 Ma for the diorite unit are similar to those for the granodiorite (97–95 Ma, Table 2; Fox, 2000; Jara et al., 2021a).

A summary of available $^{40}Ar/^{39}Ar$ and U-Pb ages for the four plutonic complexes is reported in Table 2.

3. Samples and Methods

Twenty intrusive rock samples were collected from outcrops at the Infiernillo, Retamilla, and La Higuera plutonic complexes along a transect at ~28.7°S (Fig. 6). Selected samples were examined by using polarized light microscopy to determine their modal composition and alteration mineralogy. Fifteen samples were chosen for zircon petrochronology studies (Fig. 6; Table 3). Zircon separation was performed at Zirchron LLC, Tucson, Arizona, USA. Separation was performed by using electro-pulse disaggregation followed by conventional procedures including concentration of heavy minerals in a Gemini water table, and mineral separation by Frantz magnetic separator and heavy liquids. Approximately 100 zircons per sample were hand-picked from the mineral concentrate and mounted in epoxy resin under a binocular loupe. Cathodoluminescence (CL) images were taken with an FEI Quanta 250 scanning electron microscope (SEM) coupled to a Centaurus sensor. U–Pb dating was performed simultaneously with trace element measurements with a laser ablation inductively coupled plasma mass spectrometer (LA-ICP-MS). The analyses were carried out by using a 193 nm ArF excimer laser (Photon Machine Analyte G2) coupled to an iCAP-Q quadrupole ICP-MS (Thermo Scientific) at the Mass Spectrometry Laboratory, Department of Geology, University of Chile.

For U–Pb dating, the Plešovice zircon (Sláma et al., 2008) was used as the primary standard, and Zircon 91500 as a secondary standard (Wiedenbeck et al., 2004). For trace element

quantification, the USGS NIST 610 reference material was used (Jochum et al., 2011). Signal selection and integration, corrections and calibrations were performed using Iolite (Paton et al., 2011), and Concordia and weighted average plots were constructed using Isoplot 4.15 (Ludwig, 2010). For trace element analyses in zircon, samples with >6 ppm La (Grimes et al., 2015) — or samples in which P, Ti, Fe, Fe, La, and Ce exceeded the average value plus three standard deviations within each sample— were excluded.

4. Results

The studied rock samples have a composition that ranges from diorite to granodiorite (Table 3). Hydrothermal alteration, when present, is moderate to weak and is represented mainly by albite, epidote, biotite, sericite, and chlorite. Fifteen samples were selected from the plutonic complexes for zircon U–Pb dating and trace element measurements: La Higuera (n=6), Retamilla (n=8), and Infiernillo (n=1). In addition, we re-examined previously reported zircon data from Camarones (n=4) and Infiernillo (n=2) (Jara et al., 2021a).

4.1. Zircon Morphology, Textures and U–Pb Geochronology

Analyzed zircons are transparent, prismatic, and subhedral to euhedral. Sizes typically range between 50–250 µm and have a length-to-width ratio varying from 1.0 to ~3.5–4, typical of magmatic zircon morphologies (Corfu et al., 2003). Textures revealed by cathodoluminescence images (Fig. 7) are mostly oscillatory zonation, but some samples from Retamilla and La Higuera display local evidence of recrystallization (Fig. 7b-c), probably associated with late-stage or post-magmatic cooling (Corfu et al., 2003; Bell et al., 2019).

Zircon U–Pb LA-ICP-MS ages are summarized in Table 3 and plotted in Figure 8. All data are reported in Appendix 1. The location of each sample with its respective age is also shown in

Figure 6, and Concordia diagrams and weighted average $^{206}Pb/^{238}U$ age plots are presented in Appendix 2.

The oldest unit is the Infiernillo Plutonic Complex, with ages ranging from 136.3 ± 0.7 to 128.4 ± 1.1 Ma. Retamilla U–Pb ages extend from 128.3 ± 1.0 to 126.3 ± 1.3 Ma, and La Higuera between 127.3 ± 1.0 and 121.9 ± 1.1 Ma. The youngest plutonic complex studied is Camarones, with ages varying from 97.3 ± 0.7 to 95.1 ± 0.4 Ma (Table 3, Fig. 8). An apparent magmatic gap of ~ 25 Myr, between 122 and 97 Ma, is observed in our results. However, intrusive rocks within this age range have been reported south of the studied area, i.e., El Pingo diorite (110–104 Ma) and Florida granodiorite (~101 Ma) (Arévalo et al., 2009).

4.2. Zircon Geochemistry

A summary of zircon minor and trace element concentrations, as well as geochemical indicators and elemental ratios, are presented in Table 4. All data are reported in Appendix 3.

Chondrite-normalized REE in zircon exhibit patterns typical of zircon grains of igneous rocks from continental arcs, with an enrichment in heavy REE (HREE) with respect to light REE (LREE), and positive Ce and negative Eu anomalies (Fig. 9). Zircon grains from Camarones (Fig. 9d) display a relatively smaller Eu anomaly (Eu/Eu*=0.36–0.66, 5%, and 95% percentile, respectively, $Eu/Eu^* = Eu_N/\sqrt{(Sm_N*Gd_N)}$, Table 4), similar to that observed in fertile porphyry Cu–Mo systems (Lu et al., 2016; Lee et al., 2017). Two samples, AOLH2-03 and RRJP-01, taken from the La Higuera Plutonic Complex (Fig. 9c), exhibit a smaller Eu anomaly compared to the rest of the samples of the same complex. The median Eu anomaly for AOLH2-03 and RRJP-01 is 0.41, while the median for all other La Higuera samples is 0.18 (Table 4). Moreover, these samples display REE trends that are similar to those observed in Camarones. Therefore, the samples of La

Higuera were subdivided into two groups where La Higuera-B includes samples AOLH2-03 and RRJP-01, and La Higuera-A includes the rest of the analyzed samples from this complex.

Crystallization temperature values were calculated according to the Ti-in-zircon thermometer using a SiO_2 and Ti activity of 1.0 and 0.7, respectively, based on the presence of quartz in the samples and inclusions of Ti-rich phases in zircon (Ferry and Watson, 2007). The calculated crystallization temperatures, which are plotted as a function of age in Figure 10a, show a slight decrease from ~850–750 °C at ca. 136 Ma to ~750–725 °C at 122 Ma in the La Higuera (Fig. 10a). For Camarones (95–97 Ma), temperatures increase slightly, reaching a range of ~800–740 °C (Fig. 10a-b, Table 4). Overall, the median temperature for all plutonic complexes is similar (~740–760°C, Fig. 10b).

Zircon Eu anomalies data are plotted as a function of age in Fig. 10c. Data show that during the period between 136 and 123 Ma, the Eu/Eu* ratios are considerably low (median <0.24), with a slight and progressive decrease in younger intrusive rocks, i.e., median of 0.24, 0.20 and 0.18 for the Infiernillo, Retamilla and La Higuera-A plutonic complexes, respectively (Fig. 10c-d, Table 4). Importantly, the Eu anomaly shows a sudden and marked increase at 123–122 Ma, reaching a median of 0.41 for the La Higuera-B samples. Camarones, the youngest plutonic complex, show even more higher Eu/Eu* ratios with values reaching a median of 0.55 (Fig. 10c-d, Table 4).

Figure 10e shows the magmatic oxygen fugacity (fO_2) plotted as a function of age. The zircon fO_2 was estimated based on Loucks et al. (2020) and expressed as logarithmic units above or below the Fayalite-Magnetite-Quartz buffer (ΔFMQ) with a precision of 0.6 log unit. The analysis revealed ΔFMQ values close to 0 for Infiernillo and Retamilla, with a median of approximately –0.02 and –0.19, respectively. However, there is a significant dispersion of values,

ranging from –1.19 to +0.41 for Infiernillo and from –0.94 to +1.13 for Retamilla (5-95% percentile). In the case of La Higuera-A, the median ΔFMQ decreased to –0.71, with a range between –1.52 and +0.23 (5-95% percentile). On the other hand, La Higuera-B samples exhibit an increase in ΔFMQ, with a median of +0.37 and a range of between –0.02 and +0.94 (5-95% percentile) (Fig. 10e-f and Table 4). Finally, the Camarones shows the most oxidized signature of the studies, with a median ΔFMQ of +1.05, reaching up to +2.15 (95% percentile; 5% percentile = 0.0; Table 4).

5. Discussion

5.1. Secular changes in magmatic temperature and water content

The investigated intrusive rocks exhibit similar crystallization temperatures, ranging from 850 to 725 °C (Table 4; Fig. 10a-b). These temperatures are consistent with zircon formation in equilibrium with granitoid melts, according to experimental evidence of zircon saturation in magmas and well-constrained calculated temperature data from the analysis of rocks with intermediate composition (Miller et al., 2003; Watson et al., 2006). Furthermore, the temperatures (850–725 °C) of the studied rocks are slightly higher than those reported for ore-related stocks in Oligocene–Eocene porphyry Cu–Mo deposits from the Chilean Andes (650–750 °C), but similar to those of barren intrusions in porphyry Cu systems (Dilles et al., 2015; Lee et al., 2017).

The normalized REE pattern of the zircon grains of intrusive rocks spatially associated with IOA deposits show a marked negative Eu anomaly (Fig. 9b-c), with a Eu/Eu* value of 0.1–0.3 for Retamilla and La Higuera-A (Table 4, Fig. 10c-d). This suggests a high degree of fractionation of Eu^{2+}-rich plagioclase before zircon crystallization, leaving a residual magma depleted in Eu (Hoskin et al., 2000; Hoskin and Schaltegger, 2003; Dilles et al., 2015; Lee et al., 2017; Rezeau et

al., 2019). In contrast, the Camarones complex, which is associated with the period of porphyry-type mineralization (Fig. 6), has a less pronounced Eu anomaly (Eu/Eu* mean value of 0.55; Table 4, Fig. 10c-d), indicating reduced or suppressed plagioclase crystallization before zircon. A similar effect is observed for the youngest rocks of the La Higuera Plutonic Complex (La Higuera-B: 122–123 Ma), with values close to 0.4 (Fig. 10c-d), marking an incipient suppression effect of early plagioclase crystallization.

It is well documented that amphibole fractionation produces a depletion in MREE relative to HREE in the residual magma (Davidson et al., 2007; Davidson et al., 2013; Nandedkar et al., 2016) and hence, fractionation can be inferred based on changes in a Dy_N vs. $(Yb/Dy)_N$ plot. If hornblende is being fractionated, the $(Yb/Dy)_N$ ratio should increase as the magma is depleted in Dy (Davidson et al., 2007; Davidson et al., 2013; Rezeau et al., 2019). This effect is observed in all studied samples (Fig. 11), but is more evident in La Higuera-B and Camarones, with high $(Yb/Dy)_N$ values of up to ~12.

In summary, zircon data for the intrusive rocks (128–123 Ma) associated with IOA deposits suggest that both plagioclase and hornblende crystallized before zircon. In contrast, zircon data for younger stocks more akin to porphyry Cu systems (97–95 Ma) show evidence of higher degrees of hornblende fractionation, with plagioclase crystallization being delayed. Two possible scenarios can be considered to explain this difference, which are discussed below.

In H_2O-rich magmas, a change in the saturation temperatures of minerals such as feldspar and amphibole can occur at pressures exceeding 0.2–0.3 GPa (Foden and Green, 1992; Müntener et al., 2001; Costa et al., 2004; Feig et al., 2006). At such conditions, hornblende forms earlier than plagioclase (Foden and Green, 1992; Moore et al., 1998; Müntener et al., 2001; Chiaradia et al.,

2012; Loucks, 2014). Our data suggest that magmas associated with IOA-type mineralization were H_2O-poor at the time of differentiation, resulting in the crystallization of larger amounts of plagioclase and Eu depletion of the residual magma. In contrast, and as documented by several studies, magmas associated with porphyry systems are H_2O-rich (e.g., Loucks et al., 2014; Dilles et al., 2015; Lu et al., 2016; Lee et al., 2017, 2021), suppressing plagioclase and increasing hornblende crystallization, leaving a residual magma with higher Eu/Eu* and $(Yb/Dy)_N$ ratios.

Pressure is another factor that may explain the change in the crystallization sequence, particularly in magmas that are H_2O poor. At pressures of $\gtrsim$1.0 GPa (~30 km depth), hornblende forms early, whereas plagioclase crystallizes at a later stage (Chiaradia et al., 2011, 2012; Loucks, 2014, 2021). This alternative explanation is consistent with features observed in the Camarones Plutonic Complex, where hornblende fractionation is enhanced, and plagioclase formation is delayed or suppressed. Conversely, at lower pressures ($\lesssim$1.0 GPa), plagioclase crystallizes at an early stage or at the same time as hornblende (Chiaradia et al., 2011, 2012; Loucks, 2014, 2021), suggesting that intrusive rocks with ages between ~136 and 123 Ma formed by magmas differentiated at lower pressures—where plagioclase crystallization precedes zircon formation—resulting in an Eu-depleted residual magma.

To quantify the effect of plagioclase and hornblende fractionation, the ratio $(Eu/Eu^*)/(Dy/Yb)_N$ is used. A higher $(Eu/Eu^*)/(Dy/Yb)_N$ ratio implies a suppressed or delayed plagioclase formation (i.e., higher Eu/Eu*) and a higher degree of hornblende fractionation (i.e., lower $(Dy/Yb)_N$), due to either a high magmatic H_2O content (i.e., > 4–5 wt%; Ridolfi et al., 2010; Richards, 2011; Loucks et al., 2014), or magma differentiation at depth (>~30 km; Chiaradia et al., 2011, 2012; Loucks, 2014, 2021). On the other hand, a lower $(Eu/Eu^*)/(Dy/Yb)_N$ ratio would indicate a higher plagioclase and a lower hornblende fractionation suggesting differentiation at

relatively shallow depths (<~30 km), or a low magmatic H_2O content. It should be noted that the ratio $(Dy/Yb)_N$ is taken as the denominator and not Dy_N or Yb_N (or Y, which is also incorporated in hornblende) because the ∑REE is different for each plutonic complex (Table 4). We use the $(Eu/Eu^*)/(Dy/Yb)_N$ ratio to avoid such differences and potential misinterpretations.

Figure 12 shows a plot of the $(Eu/Eu^*)/(Dy/Yb)_N$ ratio vs. age of intrusive rocks investigated here. A trend of slightly decreasing values ($\lesssim 3$) can be observed from 136 to 123 Ma. This is followed by a sharp increase in values (>3) for the period 123–95 Ma (median values of 1.66, 1.12 and 1.15 for Infiernillo, Retamilla and La Higuera-A, respectively, and 3.75 and 4.06 for La Higuera-B and Camarones, Table 4). Hence, the effect of H_2O content in the magma—or the depth at which the magma undergoes is differentiation and fractionation—decreased progressively from 136 Ma, and reached a minimum at the inferred period of magmatism related to IOA mineralization (e.g., Algarrobo, 128–123 Ma). As shown in Figure 12, the $(Eu/Eu^*)/(Dy/Yb)_N$ ratio increases abruptly at ~123 Ma, reaching values >3 in La Higuera-B and Camarones, where the latter is more aking with conditions of formation of porphyry-type mineralization. Furthermore, the geochemical trend in Figure 12a may reflect a change in the tectono-magmatic conditions at ~123 Ma. The largest degree of differentiation and fractionation processes occur at deep crustal levels, close to crust-mantle boundary, i.e., the MASH zone (Hildreth and Moorbath, 1988; Annen et al., 2006). In a thinned crust (<~30 km), these processes may occur at shallow levels, i.e., at lower pressures, and consequently, high plagioclase fractionation (and Eu sequestration) and lower hornblende formation is expected. The increase in crustal thickness after ~123 Ma would result in fractionation and differentiation at higher pressures, where hornblende formation is favored and plagioclase crystallization was either suppressed or delayed, leaving a magma enriched in Eu and relatively depleted in MREE. The latter scenario

requires development of a thick crust (>~30 km) and deepening of the Moho discontinuity over a narrow time frame of a few million years or less (Fig. 12), which seems unlikely. Indeed, the crustal thickness calculated using the whole rock La/Yb ratio (Profeta et al., 2015), carried out along a transect south of the Algarrobo district, shows a trend of gradually increasing crustal thickness from ~20–30 km to ~40 km between 135 and 90 Ma (Creixell et al., 2020). Hence, the abrupt change in $(Eu/Eu^*)/(Dy/Yb)_N$ observed at ~123 Ma does not necessarily reflect an increase in crustal thickness, which is unlikely to be a geologically rapid process (Loucks, 2021). The observed geochemical difference among plutonic complexes is thus probably related to changes in the magmatic H_2O content. Loucks (2021, and references therein), proposed that in compressional environments, magmas could stall for longer periods at the crust-mantle boundary, conditions under which residual magmas can be replenished by injection of mantle-derived melts, increasing the H_2O and other volatile content of magmas. In contrast, under extensional conditions, magmas ascend rapidly to shallower levels resulting in melts with lower water content. We interpret that the $(Eu/Eu^*)/(Dy/Yb)_N$ ratio be tracing the transition from an extensional or transtensional to a compressional or transpressive regime at around 123–122 Ma. This transition resulted in magmas progressively residing for a longer time at mid to deep crustal levels, increasing their H_2O content. The higher ratios suggest a shift in the geochemical signature, potentially reflecting the evolving tectonic regime and associated changes in the magma sources and processes occurring at deep crustal levels. This interpretation is consistent with the notion of a change in the tectonic regime from extensional to compressional (transpressive) conditions at ~125–120 Ma (Dallmeyer et al., 1996; Scheuber and Gonzalez, 1999; Grocott and Taylor, 2002; Creixell et al., 2020). Furthermore, Grocott et al. (2009) provided evidence that the Infiernillo and Retamilla plutonic complexes were emplaced during an extensional regime, and their growth was related to the development of extensional faults. This interpretation is consistent with the notion that the Early Cretaceous

intrusive rocks that are associated with IOA and IOCG deposits are more mafic than those related to porphyry-type deposits (Richards et al., 2017).

5.2 Magmatic redox conditions

Another critical parameter in intrusion-related ore deposits is the redox state or oxygen fugacity (fO_2) of magmas, which has first-order implications for the potential to form a mineral deposit (Audétat and Simon, 2012; Richards, 2015, 2021; Meng et al., 2021). In silicate melts, the transition from S^{2-} to S^{6+} occurs at $\Delta FMQ \gtrsim 1$, which has significance in terms of the solubility of sulfur, because S^{2-} is considerably less soluble than S^{6+} (Carroll and Rutherford, 1985; Nilsson and Peach, 1993; Jugo, 2009; Jugo et al., 2010; Kleinsasser et al., 2022). Hence, relatively reduced magmas ($\Delta FMQ < 1$) may undergo sulfur loss by sulfide saturation and fractionation—coupled with sequestration of siderophile and chalcophile elements—in early magmatic stages within the deep crust, reducing the potential to form a sulfide-rich, porphyry-type deposit.

The fO_2 values of the studied intrusive rocks associated with IOA deposits (136–123 Ma) are significantly different from those of the younger plutonic bodies (97–95 Ma), which have more affinity to porphyry-style mineralization (Fig. 10). The former group displays ΔFMQ values $<+1$ (median ΔFMQ of –0.02, –0.19, and –0.71 for Infiernillo, Retamilla, and La Higuera-A, respectively; Table 4), reaching values of ΔFMQ –1.52 (percentile 5%) in La Higuera-A. In contrast, the Camarones Plutonic Complex exhibit ΔFMQ values above +1 with maximum values reaching up to ΔFMQ +2.2 (median ΔFMQ = 1.1; percentile 5% ΔFMQ = 0.0; percentile 95% ΔFMQ = +2.2; Fig. 10e-f; Table 4). The relatively reduced nature of mafic to intermediate intrusions associated with IOA mineralization is consistent with their relatively poor sulfur content. This can be attributed to the early saturation of magmatic sulfides at depth, resulting in S-poor magmas with restricted capacity to transport S to mid or upper-crustal levels. In contrast, magmas

with a higher oxidation state, such as the Camarones Plutonic Complex (ΔFMQ = 0 to +2.2), can solubilize and transport larger quantities of S, which is possible later transfer to the volatile phase during late magmatic stages and yielding porphyry Cu systems. Indeed, Richards et al. (2017) reported variations in S of up to an order of magnitude greater in magmas associated with porphyry systems, in comparison to IOCG deposits in the Cretaceous Coastal Cordillera of northern Chile. Our results are in agreement with those reported by Richards et al. (2017), where the differences in sulfur content is attributed mainly to the contrasting oxidation states between magmas during different periods, i.e., 97–95 Ma: ΔFMQ = 0 to +2.2 and 136–122 Ma: ΔFMQ –1.52 to +1.1.

Although the mechanisms of magma oxidation are still a matter of debate, it is broadly accepted that processes associated with the subduction of oceanic crust are responsible for the redox state of arc magmas, mainly fluids derived from slab devolatilization that oxidized the mantle wedge (Kelley and Cottrell, 2009, 2012; Crabtree and Lange, 2012; Evans et al., 2012; Brounce et al., 2014, 2021; Richards, 2015; Grocke et al., 2016; Bénard et al., 2018; Cottrell et al., 2021; Ague et al., 2022). Some researchers have proposed that the oxidized signature of arc magmas is the result of processes within the crust, including the loss of reduced components by degassing of C-O-H-S fluids (Burgisser and Scaillet, 2007; Bell and Simon, 2011; Dilles et al., 2015; Moussallam et al., 2016), or fractional crystallization of Fe^{2+}-rich phases such as garnet at deep crustal levels (Lee et al., 2005; Chin et al., 2018; Tang et al., 2018; Lee and Tang, 2020). Regardless, the effect of these crustal processes seems to have little inference on the oxidation state of arc magmas (Crabtree and Lange, 2012; Kelley and Cottrell, 2012; Brounce et al., 2014; Grocke et al., 2016; Cottrell et al., 2021; Holycross and Cottrell, 2023). Hence, the contrasting fO_2 values observed for the two main periods is more likely the result of a change in tectono-magmatic processes from a period characterized by limited contributions of subduction-derived fluids onto the mantle wedge

(~136 and 123 Ma); i.e., a stage related to the formation of IOA deposits, to a period with a more significant input of slab fluids after 123 Ma, where Cretaceous porphyry Cu systems were formed. This interpretation is consistent with whole rock geochemistry that show a significant increase in Ba/La ratios— a commonly used geochemical indicator of slab-derived fluids to the mantle wedge (Pearce and Peate, 1995; Elliott et al., 1997; Brounce et al., 2014)— at 122–123 Ma (Jara et al., 2021a).

In summary, Early Cretaceous plutonic rocks associated with IOA deposits emplaced between ~136 to 123 Ma, were most likely derived from water-poor magmas that differentiated during a restricted period within a thinned crust (~20–30 km). Their distinct reduced signature (ΔFMQ between –1.52 and +1.13) is probably related to a diminished contribution of volatiles from the subducting slab onto the mantle wedge, a characteristic feature of the early Andean arc for the studied segment (Jara et al., 2021a,b) (Fig. 13a). At 123 Ma and as evidenced by the La Higuera-B data, tectono-magmatic conditions changed, leading to increased magmatic residence time at deep crustal levels, higher volatiles content and differentiation at higher pressures. This process may have been protracted and continuous over the period between 97 and 95 Ma, where data from the Camarones Plutonic Complex show evidence of H_2O-rich magmas that probably underwent differentiation at higher pressures (~40 km), with longer residence times, and characterized by ΔFMQ values ranging from 0.0 to +2.2, as a response to a higher volatile flux from the subducting slab (Fig. 13b).

Based on our data, we can infer a change in the geodynamic setting at ~123–122 Ma, from a period of decoupling between the oceanic and continental plates in an extensional environment and formation of IOA deposits (Fig. 13a), to a period of coupling between the plates in a

compressional regime (Jara et al., 2021a; Scheuber and Gonzalez, 1999), with conditions more favorable for the formation of sulfur-rich porphyry systems (Fig. 13b).

5.3 Ore fertility indicators

The data reported in this study provides key aspects to understand the formation of IOA deposits. Unlike porphyry fertility indicators, where zircon trace element ratios reflect hydrated and oxidized magmas (Ballard et al., 2002; Dilles et al., 2015; Lu et al., 2016; Loader et al., 2017; Lee et al., 2017, 2021), plutonic rocks related to IOA deposits have geochemical signatures that indicate water-poor and relatively low redox (ΔFMQ <1) conditions. These parameters can be assessed by using three main tools: the Eu anomaly (Eu/Eu*), the $(Dy/Yb)_N$ ratio, and the fO_2. Thus, a useful discriminator to identify intrusion-related IOA deposits is the $(Eu/Eu^*)/(Dy/Yb)_N$ ratio and the ΔFMQ value (Fig. 14). In figure 14, the field of magmas associated with IOA deposits is represented by ΔFMQ <1 and $(Eu/Eu^*)/(Dy/Yb)_N$ <3. These values could possibly overlap with barren intrusive rocks from arc settings (Dilles et al., 2015; Lu et al., 2016; Lee et al., 2017, 2021); however, plutons associated with IOA mineralization have a distinctive reduced signature with fO_2 values as low as –1.5 (median ΔFMQ for La Higuera-A = –0.7). These reduced signatures are uncommon in arc settings, where fO_2 values are close to +1 and > 0 (Richards, 2015; Cottrell et al., 2021). Therefore, we propose that these reduced values are a distinguishing characteristic of granitoids associated with IOA deposits.

Although there are no previous works on the ore fertility of Andean IOA–IOCG deposits, a recent study carried out on IOCG deposits in southern Australia report zircon Dy/Yb values between 0.2 and 0.4 and Eu/Eu* up to 0.6, resulting in a $(Eu/Eu^*)/(Dy/Yb)_N$ <3 (Wade et al., 2020). In addition, a comparison with zircon data reported by Watts and Mercer (2020) for the Mesoproterozoic Pea Ridge and Bourbon IOA deposits in the US, show similar Dy/Yb values, but

lower Eu/Eu* ratios (<0.3), and a $(Eu/Eu^*)/(Dy/Yb)_N$ <2 (Wade et al., 2020). These findings are consistent with our results independent of the composition or age of the intrusive rocks.

Figure 14 can also be used to discriminate possible fertile signatures for Cretaceous porphyry systems with ΔFMQ >1 and $(Eu/Eu^*)/(Dy/Yb)_N$ >3. The Camarones Plutonic Complex plots within this field but with significant dispersion. In comparison with previously published data for the Eocene–Oligocene El Salvador and Chuquicamata–El Abra, and the Pliocene El Teniente porphyry Cu deposits (Muñoz et al., 2012; Dilles et al., 2015; Lee et al., 2017), the Camarones complex displays similar $(Eu/Eu^*)/(Dy/Yb)_N$ values but is less oxidized than the large Andean porphyry Cu systems. Furthermore, Figure 14 also shows that the La Higuera-B intrusion (123–122 Ma) has high values of $(Eu/Eu^*)/(Dy/Yb)_N$, representing a high water content, but below ΔFMQ >1 values favorable for the formation of sulfide-rich porphyry deposits. This could be explained by a slow and gradual change of the oxidation state in the mantle wedge, a process that may take up to 10 Ma (Reagan et al., 2008; Ishizuka et al., 2011; Evans et al., 2012; Brounce et al., 2021). Thus, areas with intrusive rocks slightly younger than 123 Ma may represent unfavorable zones for porphyry deposits exploration, whereas plutons younger than ~115–110 Ma may be more favorable targets. In addition, data for Infiernillo (136–128 Ma) are largely indistinguishable from those associated with IOA deposits (La Higuera and Retamilla). Therefore, areas located along or near this plutonic complex could be of interest for further exploration of IOA deposits, where a few minor prospects have been recognized (Arévalo and Welkner, 2008; Arévalo et al., 2009).

The proposed IOA fertility indicators, as outlined in this study, hold potential for application in other IOA-IOCG districts. However, they should be used with caution and consider them as complementary to conventional exploration techniques. Further testing and validation of

these indicators in different IOA-IOCG districts are necessary to assess their robustness and reliability.

5.4 Insights on the origin of reduced arc-related intrusion

Our results show that intrusion-related IOA deposits have a reduced signature. In the case of La Higuera-A data, the fO_2 values yield a median of ΔFMQ = –0.7, which is considered anomalous in subduction-related arcs (Richards, 2015; Cottrell et al., 2021). Only a few mechanisms have been proposed to generate reduced magmas in arc settings including: (i) Crystallization and concentration of large amounts of magnetite, leading to Fe^{3+} over Fe^{2+} fractionation, which leaves a residual magma with lower Fe^{3+}/Fe^{2+} ratio, i.e., the "magnetite crisis" (Jenner et al., 2010), (ii) Assimilation of reduced crustal rocks such as graphitic metasediments (Sato, 2012; Tomkins et al., 2012, Yu et al., 2021; Tassara and Ague, 2022); however, limited $^{87}Sr/^{86}Sr$ data for Early Cretaceous rocks show a depleted mantle source with minor contamination by crustal-derived materials (Morata and Aguirre, 2003; Lucassen et al., 2006; Girardi, 2014; Tornos et al., 2021), and (iii) A reduced mantle source; this can be achieved by subduction of reduced meta-sediments, (Fig. 13a; Takagi, 2004; J. Wang et al., 2007; K. Wang et al., 2021; Ague et al., 2022; Yan et al., 2023). Recent investigations have noted a correlation between oceanic anoxia events and reduced magmas derived by subduction of organic-rich black shales formed during these events (Richards and Şengör, 2017; K. Wang et al., 2021). The early Aptian Oceanic Anoxia event occurred at ~120 Ma (Li et al., 2008; Jenkins, 2010, 2018), and could possibly be responsible for the reduced signature of intrusions reported here (La Higuera-A; 127–123 Ma). Another possible scenario is a mantle source reduction by subduction of an oceanic ridge and formation of a slab window. In this setting, reduced volatiles may ascent from the asthenospheric mantle and affect the redox state of the overlying mantle wedge (Smith et al., 2012; Cao et al.,

2016). These two scenarios for a reduced mantle source, however, are not likely because the oxidation of the mantle wedge is a slow and gradual process (Reagan et al., 2008; Ishizuka et al., 2011; Evans et al., 2012; Brounce et al., 2021), which contrasts with the abrupt change to more oxidized conditions as evidenced by La Higuera-B (123–122 Ma, median ΔFMQ = +0.37; Table 4, Fig. 10e, f).

Although is it not possible to determine the precise origin of the reduced magma signatures in the studied intrusives from the Coastal Cordillera with our approach, their direct relation to IOA deposits supports the hypothesis that these anomalous reduced conditions are a consequence of the crystallization and segregation of large amounts of significant amounts of magnetite during the formation of these magnetite-rich deposits. Consequently, these reduced conditions may be attributed to the formation of IOA deposits, and the negative ΔFMQ values could indicate the reduction of magmas with low oxygen fugacity values in arc settings (ΔFMQ ~ 0, Fig. 13a). Our study highlights the need for further research to investigate the magmatic mechanisms of formation of IOA deposits and their potential effect on reducing the oxygen fugacity of granitoids.

6. Conclusions

El Algarrobo district located between 28 and 29°S comprises IOA–IOCG and porphyry Cu systems spatially associated with plutonic complexes (Infiernillo, Retamilla, La Higuera and Camarones; Fig. 6). Our zircon petrochronology approach allowed us to constrain water content, oxidation state, and tectono-magmatic processes responsible for the formation of intrusion-related IOA deposits and porphyry Cu–Mo±Au deposits during the Early Cretaceous, covering a period of ~40 Ma within the metallogeny of the Coastal Cordillera of northern Chile.

The plutonic bodies in the El Algarrobo district spatially related to IOA mineralization were emplaced during the period 128–123 Ma. These intrusive rocks are characterized by a low water content (below saturation levels) and relatively reduced conditions for arc settings (ΔFMQ <1, minimum –1.52); this possibly explains the low content of sulfide in the associated IOA deposits due to depletion of S at depth through early precipitation of sulfides. These magmatic conditions could be directly related to an extensional (or transtensional) tectonic regime, where magmas reside for a short time at deep crustal levels, and a relatively low contribution of slab-derived volatiles resulting in a reduced mantle source. A change to a compressional regime caused an increased coupling between plates and a higher input of slab-derived volatiles to the mantle source and hence, an increase in the water content and a shift towards higher oxygen fugacity of the magmas. These tectonic conditions were likely maintained during the period 97–95 Ma (Camarones Plutonic Complex), yielding H_2O-rich magmas with a high oxidation state (ΔFMQ = 0 – +2.2), typical of porphyry Cu–Mo±Au systems and possibly IOCG deposits.

Reduced intrusions such as Higuera-A (median of ΔFMQ = –0.7) are relatively unusual in arc settings. Three scenarios have been proposed to explain these reduced signatures, but the hypothesis of the large crystallization and segregation of magnetite is favored due to the direct spatial relationship between these reduced granitoids and the magnetite-rich IOA deposits. Thus, the reduced conditions found here are a fingerprint of the magmatic process involved at the formation of an IOA deposit.

Based on our results, we propose potential IOA fertility indicators for Andean IOA deposits. Our findings indicate that intrusion-related IOA deposits are characterized by a $(Eu/Eu^*)/(Dy/Yb)_N$ ratio <3 and relatively reduced conditions (ΔFMQ <+1). It is worth noting that the anomalous reduced condition (ΔFMQ < 0) may play a crucial role in ore fertility, as it could be

directly linked to the formation of IOA deposits. We highlight the need for further studies to test these fertility indicators in other IOA districts elsewhere in order to validate their usefulness in mineral exploration.

ACKNOWLEDGMENTS

This work was funded by ANID-FONDECYT grant #1190105 “Source and Metal Fertility of Magmas from the Early Jurassic to Late Cretaceous Continental Magmatic Arc, Coastal Cordillera of Northern Chile (26° to 30°S)” to F. Barra and M. Reich, and the Millennium Science Initiative (MSI) through Millennium Nucleus for Metal Tracing along Subduction grant NC130065. The LA-ICP-MS analytical work was supported by ANID-FONDEQUIP instrumentation grant EQM120098. We are grateful to Makarina Orellana from Compañía Minera del Pacífico (CMP) for providing access to the El Algarrobo mine.

Competing interests

All authors certify that they have no affiliations with or involvement in any organization or entity with any financial interest or non-financial interest in the subject matter or materials discussed in this manuscript.

Figure Captions

FIG. 6 Spatial distribution of the plutonic complexes in the El Algarrobo district. Also shown are the location of main ore deposits and analyzed samples with their respective $^{206}Pb/^{238}U$ weighted average age (Ma). The number in brackets refers to the sample code in Table 3.

FIG. 7 Representative cathodoluminescence (CL) images for zircon grains from the studied intrusive rocks. The red circle shows the location of the laser ablation spot for U–Pb dating and trace element analysis. Laser ablation spot size = 50 µm.

FIG. 8 Summary of $^{206}Pb/^{238}U$ weighted average ages with their respective uncertainties for each plutonic complex. The number in parenthesis indicates the total zircon grains analyzed per sample. *: Data from Jara et al. (2021a).

FIG. 9 Chondrite-normalized rare earth elements plots for zircon grains of a) Infiernillo Plutonic Complex, b) Retamilla Plutonic Complex, c) La Higuera Plutonic Complex, and d) Camarones Plutonic Complex. For La Higuera Plutonic Complex (c), samples RRJP-01 and AOLH2-03 are shown as a separate group due to their different trend characterized by a less pronounced Eu anomaly. Shaded areas represent the 5–95% percentile range. Line colors refer to the median value for each sample. Normalizing values are from McDonough and Sun (1995).

FIG. 10 Physicochemical parameters for zircon vs age plots. (a) Crystallization temperature (°C); (c) Eu/Eu*; (e) ΔFMQ in log units. Large circles represent the average value for each sample with its respective $^{206}Pb/^{238}U$ weighted mean age. Open circles represent the values for each analyzed zircon. b), d), and f) Box and whisker plots for crystallization temperature (°C), Eu/Eu*, and ΔFMQ, respectively.

FIG. 11 Dy_N vs. $(Yb/Dy)_N$ plots for a) Infiernillo, b) Retamilla, c) La Higuera, and d) Camarones. All plots show patterns of hornblende fractionation, i.e., negative correlation of Dy_N and $(Yb/Dy)_N$, with samples from La Higuera-B and Camarones showing a larger $(Yb/Dy)_N$ value, possibly due to a larger fractionation of hornblende. See text for discussion.

FIG. 12 a) Plot showing the $(Eu_N/Eu^*)/(Dy/Yb)_N$ ratio vs. U–Pb zircon age (Ma) for each plutonic complex. Large circles represent the average value for each sample with its respective $^{206}Pb/^{238}U$ weighted mean age. Open circles represent the values for each zircon grain. Horizontal bars indicate the periods in which IOA (blue bar), and porphyry (green bar) type mineralization occurred. b) Box and whisker plot for the $(Eu_N/Eu^*)/(Dy/Yb)_N$ ratio for each plutonic complex.

FIG. 13 Schematic representation of the tectono-magmatic configuration for the Coastal Cordillera during the Cretaceous. The key processes are numbered 1–4. a) Formation of IOA deposits in a high-angle subduction (slab roll-back) environment (136–123 Ma). 1) Restricted slab-derived fluid contribution onto the mantle wedge; 2) formation of relatively reduced magmas ($\Delta FMQ \sim 0$); 3) short residence time of magmas at deep crustal levels due to an extensional environment; high plagioclase and low amphibole fractionation in response to H_2O-poor nature of the magma and relatively shallow depth of fractionation, and early sulfide saturation caused by limited sulfur carrying capacity of the magmas; 4) S-poor silicate melts and anomalous reduction ($\Delta FMQ < 0$) due to high crystallization and segregation of magnetite. See text for discussion. b) Formation of porphyry systems in a low-angle subduction setting (97–95 Ma). 1) High transfer of fluids to the mantle wedge; 2) production of oxidized magmas as a result of a high fluid flux from the slab; 3) stalling of magmas at deep crustal levels under a compressive tectonic regime allows for multicyclic replenishment and promotes an increase in the water content of the magmas, high amphibole production and fractionation and suppressed plagioclase precipitation; 4) emplacement

of S-rich oxidized magmas. SLM: Subcontinental Lithospheric Mantle; MASH: Melting, assimilation, storage, and homogenization. Figure modified from (Wilkinson, 2013).

FIG. 14 $(Eu_N/Eu^*)/(Dy/Yb)_N$ vs. ΔFMQ (in log units) plot for the investigated plutonic complexes. Colored-filled symbols represent the average value for each sample. Open circles represent the value for each zircon. The fertility field for IOA deposits is delimited by a $(Eu_N/Eu^*)/(Dy/Yb)_N = 3$ and ΔFMQ = 1, and includes the Retamilla Plutonic Complex and La Higuera-A. The brown gradient in this field represents uncommon conditions in arc magmas, a potential key factor in IOA fertility. Also shown is the fertility field for Andean porphyry Cu–Mo deposits (data from El Teniente, Muñoz et al. (2012); Chuquicamata–El Abra, Dilles et al. (2015); and El Salvador, Lee et al. (2017). See text for discussion.

Figures

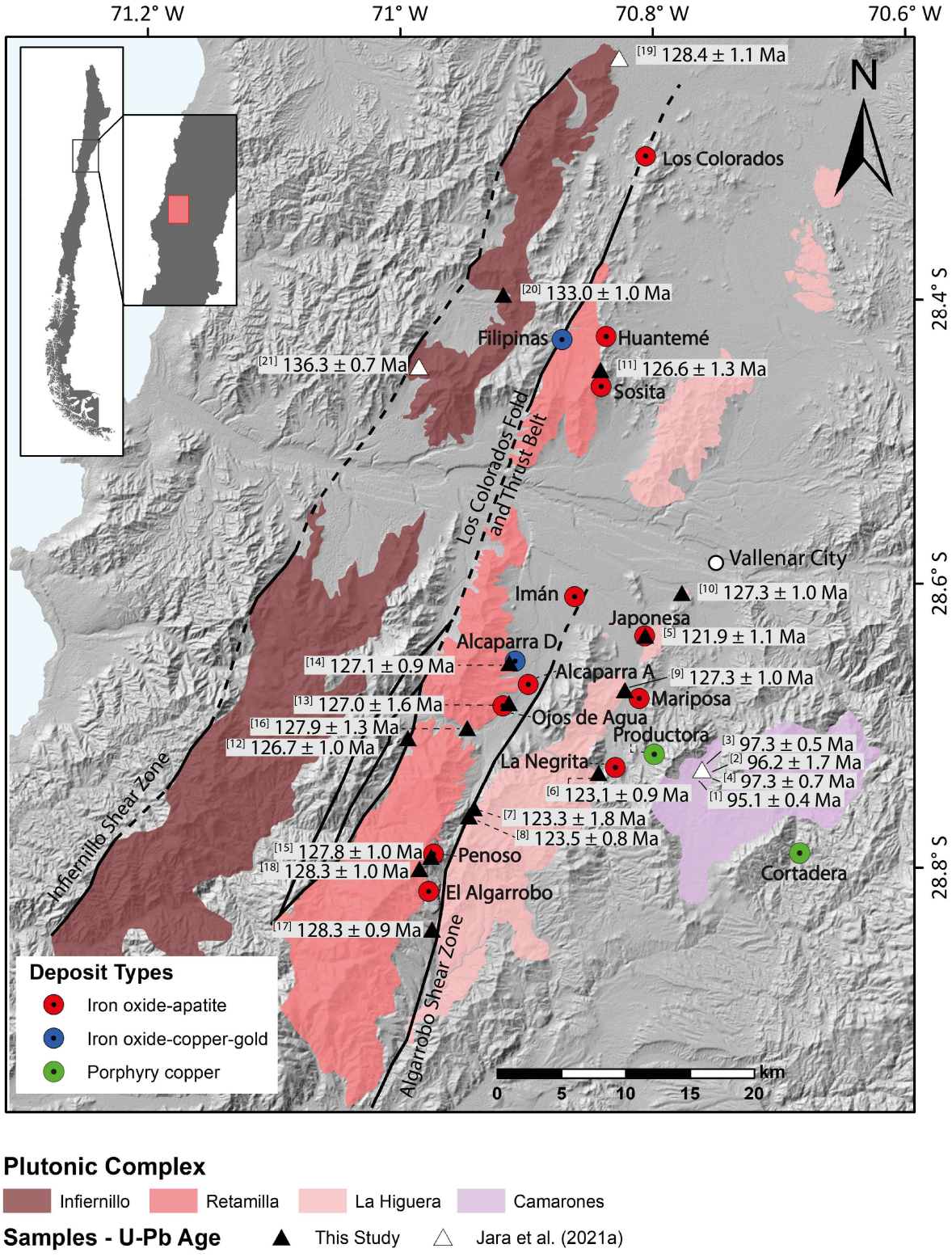

Figure 6

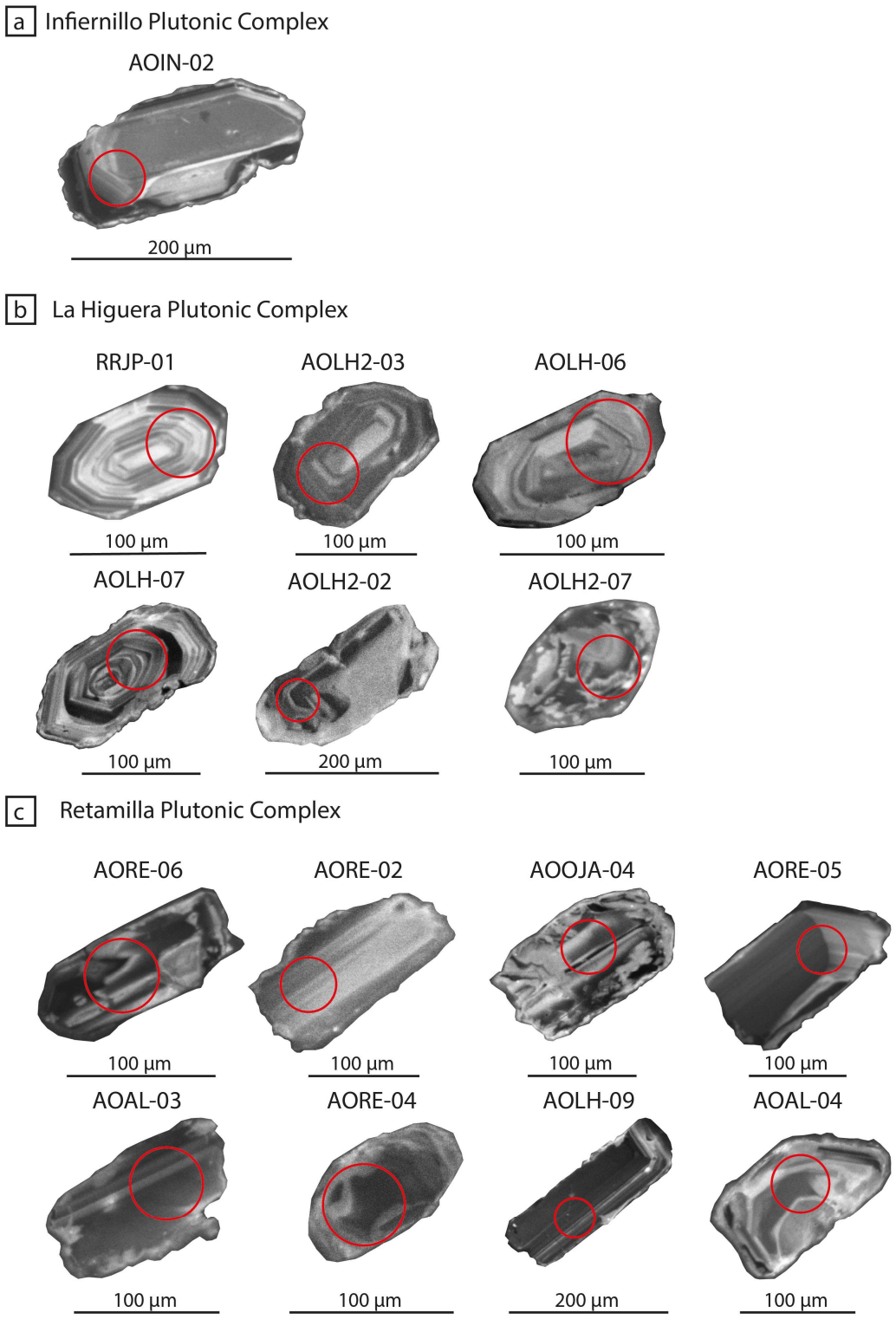
a Infiernillo Plutonic Complex
AOIN-02
200 µm
b La Higuera Plutonic Complex
RRJP-01
100 µm
AOLH2-03
100 µm
AOLH-06
100 µm
AOLH-07
100 µm
AOLH2-02
200 µm
AOLH2-07
100 µm
c Retamilla Plutonic Complex
AORE-06
100 µm
AORE-02
100 µm
AOOJA-04
100 µm
AORE-05
100 µm
AOAL-03
100 µm
AORE-04
100 µm
AOLH-09
200 µm
AOAL-04
100 µm

Figure 7

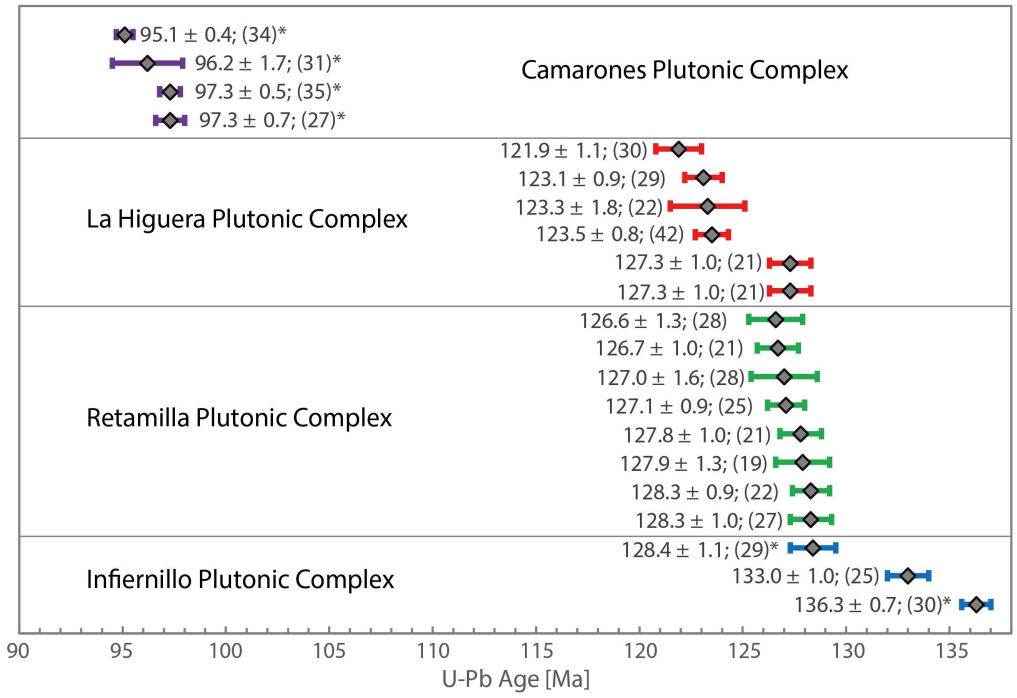

Figure 8

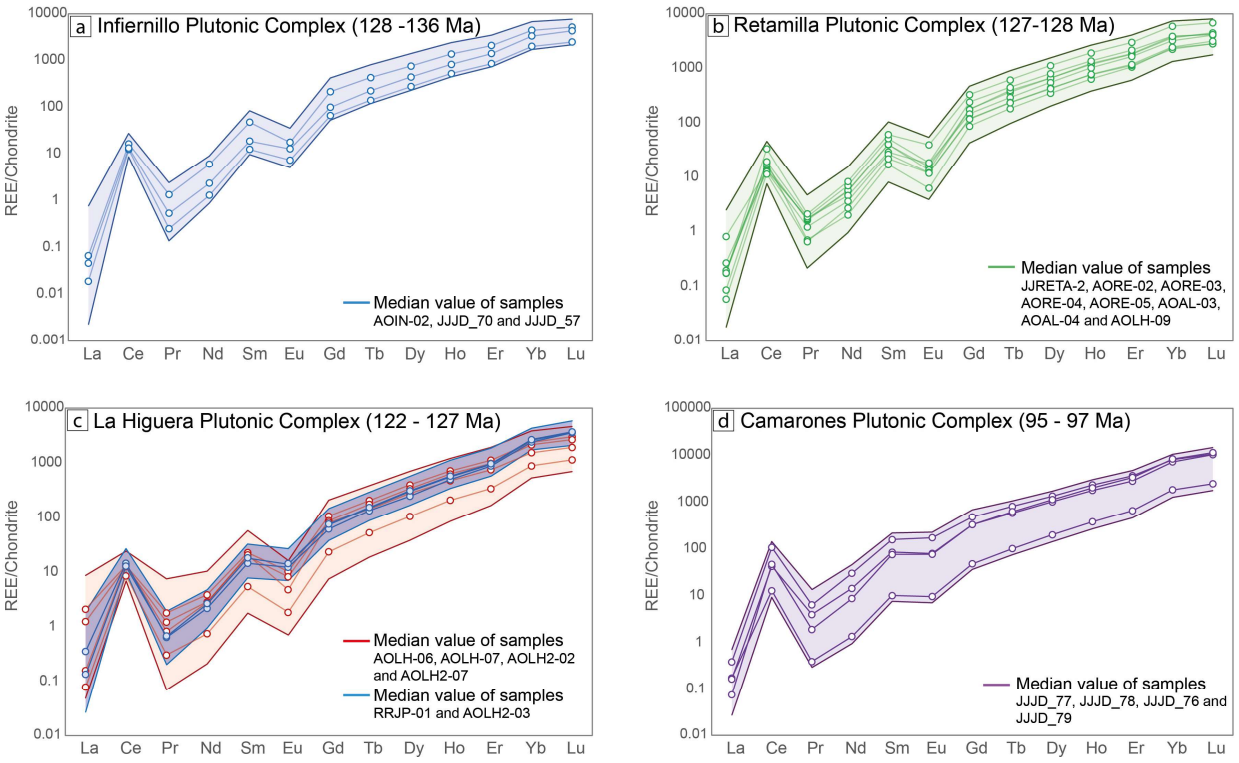

Figure 9

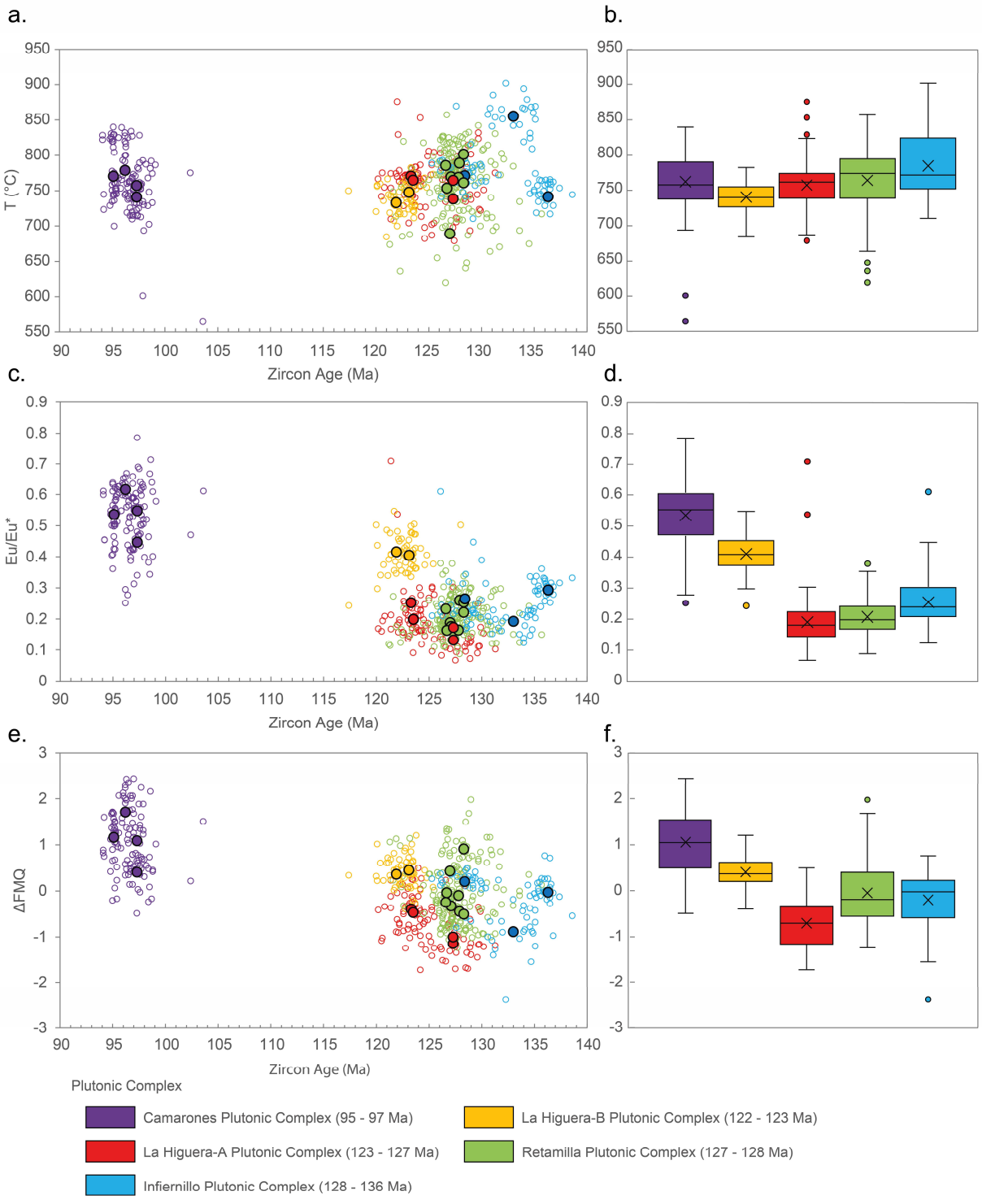
a.
b.
c.
d.
e.
f.
T (°C)
Eu/Eu*
ΔFMQ
Zircon Age (Ma)
Plutonic Complex
Camarones Plutonic Complex (95 - 97 Ma)
La Higuera-B Plutonic Complex (122 - 123 Ma)
La Higuera-A Plutonic Complex (123 - 127 Ma)
Retamilla Plutonic Complex (127 - 128 Ma)
Infiernillo Plutonic Complex (128 - 136 Ma)

Figure 10

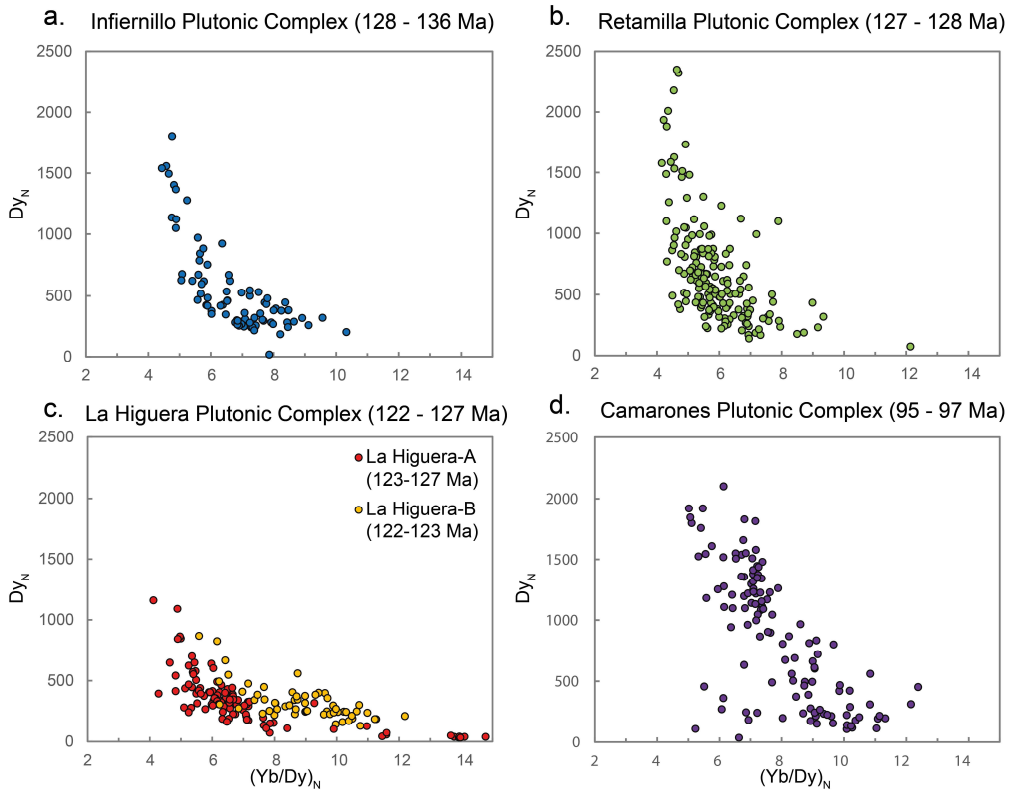

Figure 11

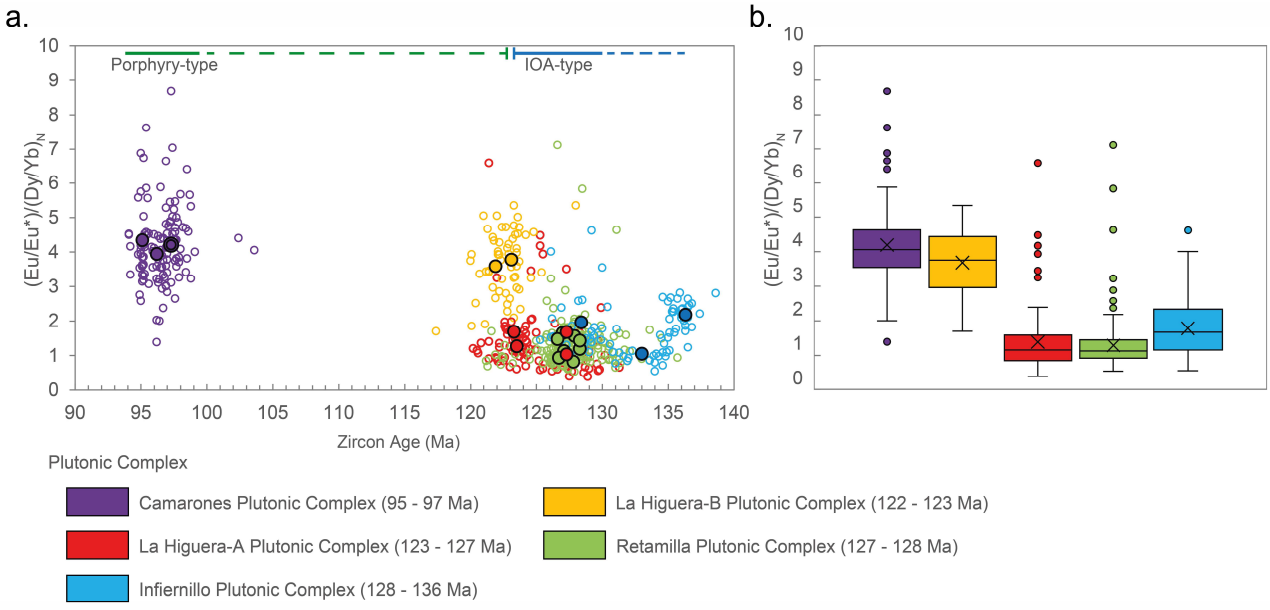

Figure 12

a. 136 - 123 Ma, IOA period

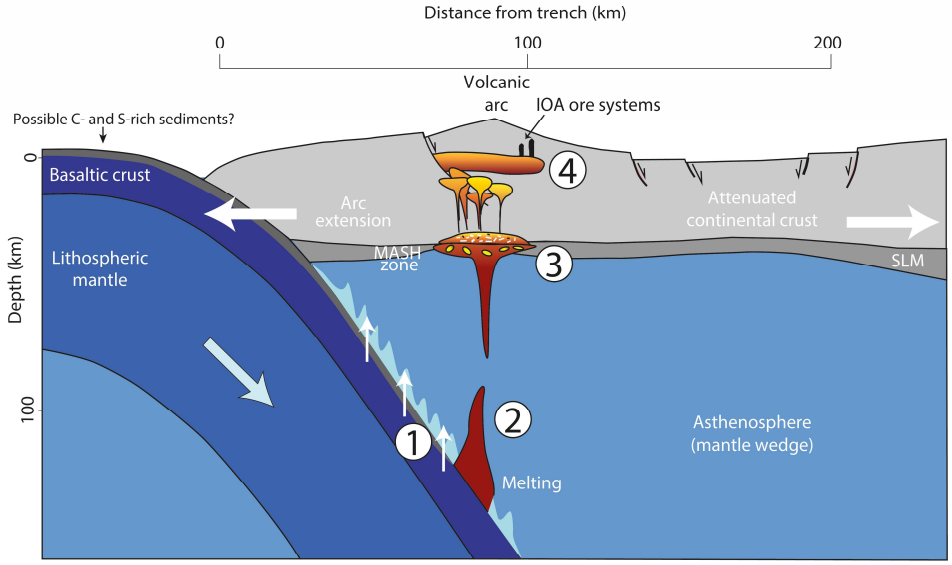

b. 97 - 95 Ma, Cretaceous Porphyry period

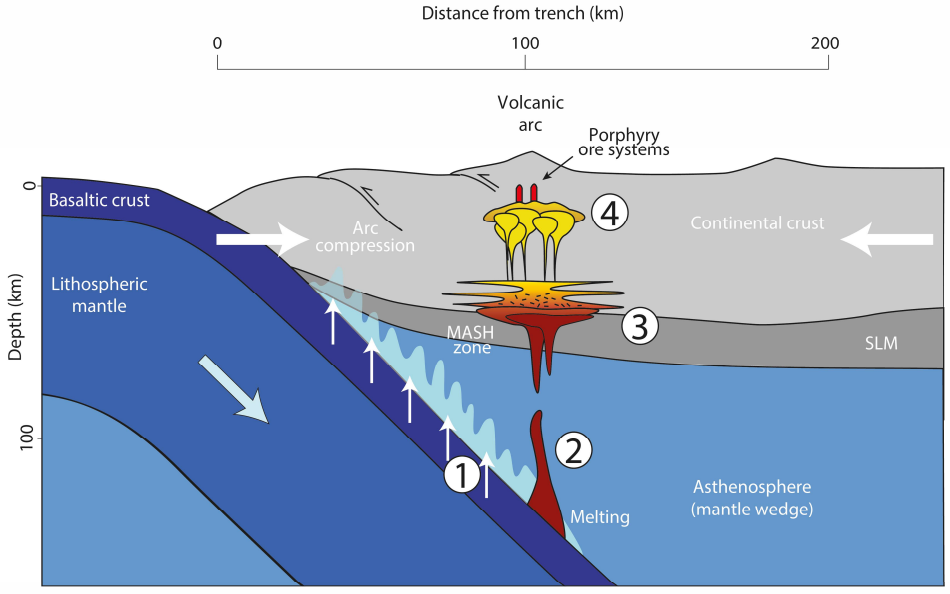

Figure 13

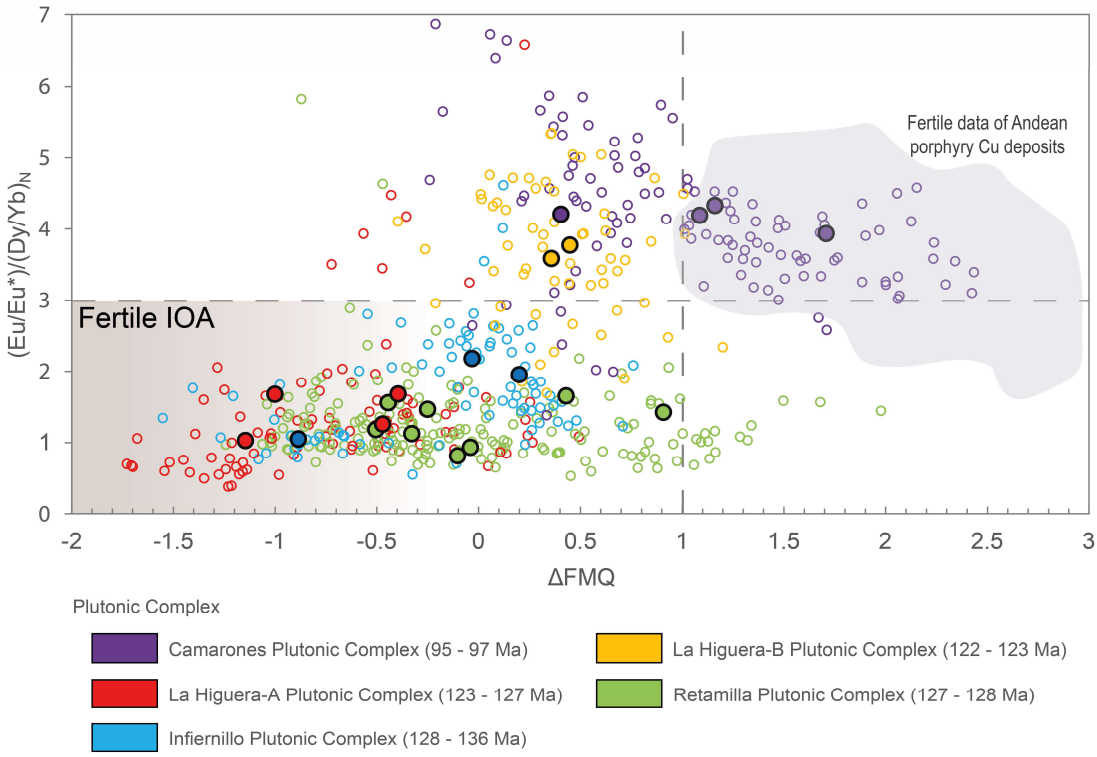
Fertile data of Andean porphyry Cu deposits
Fertile IOA
(Eu/Eu*)/(Dy/Yb)N
ΔFMQ
Plutonic Complex
Camarones Plutonic Complex (95 - 97 Ma)
La Higuera-A Plutonic Complex (123 - 127 Ma)
Infiernillo Plutonic Complex (128 - 136 Ma)
La Higuera-B Plutonic Complex (122 - 123 Ma)
Retamilla Plutonic Complex (127 - 128 Ma)

Figure 14

Tables

Table 2: Location, composition, and previously reported ages of studied plutonic complexes.

Plutonic Complex	UTM Location N	UTM Location E	Composition	Reported Age (Ma)	References
Infiernillo	6851856	307138	Diorite (Px - Amp)	131.4 ± 0.2 [1]	(Cruden et al., 2004)
			Granodiorite (Bt - Amp - Px)	129.0 ± 0.2 [1]	(Cruden et al., 2004)
				128.7 ± 0.2 [1]	(Cruden et al., 2004)
				136.3 ± 0.7 [1]	(Jara et al., 2021a)
				128.4 ± 1.1 [1]	(Jara et al., 2021a)
				130.0 ± 1.0 [2]	(Gipson et al., 2003)
				129.0 ± 1.1 [3]	(Valenzuela, 2002)
				129.9 ± 0.9 [3]	(Valenzuela, 2002)
Retamilla	6828919	309203	Diorite - Quartz Diorite (Amp - Bt)	-	
			Granodiorite - Tonalite (Px -Bt)	127.0 ± 1.6 [3]	(Arévalo and Welkner, 2008)
				126.4 ± 0.9 [3]	(Arévalo and Welkner, 2008)
				126.9 ± 0.8 [3]	(Valenzuela, 2002)
				127.1 ± 1.0 [3]	(Arévalo et al., 2009)
La Higuera	6819887	312836	Diorite - Quartz Diorite (Px - Amp)	123.7 ± 0.9 [3]	(Gipson et al., 2003)
			Granodiorite - Tonalite (Amp - Bt - Px)	122.1 ± 1.3 [3]	(Arévalo and Welkner, 2008)
				124.3 ± 1.9 [3]	(Arévalo et al., 2009)
				123.3 ± 1.9 [3]	(Arévalo et al., 2009)
				122.7 ± 1.5 [3]	(Arévalo et al., 2009)
				122.3 ± 1.3 [2]	(Valenzuela, 2002)
Camarones	6816996	329104	Diorite (Amp - Px - Bt)	97.3 ± 0.7 [1]	(Jara et al., 2021a)
				96.1 ± 0.2 [1]	(Fox, 2000)
				93.0 ± 0.9 [3]	(Arévalo et al., 2009)
			Granodiorite (Bt - Amp)	97.3 ± 0.5 [1]	(Jara et al., 2021a)
				96.2 ± 1.7 [1]	(Jara et al., 2021a)
				95.1 ± 0.4 [1]	(Jara et al., 2021a)
				94.8 ± 1.2 [1]	(Jara et al., 2021a)
				96.1 ± 0.8 [3]	(Arévalo et al., 2009)
				93.5 ± 0.4 [2]	(Arévalo et al., 2009)

Numbers next to ages refers to the analytical method. [1] zircon U–Pb; [2] biotite $^{40}Ar/^{39}Ar$; [3] amphibole $^{40}Ar/^{39}Ar$. Abbreviations: Amp: amphibole; Bt: biotite; Px: pyroxene.

Table 3: Sample location, lithology, and weighted average $^{206}Pb/^{238}U$ age.

N°	Sample	UTM Location		Plutonic Complex	Lithology	U-Pb age	MSDW; n
		N	E			Ma	
1	JJJD_79*	6820818	327209	Camarones	Granodiorite	95.1 ± 0.4	0.15; 34
2	JJJD_76*	6820818	327209		Granodiorite	96.2 ± 1.7	0.24; 31
3	JJJD_78*	6820818	327209		Granodiorite	97.3 ± 0.5	0.33; 35
4	JJJD_77*	6820818	327209		Diorite	97.3 ± 0.7	0.20; 27
5	RRJP-01**	6831202	322790	La Higuera	Diorite	121.9 ± 1.1	0.19; 30
6	AOLH2-03	6820544	319161		Granodiorite	123.1 ± 0.9	0.39; 29
7	AOLH-06	6817758	309472		Andesitic Dike	123.3 ± 1.8	0.12; 22
8	AOLH-07	6817129	309069		Granodiorite	123.5 ± 0.8	0.47; 42
9	AOLH2-02	6826980	321201		Tonalite	127.3 ± 1.0	0.59; 21
10	AOLH2-07	6817129	309069		Pervasive silicification	127.3 ± 1.0	0.98; 21
11	JJRETA2	6851943	319304	Retamilla	Granodiorite	126.6 ± 1.3	0.1; 28
12	AORE-02	6823255	304318		Quartz-Diorite	126.7 ± 1.0	0.36; 21
13	AOOJA-04	6825970	312171		Granodiorite	127.0 ± 1.6	3.1; 28
14	AORE-05	6829084	312212		Tonalite	127.1 ± 0.9	0.29; 25
15	AOAL-03	6813979	306112		Granodiorite	127.8 ± 1.0	0.45; 21
16	AORE-04	6824038	308938		Granodiorite	127.9 ± 1.3	0.33; 19
17	AOLH-09	6808331	306196		Tonalite	128.3 ± 0.9	0.39; 22
18	AOAL-04	6813030	305210		Granodiorite	128.3 ± 1.0	0.29; 27
19	JJJD_57*	6876286	320753	Infiernillo	Granodiorite	128.4 ± 1.1	0.38; 29
20	AOIN-02	6857837	311728		Quartz-Diorite	133.0 ± 1.0	0.51; 25
21	JJJD_70*	6852201	305182		Granodiorite	136.3 ± 0.7	0.76; 30

U–Pb age and error are the $^{206}Pb/^{238}U$ age.

*: Data from Jara et al. (2021a).

**: Sample collected from drill cores from the abandoned La Japonesa mine. The exact location and depth are unknown. The UTM coordinates shown correspond to the center point of the mine.

Table 4: Summary of zircon trace element data for each plutonic complex.

ppm	P	Ti	Y	Nb	Hf	Ta	Th	U	La	Ce	Pr	Nd	Sm
Camarones Plutonic Complex (95–97 Ma): Samples JJJD_77, JJJD_78, JJJD_76 and JJJD_79													
Mean	524	8.97	2718	1.71	8925	0.85	343	910	0.06	30.3	0.34	6.09	11.2
SD	495	3.70	1671	14.17	21518	3.64	340	588	0.11	24.6	0.38	6.39	9.5
P5%	137	4.87	481	0.75	7230	0.38	30	161	0.00	6.1	0.03	0.43	1.2
Median	407	7.98	2860	2.70	10330	1.18	257	886	0.03	25.6	0.20	3.70	9.0
P95%	1690	15.90	5340	10.34	19340	3.21	1109	2071	0.17	87.6	1.00	17.32	29.2
n	121	121	121	121	121	121	121	121	88	121	121	121	121
La Higuera-B Plutonic Complex (122–123 Ma): Samples RRJP-01 and AOLH2-03													
Mean	295	6.74	1050	1.27	8458	0.60	78	350	0.11	9.6	0.08	1.19	2.60
SD	65	1.40	372	0.40	990	0.15	36	130	0.14	3.2	0.06	0.63	1.35
P5%	211	4.77	608	0.77	6593	0.41	36	178	0.01	6.3	0.02	0.45	1.18
Median	283	6.60	930	1.21	8720	0.55	69	313	0.04	8.5	0.06	1.08	2.28
P95%	409	8.88	1832	1.96	9673	0.85	146	579	0.46	16.7	0.18	2.23	4.92
n	58	58	58	58	58	58	58	58	30	58	57	58	58
La Higuera-A Plutonic Complex (123–127 Ma): Samples AOLH-06, AOLH-07, AOLH2-02 and AOLH2-07													
Mean	318	8.64	1047	1.27	8484	0.79	209	848	0.50	8.44	0.23	1.90	3.30
SD	140	3.26	596	0.53	1254	0.44	210	602	0.97	3.99	0.57	2.63	2.53
P5%	84	4.10	177	0.67	7078	0.50	60	290	0.01	4.32	0.01	0.10	0.27
Median	322	8.60	1026	1.15	8200	0.70	132	604	0.08	7.75	0.10	1.26	2.92
P95%	534	14.08	2018	2.26	10948	1.13	653	1995	2.08	15.02	0.71	4.85	8.68
n	99	98	99	99	99	99	99	99	68	99	93	99	99
Retamilla Plutonic Complex (127–128 Ma): Samples JJRETA2, AORE-02, AOOJA-04, AORE-05, AOAL-03, AORE-04, AOLH-09 and AOAL-04													
Mean	391	9.21	1816	1.50	9354	0.92	183	653	0.13	12.1	0.16	2.55	5.90
SD	140	3.73	1013	0.78	1444	0.51	136	421	0.28	8.0	0.14	2.04	4.46
P5%	213	3.10	621	0.70	7350	0.42	36	193	0.00	4.7	0.02	0.44	1.23
Median	372	9.40	1650	1.32	9160	0.74	146	540	0.04	9.6	0.13	1.95	4.70
P95%	646	15.30	4027	3.04	12044	1.75	486	1443	0.60	28.5	0.44	7.14	15.76
n	183	180	183	183	183	182	183	183	108	183	174	182	183
Infiernillo Plutonic Complex (128–136 Ma): Samples JJJD_57, AOIN-02 and JJJD_70													
Mean	363	11.67	1582	1.38	10788	0.81	193	611	0.03	9.4	0.08	1.60	4.38
SD	211	6.25	961	0.81	1632	0.44	278	507	0.05	3.9	0.08	1.42	3.79
P5%	175	5.51	758	0.61	8981	0.43	34	165	0.00	5.0	0.00	0.35	1.33
Median	278	9.16	1259	1.08	10870	0.67	83	369	0.01	8.6	0.04	0.94	2.84
P95%	890	22.69	3867	2.86	12719	1.83	611	1615	0.15	18.2	0.24	4.61	12.79
n	83	83	83	83	83	83	83	83	34	83	83	83	83

ppm	Eu	Gd	Tb	Dy	Ho	Er	Yb	Lu	∑REE	Eu_N/Eu^*	Yb_N/Dy_N	T (°C)	ΔFMQ	$(Eu/Eu^*)/(Dy/Yb)_N$
Camarones Plutonic Complex (95–97 Ma): Samples JJJD_77, JJJD_78, JJJD_76 and JJJD_79														
Mean	4.55	55.4	18.0	214	82.8	391	1002	206	2021	0.53	7.89	762	1.05	4.19
SD	3.83	39.5	12.0	135	50.2	227	536	107	1132	0.10	1.64	43	0.67	1.12
P5%	0.38	7.3	2.6	35	15.6	79	219	47	409	0.36	5.46	713	0.03	2.75
Median	3.97	56.0	18.7	220	85.4	416	1096	227	2217	0.55	7.36	758	1.05	4.06
P95%	11.91	122.3	35.8	442	165.0	728	1714	346	3652	0.66	10.84	829	2.15	6.40
n	121	121	121	121	121	121	121	121	121	121	121	121	121	121
La Higuera-B Plutonic Complex (122–123 Ma): Samples RRJP-01 and AOLH2-03														
Mean	0.84	15.9	6.2	80	33.9	169	440	93	852	0.41	8.89	741	0.40	3.68
SD	0.39	8.1	2.9	36	13.8	61	131	28	278	0.06	1.49	20	0.32	0.92
P5%	0.40	7.7	3.2	42	19.0	94	282	52	525	0.34	6.24	711	-0.02	2.07
Median	0.77	14.2	5.2	70	29.8	149	411	90	782	0.41	8.99	740	0.37	3.75
P95%	1.53	29.6	10.8	141	61.7	301	703	145	1459	0.50	11.03	769	0.94	5.05
n	58	58	58	58	58	58	58	58	58	58	58	58	58	58
La Higuera-A Plutonic Complex (123–127 Ma): Samples AOLH-06, AOLH-07, AOLH2-02 and AOLH2-07														
Mean	0.49	18.8	6.8	85	33.8	155	333	61	709	0.19	7.09	761	-0.70	1.37
SD	0.50	12.8	4.5	53	20.1	86	159	28	368	0.09	2.49	35	0.52	0.93
P5%	0.04	1.5	0.7	10	4.8	27	88	18	154	0.09	4.89	698	-1.52	0.55
Median	0.45	17.3	6.3	80	32.5	152	338	62	704	0.18	6.35	765	-0.71	1.15
P95%	0.93	42.3	14.1	176	66.9	309	620	114	1348	0.30	13.92	816	0.23	3.46
n	98	99	99	99	99	99	99	99	99	98	99	98	98	98
Retamilla Plutonic Complex (127–128 Ma): Samples JJRETA2, AORE-02, AOOJA-04, AORE-05, AOAL-03, AORE-04, AOLH-09 and AOAL-04														
Mean	1.01	36.8	13.2	164	65.0	292	592	106	1290	0.21	6.09	764	-0.05	1.28
SD	0.87	27.3	8.9	106	39.9	174	313	51	727	0.06	1.88	46	0.66	0.73
P5%	0.22	8.6	3.6	51	21.1	98	218	44	464	0.12	4.49	675	-0.94	0.72
Median	0.78	29.3	10.8	138	56.5	259	533	96	1146	0.20	5.70	774	-0.19	1.12
P95%	3.08	95.0	32.9	387	145.9	655	1200	200	2729	0.30	7.95	825	1.13	2.05
n	183	183	183	183	183	183	183	183	183	183	183	180	180	183
Infiernillo Plutonic Complex (128–136 Ma): Samples JJJD_57, AOIN-02 and JJJD_70														
Mean	0.86	28.7	10.4	131	52.7	244	528	100	1111	0.25	6.79	785	-0.20	1.78
SD	0.68	23.5	7.8	91	33.3	140	255	45	599	0.07	1.27	56	0.57	0.75
P5%	0.30	10.3	4.3	59	25.1	121	282	53	569	0.15	4.77	724	-1.19	0.85
Median	0.67	19.1	7.7	103	41.5	206	472	90	972	0.24	6.86	772	-0.02	1.66
P95%	2.40	84.2	29.3	344	132.0	559	1087	191	2467	0.34	8.64	870	0.41	2.79
n	83	83	83	83	83	83	83	83	83	83	83	83	83	83

$Eu/Eu^* = Eu_N/SQRT(Sm_N*Gd_N)$; T (°C) is calculated using the Ti-in-zircon thermometer of (Ferry and Watson, 2007) using the activity of SiO_2 = 1.0 and activity of Ti = 0.7; ΔFMQ is calculated using the oxybarometer of (Loucks et al., 2020). Normalized values are from (McDonough and Sun, 1995).

Capítulo 5

Conclusiones

En este estudio se ha llevado a cabo una caracterización exhaustiva de las edades U-Pb junto a la determinación y análisis de elementos traza en circones de los intrusivos del Cretácico Temprano asociados a mineralización de yacimientos IOA en el distrito El Algarrobo. En consecuencia, y en respuesta al objetivo general de esta investigación, se han identificado las características químicas de dichos cuerpos intrusivos, lo que ha permitido inferir la evolución magmática durante este periodo y establecer posibles indicadores de fertilidad de magmas asociados los yacimientos de óxidos de hierro-apatito. A continuación, según los expuesto en este trabajo, se presentan los hallazgos y conclusiones más relevantes de esta investigación.

En primer lugar, los intrusivos asociados a yacimientos IOA, representados por los complejos plutónicos La Higuera y Retamilla (128-123 Ma), presentan características que indican un contenido relativamente bajo de H_2O. Así mismo, las condiciones de fugacidad de oxígeno predominantes en el periodo apuntan a condiciones relativamente reducidas (ΔFMQ < +1, hasta -1.5), lo que explica la signatura pobre en sulfuros de estos yacimientos. Estas condiciones se explican por la generación de magmas en un ambiente extensional, en el cual los magmas son retenidos por un corto tiempo en zonas profundas de la corteza y la influencia de la placa subductante hacia la cuña del manto es baja, dejando un manto sin mayor oxidación por agentes ligados a la subducción.

A los 123 Ma se produce un cambio en las condiciones antes mencionadas, donde los indicadores de contenido de agua y fugacidad de oxígeno experimentan un aumento repentino. Este cambio se interpreta como el momento en que se produce una variación en la configuración tectónica, iniciando un periodo de compresión (o transpresión), en el que los magmas residen mayor tiempo en la corteza profunda, donde incrementa el contenido de agua de estos y también existe una influencia creciente de los agentes de la subducción en la cuña del manto.

La compresión se mantuvo hasta el periodo en donde se desarrolla el Complejo Plutónico Camarones (97-95 Ma), en el que los datos indican condiciones de magmas ricos en H_2O y oxidación relativamente alta (ΔFMQ entre 0 y +2.2). Estas condiciones resultan favorables para la formación de yacimientos tipo pórfido y se interpretan como el resultado de magmas que son formados en ambientes compresivos, donde la influencia de la subducción es importante y estable y los magmas son retenidos en la corteza profunda donde se incrementa el contenido de agua debido a la acumulación y reposición multicílica de magmas en esa zona.

Por tanto, las diferencias encontradas entre las condiciones químicas de los magmas responden a un cambio en el régimen técnico, el cual se traduce en una mayor residencia de los magmas en la corteza profunda y un consecuente aumento en el contenido de agua. Esto difiere de la concepción general en que se piensa que las diferencias entre los periodos deben estar ligadas a cambios en el espesor cortical desde una corteza adelgazada en el periodo asociado a depósitos IOA a un engrosamiento para el periodo asociado a pórfidos. Esto, se descartó por lo rápido y repentino en el cambio de las condiciones de los intrusivos a los 123 Ma. Sin embargo, un espesor cortical mayor sí puede tener un efecto secundario sobre todo para los magmas del final del Cretácico Temprano, como resultado de la compresión ya instalada desde los 123 Ma.

Por otro lado, en respuesta a la hipótesis planteada que sugiere que deben existir procesos y condiciones particulares que generen depósitos IOA, se concluye que existen características que reflejan un periodo particularmente fértil en la historia geológica para la metalogénesis de estos yacimientos que son caracterizados por una signatura relativamente reducida de fugacidad de oxígeno y un bajo contenido de agua en los magmas. Estas condiciones difieren notablemente a las características comúnmente asociadas a depósitos tipo pórfidos de Cu-Mo. Asimismo, se corrobora la hipótesis planteada que postula que se pueden encontrar indicadores de fertilidad para depósitos IOA de una forma similar a lo que se ha realizado para pórfidos. El mejor indicador se considera el gráfico de $(Eu/Eu^*)/(Dy/Yb)_N$ vs. ΔFMQ, donde el campo fértil de IOA queda restringido a $(Eu/Eu^*)/(Dy/Yb)_N < 3$ y $\Delta FMQ < +1$. Por otro lado, este indicador también es útil para magmas con signaturas fértiles para pórfidos Cretácicos, los cuales se reconocen en el campo de $(Eu/Eu^*)/(Dy/Yb)_N > 3$ y $\Delta FMQ > +1$.

Las condiciones de fugacidad de oxígeno no solo son relativamente bajas comparadas con lo reportado en ambientes de arco, sino que incluso llegan a ser anormales en estos. Este es el caso de los datos del Complejo Plutónico La-Higuera-A, en donde la media es de $\Delta FMQ = -0.7$ (Incluso llegando a valores $\Delta FMQ = -1.5$). Estas condiciones anómalas son interpretadas como un posible punto clave en la fertilidad de depósitos IOA, sin embargo, no es claro si estas son un reflejo del proceso de formación de estos yacimientos o son un factor para la génesis de estos. Se proponen tres posibles orígenes para explicar estas condiciones, las cuales consideran: (i) Asimilación de rocas con alto contenido de grafito en la corteza; (ii) una fuente mantélica reducida o (iii) cristalización y segregación masiva de magnetita. Por la asociación de estos magmas reducidos con los cuerpos masivos de magnetita la última opción es favorecida, no obstante, es necesario realizar más estudios para probar estos indicadores en otros distritos y dilucidar el origen de estas condiciones reducidas en un ambiente de arco.

Bibliografía

Ague, J.J., Tassara, S., Holycross, M.E., Li, J.L., Cottrell, E., Schwarzenbach, E.M., Fassoulas, C., and John, T., 2022, Slab-derived devolatilization fluids oxidized by subducted metasedimentary rocks: Nature Geoscience, v. 15, no. 4, p. 320–326.

Annen, C., Blundy, J.D., and Sparks, R.S.J., 2006, The genesis of intermediate and silicic magmas in deep crustal hot zones: Journal of Petrology, v. 47, no. 3, p. 505–539.

Arancibia, G., 2004, Mid-cretaceous crustal shortening: Evidence from a regional-scale ductile shear zone in the Coastal Range of central Chile (32° S): Journal of South American Earth Sciences, v. 17, no. 3, p. 209–226.

Arévalo, C., and Welkner, D., 2008, Geología Del Área Carrizal Bajo - Chacritas, Región de Atacama. Servicio Nacional de Geología y Minería, Carta Geologíca de Chile No. 111:

Arévalo, C., Mourgues, F., and Chávez, R., 2009, Geología Del Área Vallenar-Domeyko, Región de Atacama. Servicio Nacional de Geología y Minería, Carta Geologíca de Chile No. 120:

Audétat, A., and Simon, A.C., 2012, Magmatic Controls on Porphyry Copper Genesis, in Geology and Genesis of Major Copper Deposits and Districts of the World. A Tribute to Richard H. Sillitoe: Society of Economic Geologists, p. 553–572.

Balica, C., Ducea, M.N., Gehrels, G.E., Kirk, J., Roban, R.D., Luffi, P., Chapman, J.B., Triantafyllou, A., Guo, J., Stoica, A.M., Ruiz, J., Balintoni, I., Profeta, L., Hoffman, D., et al., 2020, A zircon petrochronologic view on granitoids and continental evolution: Earth and Planetary Science Letters, v. 531, p. 116005.

Ballard, J.R., Palin, J.M., and Campbell, I.H., 2002, Relative oxidation states of magmas inferred from Ce“IV”/Ce“III” in zircon: Application to porphyry copper deposits of northern Chile: Contributions to Mineralogy and Petrology, v. 144, no. 3, p. 347–364.

Barra, F., Reich, M., Selby, D., Rojas, P., Simon, A., Salazar, E., and Palma, G., 2017, Unraveling the origin of the Andean IOCG clan: A Re-Os isotope approach: Ore Geology Reviews, v. 81, no. October 2016, p. 62–78.

Barton, M.D., 2013, Iron Oxide(-Cu-Au-REE-P-Ag-U-Co) Systems, in Treatise on Geochemistry: Second Edition: Elsevier, p. 515–541.

Bell, A.S., and Simon, A., 2011, Experimental evidence for the alteration of the Fe3+/ΣFe of silicate melt caused by the degassing of chlorine-bearing aqueous volatiles: Geology, v. 39, no. 5, p. 499–502.

Bell, E.A., Boehnke, P., Barboni, M., and Harrison, T.M., 2019, Tracking chemical alteration in magmatic zircon using rare earth element abundances: Chemical Geology, v. 510, no. February, p. 56–71.

Bénard, A., Klimm, K., Woodland, A.B., Arculus, R.J., Wilke, M., Botcharnikov, R.E., Shimizu, N., Nebel, O., Rivard, C., and Ionov, D.A., 2018, Oxidising agents in sub-arc mantle melts link slab devolatilisation and arc magmas: Nature Communications, v. 9, no. 1, p. 1–10.

Benavides, J., Kyser, T.K., Clark, A.H., Oates, C.J., Zamora, R., Tarnovschi, R., and Castillo, B.,

2007, The Mantoverde Iron Oxide-Copper-Gold District, III Region, Chile: The Role of Regionally Derived, Nonmagmatic Fluids in Chalcopyrite Mineralization: Economic Geology, v. 102, no. 3, p. 415–440.

Brounce, M., Kelley, K.A., and Cottrell, E., 2014, Variations in Fe3+/PFe of Mariana Arc Basalts and MantleWedge fO2: Journal of Petrology, v. 55, no. 12, p. 2514–2536.

Brounce, M., Reagan, M.K., Kelley, K.A., Cottrell, E., Shimizu, K., and Almeev, R., 2021, Covariation of Slab Tracers, Volatiles, and Oxidation During Subduction Initiation: Geochemistry, Geophysics, Geosystems, v. 22, no. 6, p. 1–30.

Brown, M., Diáz, F., and Grocott, J., 1993, Displacement history of the Atacama fault system 25°00 S-27° 00 S, northern Chile: Geological Society of America Bulletin, v. 105, no. 9, p. 1165–1174.

Burgisser, A., and Scaillet, B., 2007, Redox evolution of a degassing magma rising to the surface: Nature, v. 445, no. 7124, p. 194–197.

Cao, M.J., Qin, K.Z., Li, G.M., Evans, N.J., Hollings, P., and Jin, L.Y., 2016, Genesis of ilmenite-series I-type granitoids at the Baogutu reduced porphyry Cu deposit, western Junggar, NW-China: Lithos, v. 246–247, p. 13–30.

Carroll, M.R., and Rutherford, M.J., 1985, Sulfide and sulfate saturation in hydrous silicate melts: Journal of Geophysical Research, v. 90, no. S02, p. C601.

Cembrano, J., González, G., Arancibia, G., Ahumada, I., Olivares, V., and Herrera, V., 2005, Fault zone development and strain partitioning in an extensional strike-slip duplex: A case study from the Mesozoic Atacama fault system, Northern Chile: Tectonophysics, v. 400, nos. 1–4, p. 105–125.

Charrier, R., Pinto, L., and Rodríguez, M.., 2007, Tectonostratigraphic evolution of the Andean Orogen in Chile, in The Geology of Chile:, p. 21–114.

Cherniak, D.J., and Watson, E.B., 2003, 5. Diffusion in Zircon, in Zircon: De Gruyter, p. 113–144.

Chiaradia, M., Müntener, O., and Beate, B., 2011, Enriched basaltic andesites from mid-crustal fractional crystallization, recharge, and assimilation (Pilavo volcano, Western Cordillera of Ecuador): Journal of Petrology, v. 52, no. 6, p. 1107–1141.

Chiaradia, M., Ulianov, A., Kouzmanov, K., and Beate, B., 2012, Why large porphyry Cu deposits like high Sr/Y magmas? Scientific Reports, v. 2.

Chin, E.J., Shimizu, K., Bybee, G.M., and Erdman, M.E., 2018, On the development of the calc-alkaline and tholeiitic magma series: A deep crustal cumulate perspective: Earth and Planetary Science Letters, v. 482, p. 277–287.

CAP, 2021, Integrated Annual Report 2021, p. 61 (https://www.cap.cl/MemoriaIntegrada2021EN/pdf/Memoria_Integrada_CAP_2021.pdf)

Corfu, F., Hanchar, J.M., Hoskin, P.W.O., and Kinny, P., 2003, 16. Atlas of Zircon Textures, in Zircon: De Gruyter, p. 469–502.

Costa, F., Scaillet, B., and Pichavant, M., 2004, Petrological and experimental constraints on the pre-eruption conditions of Holocene dacite from Volcň San Pedro (36°S, Chilean Andes) and the importance of sulphur in silicic subduction-related magmas: Journal of Petrology, v. 45,

no. 4, p. 855–881.

Cottrell, E., Birner, S.K., Brounce, M., Davis, F.A., Waters, L.E., and Kelley, K.A., 2021, Oxygen Fugacity Across Tectonic Settings, in Magma Redox Geochemistry:, p. 33–61.

Crabtree, S.M., and Lange, R.A., 2012, An evaluation of the effect of degassing on the oxidation state of hydrous andesite and dacite magmas: A comparison of pre- and post-eruptive Fe 2+ concentrations: Contributions to Mineralogy and Petrology, v. 163, no. 2, p. 209–224.

Creixell, C., Fuentes, J., Bierma, H., and Salazar, E., 2020, Tectonic setting of cretaceous porphyry copper deposits of northern chile (28°-30° s) and its relations with magmatic evolution and metallogeny: Andean Geology, v. 47, no. 3, p. 469–507.

Cruden, A., Arévalo, C., Davis, D., and Grocott, J., 2004, Magmatic migration and pluton construction rates in the mesozoic chilean coastal cordillera batholith (27° to 29°S): International Geological Congress, Florence, v. No 32, CD-.

Dallmeyer, R.D., Brown, M., Grocott, J., Taylor, G.K., and Treloar, P.J., 1996, Mesozoic magmatic and tectonic events within the andean plate boundary zone, 26°27°27°30′S, North Chile: Constraints from 40Ar/39Ar mineral ages: Journal of Geology, v. 104, no. 1, p. 19–40.

Davidson, J., Turner, S., Handley, H., Macpherson, C., and Dosseto, A., 2007, Amphibole "sponge" in arc crust? Geology, v. 35, no. 9, p. 787–790.

Davidson, J., Turner, S., and Plank, T., 2013, Dy/Dy*: Variations arising from mantle sources and petrogenetic processes: Journal of Petrology, v. 54, no. 3, p. 525–537.

Davis, D.W., Williams, I.S., and Krogh, T.E., 2003, 6. Historical Development of Zircon Geochronology, in Zircon: De Gruyter, p. 145–182.

Dilles, J.H., Kent, A.J.R., Wooden, J.L., Tosdal, R.M., Koleszar, A., Lee, R.G., and Farmer, L.P., 2015, Zircon compositional evidence for sulfur-degassing from ore-forming arc magmas: Economic Geology, v. 110, no. 1, p. 241–251.

Elliott, T., Plank, T., Zindler, A., White, W., and Bourdon, B., 1997, Element transport from slab to volcanic front at the Mariana arc: Journal of Geophysical Research: Solid Earth, v. 102, no. B7, p. 14991–15019.

Escolme, A., Cooke, D.R., Hunt, J., Berry, R.F., Maas, R., and Creaser, R.A., 2020, The Productora Cu-Au-Mo Deposit, Chile: A Mesozoic Magmatic-Hydrothermal Breccia Complex with Both Porphyry and Iron Oxide Cu-Au Affinities: Economic Geology, v. 115, no. 3, p. 543–580.

Espinoza, S., 1990, The Atacama-Coquimbo Ferriferous Belt, Northern Chile, in Stratabound Ore Deposits in the Andes: Berlin, Heidelberg, Springer Berlin Heidelberg, p. 353–364.

Espinoza, S., Véliz, H., Esquivel, J., Arias, J., and Moraga, A., 1996, The Cupriferous Province of the Coastal Range, Northern Chile, in Andean Copper Deposits: Society of Economic Geologists, p. 19–32.

Evans, K.A., Elburg, M.A., and Kamenetsky, V.S., 2012, Oxidation state of subarc mantle: Geology, v. 40, no. 9, p. 783–786.

Feig, S.T., Koepke, J., and Snow, J.E., 2006, Effect of water on tholeiitic basalt phase equilibria: An experimental study under oxidizing conditions: Contributions to Mineralogy and Petrology, v. 152, no. 5, p. 611–638.

Ferry, J.M., and Watson, E.B., 2007, New thermodynamic models and revised calibrations for the Ti-in-zircon and Zr-in-rutile thermometers: Contributions to Mineralogy and Petrology, v. 154, no. 4, p. 429–437.

Foden, J.D., and Green, D.H., 1992, Possible role of amphibole in the origin of andesite: some experimental and natural evidence: Contributions to Mineralogy and Petrology, v. 109, no. 4, p. 479–493.

Fox, K.A., 2000,Fe-Oxide (Cu-U-Au-REE) Mineralization and Alteration at the Productora Prospect: Colorado School of Mines: 153 p.

Fredes, M., 2017,Geología del prospecto IOCG Alcaparra D, Comuna de Huasco, Región de Atacama: Universidad de Chile: 81 p.

Gipson, M., Taylor, G.K., and Grocott, J., 2003, New palaeomagnetic results and 40Ar/39Ar geochronology from the Vallenar region (29°S): General Assembly of the European Geophysical Society, v. 27.

Girardi, J., 2014,Comparison of Mesozoic Magmatic Evolution and Iron Oxide (Copper-Gold) "IOCG" Mineralization, Central Andes and Western North America: The University of Arizona: 363 p.

Grimes, C.B., Wooden, J.L., Cheadle, M.J., and John, B.E., 2015, "Fingerprinting" tectono-magmatic provenance using trace elements in igneous zircon: Contributions to Mineralogy and Petrology, v. 170, nos. 5–6, p. 1–26.

Grocke, S.B., Cottrell, E., de Silva, S., and Kelley, K.A., 2016, The role of crustal and eruptive processes versus source variations in controlling the oxidation state of iron in Central Andean magmas: Earth and Planetary Science Letters, v. 440, p. 92–104.

Grocott, J., and Taylor, G.K., 2002, Magmatic arc fault systems, deformation partitioning and emplacement of granitic complexes in the Coastal Cordillera, north Chilean Andes (25°30 S to 27°00 S): Journal of the Geological Society, v. 159, no. 4, p. 425–443.

Grocott, J., Arévalo, C., Welkner, D., and Cruden, A., 2009, Fault-assisted vertical pluton growth: Coastal Cordillera, north Chilean Andes: Journal of the Geological Society, v. 166, no. 2, p. 295–301.

Groves, D.I., Bierlein, F.P., Meinert, L.D., and Hitzman, M.W., 2010, Iron oxide copper-gold (IOCG) deposits through earth histoiy: Implications for origin, lithospheric setting, and distinction from other epigenetic iron oxide deposits: Economic Geology, v. 105, no. 3, p. 641–654.

Hildreth, W., and Moorbath, S., 1988, Crustal contributions to arc magmatism in the Andes of Central Chile: Contributions to Mineralogy and Petrology, v. 98, no. 4, p. 455–489.

Hitzman, M.W., 2000, Iron Oxide-Cu-Au deposits: what, where, when and why? Porter, T.M. (Ed.), Hydrothermal Iron Oxide Copper-Gold and related deposits: A Global Perspective, vol 1.Australian Mineral Foundation., p. 9–25.

Holycross, M., and Cottrell, E., 2023, Garnet crystallization does not drive oxidation at arcs: v. 509, no. May, p. 506–509.

Hoskin, P.W.O., and Schaltegger, U., 2003, 2. The Composition of Zircon and Igneous and Metamorphic Petrogenesis, in Zircon: De Gruyter, p. 27–62.

Hoskin, P.W.O., Kinny, P.D., Wyborn, D., and Chappell, B.W., 2000, Identifying accessory mineral saturation during differentiation in granitoid magmas: An integrated approach: Journal of Petrology, v. 41, no. 9, p. 1365–1396.

Hou, T., Charlier, B., Holtz, F., Veksler, I., Zhang, Z., Thomas, R., and Namur, O., 2018, Immiscible hydrous Fe-Ca-P melt and the origin of iron oxide-apatite ore deposits: Nature Communications, v. 9, no. 1, p. 1–8.

Ishizuka, O., Tani, K., Reagan, M.K., Kanayama, K., Umino, S., Harigane, Y., Sakamoto, I., Miyajima, Y., Yuasa, M., and Dunkley, D.J., 2011, The timescales of subduction initiation and subsequent evolution of an oceanic island arc: Earth and Planetary Science Letters, v. 306, nos. 3–4, p. 229–240.

Jara, J.J., Barra, F., Reich, M., Leisen, M., Romero, R., and Morata, D., 2021a, Episodic construction of the early Andean Cordillera unravelled by zircon petrochronology: Nature Communications, v. 12, no. 1, p. 1–8.

Jara, J.J., Barra, F., Reich, M., Morata, D., Leisen, M., and Romero, R., 2021b, Geochronology and petrogenesis of intrusive rocks in the Coastal Cordillera of northern Chile: Insights from zircon U-Pb dating and trace element geochemistry: Gondwana Research, v. 93, p. 48–72.

Jenkyns, H.C., 2010, Geochemistry of oceanic anoxic events: Geochemistry, Geophysics, Geosystems, v. 11, no. 3, p. 1–30.

Jenkyns, H.C., 2018, Transient cooling episodes during Cretaceous Oceanic Anoxic Events with special reference to OAE 1a (Early Aptian): Philosophical Transactions of the Royal Society A: Mathematical, Physical and Engineering Sciences, v. 376, no. 2130.

Jenner, F.E., O'Neill, H.S.C., Arculus, R.J., and Mavrogenes, J.A., 2010, The magnetite crisis in the evolution of arc-related magmas and the initial concentration of Au, Ag and Cu: Journal of Petrology, v. 51, no. 12, p. 2445–2464.

Jochum, K.P., Weis, U., Stoll, B., Kuzmin, D., Yang, Q., Raczek, I., Jacob, D.E., Stracke, A., Birbaum, K., Frick, D.A., Günther, D., and Enzweiler, J., 2011, Determination of reference values for NIST SRM 610-617 glasses following ISO guidelines: Geostandards and Geoanalytical Research, v. 35, no. 4, p. 397–429.

Jugo, P.J., 2009, Sulfur content at sulfide saturation in oxidized magmas: Geology, v. 37, no. 5, p. 415–418.

Jugo, P.J., Wilke, M., and Botcharnikov, R.E., 2010, Sulfur K-edge XANES analysis of natural and synthetic basaltic glasses: Implications for S speciation and S content as function of oxygen fugacity: Geochimica et Cosmochimica Acta, v. 74, no. 20, p. 5926–5938.

Kelley, K.A., and Cottrell, E., 2009, Water and the oxidation state of subduction zone magmas: Science, v. 325, no. 5940, p. 605–607.

Kelley, K.A., and Cottrell, E., 2012, The influence of magmatic differentiation on the oxidation state of Fe in a basaltic arc magma: Earth and Planetary Science Letters, v. 329–330, p. 109–121.

Kleinsasser, J.M., Simon, A.C., Konecke, B.A., Kleinsasser, M.J., Beckmann, P., and Holtz, F., 2022, Sulfide and sulfate saturation of dacitic melts as a function of oxygen fugacity: Geochimica et Cosmochimica Acta, v. 326, p. 1–16.

Knipping, J.L., Bilenker, L.D., Simon, A.C., Reich, M., Barra, F., Deditius, A.P., Wälle, M., Heinrich, C.A., Holtz, F., and Munizaga, R., 2015a, Trace elements in magnetite from massive iron oxide-apatite deposits indicate a combined formation by igneous and magmatic-hydrothermal processes: Geochimica et Cosmochimica Acta, v. 171, p. 15–38.

Knipping, J.L., Bilenker, L.D., Simon, A.C., Reich, M., Barra, F., Deditius, A.P., Lundstrom, C., Bindeman, I., and Munizaga, R., 2015b, Giant Kiruna-type deposits form by efficient flotation of magmatic magnetite suspensions: Geology, v. 43, no. 7, p. 591–594.

Lee, C.T., and Tang, M., 2020, How to make porphyry copper deposits: Earth and Planetary Science Letters, v. 529, p. 115868.

Lee, C.T., Leeman, W.P., Canil, D., and Li, Z.X.A., 2005, Similar V/Sc systematics in MORB and arc basalts: Implications for the oxygen fugacities of their mantle source regions: Journal of Petrology, v. 46, no. 11, p. 2313–2336.

Lee, R.G., Dilles, J.H., Tosdal, R.M., Wooden, J.L., and Mazdab, F.K., 2017, Magmatic evolution of granodiorite intrusions at the El Salvador porphyry copper deposit, Chile, based on trace element composition and U/Pb age of zircons: Economic Geology, v. 112, no. 2, p. 245–273.

Lee, R.G., Byrne, K., D'Angelo, M., Hart, C.J.R., Hollings, P., Gleeson, S.A., and Alfaro, M., 2021, Using zircon trace element composition to assess porphyry copper potential of the Guichon Creek batholith and Highland Valley Copper deposit, south-central British Columbia: Mineralium Deposita, v. 56, no. 2, p. 215–238.

Li, Y.X., Bralower, T.J., Montañez, I.P., Osleger, D.A., Arthur, M.A., Bice, D.M., Herbert, T.D., Erba, E., and Premoli Silva, I., 2008, Toward an orbital chronology for the early Aptian Oceanic Anoxic Event (OAE1a, ~ 120 Ma): Earth and Planetary Science Letters, v. 271, nos. 1–4, p. 88–100.

Lledo, H.L., Naslund, H.R., and Jenkins, D.M., 2020, Experiments on phosphate–silicate liquid immiscibility with potential links to iron oxide apatite and nelsonite deposits: Springer Berlin Heidelberg, 1–33 p.

Loader, M.A., Wilkinson, J.J., and Armstrong, R.N., 2017, The effect of titanite crystallisation on Eu and Ce anomalies in zircon and its implications for the assessment of porphyry Cu deposit fertility: Earth and Planetary Science Letters, v. 472, p. 107–119.

Loucks, R.R., 2014, Distinctive composition of copper-ore-forming arcmagmas: Australian Journal of Earth Sciences, v. 61, no. 1, p. 5–16.

Loucks, R.R., 2021, Deep entrapment of buoyant magmas by orogenic tectonic stress: Its role in producing continental crust, adakites, and porphyry copper deposits: Earth-Science Reviews, v. 220, p. 103744.

Loucks, R.R., Fiorentini, M.L., and Henriquez, G.J., 2020, New magmatic oxybarometer using trace elements in zircon: Journal of Petrology, v. 61, no. 3.

Lu, Y., Loucks, R.R., Fiorentini, M., Mccuaig, T.C., Evans, N.J., Yang, Z., Hou, Z., Kirkland, C.L., Parra-avila, L.A., and Kobussen, A., 2016, Zircon Compositions as a Pathfinder for Porphyry Cu ± Mo ± Au Deposits: Economic Geology Special Publication, v. 19, no. May, p. 329–347.

Lucassen, F., Kramer, W., Bartsch, V., Wilke, H.G., Franz, G., Romer, R.L., and Dulski, P., 2006, Nd, Pb, and Sr isotope composition of juvenile magmatism in the Mesozoic large magmatic

province of northern Chile (18-27°S): Indications for a uniform subarc mantle: Contributions to Mineralogy and Petrology, v. 152, no. 5, p. 571–589.

Ludwig, K., 2010, Isoplot/Ex version 4.1, a geochronological toolkit for Microsoft Excel: Berkeley Geochronology Center,Special Publication, No. 4:

Maksaev, V., and Zentilli, M., 2002, Chilean Strata-Bound Cu-(Ag) Deposits: An Overview, in Hydrothermal iron oxide copper-gold and related deposits: A global perspective: PCG Publishing, p. 185–205.

Maksaev, V., Munizaga, F., Fanning, M., Palacios, C., and Tapia, J., 2006, SHRIMP U-Pb dating of the Antucoya porphyry copper deposit: New evidence for an Early Cretaceous porphyry-related metallogenic epoch in the Coastal Cordillera of northern Chile: Mineralium Deposita, v. 41, no. 7, p. 637–644.

Maksaev, V., Munizaga, F., Valencia, V., and Barra, F., 2009, LA-ICP-MS zircon U-Pb geochronology to constrain the age of post-Neocomian continental deposits of the Cerrillos Formation, Atacama Region, northern Chile: Tectonic and metallogenic implications: Andean Geology, v. 36, no. 2, p. 264–287.

Maksaev, V., Almonacid, T.A., Munizaga, F., Valencia, V., McWilliams, M., and Barra, F., 2010, Geochronological and thermochronological constraints on porphyry copper mineralization in the Domeyko alteration zone, northern Chile: Andean Geology, v. 37, no. 1, p. 144–176.

McDonough, W.F., and Sun, S. -s., 1995, The composition of the Earth: Chemical Geology, v. 120, nos. 3–4, p. 223–253.

Ménard, J.J., 1995, Relationship between altered pyroxene diorite and the magnetite mineralization in the Chilean Iron Belt, with emphasis on the El Algarrobo iron deposits (Atacama region, Chile): Mineralium Deposita, v. 30, nos. 3–4, p. 268–274.

Meng, X., Kleinsasser, J.M., Richards, J.P., Tapster, S.R., Jugo, P.J., Simon, A.C., Kontak, D.J., Robb, L., Bybee, G.M., Marsh, J.H., and Stern, R.A., 2021, Oxidized sulfur-rich arc magmas formed porphyry Cu deposits by 1.88 Ga: Nature Communications, v. 12, no. 1, p. 1–9.

Miller, C.F., McDowell, S.M., and Mapes, R.W., 2003, Hot and cold granites: Implications of zircon saturation temperatures and preservation of inheritance: Geology, v. 31, no. 6, p. 529–532.

Moore, G., Vennemann, T., and Carmichael, I.S.E., 1998, An empirical model for the solubility of H2O in magmas to 3 kilobars: American Mineralogist, v. 83, nos. 1–2, p. 36–42.

Morata, D., and Aguirre, L., 2003, Extensional Lower Cretaceous volcanism in the Coastal Range (29°20′-30°S), Chile: Geochemistry and petrogenesis: Journal of South American Earth Sciences, v. 16, no. 6, p. 459–476.

Moscoso, R., Nasi, C., and Salinas, P., 1982, Geología de la Hoja de la Hoja de Vallenar y parte norte de La Serena. Regiones de Atacama y Coquimbo. Servicio Nacional de Geología y Minería. Carta Geológica de Chile No. 55:

Moussallam, Y., Edmonds, M., Scaillet, B., Peters, N., Gennaro, E., Sides, I., and Oppenheimer, C., 2016, The impact of degassing on the oxidation state of basaltic magmas: A case study of Kīlauea volcano: Earth and Planetary Science Letters, v. 450, p. 317–325.

Mpodozis, C., and Ramos, V.A., 1989, The Andes of Chile and Argentina. In Geology of the Andes

and its Relation to Hidrocarbon and Mineral Resources (Ericksen, G., Cañas-Pinochet, M., Reinemund, J., editors): Earth Sciences Series, Circum-Pacific Council for Energy and Mineral Resources, no. 11, p. 59–90.

Muñoz, M., Charrier, R., Fanning, C.M., Maksaev, V., and Deckart, K., 2012, Zircon trace element and O-Hf isotope analyses of mineralized intrusions from El teniente ore deposit, chilean andes: Constraints on the source and magmatic evolution of porphyry Cu-Mo related magmas: Journal of Petrology, v. 53, no. 6, p. 1091–1122.

Müntener, O., Kelemen, P.B., and Grove, T.L., 2001, The role of H2O during crystallization of primitive arc magmas under uppermost mantle conditions and genesis of igneous pyroxenites: An experimental study: Contributions to Mineralogy and Petrology, v. 141, no. 6, p. 643–658.

Nandedkar, R.H., Hürlimann, N., Ulmer, P., and Müntener, O., 2016, Amphibole–melt trace element partitioning of fractionating calc-alkaline magmas in the lower crust: an experimental study: Contributions to Mineralogy and Petrology, v. 171, nos. 8–9, p. 1–25.

Naslund, H.R., Henríquez, F., Nyström, J.O., Vivallo, W., and Dobbs, F.M., 2002, Magmatic Iron Ores and associated Mineralization: Examples from the Chilean High Andes and Coastal Cordillera: Porter, TM, Hydrothermal Iron Oxide Copper-Gold & Related Deposits: A Global Perspective, v. 2, p. 207–226.

Nathwani, C.L., Simmons, A.T., Large, S.J.E., Wilkinson, J.J., Buret, Y., and Ihlenfeld, C., 2021, From long-lived batholith construction to giant porphyry copper deposit formation: petrological and zircon chemical evolution of the Quellaveco District, Southern Peru: Contributions to Mineralogy and Petrology, v. 176, no. 2, p. 1–21.

Nazir, N., Ayyamperumal, R., Majeed, K.U., and Zhang, C., 2022, A comprehensive review on zircon U–Pb geochronology, geochemistry and geological significance of granite rocks, provenance, tectonic implications, exhumation history, current status, and perspectives: Geological Journal, v. 57, no. 9, p. 3463–3477.

Nilsson, K., and Peach, C.L., 1993, Sulfur speciation, oxidation state, and sulfur concentration in backarc magmas: Geochimica et Cosmochimica Acta, v. 57, no. 15, p. 3807–3813.

Palma, G., Barra, F., Reich, M., Simon, A.C., and Romero, R., 2020, A review of magnetite geochemistry of Chilean Iron Oxide-Apatite (IOA) deposits and its implications for ore-forming processes: Ore Geology Reviews, v. 126, no. July, p. 103748.

Parada, M.Á., López-Escobar, L., Oliveros, V., Fuentes, F., Morata, D., Calderón, M., Aguirre, L., Féraud, G., Espinoza, F., Moreno, H., Figueroa, O., Muñoz, J., Troncoso, R., and Stern, C., 2007, Andean Magmatism, in The Geology of Chile:, p. 115–154.

Paton, C., Hellstrom, J., Paul, B., Woodhead, J., and Hergt, J., 2011, Iolite: Freeware for the visualisation and processing of mass spectrometric data: Journal of Analytical Atomic Spectrometry, v. 26, no. 12, p. 2508–2518.

Pearce, J.A., and Peate, D.W., 1995, Tectonic Implications of the Composition of Volcanic ARC Magmas: Annual Review of Earth and Planetary Sciences, v. 23, no. 1, p. 251–285.

Profeta, L., Ducea, M.N., Chapman, J.B., Paterson, S.R., Gonzales, S.M.H., Kirsch, M., Petrescu, L., and DeCelles, P.G., 2015, Quantifying crustal thickness over time in magmatic arcs: Scientific Reports, v. 5, p. 1–7.

Reagan, M.K., Hanan, B.B., Heizler, M.T., Hartman, B.S., and Hickey-Vargas, R., 2008, Petrogenesis of volcanic rocks from Saipan and Rota, Mariana Islands, and implications for the evolution of Nascent Island Arcs: Journal of Petrology, v. 49, no. 3, p. 441–464.

del Real, I., Thompson, J.F.H., and Carriedo, J., 2018, Lithological and structural controls on the genesis of the Candelaria-Punta del Cobre Iron Oxide Copper Gold district, Northern Chile: Ore Geology Reviews, v. 102, no. September, p. 106–153.

del Real, I., Reich, M., Simon, A.C., Deditius, A., Barra, F., Rodríguez-Mustafa, M.A., Thompson, J.F.H., and Roberts, M.P., 2021, Formation of giant iron oxide-copper-gold deposits by superimposed, episodic hydrothermal pulses: Communications Earth & Environment, v. 2, no. 1, p. 1–9.

Reich, M., Simon, A.C., Deditius, A., Barra, F., Chryssoulis, S., Lagas, G., Tardani, D., Knipping, J., Bilenker, L., Sánchez-Alfaro, P., Roberts, M.P., and Munizaga, R., 2016, Trace element signature of pyrite from the Los Colorados Iron-Oxide-Apatite (IOA) deposit, Chile: A missing link between andean IOA and Iron Oxide Copper-Gold systems? Economic Geology, v. 111, no. 3, p. 743–761.

Reich, M., Simon, A.C., Barra, F., Palma, G., Hou, T., and Bilenker, L.D., 2022, Formation of iron oxide–apatite deposits: Nature Reviews Earth & Environment, v. 2.

Rezeau, H., Moritz, R., Wotzlaw, J.F., Hovakimyan, S., and Tayan, R., 2019, Zircon petrochronology of the Meghri-Ordubad pluton, Lesser caucasus: Fingerprinting igneous processes and implications for the exploration of porphyry Cu-Mo deposits: Economic Geology, v. 114, no. 7, p. 1365–1388.

Richards, J.P., 2011, HIGH Sr/Y ARC MAGMAS AND PORPHYRY Cu Mo Au DEPOSITS: JUST ADD WATER: Economic Geology, v. 106, no. 7, p. 1075–1081.

Richards, J.P., 2015, The oxidation state, and sulfur and Cu contents of arc magmas: implications for metallogeny: Lithos, v. 233, p. 27–45.

Richards, J.P., 2021, Porphyry copper deposit formation in arcs: What are the odds? Geosphere, v. 18, no. 1, p. 130–155.

Richards, J.P., and Celâl Şengör, A.M., 2017, Did paleo-tethyan anoxia kill arc magma fertility for porphyry copper formation? Geology, v. 45, no. 7, p. 591–594.

Richards, J.P., López, G.P., Zhu, J., Creaser, R.A., Locock, A.J., and Mumin, A.H., 2017, Contrasting Tectonic Settings and Sulfur Contents of Magmas Associated with Cretaceous Porphyry Cu ± Mo ± Au and Intrusion-Related Iron Oxide Cu-Au Deposits in Northern Chile: Economic Geology, v. 112, no. 2, p. 295–318.

Ridolfi, F., Renzulli, A., and Puerini, M., 2010, Stability and chemical equilibrium of amphibole in calc-alkaline magmas: An overview, new thermobarometric formulations and application to subduction-related volcanoes: Contributions to Mineralogy and Petrology, v. 160, no. 1, p. 45–66.

Rieger, A.A., Marschik, R., Diaz, M., Holzl, S., Chiaradia, M., Akker, B., and Spangenberg, J.E., 2010, The Hypogene Iron Oxide Copper-Gold Mineralization in the Mantoverde District, Northern Chile: Economic Geology, v. 105, no. 7, p. 1271–1299.

Rieger, A.A., Marschik, R., and Díaz, M., 2012, The evolution of the hydrothermal IOCG system

in the Mantoverde district, northern Chile: new evidence from microthermometry and stable isotope geochemistry: Mineralium Deposita, v. 47, no. 4, p. 359–369.

Rojas, P.A., Barra, F., Deditius, A., Reich, M., Simon, A., Roberts, M., and Rojo, M., 2018a, New contributions to the understanding of Kiruna-type iron oxide-apatite deposits revealed by magnetite ore and gangue mineral geochemistry at the El Romeral deposit, Chile: Ore Geology Reviews, v. 93, no. January, p. 413–435.

Rojas, P.A., Barra, F., Reich, M., Deditius, A., Simon, A., Uribe, F., Romero, R., and Rojo, M., 2018b, A genetic link between magnetite mineralization and diorite intrusion at the El Romeral iron oxide-apatite deposit, northern Chile: Mineralium Deposita, v. 53, no. 7, p. 947–966.

Romer, R.L., Martinsson, O., and Perdahl, J.A., 1994, Geochronology of the Kiruna iron ores and hydrothermal alterations: Economic Geology, v. 89, no. 6, p. 1249–1261.

Ruthven, R., Singleton, J., Seymour, N., Gomila, R., Arancibia, G., Stockli, D.F., Ridley, J., and Magloughlin, J., 2020, The geometry, kinematics, and timing of deformation along the southern segment of the Paposo fault zone, Atacama fault system, northern Chile: Journal of South American Earth Sciences, v. 97, no. May 2019, p. 102355.

Salazar, E., Barra, F., Reich, M., Simon, A., Leisen, M., Palma, G., Romero, R., and Rojo, M., 2019, Trace element geochemistry of magnetite from the Cerro Negro Norte iron oxide-apatite deposit, northern Chile: Mineralium Deposita, v. 55, no. 3, p. 409–428.

Sato, K., 2012, Sedimentary Crust and Metallogeny of Granitoid Affinity: Implications from the Geotectonic Histories of the Circum-Japan Sea Region, Central Andes and Southeastern Australia: Resource Geology, v. 62, no. 4, p. 329–351.

Scheuber, E., and Andriessen, P.A.M., 1990, The kinematic and geodynamic significance of the Atacama fault zone, northern Chile: Journal of Structural Geology, v. 12, no. 2, p. 243–257.

Scheuber, E., and Gonzalez, G., 1999, Tectonics of the Jurassic-Early Cretaceous magmatic arc of the north Chilean Coastal Cordillera (22°-26°S): A story of crustal deformation along a convergent plate boundary: Tectonics, v. 18, no. 5, p. 895–910.

Seymour, N.M., Singleton, J.S., Mavor, S.P., Gomila, R., Stockli, D.F., Heuser, G., and Arancibia, G., 2020, The Relationship Between Magmatism and Deformation Along the Intra-arc Strike-Slip Atacama Fault System, Northern Chile: Tectonics, v. 39, no. 3.

Sillitoe, R.H., 2003, Iron oxide-copper-gold deposits: an Andean view: Mineralium Deposita, v. 38, no. 7, p. 787–812.

Simon, A.C., Knipping, J., Reich, M., Barra, F., Deditius, A.P., Bilenker, L., and Childress, T., 2018, Kiruna-Type Iron Oxide-Apatite (IOA) and Iron Oxide Copper-Gold (IOCG) Deposits Form by a Combination of Igneous and Magmatic-Hydrothermal Processes: Evidence from the Chilean Iron Belt, in Metals, Minerals, and Society: Society of Economic Geologists (SEG), p. 89–114.

Skirrow, R.G., 2022, Iron oxide copper-gold (IOCG) deposits – A review (part 1): Settings, mineralogy, ore geochemistry and classification: Ore Geology Reviews, v. 140, no. November 2021, p. 104569.

Sláma, J., Košler, J., Condon, D.J., Crowley, J.L., Gerdes, A., Hanchar, J.M., Horstwood, M.S.A.,

Morris, G.A., Nasdala, L., Norberg, N., Schaltegger, U., Schoene, B., Tubrett, M.N., and Whitehouse, M.J., 2008, Plešovice zircon - A new natural reference material for U-Pb and Hf isotopic microanalysis: Chemical Geology, v. 249, nos. 1–2, p. 1–35.

Smith, C.M., Canil, D., Rowins, S.M., and Friedman, R., 2012, Reduced granitic magmas in an arc setting: The Catface porphyry Cu-Mo deposit of the Paleogene Cascade Arc: Lithos, v. 154, p. 361–373.

Takagi, T., 2004, Origin of magnetite-and ilmenite-series granitic rocks in the Japan Arc: American Journal of Science, v. 304, no. 2, p. 169–202.

Tang, M., Erdman, M., Eldridge, G., and Lee, C.T.A., 2018, The redox "filter" beneath magmatic orogens and the formation of continental crust: Science Advances, v. 4, no. 5, p. 1–8.

Tassara, S., and Ague, J.J., 2022, A Role for Crustal Assimilation in the Formation of Copper-Rich Reservoirs at the Base of Continental Arcs: Economic Geology, v. 117, no. 7, p. 1481–1496.

Tomkins, A.G., Rebryna, K.C., Weinberg, R.F., and Schaefer, B.F., 2012, Magmatic sulfide formation by reduction of oxidized arc basalt: Journal of Petrology, v. 53, no. 8, p. 1537–1567.

Tornos, F., Hanchar, J.M., Munizaga, R., Velasco, F., and Galindo, C., 2021, The role of the subducting slab and melt crystallization in the formation of magnetite-(apatite) systems, Coastal Cordillera of Chile: Mineralium Deposita, v. 56, no. 2, p. 253–278.

Valenzuela, J., 2002,Caracterización, geocronología y mecanismos de emplazamiento del Batolito de la Costa en Vallenar (28°22'-28°41'S y 70°45'-71°7'W), III Región, Chile: Universidad de Concepción: 118 p.

Velasco, F., Tornos, F., and Hanchar, J.M., 2016, Immiscible iron- and silica-rich melts and magnetite geochemistry at the El Laco volcano (northern Chile): Evidence for a magmatic origin for the magnetite deposits: Ore Geology Reviews, v. 79, p. 346–366.

Wade, C.E., Payne, J.L., Barovich, K., Gilbert, S., Wade, B.P., Crowley, J.L., Reid, A., and Jagodzinski, E.A., 2022, Zircon Trace Element Geochemistry As an Indicator of Magma Fertility in Iron Oxide Copper-Gold Provinces: Economic Geology, v. 117, no. 3, p. 703–718.

Wang, J., Hattori, K.H., Kilian, R., and Stern, C.R., 2007, Metasomatism of sub-arc mantle peridotites below southernmost South America: Reduction of fO2 by slab-melt: Contributions to Mineralogy and Petrology, v. 153, no. 5, p. 607–624.

Wang, K., Zhang, L.P., Deng, J.H., Sui, Q.L., Xie, G.Z., and Sun, W.D., 2021, The influence of oceanic anoxic events on convergent margin magmas: Lithos, v. 406–407, no. November, p. 106529.

Watson, E.B., Wark, D.A., and Thomas, J.B., 2006, Crystallization thermometers for zircon and rutile: Contributions to Mineralogy and Petrology, v. 151, no. 4, p. 413–433.

Watts, K.E., and Mercer, C.N., 2020, Zircon-hosted melt inclusion record of silicic magmatism in the Mesoproterozoic St. Francois Mountains terrane, Missouri: Origin of the Pea Ridge iron oxide-apatite-rare earth element deposit and implications for regional crustal pathways of mineralizatio: Geochimica et Cosmochimica Acta, v. 272, p. 54–77.

Wiedenbeck, M., Hanchar, J.M., Peck, W.H., Sylvester, P., Valley, J., Whitehouse, M., Kronz, A., Morishita, Y., and Nasdala, L., 2004, Further Characterisation of the 91500 Zircon Crystal:

Geostandards and Geoanalytical ResearcH, v. 28, p. 9–39.

Wilkinson, J.J., 2013, Triggers for the formation of porphyry ore deposits in magmatic arcs: Nature Geoscience, v. 6, no. 11, p. 917–925.

Williams, P.J., Barton, M.D., Johnson, D.A., Fontboté, L., Haller, A. de, Mark, G., Oliver, N.H.S., and Marschik, R., 2005, Iron Oxide Copper-Gold Deposits Geology, Space-Time Distribution, and Possible Modes of Origin, in One Hundredth Anniversary Volume: Society of Economic Geologists.

Xie, Q., Zhang, Z., Hou, T., Cheng, Z., Campos, E., Wang, Z., and Fei, X., 2019, New insights for the formation of kiruna-type iron deposits by immiscible hydrous Fe-P melt and high-temperature hydrothermal processes: Evidence from El Laco deposit: Economic Geology, v. 114, no. 1, p. 35–46.

Yan, S., Niu, H., Zhao, Z., Li, N., Yang, W., Zhou, R., An, Y., and Huang, F., 2023, Extremely low δ56Fe in arc tholeiites linked to ferrocarbonate recycling: Implications for Fe enrichment in the Awulale Arc, Central Asia: GSA Bulletin, no. April, p. 1–17.

Yu, K., Liu, Y., Foley, S.F., Zhu, Y., Hu, Z., Zong, K., and Chen, H., 2021, Transformation from oxidized to reduced alkaline magmas in the northern North China Craton: Lithos, v. 390–391, p. 106104.

Anexos

Anexo A: Diagramas de concordia y promedio ponderado para las dataciones U-Pb de este estudio.

Anexo A.1: Diagramas de concordia y promedio ponderado para las muestras del Complejo Plutónico La Higuera.

Muestra RRJP-01 – 121.9 ± 1.1 Ma

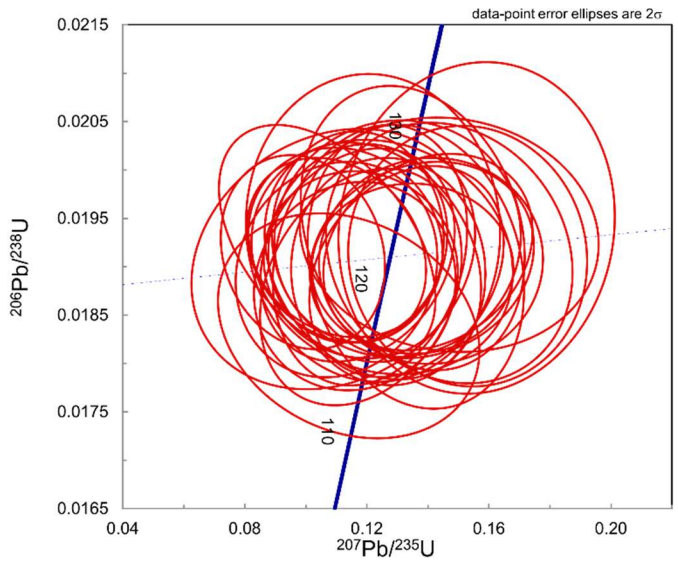

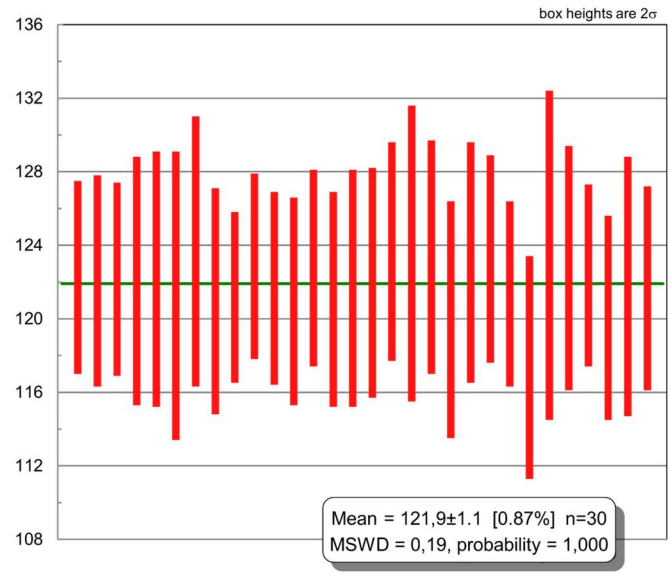

Muestra AOLH2-03 – 123.1 ± 0.9 Ma

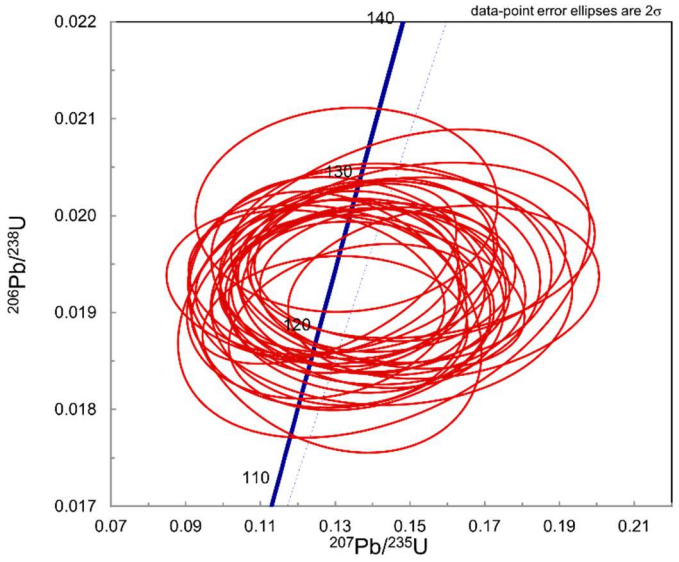

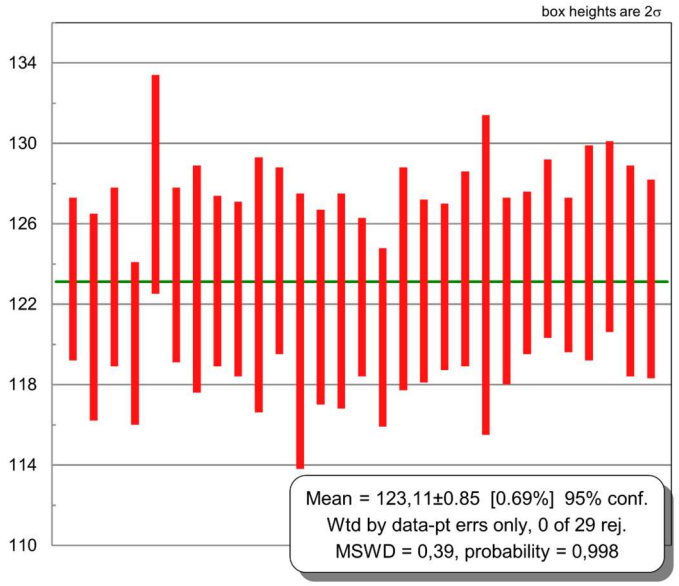

AOLH-06 – 123.3 ± 1.8 Ma

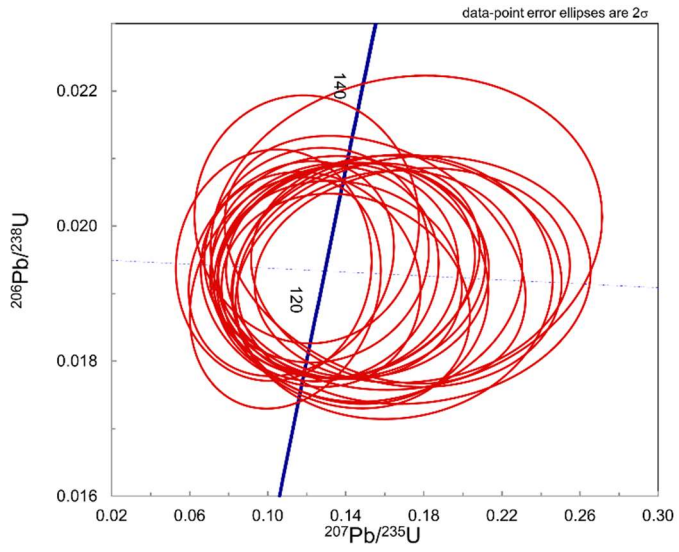

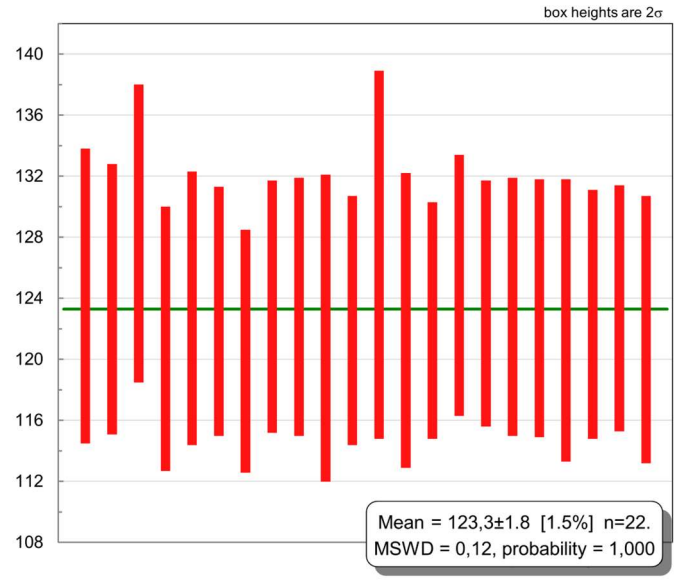

Muestra AOLH-07 – 123.5 ± 0.8 Ma

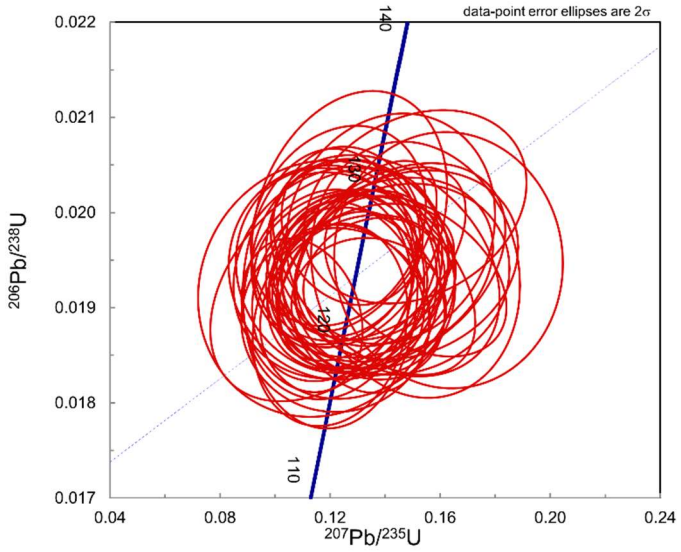

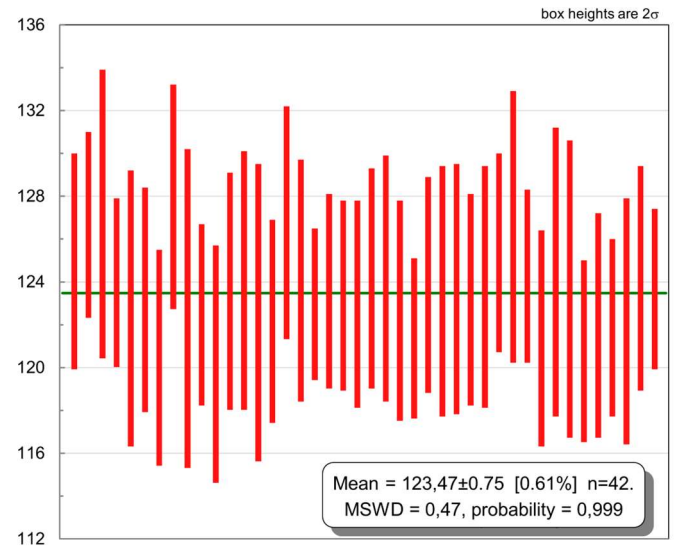

Muestra AOLH2-02 – 127.3 ± 1.0 Ma

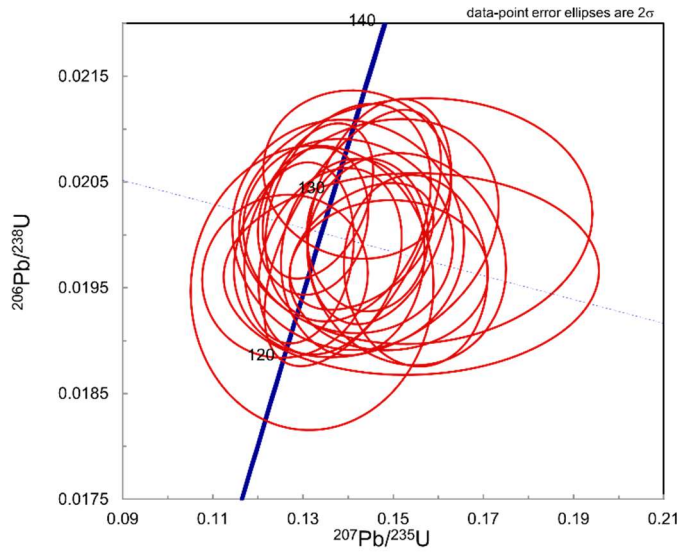

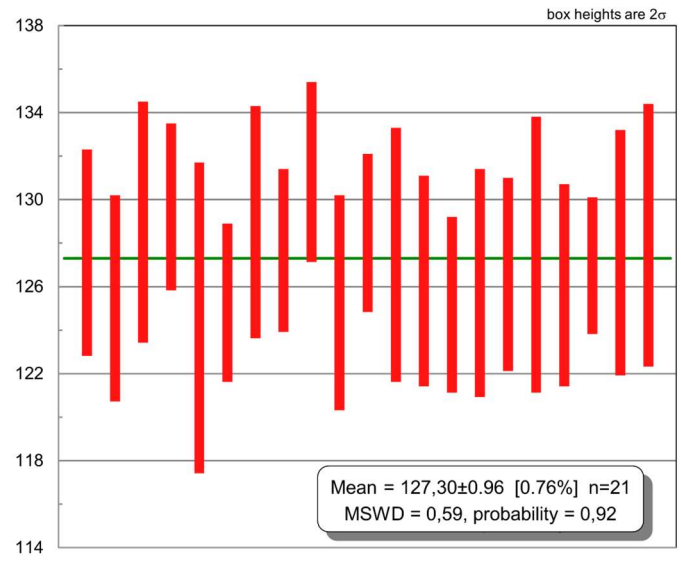

Muestra AOLH2-07 – 127.3 ± 1.0 Ma

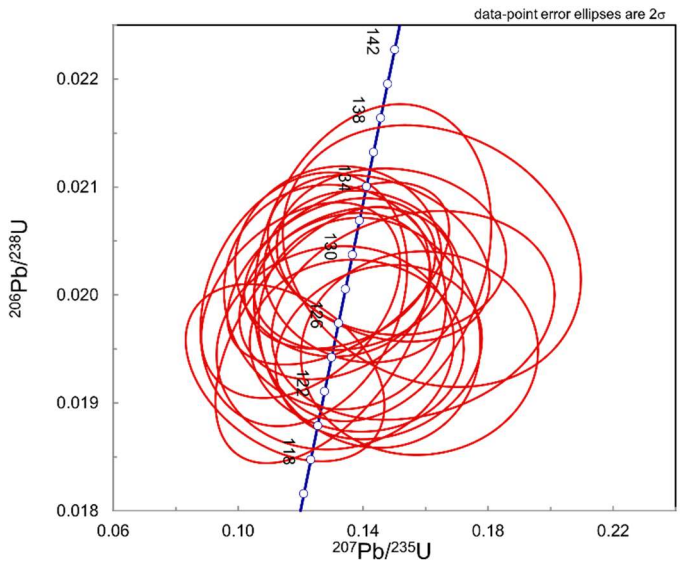

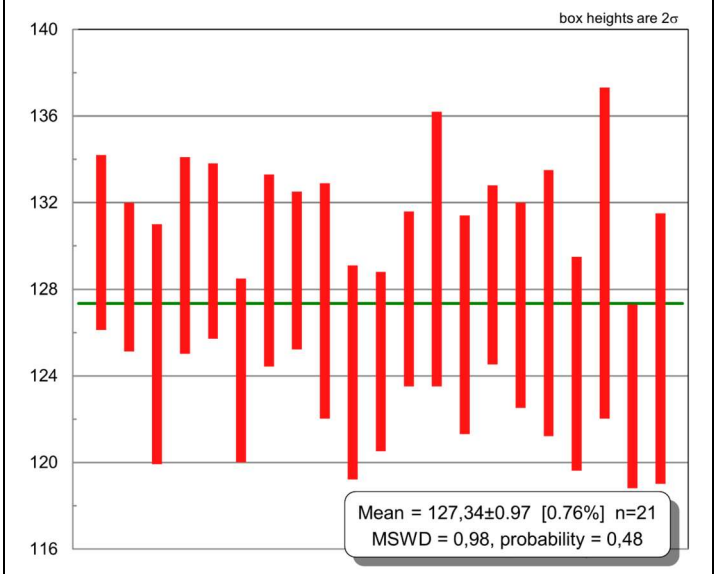

Anexo A.3: Diagramas de concordia y promedio ponderado para las muestras del Complejo Plutónico Retamilla

Muestra JJRETA2 – 126.6 ± 1.3 Ma

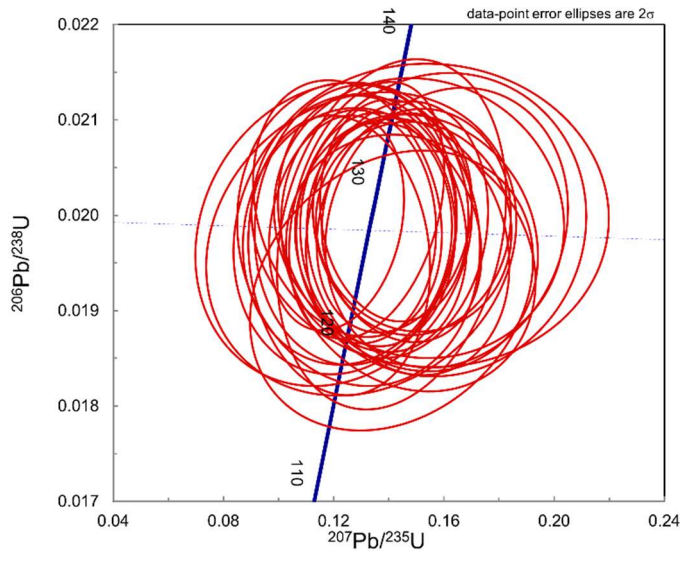

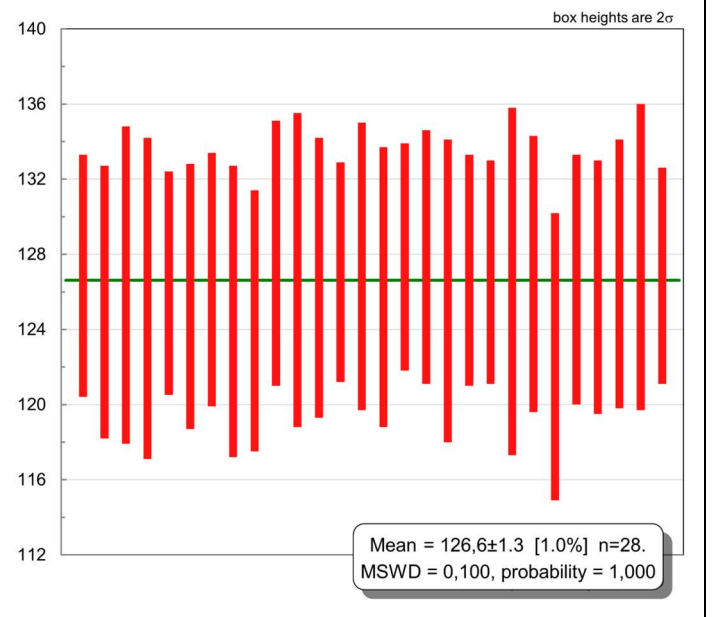

Muestra AORE-02 – 126.7 ± 1.3 Ma

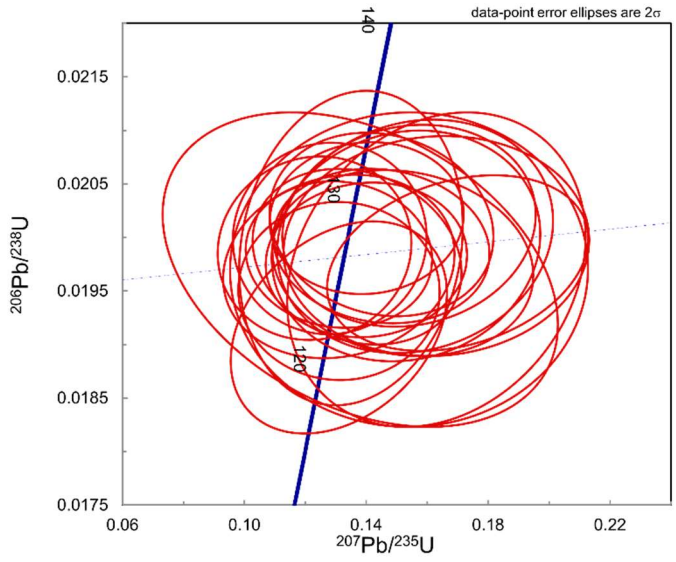

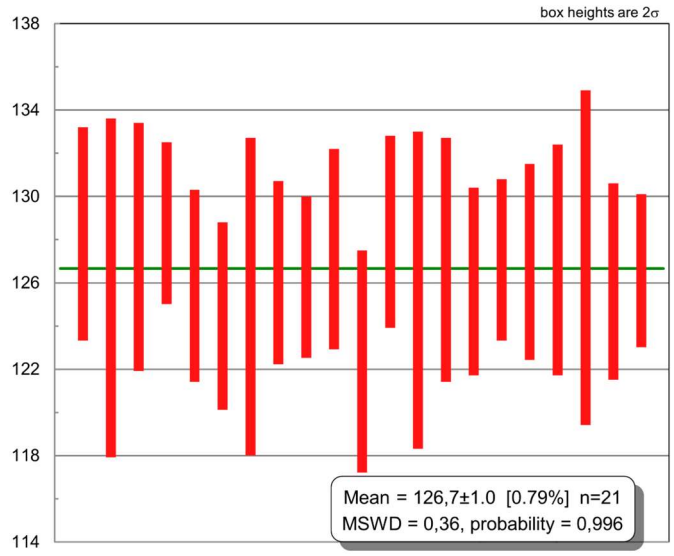

Muestra AOOJA-04 – 127.0 ± 1.6 Ma

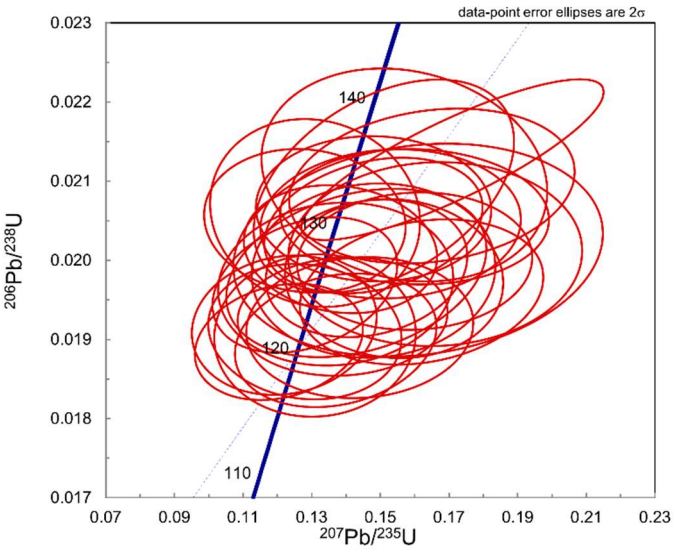

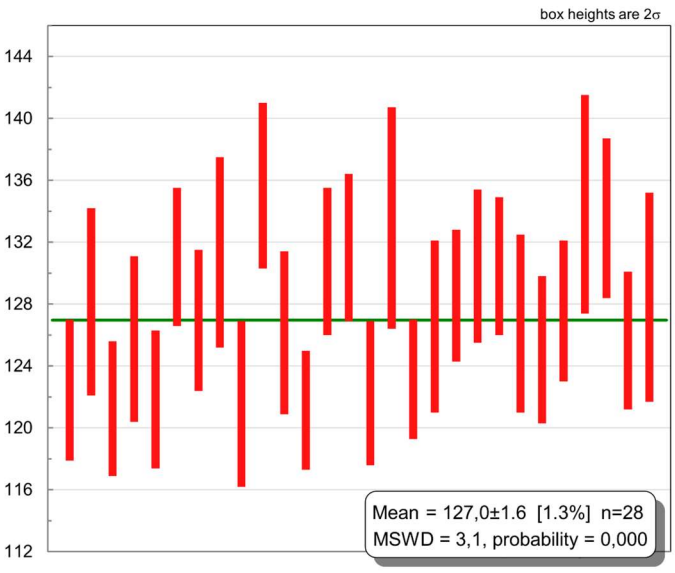

Muestra AORE-05 – 127.1 ± 0.9 Ma

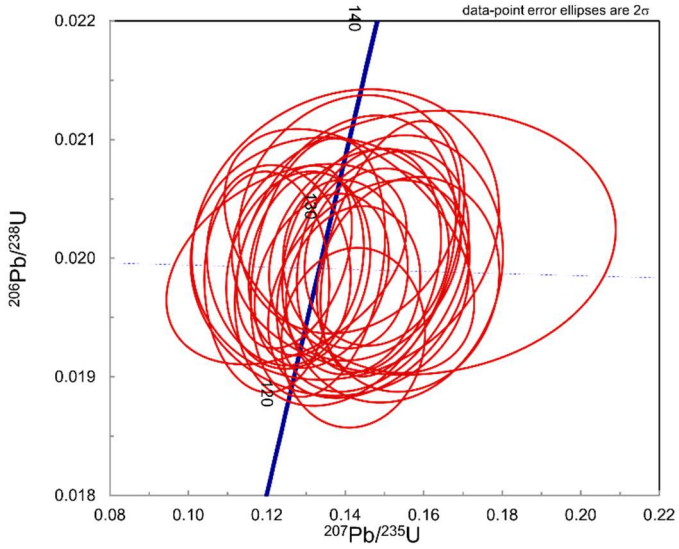

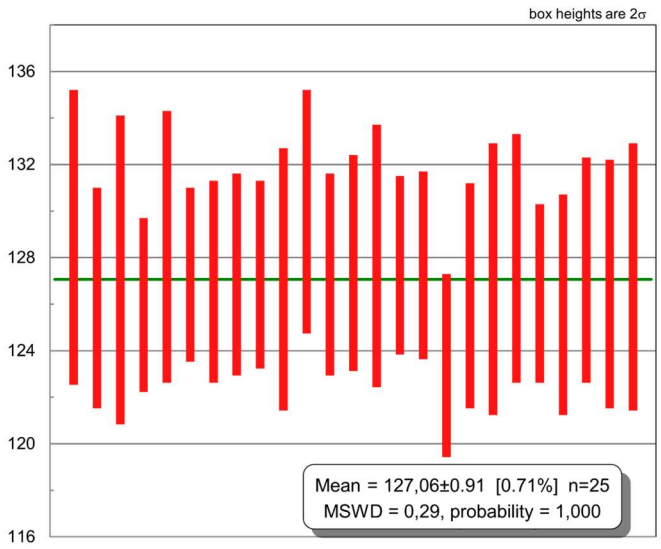

Muestra AOAL-03 – 127.8 ± 1.0 Ma

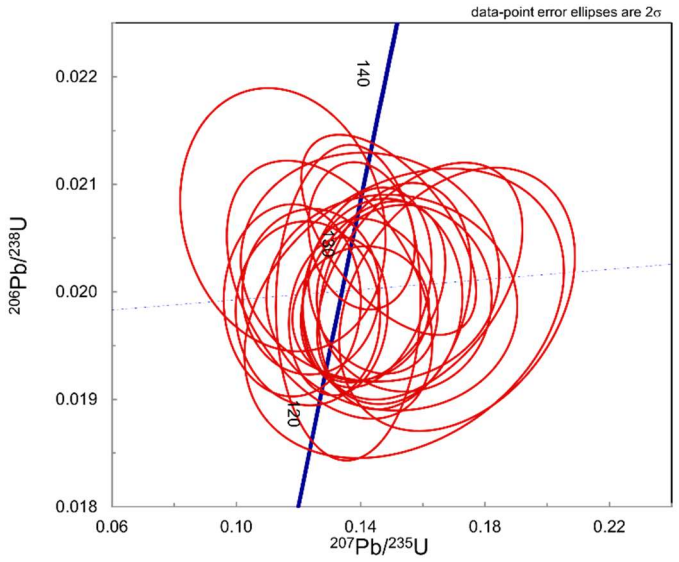

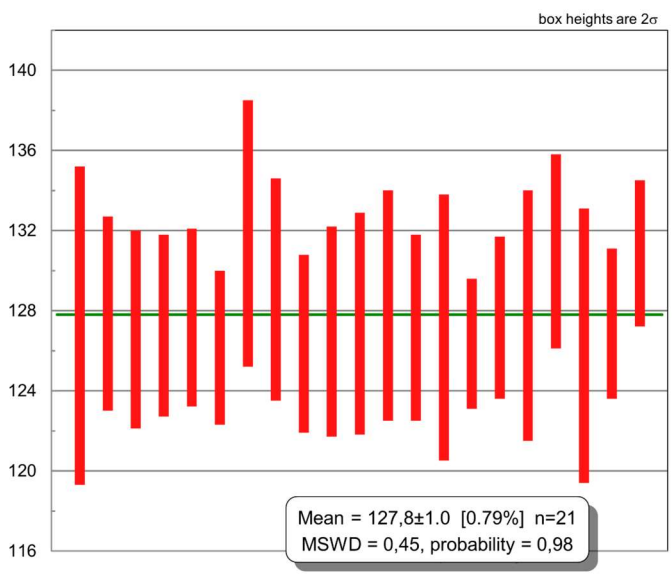

Muestra AORE-04 – 127.9 ± 1.3 Ma

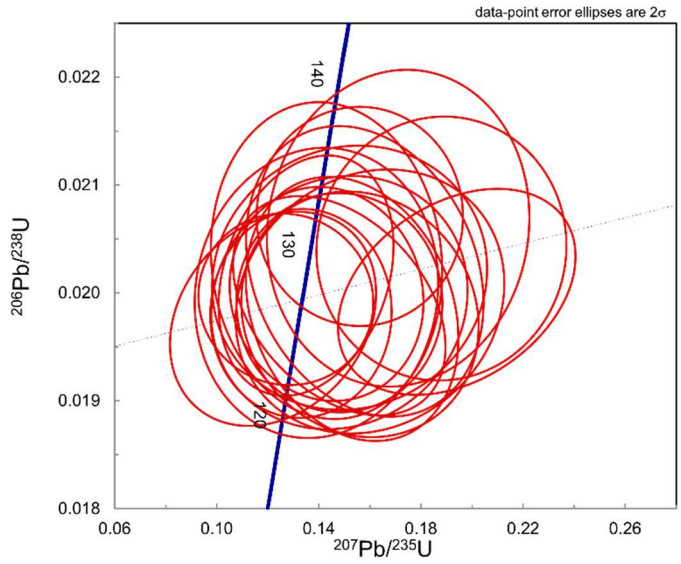

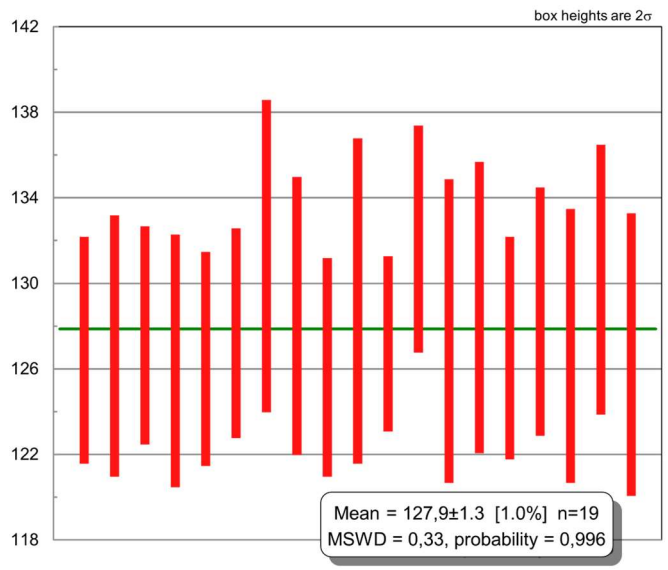

Muestra AOLH-09 – 128.3 ± 0.9 Ma

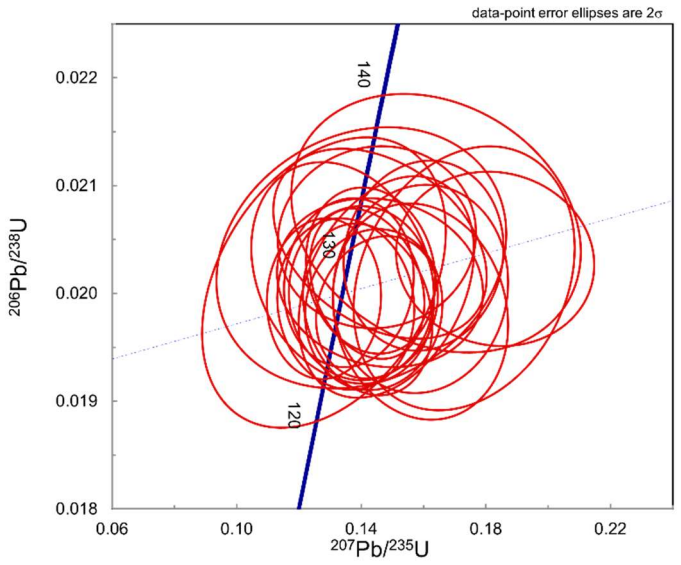

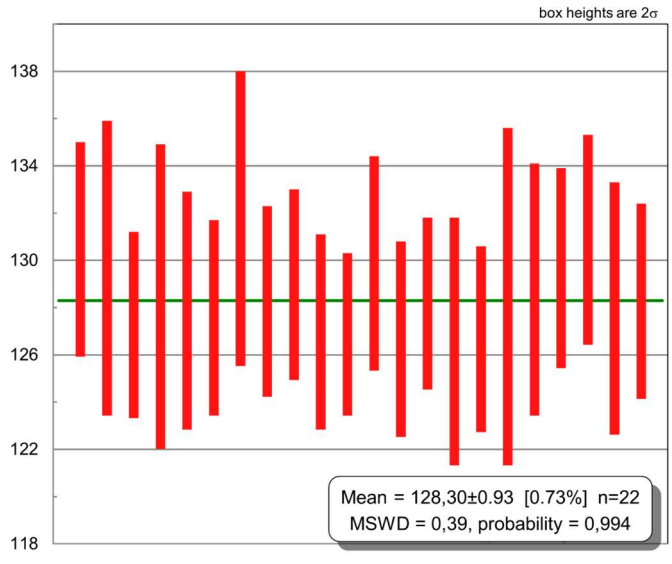

Muestra AOAL-04 – 128.3 ± 1.0 Ma

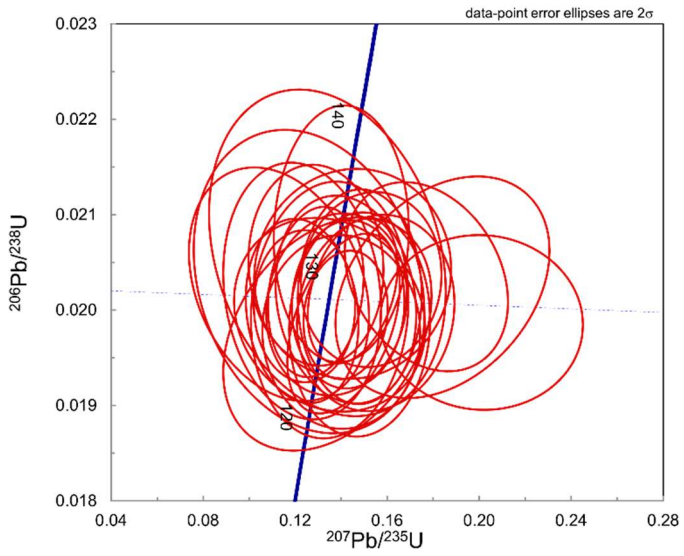

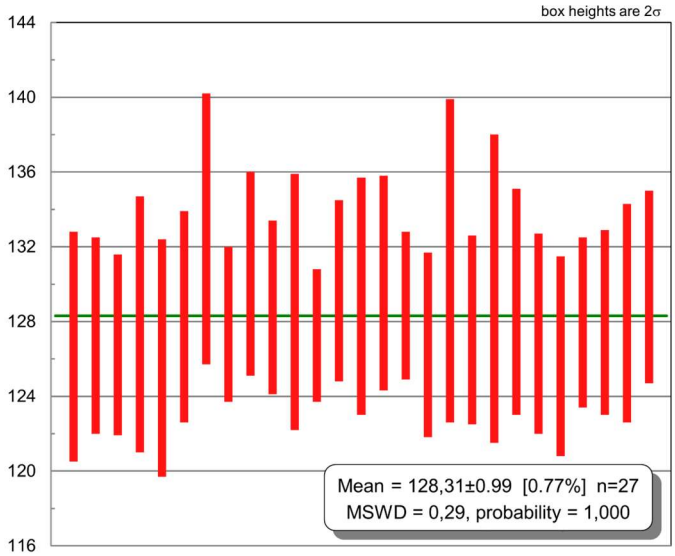

Anexo A.4: Diagramas de concordia y promedio ponderado para las muestras del Complejo Plutónico Infiernillo

Muestra AOIN-02 – 133.0 ± 1.0 Ma

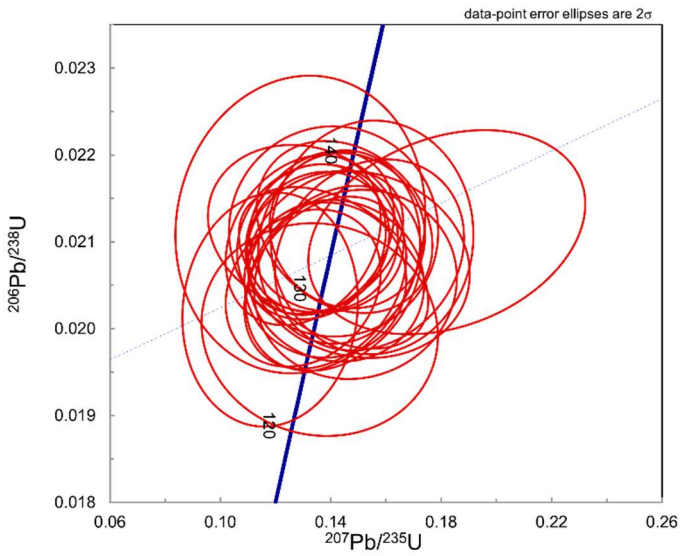

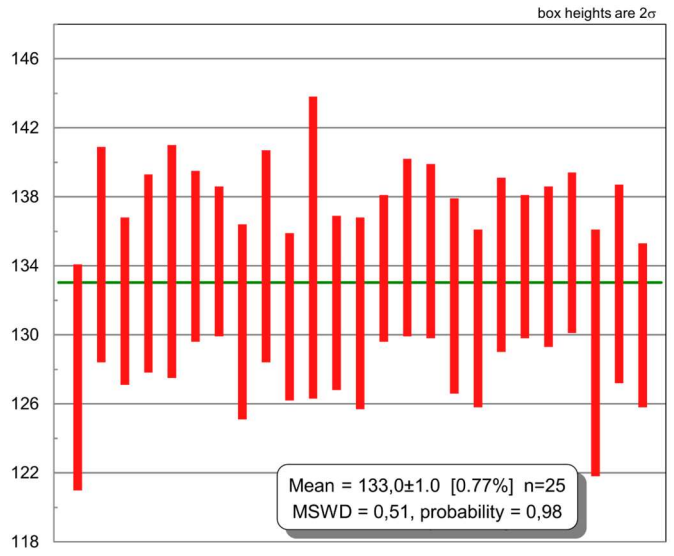

Anexo B: Radios Isotópicos, Correlaciones de errores y edades U-Pb para todos los análisis de este estudio.

Sample/Zircon	Isotope ratios								Error Correlations		U-Pb ages (Ma)			
	207Pb	±	207Pb	±	206Pb	±	238U	±	$^{206}Pb/^{238}U$	$^{238}U/^{206}Pb$	206Pb	±	207Pb	±
	206Pb	(abs)	235U	(abs)	238U	(abs)	20Pb	(abs)	$^{207}Pb/^{235}U$	$^{207}Pb/^{206}Pb$	238U	(Ma)	235U	(Ma)
X_AOLH_06_0	0.0620	0.0250	0.1550	0.0630	0.0195	0.0015	51.2821	3.9448	-0.3030	0.4404	124.2	9.6	144	54
X_AOLH_06_2	0.0366	0.0140	0.1030	0.0410	0.0194	0.0014	51.4933	3.7122	0.0349	0.1186	124	8.8	98	37
X_AOLH_06_5	0.0426	0.0160	0.1200	0.0470	0.0201	0.0015	49.7512	3.7128	-0.0286	0.2026	128.3	9.7	114	42
X_AOLH_06_6	0.0429	0.0150	0.1090	0.0400	0.0190	0.0014	52.6039	3.8740	0.1966	0.2032	121.4	8.6	104	36
X_AOLH_06_7	0.0670	0.0250	0.1710	0.0650	0.0193	0.0014	51.7331	3.7468	-0.1031	0.3137	123.4	8.9	158	55
X_AOLH_06_9	0.0535	0.0190	0.1300	0.0470	0.0193	0.0013	51.8403	3.4936	0.0974	0.2450	123.2	8.1	123	43
X_AOLH_06_11	0.0621	0.0220	0.1400	0.0520	0.0189	0.0013	52.9381	3.6432	-0.1337	0.4663	120.6	7.9	135	42
X_AOLH_06_12	0.0594	0.0210	0.1460	0.0550	0.0194	0.0013	51.6796	3.4720	0.0046	0.2870	123.5	8.2	137	48
X_AOLH_06_14	0.0532	0.0200	0.1340	0.0520	0.0193	0.0013	51.7063	3.4756	0.0529	0.0870	123.5	8.4	126	47
X_AOLH_06_15	0.0640	0.0250	0.1640	0.0670	0.0191	0.0016	52.3560	4.3858	0.0542	0.1958	122.1	10	153	58
X_AOLH_06_16	0.0459	0.0170	0.1220	0.0460	0.0192	0.0013	52.0562	3.5228	-0.1044	0.3797	122.6	8.1	115	42
X_AOLH_06_19	0.0600	0.0270	0.1710	0.0820	0.0199	0.0019	50.2513	4.7979	0.0999	0.1341	126.9	12	157	70
X_AOLH_06_20	0.0650	0.0260	0.1750	0.0740	0.0192	0.0015	52.0833	4.0690	0.0791	0.1447	122.6	9.6	162	64
X_AOLH_06_24	0.0527	0.0190	0.1370	0.0510	0.0192	0.0012	52.0833	3.2552	-0.0810	0.2504	122.6	7.7	129	45
X_AOLH_06_26	0.0491	0.0180	0.1250	0.0470	0.0196	0.0013	51.0986	3.3944	0.0467	0.1949	124.9	8.5	122	46
X_AOLH_06_27	0.0371	0.0130	0.1120	0.0430	0.0194	0.0013	51.6262	3.4648	0.2002	-0.0405	123.7	8	106	39
X_AOLH_06_28	0.0490	0.0180	0.1430	0.0560	0.0193	0.0013	51.7063	3.4756	0.0802	0.0140	123.5	8.4	134	49
X_AOLH_06_29	0.0490	0.0180	0.1400	0.0540	0.0193	0.0013	51.7063	3.4756	0.1315	0.1391	123.4	8.4	130	48
X_AOLH_06_32	0.0540	0.0220	0.1420	0.0580	0.0192	0.0015	52.0833	4.0690	-0.0932	0.2759	122.6	9.2	132	52
X_AOLH_06_37	0.0710	0.0260	0.1740	0.0660	0.0193	0.0013	51.8941	3.5009	0.0929	0.2000	123	8.1	160	57
X_AOLH_06_40	0.0622	0.0210	0.1450	0.0520	0.0193	0.0013	51.7063	3.4756	0.2082	0.1899	123.4	8	139	49
X_AOLH_06_41	0.0680	0.0250	0.1570	0.0600	0.0191	0.0014	52.3286	3.8336	0.1398	0.2427	122	8.7	147	52
X_AOLH_07_0	0.0447	0.0089	0.1220	0.0250	0.0196	0.0008	51.0725	2.0606	0.1738	-0.0259	125	5	115	23
X_AOLH_07_1	0.0468	0.0074	0.1280	0.0210	0.0199	0.0007	50.3525	1.7241	-0.1177	0.3942	126.7	4.3	121.4	19
X_AOLH_07_4	0.0465	0.0099	0.1270	0.0290	0.0199	0.0011	50.1756	2.7694	0.2372	0.0055	127.2	6.7	120	25
X_AOLH_07_5	0.0496	0.0094	0.1310	0.0260	0.0194	0.0006	51.4933	1.6440	0.0560	0.1244	124	3.9	124	23
X_AOLH_07_6	0.0440	0.0120	0.1180	0.0340	0.0192	0.0010	51.9751	2.7014	0.3861	-0.0988	122.8	6.4	111	30
X_AOLH_07_9	0.0550	0.0120	0.1460	0.0320	0.0193	0.0008	51.8135	2.2014	0.1090	0.1111	123.2	5.2	136	28
X_AOLH_07_10	0.0475	0.0110	0.1220	0.0280	0.0189	0.0008	52.9942	2.2186	-0.0008	0.2003	120.5	5	115	25
X_AOLH_07_11	0.0542	0.0110	0.1510	0.0330	0.0201	0.0008	49.8505	2.0626	0.2495	-0.1267	128	5.2	142	29
X_AOLH_07_14	0.0459	0.0099	0.1200	0.0260	0.0192	0.0012	52.0833	3.2552	0.0387	0.2291	122.8	7.4	114	23

Anexo B, continuación.

Sample/Zircon	Isotope ratios								Error Correlations		U-Pb ages (Ma)			
	207Pb/206Pb	± (abs)	207Pb/235U	± (abs)	206Pb/238U	± (abs)	238U/20Pb	± (abs)	$^{206}Pb/^{238}U$ / $^{207}Pb/^{235}U$	$^{238}U/^{206}Pb$ / $^{207}Pb/^{206}Pb$	206Pb/238U	± (Ma)	207Pb/235U	± (Ma)
X_AOLH_07_15	0.0479	0.0073	0.1260	0.0200	0.0192	0.0007	52.1105	1.8194	0.2498	0.1101	122.5	4.2	120	18
X_AOLH_07_16	0.0469	0.0087	0.1200	0.0230	0.0188	0.0009	53.1350	2.4563	0.1460	0.1786	120.2	5.5	114	21
X_AOLH_07_17	0.0513	0.0120	0.1360	0.0300	0.0194	0.0009	51.6529	2.3212	-0.4822	0.6321	123.6	5.5	128	27
X_AOLH_07_18	0.0530	0.0130	0.1400	0.0340	0.0194	0.0010	51.4403	2.5138	-0.2952	0.4830	124.1	6	131	30
X_AOLH_07_19	0.0450	0.0140	0.1160	0.0360	0.0192	0.0011	52.0833	2.9839	0.0731	0.2385	122.6	6.9	111	33
X_AOLH_07_20	0.0506	0.0098	0.1310	0.0250	0.0192	0.0007	52.2193	2.0179	-0.2322	0.4505	122.2	4.7	124	22
X_AOLH_07_21	0.0455	0.0094	0.1230	0.0260	0.0199	0.0009	50.3525	2.1804	0.2042	0.1112	126.8	5.4	117	23
X_AOLH_07_22	0.0520	0.0120	0.1420	0.0340	0.0194	0.0009	51.4403	2.3286	0.3528	-0.1018	124.1	5.6	133	31
X_AOLH_07_23	0.0515	0.0076	0.1359	0.0210	0.0193	0.0006	51.8941	1.4812	0.1199	0.0980	123	3.5	129	19
X_AOLH_07_24	0.0492	0.0110	0.1290	0.0300	0.0194	0.0007	51.6529	1.9210	0.0439	0.1229	123.6	4.5	122	26
X_AOLH_07_26	0.0581	0.0110	0.1510	0.0270	0.0193	0.0007	51.7331	1.8467	-0.3869	0.5883	123.4	4.4	142	24
X_AOLH_07_27	0.0483	0.0093	0.1260	0.0240	0.0193	0.0008	51.9211	2.0488	0.0310	0.1762	123	4.8	119	22
X_AOLH_07_29	0.0559	0.0120	0.1480	0.0330	0.0195	0.0008	51.4139	2.1411	0.1868	0.0293	124.2	5.1	139	30
X_AOLH_07_30	0.0499	0.0110	0.1310	0.0280	0.0195	0.0009	51.3875	2.3766	-0.1328	0.2716	124.2	5.7	124	25
X_AOLH_07_31	0.0456	0.0089	0.1210	0.0240	0.0192	0.0008	52.0291	2.1927	0.2327	-0.0577	122.7	5.1	114	22
X_AOLH_07_32	0.0512	0.0082	0.1340	0.0230	0.0190	0.0006	52.6039	1.6326	-0.0289	0.1929	121.4	3.7	126	20
X_AOLH_07_34	0.0529	0.0120	0.1400	0.0320	0.0194	0.0008	51.5464	2.0991	0.2394	-0.0291	123.9	5	132	29
X_AOLH_07_35	0.0450	0.0110	0.1210	0.0310	0.0194	0.0009	51.6262	2.4520	-0.0594	0.0316	123.6	5.8	113	28
X_AOLH_07_36	0.0460	0.0120	0.1240	0.0320	0.0194	0.0009	51.6262	2.4254	0.1322	-0.0175	123.7	5.8	117	29
X_AOLH_07_37	0.0481	0.0091	0.1290	0.0260	0.0193	0.0008	51.8403	2.0693	0.2714	-0.0067	123.2	4.9	123	23
X_AOLH_07_38	0.0454	0.0110	0.1200	0.0280	0.0194	0.0009	51.5730	2.3406	-0.0864	0.3897	123.8	5.6	114	25
X_AOLH_07_39	0.0483	0.0073	0.1330	0.0210	0.0197	0.0007	50.8906	1.8906	0.5506	-0.0398	125.4	4.6	126.7	19
X_AOLH_07_40	0.0518	0.0110	0.1420	0.0310	0.0198	0.0010	50.4286	2.5176	0.1204	0.1338	126.6	6.3	133	27
X_AOLH_07_41	0.0478	0.0074	0.1270	0.0200	0.0195	0.0006	51.3611	1.6619	0.2200	0.0630	124.3	4	120.5	18
X_AOLH_07_42	0.0511	0.0110	0.1300	0.0290	0.0190	0.0008	52.6039	2.1861	0.2029	0.0012	121.4	5	123	26
X_AOLH_07_43	0.0610	0.0130	0.1630	0.0340	0.0195	0.0011	51.2821	2.8928	-0.0265	0.2771	124.5	6.7	152	31
X_AOLH_07_45	0.0589	0.0120	0.1510	0.0310	0.0194	0.0011	51.5464	2.9227	-0.1223	0.4369	123.7	6.9	142	26
X_AOLH_07_47	0.0432	0.0071	0.1098	0.0180	0.0189	0.0007	52.8541	1.8437	-0.2105	0.4540	120.8	4.2	105.4	17
X_AOLH_07_48	0.0494	0.0086	0.1290	0.0220	0.0191	0.0008	52.3286	2.2454	-0.2610	0.5544	122	5.2	123	20
X_AOLH_07_49	0.0491	0.0088	0.1260	0.0230	0.0191	0.0006	52.3835	1.7562	-0.1567	0.3285	121.9	4.1	120	21
X_AOLH_07_51	0.0455	0.0092	0.1190	0.0250	0.0191	0.0009	52.2466	2.4567	0.1003	0.0536	122.2	5.7	113	22
X_AOLH_07_52	0.0516	0.0100	0.1350	0.0280	0.0195	0.0008	51.3875	2.1918	0.5426	-0.3466	124.2	5.2	128	25
X_AOLH_07_53	0.0496	0.0095	0.1320	0.0270	0.0194	0.0006	51.6262	1.5725	0.3170	-0.0941	123.7	3.7	124	24
X_AOLH2_02_1	0.0510	0.0065	0.1400	0.0190	0.0200	0.0008	50.0250	1.8769	-0.0794	0.2723	127.6	4.7	140	22
X_AOLH2_02_2	0.0576	0.0055	0.1550	0.0130	0.0197	0.0007	50.8647	1.9145	-0.0568	0.5006	125.5	4.7	146	12
X_AOLH2_02_3	0.0533	0.0045	0.1470	0.0130	0.0202	0.0009	49.4560	2.1279	0.3082	0.1433	129	5.5	139	11
X_AOLH2_02_4	0.0479	0.0036	0.1333	0.0100	0.0203	0.0006	49.2126	1.4531	0.3723	-0.0259	129.7	3.8	126.9	9.3
X_AOLH2_02_9	0.0476	0.0077	0.1320	0.0220	0.0195	0.0011	51.2821	2.8928	0.0251	0.1814	124.6	7.1	125	20
X_AOLH2_02_10	0.0555	0.0066	0.1490	0.0180	0.0196	0.0006	50.9684	1.5067	0.0243	0.1524	125.3	3.6	141	16

Anexo B, continuación.

Sample/Zircon	Isotope ratios								Error Correlations		U-Pb ages (Ma)			
	207Pb/206Pb	± (abs)	207Pb/235U	± (abs)	206Pb/238U	± (abs)	238U/20Pb	± (abs)	$^{206}Pb/^{238}U$ / $^{207}Pb/^{235}U$	$^{238}U/^{206}Pb$ / $^{207}Pb/^{206}Pb$	206Pb/238U	± (Ma)	207Pb/235U	± (Ma)
X_AOLH2_02_11	0.0505	0.0049	0.1400	0.0150	0.0202	0.0008	49.4805	2.0566	0.2792	0.0003	129	5.3	133	13
X_AOLH2_02_12	0.0522	0.0040	0.1443	0.0110	0.0200	0.0006	50.0000	1.4750	-0.0036	0.2683	127.7	3.7	136.6	9.6
X_AOLH2_02_13	0.0497	0.0061	0.1420	0.0170	0.0206	0.0007	48.6145	1.5362	-0.0583	0.2355	131.3	4.1	134	15
X_AOLH2_02_14	0.0570	0.0120	0.1540	0.0340	0.0196	0.0008	50.9424	2.0242	0.0304	0.0556	125.3	4.9	143	30
X_AOLH2_02_15	0.0479	0.0043	0.1322	0.0100	0.0201	0.0006	49.6771	1.4067	0.1407	0.2559	128.5	3.6	125.8	9.3
X_AOLH2_02_18	0.0514	0.0079	0.1440	0.0240	0.0200	0.0009	50.0751	2.3069	0.2668	-0.0354	127.5	5.8	136	21
X_AOLH2_02_19	0.0512	0.0051	0.1410	0.0130	0.0198	0.0008	50.5306	1.9405	0.0593	0.3114	126.3	4.8	134	12
X_AOLH2_02_20	0.0461	0.0054	0.1260	0.0150	0.0196	0.0006	50.9944	1.6383	0.0418	0.1781	125.2	4	120	14
X_AOLH2_02_21	0.0561	0.0074	0.1530	0.0180	0.0198	0.0008	50.5817	2.0980	-0.0884	0.4419	126.2	5.2	144	16
X_AOLH2_02_22	0.0468	0.0036	0.1291	0.0099	0.0198	0.0007	50.4286	1.7801	0.1632	0.2475	126.6	4.4	123.2	8.9
X_AOLH2_02_23	0.0514	0.0050	0.1410	0.0160	0.0200	0.0010	50.0751	2.4824	0.5901	-0.1201	127.5	6.3	134	14
X_AOLH2_02_24	0.0495	0.0046	0.1360	0.0130	0.0198	0.0007	50.6329	1.8459	0.2464	0.1559	126.1	4.6	129	12
X_AOLH2_02_25	0.0537	0.0045	0.1430	0.0130	0.0199	0.0005	50.2765	1.2386	0.4287	0.4657	127	3.1	135	11
X_AOLH2_02_27	0.0509	0.0082	0.1400	0.0210	0.0200	0.0009	50.0000	2.2250	-0.0591	0.3899	127.6	5.6	133	19
X_AOLH2_02_29	0.0570	0.0120	0.1550	0.0320	0.0201	0.0010	49.6771	2.3444	0.0593	0.1108	128.4	6	145	28
X_AOLH2_03_0	0.0470	0.0097	0.1300	0.0270	0.0193	0.0006	51.7866	1.6896	0.3335	-0.1690	123.3	4	122	24
X_AOLH2_03_1	0.0505	0.0120	0.1310	0.0280	0.0190	0.0008	52.5762	2.2114	-0.0407	0.2842	121.4	5.1	124	25
X_AOLH2_03_2	0.0530	0.0110	0.1400	0.0300	0.0193	0.0007	51.7598	1.8754	-0.1267	0.3271	123.4	4.4	132	26
X_AOLH2_03_3	0.0500	0.0110	0.1300	0.0290	0.0188	0.0006	53.1915	1.8108	0.0440	0.1040	120.1	4	123	26
X_AOLH2_03_4	0.0475	0.0120	0.1330	0.0330	0.0201	0.0009	49.8505	2.1372	0.0643	0.1558	128	5.4	125	29
X_AOLH2_03_5	0.0500	0.0110	0.1320	0.0270	0.0193	0.0007	51.7063	1.7913	-0.0514	0.3295	123.5	4.3	125	25
X_AOLH2_03_7	0.0527	0.0130	0.1360	0.0320	0.0193	0.0009	51.7866	2.3869	-0.2331	0.4680	123.3	5.6	128	29
X_AOLH2_03_8	0.0462	0.0120	0.1240	0.0320	0.0193	0.0007	51.8403	1.8006	-0.1137	0.2603	123.2	4.2	117	29
X_AOLH2_03_11	0.0544	0.0120	0.1390	0.0300	0.0192	0.0007	52.0021	1.8659	0.0013	0.2355	122.8	4.3	130	27
X_AOLH2_03_12	0.0530	0.0160	0.1420	0.0420	0.0193	0.0010	51.8941	2.6930	-0.0245	0.1282	123	6.3	132	37
X_AOLH2_03_13	0.0487	0.0120	0.1330	0.0330	0.0195	0.0007	51.3875	1.9277	0.3007	-0.1735	124.2	4.6	125	30
X_AOLH2_03_14	0.0500	0.0130	0.1300	0.0320	0.0189	0.0011	52.9101	3.0794	-0.2234	0.4918	120.7	6.8	123	29
X_AOLH2_03_15	0.0523	0.0110	0.1360	0.0290	0.0191	0.0008	52.3835	2.0580	-0.0756	0.3781	121.9	4.8	129	26
X_AOLH2_03_16	0.0487	0.0120	0.1270	0.0300	0.0191	0.0008	52.2466	2.2930	0.1624	0.0590	122.2	5.3	120	27
X_AOLH2_03_18	0.0542	0.0120	0.1440	0.0300	0.0192	0.0006	52.1376	1.6854	-0.2921	0.4848	122.4	3.9	136	26
X_AOLH2_03_19	0.0528	0.0110	0.1370	0.0290	0.0189	0.0007	53.0504	1.9700	0.2173	0.0687	120.4	4.4	129	25
X_AOLH2_03_20	0.0535	0.0140	0.1420	0.0350	0.0193	0.0009	51.7866	2.3064	0.0092	0.2071	123.3	5.5	134	31
X_AOLH2_03_21	0.0550	0.0120	0.1430	0.0310	0.0192	0.0007	52.0562	1.8969	-0.0388	0.2693	122.7	4.5	134	28
X_AOLH2_03_22	0.0477	0.0110	0.1250	0.0280	0.0193	0.0007	51.9481	1.7811	-0.2336	0.3335	122.9	4.1	118	25
X_AOLH2_03_23	0.0469	0.0110	0.1270	0.0290	0.0194	0.0008	51.5464	2.0193	0.4823	-0.2781	123.8	4.8	120	26
X_AOLH2_03_24	0.0520	0.0160	0.1430	0.0450	0.0193	0.0013	51.8135	3.4900	0.3869	-0.3121	123.5	7.9	134	40
X_AOLH2_03_25	0.0601	0.0130	0.1590	0.0340	0.0192	0.0007	52.0562	1.9782	0.1843	0.1210	122.7	4.6	147	29
X_AOLH2_03_26	0.0495	0.0110	0.1370	0.0310	0.0194	0.0006	51.6529	1.6809	0.2074	-0.0152	123.6	4	129	27
X_AOLH2_03_27	0.0551	0.0130	0.1500	0.0340	0.0196	0.0007	51.1509	1.8053	0.0807	0.1079	124.8	4.4	141	30

Anexo B, continuación.

Sample/Zircon	Isotope ratios								Error Correlations		U-Pb ages (Ma)			
	207Pb	±	207Pb	±	206Pb	±	238U	±	$^{206}Pb/^{238}U$	$^{238}U/^{206}Pb$	206Pb	±	207Pb	±
	206Pb	(abs)	235U	(abs)	238U	(abs)	20Pb	(abs)	$^{207}Pb/^{235}U$	$^{207}Pb/^{206}Pb$	238U	(Ma)	235U	(Ma)
X_AOLH2_03_28	0.0548	0.0100	0.1440	0.0280	0.0193	0.0006	51.7063	1.6309	0.1110	0.1713	123.5	3.8	136	24
X_AOLH2_03_29	0.0554	0.0140	0.1450	0.0350	0.0195	0.0008	51.2558	2.2068	-0.0834	0.3094	124.6	5.3	135	31
X_AOLH2_03_30	0.0571	0.0140	0.1530	0.0380	0.0196	0.0007	50.9165	1.9184	0.1885	-0.0202	125.4	4.7	143	33
X_AOLH2_03_31	0.0511	0.0110	0.1370	0.0290	0.0194	0.0008	51.5996	2.1833	0.2631	0.0527	123.7	5.2	129	26
X_AOLH2_03_32	0.0524	0.0110	0.1370	0.0270	0.0193	0.0008	51.7866	2.0650	-0.0631	0.3980	123.3	4.9	130	25
AOLH2_07_0	0.0529	0.0110	0.1490	0.0300	0.0204	0.0006	49.0196	1.5138	-0.0642	0.2875	130.2	4	140	27
AOLH2_07_1	0.0502	0.0096	0.1370	0.0260	0.0202	0.0005	49.6278	1.3300	0.2079	0.0252	128.6	3.4	130.5	23
AOLH2_07_2	0.0521	0.0110	0.1420	0.0290	0.0197	0.0009	50.8906	2.2532	-0.0869	0.3993	125.5	5.5	134	25
AOLH2_07_4	0.0473	0.0098	0.1320	0.0270	0.0203	0.0007	49.2368	1.7455	0.0375	0.2465	129.6	4.5	126	24
AOLH2_07_5	0.0523	0.0110	0.1450	0.0290	0.0203	0.0006	49.1642	1.5228	-0.2808	0.4741	129.8	4	137	26
AOLH2_07_7	0.0537	0.0100	0.1450	0.0270	0.0195	0.0007	51.3611	1.7411	0.1569	0.1381	124.3	4.2	137.1	24
AOLH2_07_8	0.0479	0.0100	0.1320	0.0290	0.0202	0.0007	49.5050	1.6910	0.4841	-0.3158	128.9	4.4	125	26
AOLH2_07_9	0.0467	0.0087	0.1325	0.0250	0.0202	0.0006	49.5050	1.3969	0.2663	0.0099	128.9	3.6	125.9	22
AOLH2_07_10	0.0483	0.0110	0.1310	0.0290	0.0200	0.0009	50.0501	2.1293	-0.0518	0.2340	127.5	5.4	124	26
AOLH2_07_11	0.0574	0.0110	0.1580	0.0310	0.0195	0.0008	51.3875	2.0333	0.0244	0.3361	124.2	4.9	148	27
AOLH2_07_12	0.0503	0.0100	0.1380	0.0280	0.0195	0.0007	51.2033	1.7042	-0.0380	0.2570	124.7	4.1	131	25
AOLH2_07_15	0.0484	0.0094	0.1310	0.0250	0.0200	0.0006	50.0250	1.5766	0.2583	0.0687	127.6	4	125	23
AOLH2_07_18	0.0580	0.0150	0.1620	0.0390	0.0204	0.0010	49.1159	2.3882	-0.1770	0.3959	129.9	6.3	152	34
AOLH2_07_20	0.0581	0.0140	0.1560	0.0370	0.0198	0.0008	50.4796	2.0131	0.1942	0.0411	126.4	5	146	33
AOLH2_07_21	0.0498	0.0097	0.1400	0.0260	0.0202	0.0007	49.5786	1.5977	-0.0865	0.3846	128.7	4.1	132.4	23
AOLH2_07_22	0.0436	0.0094	0.1200	0.0260	0.0200	0.0007	50.1253	1.8593	0.3738	-0.1710	127.3	4.7	114	24
AOLH2_07_24	0.0433	0.0097	0.1210	0.0270	0.0200	0.0010	50.1002	2.4096	0.2450	0.0273	127.4	6.1	115	24
AOLH2_07_25	0.0481	0.0120	0.1310	0.0310	0.0195	0.0008	51.2558	2.0229	0.0700	0.1232	124.6	4.9	124	28
AOLH2_07_26	0.0508	0.0110	0.1430	0.0310	0.0203	0.0012	49.2611	2.9120	0.2340	0.1690	129.7	7.6	135	28
AOLH2_07_28	0.0432	0.0100	0.1150	0.0260	0.0193	0.0007	51.8672	1.8024	-0.3688	0.5569	123.1	4.2	110	23
AOLH2_07_30	0.0460	0.0097	0.1270	0.0280	0.0196	0.0010	50.9424	2.5173	0.5207	-0.2208	125.3	6.2	121	25
X_AOOJA04_1	0.0460	0.0054	0.1220	0.0220	0.0192	0.0007	52.1376	1.9572	0.1164	0.1390	122.5	4.5	116	20
X_AOOJA04_2	0.0598	0.0099	0.1660	0.0350	0.0201	0.0010	49.8008	2.3561	0.0345	0.1704	128.2	6	154	30
X_AOOJA04_3	0.0519	0.0056	0.1370	0.0240	0.0190	0.0007	52.6593	1.9134	0.2023	0.0978	121.3	4.3	129	21
X_AOOJA04_4	0.0511	0.0079	0.1370	0.0280	0.0197	0.0008	50.7614	2.1644	0.0781	0.1688	125.8	5.3	129	25
X_AOOJA04_5	0.0488	0.0058	0.1280	0.0230	0.0191	0.0007	52.3560	1.9188	-0.1016	0.3323	121.9	4.4	121	20
X_AOOJA04_6	0.0562	0.0080	0.1600	0.0320	0.0206	0.0007	48.6618	1.6576	-0.0414	0.1826	131.1	4.4	155	31
X_AOOJA04_7	0.0531	0.0052	0.1460	0.0240	0.0199	0.0007	50.2513	1.7929	0.1761	0.2024	127	4.5	137.4	21
X_AOOJA04_10	0.0477	0.0071	0.1310	0.0250	0.0206	0.0010	48.5437	2.2858	-0.1005	0.3801	131.4	6.1	125	23
X_AOOJA04_11	0.0502	0.0061	0.1310	0.0240	0.0191	0.0008	52.4934	2.3147	0.0306	0.2968	121.6	5.3	129	25
X_AOOJA04_12	0.0595	0.0093	0.1710	0.0360	0.0213	0.0008	47.0146	1.8346	0.8424	-0.6820	135.7	5.3	159	30
X_AOOJA04_13	0.0566	0.0063	0.1540	0.0260	0.0198	0.0008	50.5817	2.0980	-0.0549	0.4423	126.2	5.2	145	23
X_AOOJA04_14	0.0468	0.0044	0.1204	0.0200	0.0190	0.0006	52.7148	1.6673	0.2174	0.1156	121.2	3.8	115.1	18
X_AOOJA04_17	0.0452	0.0060	0.1280	0.0240	0.0205	0.0007	48.7805	1.7609	-0.0807	0.3375	130.8	4.7	122	22

Anexo B, continuación.

Sample/Zircon	Isotope ratios								Error Correlations		U-Pb ages (Ma)			
	207Pb 206Pb	± (abs)	207Pb 235U	± (abs)	206Pb 238U	± (abs)	238U 20Pb	± (abs)	$^{206}Pb/^{238}U$ $^{207}Pb/^{235}U$	$^{238}U/^{206}Pb$ $^{207}Pb/^{206}Pb$	206Pb 238U	± (Ma)	207Pb 235U	± (Ma)
X_AOOJA04_18	0.0527	0.0071	0.1480	0.0280	0.0207	0.0008	48.4262	1.7588	-0.0196	0.2617	131.7	4.7	139	24
X_AOOJA04_20	0.0536	0.0071	0.1440	0.0270	0.0192	0.0007	52.2193	1.9906	0.0629	0.2108	122.3	4.6	136	24
X_AOOJA04_21	0.0525	0.0080	0.1510	0.0310	0.0209	0.0011	47.7555	2.5086	0.4192	-0.1434	133.6	7.1	142	28
X_AOOJA04_22	0.0534	0.0065	0.1390	0.0250	0.0193	0.0006	51.8403	1.6393	0.0694	0.1610	123.2	3.8	131	22
X_AOOJA04_23	0.0532	0.0094	0.1430	0.0310	0.0198	0.0009	50.4032	2.2102	0.2875	0.0058	126.6	5.5	134	28
X_AOOJA04_25	0.0503	0.0049	0.1384	0.0230	0.0201	0.0007	49.6524	1.6271	-0.1254	0.3643	128.6	4.2	131.2	20
X_AOOJA04_26	0.0550	0.0083	0.1530	0.0310	0.0205	0.0008	48.8759	1.8394	0.0607	0.2038	130.5	4.9	143	26
X_AOOJA04_28	0.0533	0.0058	0.1480	0.0260	0.0204	0.0007	48.9237	1.6755	0.2636	0.0001	130.5	4.4	139	23
X_AOOJA04_30	0.0534	0.0082	0.1480	0.0290	0.0199	0.0009	50.3271	2.2795	0.0506	0.2771	126.8	5.7	139	26
X_AOOJA04_31	0.0591	0.0066	0.1620	0.0290	0.0196	0.0008	51.0204	1.9523	0.2014	0.1112	125.1	4.7	152	25
X_AOOJA04_34	0.0600	0.0069	0.1600	0.0280	0.0200	0.0007	50.0250	1.7768	0.0532	0.2287	127.6	4.5	150	24
X_AOOJA04_35	0.0564	0.0100	0.1570	0.0340	0.0211	0.0011	47.4383	2.4754	-0.1562	0.4697	134.5	7	147	30
X_AOOJA04_36	0.0574	0.0092	0.1650	0.0340	0.0209	0.0008	47.7555	1.8245	0.1842	0.0971	133.6	5.1	154	30
X_AOOJA04_37	0.0471	0.0049	0.1280	0.0220	0.0197	0.0007	50.7872	1.8055	0.2980	0.0203	125.7	4.4	121.8	20
X_AOOJA04_38	0.0580	0.0140	0.1610	0.0440	0.0201	0.0011	49.6771	2.7146	0.1550	-0.0038	128.5	6.7	148	38
X_AORE_05_0	0.0560	0.0150	0.1400	0.0320	0.0202	0.0010	49.5050	2.4507	0.1616	0.0003	128.9	6.3	132	28
X_AORE_05_1	0.0556	0.0064	0.1560	0.0190	0.0198	0.0007	50.5561	1.8914	0.1146	0.2173	126.3	4.7	146	16
X_AORE_05_2	0.0506	0.0078	0.1400	0.0230	0.0200	0.0010	50.0501	2.5050	0.2870	0.0171	127.5	6.6	132	20
X_AORE_05_3	0.0524	0.0052	0.1420	0.0140	0.0197	0.0006	50.6842	1.4900	0.1485	0.1004	126	3.7	134	13
X_AORE_05_4	0.0570	0.0150	0.1600	0.0400	0.0201	0.0009	49.6771	2.2457	0.0986	0.1001	128.5	5.8	147	34
X_AORE_05_5	0.0514	0.0050	0.1400	0.0130	0.0200	0.0006	50.1253	1.4573	-0.0533	0.2284	127.3	3.7	132	12
X_AORE_05_6	0.0470	0.0056	0.1280	0.0150	0.0199	0.0007	50.2513	1.7171	0.1834	0.1241	127	4.3	121	14
X_AORE_05_7	0.0458	0.0058	0.1230	0.0150	0.0199	0.0007	50.1505	1.7354	-0.1082	0.3192	127.3	4.3	117	14
X_AORE_05_8	0.0475	0.0046	0.1300	0.0120	0.0200	0.0006	50.1253	1.5829	0.1940	0.0053	127.3	4	123	11
X_AORE_05_9	0.0504	0.0055	0.1330	0.0140	0.0199	0.0009	50.2008	2.2429	0.2534	0.1035	127.1	5.6	130	14
X_AORE_05_10	0.0505	0.0087	0.1410	0.0230	0.0204	0.0008	49.0918	1.9762	0.1667	0.0612	130	5.2	133	21
X_AORE_05_11	0.0418	0.0091	0.1250	0.0250	0.0200	0.0007	50.1253	1.7337	0.3600	0.4115	127.3	4.3	118	22
X_AORE_05_12	0.0509	0.0067	0.1450	0.0200	0.0200	0.0007	49.9251	1.8195	0.2063	0.0526	127.8	4.6	136	18
X_AORE_05_14	0.0542	0.0048	0.1520	0.0150	0.0201	0.0009	49.8008	2.1825	0.4159	-0.0741	128.1	5.6	143	13
X_AORE_05_15	0.0534	0.0053	0.1480	0.0150	0.0200	0.0006	49.9750	1.5235	0.1236	0.1336	127.7	3.8	140	13
X_AORE_05_16	0.0453	0.0041	0.1270	0.0120	0.0200	0.0006	49.9750	1.5734	0.3486	-0.0090	127.7	4	121	11
X_AORE_05_17	0.0520	0.0052	0.1420	0.0150	0.0193	0.0006	51.7331	1.6593	0.0609	0.2205	123.4	3.9	134	13
X_AORE_05_19	0.0429	0.0048	0.1200	0.0130	0.0198	0.0008	50.5051	1.9386	-0.0242	0.2846	126.4	4.8	115	12
X_AORE_05_20	0.0530	0.0071	0.1520	0.0230	0.0199	0.0009	50.2260	2.3208	0.1136	0.2235	127.1	5.8	142	20
X_AORE_05_21	0.0520	0.0100	0.1410	0.0260	0.0201	0.0008	49.8505	2.0875	-0.4191	0.5829	128	5.3	133	23
X_AORE_05_22	0.0490	0.0051	0.1340	0.0140	0.0198	0.0006	50.4796	1.5289	0.2774	-0.0269	126.5	3.8	127	13
X_AORE_05_23	0.0538	0.0074	0.1460	0.0210	0.0197	0.0008	50.6586	1.9247	0.3252	-0.1588	126	4.7	138	18
X_AORE_05_24	0.0532	0.0057	0.1460	0.0150	0.0200	0.0008	50.0501	1.9289	0.1992	0.1442	127.5	4.8	137	14
X_AORE_05_25	0.0533	0.0068	0.1470	0.0200	0.0199	0.0008	50.2765	2.0980	0.3427	-0.0823	126.9	5.3	137	18

Anexo B, continuación.

Sample/Zircon	Isotope ratios								Error Correlations		U-Pb ages (Ma)			
	207Pb 206Pb	± (abs)	207Pb 235U	± (abs)	206Pb 238U	± (abs)	238U 20Pb	± (abs)	$^{206}Pb/^{238}U$ $^{207}Pb/^{235}U$	$^{238}U/^{206}Pb$ $^{207}Pb/^{206}Pb$	206Pb 238U	± (Ma)	207Pb 235U	± (Ma)
X_AORE_05_26	0.0500	0.0110	0.1360	0.0290	0.0199	0.0009	50.1756	2.2407	-0.0350	0.2244	127.2	5.7	127	26
X_AORE_02_0	0.0552	0.0120	0.1540	0.0340	0.0201	0.0008	49.7265	1.9040	0.1113	0.1375	128.3	4.9	144	30
X_AORE_02_1	0.0520	0.0230	0.1380	0.0530	0.0197	0.0012	50.7614	3.0921	-0.3502	0.5574	125.8	7.8	128	45
X_AORE_02_3	0.0560	0.0140	0.1560	0.0370	0.0200	0.0009	49.9750	2.2228	0.1324	0.1348	127.7	5.7	146	33
X_AORE_02_4	0.0505	0.0095	0.1401	0.0260	0.0202	0.0006	49.5540	1.4242	0.0518	0.2011	128.8	3.7	132.6	23
X_AORE_02_5	0.0477	0.0110	0.1310	0.0310	0.0197	0.0007	50.6842	1.7982	0.1331	0.0335	125.9	4.4	123	27
X_AORE_02_6	0.0495	0.0110	0.1310	0.0270	0.0195	0.0007	51.2821	1.7883	-0.0112	0.2484	124.5	4.3	124	24
X_AORE_02_7	0.0570	0.0180	0.1540	0.0480	0.0197	0.0012	50.7614	3.0921	0.0067	0.2730	125.4	7.3	142	42
X_AORE_02_8	0.0497	0.0100	0.1370	0.0280	0.0198	0.0007	50.4541	1.7056	-0.1832	0.4077	126.5	4.2	129	25
X_AORE_02_9	0.0514	0.0099	0.1400	0.0270	0.0198	0.0006	50.5306	1.5065	0.0626	0.2290	126.3	3.7	132.9	23
X_AORE_02_10	0.0489	0.0110	0.1280	0.0260	0.0200	0.0007	50.0250	1.8268	0.0149	0.2128	127.6	4.6	122	24
X_AORE_02_13	0.0488	0.0110	0.1310	0.0290	0.0192	0.0008	52.1921	2.2065	0.3172	-0.0509	122.4	5.1	124	26
X_AORE_02_14	0.0530	0.0110	0.1450	0.0300	0.0201	0.0007	49.7018	1.7292	-0.1345	0.3344	128.4	4.4	136	27
X_AORE_02_15	0.0600	0.0150	0.1630	0.0400	0.0197	0.0012	50.7614	3.0921	0.2064	0.1267	125.7	7.3	151	34
X_AORE_02_16	0.0543	0.0130	0.1530	0.0360	0.0199	0.0009	50.2008	2.2177	0.1026	0.1369	127.1	5.6	142	31
X_AORE_02_17	0.0626	0.0130	0.1700	0.0350	0.0198	0.0007	50.6073	1.7159	0.2779	-0.0858	126.1	4.3	158	30
X_AORE_02_19	0.0527	0.0110	0.1450	0.0290	0.0199	0.0006	50.2008	1.4869	-0.1029	0.2910	127.1	3.7	137	26
X_AORE_02_20	0.0444	0.0097	0.1230	0.0260	0.0199	0.0007	50.2513	1.7676	0.0581	0.2694	127	4.5	117	24
X_AORE_02_21	0.0610	0.0150	0.1630	0.0410	0.0199	0.0008	50.2008	2.1169	0.0552	0.1312	127.1	5.3	151	35
X_AORE_02_22	0.0527	0.0130	0.1350	0.0300	0.0199	0.0012	50.2513	3.0302	0.1378	0.2363	127.2	7.7	128	27
X_AORE_02_23	0.0556	0.0130	0.1520	0.0350	0.0198	0.0007	50.6073	1.8184	-0.1318	0.3487	126.1	4.5	142	31
X_AORE_02_24	0.0481	0.0094	0.1310	0.0250	0.0198	0.0006	50.4032	1.4227	-0.0653	0.2774	126.6	3.5	124.3	22
X_AORE_04_0	0.0547	0.0140	0.1480	0.0340	0.0199	0.0008	50.3018	2.1001	-0.3769	0.5614	126.9	5.3	139	30
X_AORE_04_1	0.0530	0.0150	0.1480	0.0410	0.0199	0.0010	50.2260	2.4217	0.0939	0.0271	127.1	6.1	137	36
X_AORE_04_2	0.0525	0.0120	0.1430	0.0310	0.0200	0.0008	50.0250	2.0270	-0.0769	0.3208	127.6	5.1	134	28
X_AORE_04_3	0.0580	0.0140	0.1560	0.0380	0.0198	0.0009	50.5051	2.3722	-0.1015	0.3031	126.4	5.9	145	34
X_AORE_04_4	0.0496	0.0110	0.1330	0.0290	0.0198	0.0008	50.4796	2.0131	0.0162	0.2425	126.5	5	125	26
X_AORE_04_5	0.0699	0.0140	0.1940	0.0380	0.0200	0.0008	49.9750	1.9481	0.3441	-0.0533	127.7	4.9	179	32
X_AORE_04_7	0.0600	0.0160	0.1710	0.0420	0.0206	0.0012	48.5437	2.8278	0.0669	0.1971	131.3	7.3	158	36
X_AORE_04_8	0.0560	0.0160	0.1520	0.0440	0.0201	0.0010	49.6524	2.4654	0.0664	0.2046	128.5	6.5	140	39
X_AORE_04_9	0.0435	0.0120	0.1220	0.0330	0.0198	0.0008	50.6073	2.0745	0.2381	-0.0529	126.1	5.1	114	30
X_AORE_04_10	0.0530	0.0140	0.1430	0.0370	0.0203	0.0012	49.2611	2.9120	-0.0698	0.2934	129.2	7.6	134	33
X_AORE_04_11	0.0462	0.0100	0.1270	0.0280	0.0199	0.0007	50.1505	1.6348	-0.0404	0.2718	127.2	4.1	120	25
X_AORE_04_12	0.0554	0.0120	0.1560	0.0330	0.0207	0.0008	48.2859	1.9352	-0.0013	0.4816	132.1	5.3	146	29
X_AORE_04_14	0.0510	0.0150	0.1390	0.0390	0.0200	0.0011	50.0000	2.7500	0.0681	0.2278	127.8	7.1	130	35
X_AORE_04_15	0.0549	0.0130	0.1580	0.0380	0.0202	0.0011	49.5050	2.6958	-0.2208	0.5894	128.9	6.8	146	33
X_AORE_04_16	0.0543	0.0120	0.1480	0.0330	0.0199	0.0008	50.2260	2.0938	-0.0019	0.3159	127	5.2	139	29
X_AORE_04_17	0.0493	0.0100	0.1350	0.0280	0.0202	0.0009	49.6032	2.2390	0.2483	0.0990	128.7	5.8	128	25
X_AORE_04_18	0.0580	0.0150	0.1600	0.0430	0.0199	0.0010	50.2008	2.5201	0.1370	0.0612	127.1	6.4	147	37

Anexo B, continuación.

Sample/Zircon	Isotope ratios								Error Correlations		U-Pb ages (Ma)			
	207Pb 206Pb	± (abs)	207Pb 235U	± (abs)	206Pb 238U	± (abs)	238U 20Pb	± (abs)	$^{206}Pb/^{238}U$ $^{207}Pb/^{235}U$	$^{238}U/^{206}Pb$ $^{207}Pb/^{206}Pb$	206Pb 238U	± (Ma)	207Pb 235U	± (Ma)
X_AORE_04_19	0.0666	0.0150	0.1880	0.0400	0.0204	0.0010	48.9956	2.4006	0.0221	0.3665	130.2	6.3	173	34
X_AORE_04_21	0.0561	0.0130	0.1530	0.0340	0.0199	0.0010	50.3778	2.5379	-0.2202	0.5051	126.7	6.6	143	30
X_AOAL_03_0	0.0528	0.0100	0.1360	0.0190	0.0199	0.0012	50.2513	3.0302	0.0233	0.2773	127.3	7.9	137	26
X_AOAL_03_1	0.0508	0.0057	0.1420	0.0170	0.0200	0.0008	49.9002	1.8924	0.2506	0.1040	127.9	4.8	135	15
X_AOAL_03_3	0.0540	0.0077	0.1470	0.0210	0.0199	0.0008	50.2260	1.9677	0.0425	0.1882	127.1	4.9	138	19
X_AOAL_03_4	0.0564	0.0085	0.1540	0.0230	0.0199	0.0007	50.1505	1.7857	0.0016	0.2856	127.3	4.5	144	20
X_AOAL_03_5	0.0522	0.0063	0.1440	0.0190	0.0200	0.0007	50.0000	1.7250	0.3183	-0.0521	127.7	4.4	136	17
X_AOAL_03_6	0.0486	0.0048	0.1328	0.0130	0.0198	0.0006	50.5817	1.5351	0.0909	0.2781	126.2	3.8	126.4	12
X_AOAL_03_8	0.0410	0.0096	0.1150	0.0270	0.0207	0.0010	48.3793	2.3406	-0.1466	0.3825	131.9	6.6	109	24
X_AOAL_03_9	0.0520	0.0130	0.1430	0.0340	0.0202	0.0009	49.4315	2.1258	-0.0538	0.2161	129.1	5.5	134	29
X_AOAL_03_10	0.0456	0.0070	0.1230	0.0190	0.0198	0.0007	50.5051	1.7855	-0.0275	0.2425	126.4	4.4	117	18
X_AOAL_03_11	0.0550	0.0130	0.1500	0.0330	0.0199	0.0008	50.2513	2.0707	-0.0345	0.2624	127	5.2	140	29
X_AOAL_03_12	0.0550	0.0071	0.1510	0.0200	0.0200	0.0009	50.1002	2.1586	0.2358	0.1020	127.4	5.5	142	18
X_AOAL_03_15	0.0572	0.0089	0.1590	0.0270	0.0201	0.0009	49.7512	2.2277	0.4358	-0.0993	128.3	5.7	149	24
X_AOAL_03_16	0.0429	0.0062	0.1180	0.0180	0.0199	0.0007	50.2008	1.8397	-0.0012	0.2603	127.2	4.6	112	16
X_AOAL_03_17	0.0618	0.0110	0.1710	0.0310	0.0199	0.0010	50.1756	2.5176	0.3226	-0.2136	127.2	6.6	158	26
X_AOAL_03_18	0.0514	0.0064	0.1400	0.0180	0.0198	0.0005	50.5051	1.3009	0.0825	0.0494	126.4	3.2	133	16
X_AOAL_03_19	0.0451	0.0064	0.1240	0.0180	0.0200	0.0006	50.0000	1.5750	0.0220	0.2034	127.7	4	117	16
X_AOAL_03_21	0.0480	0.0110	0.1300	0.0270	0.0200	0.0010	49.9501	2.4451	-0.4147	0.5373	127.8	6.2	123	24
X_AOAL_03_22	0.0533	0.0090	0.1490	0.0230	0.0205	0.0008	48.7092	1.8032	-0.5658	0.7251	131	4.8	141	20
X_AOAL_03_24	0.0560	0.0150	0.1540	0.0420	0.0198	0.0011	50.5051	2.8058	0.2916	-0.1452	126.3	6.8	144	37
X_AOAL_03_26	0.0528	0.0063	0.1440	0.0170	0.0200	0.0006	50.1002	1.4809	-0.1949	0.3961	127.4	3.7	136	15
X_AOAL_03_27	0.0500	0.0048	0.1403	0.0140	0.0205	0.0006	48.7329	1.3299	-0.1470	0.4671	130.9	3.6	133.1	12
X_AOAL_04_0	0.0552	0.0092	0.1480	0.0250	0.0199	0.0010	50.3778	2.4364	0.0446	0.2232	126.7	6.1	138	22
X_AOAL_04_1	0.0500	0.0130	0.1350	0.0340	0.0200	0.0008	50.1253	2.0854	-0.1428	0.2513	127.3	5.2	126	30
X_AOAL_04_3	0.0750	0.0130	0.2010	0.0360	0.0199	0.0008	50.3271	1.8996	-0.0260	0.2754	126.8	4.8	183	31
X_AOAL_04_5	0.0494	0.0100	0.1350	0.0280	0.0200	0.0011	50.0000	2.7500	0.0785	0.1075	127.9	6.8	127	25
X_AOAL_04_7	0.0490	0.0130	0.1340	0.0370	0.0198	0.0010	50.6329	2.5637	0.3264	-0.1160	126.1	6.3	126	32
X_AOAL_04_8	0.0525	0.0093	0.1420	0.0250	0.0201	0.0009	49.7265	2.2007	-0.1434	0.3860	128.3	5.6	134	22
X_AOAL_04_9	0.0492	0.0088	0.1400	0.0240	0.0208	0.0011	48.0769	2.5425	0.0412	0.2378	133	7.2	132	21
X_AOAL_04_10	0.0455	0.0067	0.1240	0.0180	0.0200	0.0007	49.9002	1.6185	-0.0059	0.2054	127.9	4.1	118	16
X_AOAL_04_12	0.0465	0.0089	0.1290	0.0240	0.0205	0.0009	48.8520	2.0524	-0.0506	0.2917	130.6	5.4	122	22
X_AOAL_04_13	0.0467	0.0060	0.1290	0.0170	0.0202	0.0007	49.5295	1.7908	0.1758	0.1065	128.8	4.6	122	15
X_AOAL_04_14	0.0460	0.0110	0.1230	0.0280	0.0202	0.0011	49.5050	2.6958	-0.1414	0.3896	129.1	6.8	116	26
X_AOAL_04_15	0.0519	0.0052	0.1419	0.0150	0.0200	0.0006	50.1253	1.3819	0.1122	0.1653	127.3	3.5	134.3	13
X_AOAL_04_18	0.0548	0.0086	0.1530	0.0250	0.0203	0.0008	49.2126	1.8164	0.0579	0.1290	129.7	4.8	143	22
X_AOAL_04_19	0.0420	0.0120	0.1130	0.0320	0.0203	0.0010	49.3340	2.4338	-0.2755	0.3603	129.4	6.3	106	29
X_AOAL_04_20	0.0520	0.0130	0.1450	0.0350	0.0204	0.0009	49.0677	2.1669	0.0402	0.1332	130.1	5.7	135	31
X_AOAL_04_22	0.0521	0.0055	0.1450	0.0160	0.0202	0.0006	49.5050	1.5195	0.3430	0.0051	128.9	3.9	137	15

Anexo B, continuación.

Sample/Zircon	Isotope ratios								Error Correlations		U-Pb ages (Ma)			
	207Pb 206Pb	± (abs)	207Pb 235U	± (abs)	206Pb 238U	± (abs)	238U 20Pb	± (abs)	$^{206}Pb/^{238}U$ $^{207}Pb/^{235}U$	$^{238}U/^{206}Pb$ $^{207}Pb/^{206}Pb$	206Pb 238U	± (Ma)	207Pb 235U	± (Ma)
X_AOAL_04_23	0.0520	0.0071	0.1410	0.0200	0.0199	0.0008	50.3525	1.9522	0.4205	-0.1403	126.8	4.9	134	18
X_AOAL_04_26	0.0490	0.0180	0.1340	0.0420	0.0206	0.0014	48.5437	3.2991	-0.2386	0.4601	131.3	8.6	125	38
X_AOAL_04_27	0.0429	0.0065	0.1230	0.0200	0.0200	0.0008	50.0250	1.9770	-0.1349	0.5009	127.6	5	117	18
X_AOAL_04_28	0.0470	0.0150	0.1260	0.0410	0.0203	0.0013	49.2611	3.1547	-0.2110	0.3111	129.8	8.2	117	36
X_AOAL_04_29	0.0660	0.0130	0.1840	0.0380	0.0202	0.0010	49.4071	2.3190	0.3285	-0.1324	129.1	6	169	33
X_AOAL_04_30	0.0571	0.0100	0.1550	0.0280	0.0200	0.0008	50.0751	2.1063	0.1005	0.1215	127.4	5.3	145	25
X_AOAL_04_31	0.0525	0.0110	0.1400	0.0280	0.0198	0.0008	50.5817	2.1236	-0.0115	0.2654	126.2	5.3	130	25
X_AOAL_04_33	0.0524	0.0070	0.1430	0.0200	0.0201	0.0007	49.8505	1.7892	0.0361	0.1696	128	4.5	135	18
X_AOAL_04_34	0.0501	0.0088	0.1380	0.0250	0.0201	0.0008	49.8505	1.9384	0.0983	0.1630	128	4.9	130	22
X_AOAL_04_35	0.0543	0.0086	0.1480	0.0220	0.0201	0.0009	49.6524	2.2681	0.0165	0.3752	128.5	5.8	139	20
X_AOAL_04_36	0.0645	0.0110	0.1770	0.0290	0.0204	0.0008	49.1401	1.9559	-0.2678	0.4224	129.9	5.1	164	24
X_AOLH_09_1	0.0516	0.0100	0.1460	0.0280	0.0205	0.0007	48.8759	1.7200	-0.3507	0.5434	130.5	4.5	138	25
X_AOLH_09_2	0.0500	0.0140	0.1400	0.0380	0.0203	0.0010	49.1884	2.3953	0.1828	0.0246	129.7	6.2	131	34
X_AOLH_09_4	0.0469	0.0054	0.1280	0.0150	0.0200	0.0006	50.1253	1.5327	0.0357	0.3221	127.3	3.9	121.8	13
X_AOLH_09_5	0.0630	0.0110	0.1730	0.0290	0.0201	0.0010	49.6524	2.4654	0.2304	0.2123	128.5	6.4	161	25
X_AOLH_09_6	0.0566	0.0079	0.1590	0.0230	0.0200	0.0008	49.9002	1.9671	0.0649	0.1419	127.9	5	149	20
X_AOLH_09_7	0.0513	0.0070	0.1400	0.0190	0.0200	0.0007	50.0000	1.6500	-0.0030	0.1996	127.6	4.1	132	17
X_AOLH_09_9	0.0590	0.0140	0.1640	0.0380	0.0207	0.0010	48.4262	2.2982	-0.2224	0.4595	131.8	6.2	151	32
X_AOLH_09_10	0.0493	0.0060	0.1360	0.0170	0.0201	0.0006	49.7512	1.5841	0.0738	0.1974	128.3	4	128	15
X_AOLH_09_12	0.0520	0.0062	0.1430	0.0170	0.0202	0.0006	49.4805	1.5424	-0.1293	0.4238	129	4	135	15
X_AOLH_09_13	0.0493	0.0067	0.1350	0.0180	0.0199	0.0007	50.2513	1.6414	-0.0738	0.2956	127	4.1	128	17
X_AOLH_09_14	0.0531	0.0054	0.1450	0.0160	0.0199	0.0005	50.3271	1.3677	0.1713	0.1156	126.9	3.4	137	14
X_AOLH_09_15	0.0571	0.0075	0.1600	0.0210	0.0204	0.0007	49.1401	1.7386	0.0810	0.1566	129.9	4.5	150	19
X_AOLH_09_16	0.0527	0.0062	0.1420	0.0170	0.0199	0.0007	50.3778	1.6497	-0.1881	0.4538	126.7	4.1	135	15
X_AOLH_09_17	0.0514	0.0052	0.1419	0.0150	0.0201	0.0006	49.7760	1.4123	-0.2594	0.3082	128.2	3.6	134.4	13
X_AOLH_09_18	0.0588	0.0088	0.1590	0.0230	0.0198	0.0008	50.4286	2.0853	-0.1238	0.4055	126.6	5.2	149	20
X_AOLH_09_19	0.0517	0.0060	0.1440	0.0180	0.0199	0.0006	50.3778	1.5481	0.0676	0.1368	126.7	3.9	136	16
X_AOLH_09_20	0.0460	0.0110	0.1280	0.0320	0.0201	0.0011	49.7512	2.7227	0.3505	-0.1832	128.5	7.1	120	29
X_AOLH_09_21	0.0482	0.0089	0.1340	0.0240	0.0202	0.0008	49.5295	2.0607	-0.2260	0.3072	128.8	5.3	126	21
X_AOLH_09_23	0.0654	0.0096	0.1830	0.0260	0.0203	0.0007	49.2126	1.5984	-0.0710	0.1688	129.7	4.2	169	23
X_AOLH_09_25	0.0516	0.0091	0.1450	0.0260	0.0205	0.0007	48.7329	1.6387	0.0448	0.1206	130.9	4.4	137	23
X_AOLH_09_26	0.0534	0.0076	0.1480	0.0230	0.0201	0.0008	49.8505	2.0875	0.3272	-0.1245	128	5.3	139	21
X_AOLH_09_27	0.0539	0.0110	0.1460	0.0270	0.0201	0.0006	49.7512	1.5841	-0.1203	0.3745	128.3	4.1	137	24
X_RETA2_2	0.0496	0.0096	0.1290	0.0230	0.0199	0.0010	50.3018	2.5303	-0.0310	0.2575	126.9	6.4	122	21
X_RETA2_3	0.0543	0.0110	0.1470	0.0300	0.0197	0.0011	50.8388	2.8430	-0.1456	0.4085	125.5	7.2	135	26
X_RETA2_4	0.0500	0.0150	0.1290	0.0360	0.0198	0.0013	50.5051	3.3160	-0.0836	0.4166	126.4	8.4	119	33
X_RETA2_5	0.0470	0.0170	0.1300	0.0460	0.0197	0.0013	50.7614	3.3497	0.1498	0.0595	125.7	8.5	116	41
X_RETA2_6	0.0521	0.0097	0.1430	0.0250	0.0198	0.0009	50.4541	2.3929	-0.2073	0.4134	126.5	5.9	135	22
X_RETA2_7	0.0530	0.0120	0.1500	0.0360	0.0197	0.0011	50.7357	2.8315	-0.0992	0.3877	125.8	7	140	31

Anexo B, continuación.

Sample/Zircon	Isotope ratios								Error Correlations		U-Pb ages (Ma)			
	207Pb 206Pb	± (abs)	207Pb 235U	± (abs)	206Pb 238U	± (abs)	238U 20Pb	± (abs)	$^{206}Pb/^{238}U$ $^{207}Pb/^{235}U$	$^{238}U/^{206}Pb$ $^{207}Pb/^{206}Pb$	206Pb 238U	± (Ma)	207Pb 235U	± (Ma)
X_RETA2_11	0.0520	0.0098	0.1430	0.0270	0.0199	0.0011	50.3778	2.7917	0.1464	0.0994	126.7	6.7	134	24
X_RETA2_12	0.0458	0.0110	0.1220	0.0270	0.0196	0.0012	51.0725	3.1301	-0.0921	0.3488	125	7.7	115	24
X_RETA2_13	0.0580	0.0150	0.1480	0.0370	0.0195	0.0011	51.2821	2.8928	-0.1470	0.3446	124.5	6.9	134	32
X_RETA2_14	0.0467	0.0110	0.1250	0.0280	0.0201	0.0011	49.8256	2.7309	-0.2064	0.3880	128.1	7	118	25
X_RETA2_15	0.0590	0.0160	0.1590	0.0430	0.0199	0.0013	50.2513	3.2827	0.0543	0.2042	127.2	8.3	146	37
X_RETA2_16	0.0600	0.0130	0.1610	0.0360	0.0199	0.0012	50.3271	3.0394	0.1393	0.1759	126.8	7.4	149	31
X_RETA2_17	0.0445	0.0072	0.1210	0.0200	0.0199	0.0009	50.2008	2.3185	0.2184	0.0203	127.1	5.8	115	18
X_RETA2_19	0.0570	0.0170	0.1510	0.0430	0.0200	0.0012	50.0751	3.0090	-0.0622	0.3048	127.4	7.6	138	38
X_RETA2_20	0.0460	0.0120	0.1240	0.0330	0.0198	0.0012	50.5051	3.0609	0.1227	0.0402	126.3	7.4	115	29
X_RETA2_21	0.0527	0.0084	0.1420	0.0220	0.0201	0.0010	49.8753	2.3632	-0.0784	0.3658	127.9	6	134	19
X_RETA2_22	0.0500	0.0090	0.1320	0.0230	0.0201	0.0011	49.8753	2.7363	0.3143	-0.0305	127.9	6.7	129	23
X_RETA2_23	0.0440	0.0150	0.1200	0.0410	0.0198	0.0013	50.5051	3.3160	0.1420	0.0072	126.1	8	112	36
X_RETA2_24	0.0545	0.0100	0.1500	0.0280	0.0199	0.0010	50.1756	2.4421	0.0650	0.1044	127.2	6.1	141	25
X_RETA2_25	0.0512	0.0081	0.1420	0.0230	0.0199	0.0009	50.2008	2.3689	0.2033	-0.0235	127.1	5.9	134	20
X_RETA2_26	0.0560	0.0140	0.1410	0.0340	0.0198	0.0015	50.5051	3.8261	0.2189	0.2489	126.6	9.2	141	36
X_RETA2_27	0.0500	0.0120	0.1280	0.0300	0.0199	0.0012	50.2513	3.0302	0.0636	0.1985	127	7.3	119	27
X_RETA2_28	0.0520	0.0150	0.1410	0.0420	0.0192	0.0012	52.0562	3.2518	0.2212	-0.0262	122.6	7.6	129	35
X_RETA2_29	0.0485	0.0082	0.1360	0.0230	0.0199	0.0010	50.3778	2.5379	-0.0202	0.3165	126.7	6.6	128	20
X_RETA2_31	0.0449	0.0110	0.1250	0.0310	0.0198	0.0011	50.5561	2.8115	0.0768	0.0828	126.3	6.7	116	29
X_RETA2_32	0.0491	0.0110	0.1340	0.0280	0.0199	0.0011	50.2260	2.7749	-0.1673	0.2944	127	7.1	125	25
X_RETA2_33	0.0560	0.0190	0.1550	0.0530	0.0200	0.0013	50.0000	3.2500	-0.0187	0.1094	127.9	8.1	141	46
X_RETA2_34	0.0540	0.0100	0.1490	0.0290	0.0199	0.0009	50.3018	2.2772	-0.0537	0.1901	126.9	5.7	139	25
AOIN_02_1	0.0500	0.0130	0.1360	0.0350	0.0200	0.0010	50.0250	2.5025	-0.0610	0.2742	127.6	6.5	127	31
AOIN_02_2	0.0496	0.0110	0.1410	0.0310	0.0211	0.0010	47.3485	2.2195	-0.0029	0.1947	134.7	6.2	131	28
AOIN_02_3	0.0504	0.0100	0.1410	0.0280	0.0207	0.0008	48.3092	1.7737	-0.4171	0.5489	132	4.8	132	24
AOIN_02_4	0.0492	0.0081	0.1430	0.0240	0.0209	0.0009	47.7555	2.0753	0.0696	0.3275	133.6	5.7	135	21
AOIN_02_5	0.0538	0.0110	0.1550	0.0300	0.0211	0.0011	47.5059	2.4825	0.0205	0.3640	134.3	6.7	146	26
AOIN_02_6	0.0478	0.0076	0.1360	0.0220	0.0211	0.0008	47.3934	1.7295	0.2326	0.1460	134.6	4.9	129	19
AOIN_02_7	0.0480	0.0075	0.1374	0.0220	0.0211	0.0007	47.5059	1.5572	-0.0070	0.2433	134.3	4.3	130.3	19
AOIN_02_8	0.0544	0.0110	0.1490	0.0300	0.0205	0.0009	48.7567	2.1157	0.0685	0.2666	130.8	5.6	140	26
AOIN_02_9	0.0640	0.0140	0.1820	0.0410	0.0211	0.0010	47.3709	2.1542	0.2749	-0.0279	134.6	6.1	167	35
AOIN_02_10	0.0518	0.0096	0.1420	0.0260	0.0206	0.0008	48.6618	1.7997	-0.0560	0.3003	131.1	4.8	133	23
AOIN_02_11	0.0450	0.0140	0.1290	0.0370	0.0212	0.0014	47.1698	3.1150	0.0744	0.1164	135.1	8.7	120	33
AOIN_02_12	0.0493	0.0086	0.1380	0.0240	0.0206	0.0007	48.6381	1.7269	0.0063	0.2496	131.9	5	130	22
AOIN_02_13	0.0505	0.0093	0.1410	0.0260	0.0206	0.0009	48.5909	2.0541	0.2702	-0.0123	131.3	5.5	132	24
AOIN_02_14	0.0485	0.0079	0.1380	0.0230	0.0210	0.0007	47.6417	1.5207	0.3269	-0.1421	133.9	4.2	130	20
AOIN_02_15	0.0525	0.0095	0.1450	0.0260	0.0212	0.0008	47.2367	1.8074	-0.2180	0.4346	135.1	5.1	137	23
AOIN_02_16	0.0475	0.0100	0.1310	0.0290	0.0212	0.0008	47.2813	1.7661	-0.1495	0.3363	134.9	5	124	26
AOIN_02_17	0.0551	0.0120	0.1500	0.0330	0.0207	0.0009	48.2160	2.0458	-0.1015	0.3326	132.3	5.6	140	29

Anexo B, continuación.

Sample/Zircon	Isotope ratios								Error Correlations		U-Pb ages (Ma)			
	207Pb 206Pb	± (abs)	207Pb 235U	± (abs)	206Pb 238U	± (abs)	238U 20Pb	± (abs)	$^{206}Pb/^{238}U$ $^{207}Pb/^{235}U$	$^{238}U/^{206}Pb$ $^{207}Pb/^{206}Pb$	206Pb 238U	± (Ma)	207Pb 235U	± (Ma)
AOIN_02_18	0.0493	0.0080	0.1380	0.0240	0.0205	0.0008	48.7092	1.9218	0.3032	0.0165	131	5.1	133	23
AOIN_02_19	0.0471	0.0083	0.1300	0.0230	0.0210	0.0008	47.5737	1.8106	0.2513	-0.0773	134.1	5	126	22
AOIN_02_20	0.0479	0.0074	0.1354	0.0210	0.0210	0.0007	47.6191	1.4966	0.1150	0.1448	134	4.1	128.5	19
AOIN_02_21	0.0470	0.0075	0.1330	0.0220	0.0210	0.0007	47.6191	1.6553	0.1350	0.1533	134	4.6	126.6	19
AOIN_02_22	0.0515	0.0083	0.1460	0.0230	0.0211	0.0007	47.3261	1.6350	-0.0738	0.2934	134.8	4.6	138	21
AOIN_02_23	0.0461	0.0110	0.1180	0.0260	0.0202	0.0011	49.4560	2.6905	0.0699	0.2039	129	7.1	115	26
AOIN_02_24	0.0523	0.0091	0.1540	0.0280	0.0209	0.0009	47.9616	2.0703	0.1794	0.1419	133	5.7	144	25
AOIN_02_25	0.0466	0.0083	0.1300	0.0230	0.0205	0.0007	48.8520	1.7660	0.2033	-0.0430	130.6	4.7	123	21
RRJP_01_0	0.0380	0.0084	0.0990	0.0220	0.0192	0.0008	52.2193	2.2360	-0.1502	0.3171	122.3	5.2	95	20
RRJP_01_1	0.0451	0.0097	0.1170	0.0260	0.0191	0.0009	52.3013	2.4619	0.2256	0.1321	122.1	5.7	112	24
RRJP_01_3	0.0512	0.0099	0.1400	0.0280	0.0192	0.0008	52.2193	2.2633	0.2154	0.0192	122.2	5.2	131	25
RRJP_01_5	0.0463	0.0098	0.1210	0.0260	0.0191	0.0011	52.3013	3.0090	0.2015	0.1103	122.1	6.7	115	24
RRJP_01_6	0.0570	0.0140	0.1470	0.0330	0.0191	0.0011	52.2466	3.0027	-0.1501	0.3521	122.2	6.9	137	29
RRJP_01_7	0.0543	0.0120	0.1360	0.0290	0.0190	0.0012	52.6316	3.3241	-0.1653	0.4420	121.3	7.8	128	26
RRJP_01_8	0.0503	0.0110	0.1350	0.0300	0.0194	0.0012	51.5464	3.1884	-0.2061	0.5034	123.7	7.3	126	27
RRJP_01_9	0.0491	0.0100	0.1270	0.0260	0.0190	0.0010	52.7705	2.6733	-0.0223	0.2638	121	6.1	120	24
RRJP_01_10	0.0519	0.0100	0.1350	0.0270	0.0190	0.0007	52.6870	1.9987	-0.0041	0.1926	121.2	4.6	127	24
RRJP_01_11	0.0431	0.0100	0.1130	0.0260	0.0193	0.0008	51.9481	2.1589	-0.1100	0.2254	122.9	5	107	23
RRJP_01_12	0.0529	0.0110	0.1380	0.0300	0.0191	0.0008	52.4384	2.2823	0.1435	0.1541	121.7	5.2	128	26
RRJP_01_13	0.0524	0.0100	0.1330	0.0260	0.0190	0.0009	52.7705	2.4784	0.2717	-0.1620	121	5.6	125	24
RRJP_01_14	0.0452	0.0093	0.1170	0.0240	0.0192	0.0008	51.9751	2.2692	0.1000	0.1650	122.8	5.3	111	22
RRJP_01_15	0.0425	0.0100	0.1100	0.0270	0.0190	0.0009	52.7148	2.5288	0.1124	0.1532	121.1	5.8	104	25
RRJP_01_16	0.0486	0.0120	0.1220	0.0290	0.0191	0.0010	52.4659	2.7527	-0.2322	0.4698	121.7	6.4	116	27
RRJP_01_17	0.0480	0.0130	0.1250	0.0350	0.0191	0.0010	52.3560	2.7137	-0.1298	0.3383	122	6.2	117	31
RRJP_01_19	0.0584	0.0120	0.1530	0.0320	0.0191	0.0011	52.3286	3.0121	-0.0407	0.1559	123.7	5.9	143	29
RRJP_01_20	0.0460	0.0130	0.1220	0.0340	0.0194	0.0013	51.5464	3.4541	-0.0344	0.2566	123.6	8	115	30
RRJP_01_23	0.0540	0.0140	0.1470	0.0400	0.0193	0.0010	51.7331	2.6495	-0.0809	0.3551	123.4	6.3	134	35
RRJP_01_24	0.0454	0.0100	0.1180	0.0270	0.0188	0.0010	53.2198	2.8323	0.2573	-0.1126	120	6.4	111	24
RRJP_01_25	0.0510	0.0130	0.1300	0.0330	0.0193	0.0010	51.8403	2.6874	0.0271	0.1532	123.1	6.5	121	29
RRJP_01_26	0.0450	0.0089	0.1170	0.0230	0.0193	0.0009	51.7866	2.3869	-0.0249	0.2412	123.3	5.6	111	21
RRJP_01_27	0.0457	0.0100	0.1180	0.0260	0.0190	0.0008	52.5762	2.1838	-0.0677	0.2856	121.4	5	111	23
RRJP_01_28	0.0470	0.0150	0.1140	0.0350	0.0184	0.0010	54.3774	2.8091	-0.2209	0.3896	117.4	6	107	32
RRJP_01_29	0.0620	0.0150	0.1560	0.0370	0.0194	0.0014	51.5464	3.7198	0.0685	0.3425	123.5	8.9	145	33
RRJP_01_30	0.0430	0.0130	0.1070	0.0290	0.0192	0.0010	51.9751	2.7014	-0.4649	0.6268	122.8	6.6	102	26
RRJP_01_31	0.0436	0.0097	0.1100	0.0240	0.0192	0.0008	52.1648	2.1225	-0.2206	0.3528	122.4	4.9	105	22
RRJP_01_32	0.0488	0.0110	0.1160	0.0270	0.0188	0.0009	53.1915	2.4898	0.0704	0.0220	120.1	5.5	109	24
RRJP_01_33	0.0420	0.0150	0.1090	0.0380	0.0191	0.0011	52.4109	3.0216	0.1888	-0.0496	121.8	7	102	34
RRJP_01_34	0.0553	0.0120	0.1410	0.0300	0.0191	0.0009	52.4659	2.3948	0.0178	0.1893	121.7	5.5	133	26

Anexo C: Determinación de elementos traza (en ppm) en circones para todos los análisis de este estudio.

Sample/ Grain	P31 (ppm)	Ti49 (ppm)	Fe57 (ppm)	Y89 (ppm)	Zr90 (ppm)	Nb93 (ppm)	La139 (ppm)	Ce140 (ppm)	Pr141 (ppm)	Nd146 (ppm)	Sm147 (ppm)	Eu153 (ppm)	Gd157 (ppm)	Tb159 (ppm)	Dy163 (ppm)	Ho165 (ppm)	Er166 (ppm)	Yb172 (ppm)	Lu175 (ppm)	Hf178 (ppm)	Pb204 (ppm)	Pb206 (ppm)	Pb207 (ppm)	Pb208 (ppm)	Th232 (ppm)	U235 (ppm)	U238 (ppm)
AOLH_06_0	294	8.6	93	1246	419000	0.97	B-LOD	8.04	0.17	1.58	3.81	0.63	21.7	7.61	107.9	39.1	186.8	397	79.5	10270	B-LOD	13.4	1.19	1.6	119.5	534	168.4
AOLH_06_2	476	8.4	B-LOD	930	393000	1.29	1.59	9	0.54	2.36	2.99	0.49	17	6.57	80.3	31.1	149	376	57.4	7970	B-LOD	10.4	0.47	1.06	98	450	149
AOLH_06_5	322	9.6	226	1065	401400	1.52	B-LOD	6.09	0.09	0.88	2.16	0.46	14.3	6.32	80.4	32.9	161.2	345	74.6	9450	B-LOD	14.05	0.84	1.31	103	542	173.3
AOLH_06_6	272	4.7	B-LOD	1020	344000	3.31	0.87	12	0.74	6.6	4.9	2.36	21	6.1	78.5	29.2	156	477	88.3	8110	B-LOD	22.6	1.38	2.19	185	990	318
AOLH_06_7	490	10	126	1226	394000	1.75	1.99	14	0.85	5.9	4.7	0.91	23.2	8.08	100.1	39.8	185.8	387	77	8960	B-LOD	14.33	0.99	1.54	122.2	608	197.1
AOLH_06_11	242	9.5	412	1149	343000	1.05	B-LOD	5.4	0.15	1.46	3.92	0.59	21.9	7.06	97	37.5	179	349	66.2	8050	B-LOD	10.6	0.57	1.15	104.6	413	134.8
AOLH_06_12	455	8.3	63	1930	360000	2.92	0.23	11.3	0.17	1.8	5.5	0.8	29.5	13.3	157	65.5	305	615	113.7	8060	B-LOD	19.6	0.86	1.85	174	760	249
AOLH_06_14	254	6.8	B-LOD	719	369000	1.21	B-LOD	6.06	0.03	0.42	1.76	0.137	12.2	4.49	56.4	23.3	110.5	249	48.4	8310	B-LOD	10.13	0.53	1	81.9	418	132.1
AOLH_06_15	379	15.9	535	1730	346000	1.89	0.32	9.6	0.20	3.03	6	0.75	35.1	12.1	153	59	259	526	91.4	7590	B-LOD	16.1	1	2.07	178	670	222
AOLH_06_19	312	9.3	B-LOD	1221	356000	1.02	0.084	6.79	0.15	2.3	3.87	0.56	24.3	8.27	103	41.8	189	376	69.1	7860	B-LOD	12.6	0.64	1.38	128	461	152
AOLH_06_24	329	8.3	43	911	359000	1.14	0.002	6.09	0.04	0.92	2.29	0.47	13.6	5.48	72	30.6	144.2	338	61.4	7290	B-LOD	12.12	0.666	1.1	94.9	490	164
AOLH_06_26	324	12	115	1220	378000	1.45	0.47	9.3	0.10	1.11	3.09	0.49	20.9	8.35	100.1	42	189	409	74.9	8150	B-LOD	15.4	0.72	1.52	131.8	603	201
AOLH_06_27	444	6.6	B-LOD	1453	407000	1.48	B-LOD	7.28	0.07	1.2	3.16	0.71	23.2	9.26	114.3	47.7	223	471	89.4	8880	B-LOD	14.6	0.7	1.49	150.7	579	192
AOLH_06_28	650	8.3	B-LOD	1026	378000	1.1	2.05	10.7	0.69	5.4	3.27	0.42	15.1	6.01	78.6	32.5	155.4	311	63.1	8040	B-LOD	10.69	0.73	1.2	91.3	443	140.6
AOLH_06_29	288	6.8	128	1180	386000	1.56	0.031	8.2	0.04	1.4	3.12	0.72	23.2	7.94	102	40.4	180	402	67.9	7620	B-LOD	14.8	0.75	1.89	133	609	193
AOLH_06_32	291	5.8	B-LOD	940	380000	1.04	B-LOD	5.48	B-LOD	1.03	1.84	0.5	15.1	6.05	75.6	31.3	141	336	60.2	7870	B-LOD	10	0.69	1.12	77.8	380	125
AOLH_06_37	344	9	B-LOD	1206	378000	1.15	0.51	7.96	0.24	2.38	4.35	0.69	22.9	8.3	99.8	41	182.5	388	70	8080	B-LOD	9.84	0.7	1.16	97.7	411	137.9
AOLH_06_40	462	10.1	128	1287	392200	1.95	0.56	12.85	0.26	1.95	3.42	0.46	19.5	7.22	95.3	41.1	200.2	416	85.9	8980	B-LOD	18.56	1.13	2.25	215.8	784	253.9
AOLH_06_41	432	23.9	881	1866	426000	2.52	5.7	31.4	5.20	23.6	14.2	4.12	38.5	12.87	147.9	60.6	274	585	127.7	11040	B-LOD	39.7	2.81	2.63	264	1830	585
AOLH_07_0	442	12.8	B-LOD	1097	384000	1.15	B-LOD	7.02	0.04	1.22	2.46	0.61	19.7	6.67	87.2	35.3	164	354	75.2	7540	3.9	11.85	0.55	1.32	140.1	494	160.2
AOLH_07_1	396	7.22	B-LOD	1152	394000	2.17	0.1	10.81	0.10	0.84	2.6	0.49	18.3	6.81	89.3	38.3	175.4	377	79.8	8530	4	19.4	1.008	2.27	222	793	262
AOLH_07_4	351	8.3	B-LOD	1130	345000	1.15	0.48	7.6	0.18	2.12	3.35	0.42	20.5	6.87	94	38.1	170	380	73.7	7190	B-LOD	11.7	0.65	1.33	123	458	165

Anexo C, continuación

Sample/ Grain	P31 (ppm)	Ti49 (ppm)	Fe57 (ppm)	Y89 (ppm)	Zr90 (ppm)	Nb93 (ppm)	La139 (ppm)	Ce140 (ppm)	Pr141 (ppm)	Nd146 (ppm)	Sm147 (ppm)	Eu153 (ppm)	Gd157 (ppm)	Tb159 (ppm)	Dy163 (ppm)	Ho165 (ppm)	Er166 (ppm)	Yb172 (ppm)	Lu175 (ppm)	Hf178 (ppm)	Pb204 (ppm)	Pb206 (ppm)	Pb207 (ppm)	Pb208 (ppm)	Th232 (ppm)	U235 (ppm)	U238 (ppm)
AOLH_07_5	718	9.4	B-LOD	875	375000	1.39	4.27	16.4	1.42	6.67	4.1	0.434	15.8	5.28	67.8	27.3	131.1	292	61.1	8570	B-LOD	15.7	0.83	1.06	106.4	666	218
AOLH_07_6	216	9.2	B-LOD	547	357000	1.22	B-LOD	4	0.01	0.26	1.5	0.243	7.7	2.91	38.5	17	81.4	201	42	9410	5	7.07	0.354	0.543	57.1	291	98.5
AOLH_07_9	373	9.4	B-LOD	1091	371000	1.11	B-LOD	4.78	0.06	1.17	3.43	0.496	19.6	6.91	87.5	35.9	160	350	69.2	7280	B-LOD	7.77	0.447	0.71	65.9	321	105.9
AOLH_07_10	218	6.7	B-LOD	567	356000	0.97	0.014	4.67	0.04	0.47	1.36	0.183	9	3.37	43.7	18.4	86.2	205	39.7	8800	B-LOD	10.71	0.53	0.72	59.8	477	153
AOLH_07_14	370	9.1	22	880	357000	1.45	0.77	8.9	0.11	1.15	2.9	0.48	14	5.35	65	27.9	134	297	52.8	7080	B-LOD	13.3	0.84	1.41	125	510	175
AOLH_07_15	425	8.8	B-LOD	1860	367000	1.89	0.3	14.5	0.20	2.6	6.34	0.78	35.8	13.8	172	63.9	291	603	98.6	7310	B-LOD	20	1.08	3.01	260	800	275
AOLH_07_16	335	8.7	B-LOD	1020	347000	1.49	0.068	9.4	0.13	0.94	2.7	0.38	17.5	6.08	76.2	31.5	152	355	61.5	7490	B-LOD	16.2	0.82	1.93	173	629	221
AOLH_07_17	312	7.9	B-LOD	1157	388000	1.6	B-LOD	7.54	0.05	1.08	2.7	0.45	18.2	7.02	91.3	36.9	175	399	71.1	8220	3.2	12.2	0.7	1.29	108.2	458	163
AOLH_07_18	268	8.8	B-LOD	1189	380000	1.1	0.088	5.53	0.08	1.33	2.92	0.8	22.6	7.69	92.5	37.9	167.8	348	63.9	8020	2.6	8.62	0.497	1.12	95.2	336	114.9
AOLH_07_19	329	9	B-LOD	1035	370000	0.88	0.45	6.3	0.21	1.77	4.36	0.45	17.8	7.04	82.9	35	149	328	57.3	6970	2.3	7.1	0.37	0.75	67.9	261	100
AOLH_07_20	365	9.8	B-LOD	1106	387000	1.31	0.029	8	0.06	0.9	2.9	0.47	18.3	6.42	84.5	35.5	166	378	68.9	7920	2.9	14.7	0.85	2.15	164	604	205
AOLH_07_21	332	9.2	B-LOD	1490	386000	1.09	0.034	6.67	0.09	1.69	5.5	0.82	28.9	10.16	124	47.3	210	446	79.3	7590	2.7	11.7	0.65	1.55	130	497	154.2
AOLH_07_22	432	8.8	B-LOD	1590	368000	1.58	0.68	10.24	0.35	3.19	5.2	0.68	31.9	11.2	142	53.4	226	509	82.8	7230	1.7	20.6	0.96	2.01	152	773	251
AOLH_07_23	538	9.2	B-LOD	3010	392000	2.64	0.052	19.2	0.25	3.74	9.7	1.07	58.9	22.2	268	103	441	858	155.4	7700	3	37.2	2.12	6.64	563	1570	511
AOLH_07_26	405	9.5	B-LOD	992	403000	1.21	0.91	8.7	0.36	3	2.09	0.42	14.3	6.14	80.1	31.4	150.1	330	62.2	8430	2.6	10.31	0.57	1.1	91.1	421	143.1
AOLH_07_27	316	8.6	B-LOD	893	377000	1.29	0.025	5.44	0.03	0.61	1.84	0.34	15.2	5.49	71.6	29	129	299	57.3	7560	3	8.81	0.49	0.87	70.8	397	121
AOLH_07_29	423	5.7	95	1064	364000	1.62	0.46	10	0.19	1.5	2.38	0.46	16.1	5.98	80.8	32.5	159	381	65.8	7640	3.1	16.6	1.05	2.26	173	684	226
AOLH_07_30	250	7.9	B-LOD	751	409000	1.17	0.013	6.34	0.03	0.38	1.5	0.375	11.36	4.28	56.2	23.9	112.2	245.6	45.7	8890	3.1	10.44	0.581	1.03	91.7	433	140.4
AOLH_07_31	319	6.9	B-LOD	695	377000	1.26	0.8	8.02	0.29	1.41	1.81	0.35	10.1	4.13	52.3	22.8	102.8	243	43.6	7780	B-LOD	10.4	0.52	1.03	80.1	429	140.3
AOLH_07_32	531	9.4	B-LOD	1667	383000	1.42	0.74	11.23	0.37	3.32	5.25	0.73	33.6	11.4	139.5	55.9	241	492	85.4	7480	B-LOD	14.8	0.782	2.04	178	654	207
AOLH_07_34	409	9.2	92	1630	385000	1.88	0.31	9.9	0.19	2.03	4.6	0.86	28	10.5	136	51.8	239	481	92.3	8290	B-LOD	19.4	1.69	2.9	260	850	257
AOLH_07_35	276	8.5	B-LOD	744	398000	1.04	0.033	4.64	0.05	0.63	2.01	0.34	12.27	4.56	60.6	24.6	113.4	252	46.7	8150	2.5	6.49	0.334	0.651	50.5	264	87.5
AOLH_07_36	317	10.3	B-LOD	1074	403000	1.17	0.006	6.32	0.08	0.97	3.11	0.47	17.2	6.37	85.7	35.1	168.3	375	70.4	7860	4.5	10.82	0.57	1.1	96.7	466	145.5
AOLH_07_37	349	8.2	28	1116	366000	1.75	0.301	10.6	0.10	1.44	2.61	0.53	17.8	7.08	88	35.8	168	350	65.9	7840	B-LOD	19.1	1.03	2.39	193	792	251
AOLH_07_38	211	10.3	B-LOD	626	388000	1.06	B-LOD	6.8	0.03	0.47	1.23	0.187	8.89	3.98	47	19.11	91.5	201.3	37.9	9140	4.2	7.6	0.385	0.726	63.9	332	102.7
AOLH_07_40	465	6.2	B-LOD	979	364000	1.61	1.37	11.4	0.48	3.09	3.1	0.427	15.5	6.23	73.2	31.9	147.6	337	61.5	8500	B-LOD	16.5	0.84	1.74	136.2	676	216
AOLH_07_41	673	8.4	54	1525	431000	2.33	2.14	18.6	0.62	4.6	4.11	0.53	24	9.55	120.6	48.1	231	487	95.2	9840	3.1	28.7	1.47	3.84	376	1238	408

Anexo C, continuación

Sample/ Grain	P31 (ppm)	Ti49 (ppm)	Fe57 (ppm)	Y89 (ppm)	Zr90 (ppm)	Nb93 (ppm)	La139 (ppm)	Ce140 (ppm)	Pr141 (ppm)	Nd146 (ppm)	Sm147 (ppm)	Eu153 (ppm)	Gd157 (ppm)	Tb159 (ppm)	Dy163 (ppm)	Ho165 (ppm)	Er166 (ppm)	Yb172 (ppm)	Lu175 (ppm)	Hf178 (ppm)	Pb204 (ppm)	Pb206 (ppm)	Pb207 (ppm)	Pb208 (ppm)	Th232 (ppm)	U235 (ppm)	U238 (ppm)
AOLH_07_42	365	7.6	B-LOD	1013	398000	1.37	0.36	7.89	0.23	1.55	2.35	0.43	16.2	6.48	79.2	31.9	154.1	340	63.6	8240	B-LOD	11.83	0.67	1.27	106.1	524	169
AOLH_07_43	302	8.7	B-LOD	969	369000	0.98	B-LOD	5.76	0.02	0.88	2.32	0.41	17.3	6.01	76.2	31.3	145.1	299	56.6	7440	2.9	8.7	0.6	0.96	82.7	376	117.2
AOLH_07_45	384	7.9	B-LOD	1038	390000	1.19	0.9	8.6	0.36	1.73	2.99	0.37	17.1	6.05	82.2	33.7	150.2	332	63.4	8460	2.3	13.3	0.79	1.35	124.4	522	175
AOLH_07_47	357	7.7	B-LOD	1336	373000	1.98	0.083	10.29	0.09	1.11	3.26	0.57	21.3	8.17	105.8	45.2	203.7	450	79.7	7810	B-LOD	19.21	0.933	2.39	216	861	275
AOLH_07_48	408	9	B-LOD	2361	410000	1.08	B-LOD	8.28	0.19	3.88	8.6	1.21	48.2	16.94	208	84.6	362	680	124.5	8230	5.5	15.01	0.83	2.15	191.5	630	210.3
AOLH_07_49	324	9.4	B-LOD	1305	385000	0.69	0.019	5.27	0.06	1.65	3.39	0.52	24.3	7.99	110	42.2	193.4	386	72.9	7820	B-LOD	8.19	0.45	0.91	80.3	339	111.1
AOLH_07_51	397	8.4	B-LOD	1090	388000	0.93	0.043	5.71	0.12	1.2	3.5	0.49	18.1	6.86	85.3	34.9	162	367	66	7460	3.1	8.73	0.38	0.89	72.7	373	117.5
AOLH_07_52	399	10.6	B-LOD	958	372000	0.92	0.38	5.31	0.15	1.26	2.54	0.48	16	6.11	75.8	31.3	143	308	58	7150	3	7.83	0.447	0.77	59.6	324	110
AOLH_07_53	258	5.8	B-LOD	758	346000	1.16	B-LOD	5.56	B-LOD	0.56	1.22	0.24	10.7	4.47	55.6	23.3	110	258	46.5	7220	B-LOD	9.31	0.57	0.84	75	423	133
AOLH2_02_1	211	4.5	28	615	381000	0.8	B-LOD	6.4	0.06	0.54	2.09	0.26	10.8	4.07	46.8	19	87	194	36.7	8460	B-LOD	32.6	1.85	2.72	206	1179	394
AOLH2_02_2	422	12.6	140	1980	374000	1.27	0.067	10.7	0.18	3.04	7.7	0.75	37.6	13.3	159	58.8	255	484	83.7	7280	B-LOD	40.1	2.59	7.99	649	1550	511
AOLH2_02_3	391	12.3	30	1600	328000	1.15	0.27	10.6	0.43	3.33	7	0.65	34.2	11.6	133	48.1	215	421	66.9	5840	B-LOD	35.1	1.94	6.23	522	1390	456
AOLH2_02_4	533	16.3	B-LOD	2430	397000	2.08	0.049	17	0.16	3.53	9.4	0.78	48.5	17.4	212	79.2	356	690	115.8	8050	B-LOD	72.3	3.93	12.01	986	2790	924
AOLH2_02_9	85	3.4	B-LOD	158.9	397000	0.76	B-LOD	4.32	B-LOD	0.046	0.22	0.04	1.11	0.593	9.03	4.55	26.3	82.6	18.92	11020	B-LOD	9.45	0.521	1.01	79.3	378	127.2
AOLH2_02_10	258	10.6	B-LOD	849	422000	1.24	B-LOD	7.45	0.05	1	2.2	0.174	13.9	5.25	73.5	28.5	133.4	290	52.3	10560	B-LOD	26.1	1.62	2.65	228	1071	361
AOLH2_02_11	146	6.4	B-LOD	483	406000	0.59	B-LOD	7.59	0.03	0.62	1.34	0.156	8.3	2.85	37.5	14.9	74.9	193	34.5	11320	1.2	44.4	2.53	2.17	170	1820	601
AOLH2_02_12	472	12	B-LOD	2390	419000	2.25	B-LOD	14.87	0.20	3.06	10.5	0.82	48.6	17.4	207	79.7	349	664	111	9010	B-LOD	60.1	3.49	9.57	747	2350	767
AOLH2_02_13	374	9.5	B-LOD	1227	450000	1.4	B-LOD	9.71	0.11	1.71	4	0.308	21	7.7	99	40	188	416	77	10940	0.3	42.2	2.33	5.08	378	1610	526
AOLH2_02_14	101	4.3	14	178	364000	0.86	0.026	5.39	0.01	0.1	0.27	0.063	1.49	0.75	9.6	4.8	29.2	92.9	18.4	8340	1.2	10.6	0.68	1.35	105	445	149
AOLH2_02_15	231	6.2	27	539	362000	1.36	0.011	6.25	0.03	0.51	0.92	0.07	5.34	2.25	31.9	15	83.2	229	45.7	9470	B-LOD	45.5	2.4	1.76	136	1710	585
AOLH2_02_18	277	10	121	870	353000	0.94	B-LOD	8.6	0.05	1.04	2.07	0.12	14.3	5.09	66	26	122	250	48	8000	B-LOD	30.7	1.7	4.49	365	1110	403
AOLH2_02_19	199	8.6	31	819	328000	0.68	0.024	7	0.08	1.31	3.14	0.32	16.5	5.27	68.8	26.3	116.9	240	40.6	7880	B-LOD	33.8	1.92	3.71	314	1272	440
AOLH2_02_20	322	9.2	B-LOD	1301	380800	0.94	0.107	10.09	0.12	1.56	4.4	0.61	29	9.07	107.7	42.7	192.5	362	70.2	9230	B-LOD	39.7	2.04	5.55	568	1515	531
AOLH2_02_21	451	10.2	B-LOD	1411	424000	1.6	0.028	11.85	0.08	1.48	4.12	0.28	26	8.48	108.6	46.4	230	473	89.9	9460	2.5	64.7	3.5	8.69	688	2340	806
AOLH2_02_22	225	8.6	B-LOD	980	342000	0.83	B-LOD	8.08	0.08	1.38	3.21	0.274	18.5	6.38	77.7	29.8	141	281	46.4	8280	B-LOD	44.9	2.56	4.53	343	1770	604
AOLH2_02_23	210	11.1	B-LOD	838	324000	0.83	0.027	7.75	0.13	1.19	3.09	0.338	19.5	5.83	69.4	26.1	114	232	40.1	7060	B-LOD	37	2.13	3.23	264	1440	519
AOLH2_02_24	465	12.5	B-LOD	1958	411000	2.19	B-LOD	12.43	0.15	2.57	5.2	0.69	41.6	13.78	159.1	63.7	296	566	102.9	10550	B-LOD	52	2.87	7.01	582	1960	680

Anexo C, continuación

Sample/ Grain	P31 (ppm)	Ti49 (ppm)	Fe57 (ppm)	Y89 (ppm)	Zr90 (ppm)	Nb93 (ppm)	La139 (ppm)	Ce140 (ppm)	Pr141 (ppm)	Nd146 (ppm)	Sm147 (ppm)	Eu153 (ppm)	Gd157 (ppm)	Tb159 (ppm)	Dy163 (ppm)	Ho165 (ppm)	Er166 (ppm)	Yb172 (ppm)	Lu175 (ppm)	Hf178 (ppm)	Pb204 (ppm)	Pb206 (ppm)	Pb207 (ppm)	Pb208 (ppm)	Th232 (ppm)	U235 (ppm)	U238 (ppm)
AOLH2_02_25	249	10.1	B-LOD	669	402000	0.99	B-LOD	9.97	0.03	0.98	1.6	0.144	11.3	3.74	49	21.9	111.8	245	48.9	12400	B-LOD	46.3	2.8	4.49	393	1730	600
AOLH2_02_27	134	4.8	B-LOD	434	370000	1.15	B-LOD	6.42	0.04	0.61	1.24	0.098	8.2	2.76	33.7	13.7	68.1	169	31.7	9530	B-LOD	34.8	1.76	1.85	153	1300	438
AOLH2_02_29	540	6.5	B-LOD	245	328000	0.46	2.1	10.3	0.77	4.2	1.37	0.092	4.72	1.37	17.9	7.44	35.6	92	17.5	7340	B-LOD	14.2	0.84	1.06	75.9	521	194
AOLH2_03_0	365	6.9	B-LOD	1289	466000	2.23	0.007	15.97	0.09	1.03	2.64	0.85	16.11	7.82	98.2	43.1	219.8	619	145.9	10220	B-LOD	13.66	0.705	1.54	145.6	619	187.1
AOLH2_03_1	315	6.8	B-LOD	918	390000	1.17	0.27	10.1	0.20	1.77	2.19	0.75	14.3	6.23	71.9	30.7	150	393	90.8	8080	B-LOD	6.63	0.316	0.608	58.9	287	91.9
AOLH2_03_2	368	7.3	B-LOD	1355	480000	2.26	0.126	16.69	0.11	1.18	2.43	1	16.8	8.09	98.6	42.7	229	608	144.4	9640	B-LOD	11.83	0.65	1.39	125.7	537	160.8
AOLH2_03_3	398	7.8	B-LOD	1267	449000	1.84	0.45	18	0.34	2.13	3.12	1.08	18.2	8.06	92.8	39.2	202	546	139.1	9860	1.4	12.56	0.7	1.87	186	572	174
AOLH2_03_4	231	7.7	B-LOD	879	387000	1.59	B-LOD	9.11	0.04	0.64	1.5	0.66	10.72	4.94	61.7	27.4	145.2	430	99.9	7830	0.69	7.26	0.373	0.657	52.7	308	96.2
AOLH2_03_5	347	7.7	B-LOD	1213	463000	1.72	B-LOD	11.25	0.05	0.92	2.77	0.91	15.6	7.17	88.5	39.9	205.5	562	135.3	9860	B-LOD	10.68	0.588	1.047	94.2	424	144.1
AOLH2_03_7	301	6.4	B-LOD	1200	456000	1.81	0.014	9.9	0.06	1.37	2.73	0.83	16.7	6.45	84.2	38.2	193	477	111.3	9140	B-LOD	7.67	0.435	0.734	68.9	314	101.6
AOLH2_03_8	266	6.6	B-LOD	863	388000	1.55	B-LOD	7.43	0.03	0.64	1.55	0.431	8.65	3.82	52.4	25.3	134.4	418	93	7360	B-LOD	7.45	0.377	0.554	48.1	285	101.2
AOLH2_03_11	169	8	20	472	348000	0.85	B-LOD	4.93	0.03	0.45	1.18	0.36	7	2.33	32.1	14.5	73.1	226	43.9	6620	B-LOD	4.61	0.266	0.435	33.7	196	64.6
AOLH2_03_12	291	8.4	B-LOD	743	452000	1.28	B-LOD	6.86	0.05	0.57	1.89	0.544	12.1	4.27	57.1	24	119.3	285	57.1	9360	B-LOD	4.95	0.289	0.387	37	219	68.7
AOLH2_03_13	233	7.8	B-LOD	696	374000	1.27	B-LOD	6.92	0.02	0.54	1.47	0.501	8.7	3.47	47.4	20.6	108.4	326	63.9	7370	B-LOD	5.95	0.33	0.473	42.8	238	81.6
AOLH2_03_14	291	6.3	13	829	390000	1.22	0.108	7.15	0.08	1.36	1.81	0.56	11.5	4.65	61	26.5	135	359	69.1	7640	B-LOD	5.86	0.318	0.62	51.9	255	84.6
AOLH2_03_15	253	6.4	B-LOD	1076	406000	1.04	B-LOD	9.24	0.06	1.68	3.51	0.94	19.5	6.96	85.7	36.2	172.9	431	88.9	8750	B-LOD	7.64	0.446	0.885	81	348	105.4
AOLH2_03_16	258	7.2	B-LOD	902	419000	1.36	B-LOD	7.52	0.05	0.86	1.99	0.64	11	4.58	60.9	26.8	147.2	408	94.4	8300	1.4	6.65	0.364	0.588	49.5	312	90.5
AOLH2_03_18	343	8.1	B-LOD	935	390000	1.49	0.47	11.62	0.18	1.45	2.18	0.61	12.54	4.89	62.1	27.1	138.5	367	82.3	7560	0.97	8.73	0.519	0.963	93.5	392	118.9
AOLH2_03_19	335	8.1	20.8	1103	389000	1.31	0.04	11.31	0.07	1.24	2.96	0.78	16.4	7.26	84.3	34.9	171.2	406	84.6	7780	0.59	7.46	0.441	1.04	99	356	106
AOLH2_03_20	348	10.2	B-LOD	1108	437000	1.94	0.029	12.89	0.05	0.55	1.7	0.78	13.4	5.77	74.2	34.6	186.1	521	117.6	8960	2	11.21	0.659	1.21	99.7	453	144.9
AOLH2_03_21	254	7.63	B-LOD	887	349000	0.86	B-LOD	6.29	0.07	1.13	2.25	0.77	14.7	5.84	68	28.2	135	305	60.7	6630	B-LOD	3.59	0.237	0.415	36.9	171	50.5
AOLH2_03_22	280	6.1	B-LOD	895	414000	1.52	0.014	11.69	0.05	0.75	1.81	0.65	11.44	4.85	61.5	27.9	145.2	390	90.4	8670	B-LOD	10.99	0.556	1.138	99.9	478	147.6
AOLH2_03_23	398	7.5	B-LOD	1963	427000	1.93	0.006	18.26	0.13	2.67	6.32	1.81	36.5	14.08	163.6	68.2	312	689	137.8	8690	B-LOD	10.58	0.606	1.44	128.2	489	150
AOLH2_03_24	229	5.4	B-LOD	554	312000	0.88	0.14	7.6	0.15	1.02	1.5	0.47	9	3.25	40.2	17.6	85.7	268	50.7	6250	B-LOD	4.95	0.299	0.505	37.3	222	70.1
AOLH2_03_25	284	5.1	B-LOD	856	415000	1.51	B-LOD	10.66	0.03	0.78	1.69	0.59	10.4	4.31	58.8	25.9	141.6	423	87.9	7970	B-LOD	7.63	0.502	0.576	50.3	350	110.6
AOLH2_03_26	288	5.3	B-LOD	778	344000	0.91	B-LOD	7.33	0.06	0.96	2.24	0.8	11.9	4.5	55.6	23	117	349	67.6	6200	B-LOD	6.24	0.347	0.7	61	278	89
AOLH2_03_27	230	7.7	38	718	359000	1.5	0.079	8.4	0.05	0.6	1.19	0.404	7.75	3.57	46.1	21.2	111.7	340	70.3	6680	B-LOD	6.74	0.409	0.635	45.1	273	89.1

Anexo C, continuación

Sample/ Grain	P31 (ppm)	Ti49 (ppm)	Fe57 (ppm)	Y89 (ppm)	Zr90 (ppm)	Nb93 (ppm)	La139 (ppm)	Ce140 (ppm)	Pr141 (ppm)	Nd146 (ppm)	Sm147 (ppm)	Eu153 (ppm)	Gd157 (ppm)	Tb159 (ppm)	Dy163 (ppm)	Ho165 (ppm)	Er166 (ppm)	Yb172 (ppm)	Lu175 (ppm)	Hf178 (ppm)	Pb204 (ppm)	Pb206 (ppm)	Pb207 (ppm)	Pb208 (ppm)	Th232 (ppm)	U235 (ppm)	U238 (ppm)
AOLH2_03_28	460	6.1	94	1207	409000	1.23	0.251	12.98	0.20	2.03	2.9	0.95	17.2	6.92	85.4	36.3	181.3	489	106.2	8510	B-LOD	13.48	0.91	1.42	108.2	551	175.6
AOLH2_03_29	326	8.8	B-LOD	843	372000	1.27	0.168	8.06	0.09	0.85	1.77	0.53	10.58	4.38	55.9	24.4	128.6	317	71.5	6440	B-LOD	4.44	0.261	0.428	33.9	176	59.5
AOLH2_03_30	268	9.3	B-LOD	924	387000	1.16	0.086	7.89	0.09	1.07	2.55	0.7	12.61	4.98	62.6	27.6	142.1	371	83.2	6980	B-LOD	6.24	0.41	0.73	53.8	243	82.6
AOLH2_03_31	212	5.7	B-LOD	531	359000	1.03	0.034	6.87	0.03	0.541	0.94	0.379	6.36	2.71	35.7	15.66	81.5	233	49	6960	B-LOD	6.18	0.358	0.616	49.2	257	83.7
AOLH2_03_32	312	7.5	B-LOD	988	374000	0.92	B-LOD	6.42	0.04	1.11	2.7	0.73	16.3	6.11	75.6	31.4	143.4	309	65.6	7110	B-LOD	3.85	0.237	0.389	37.8	145	52.1
AOLH2_07_0	190	7.4	B-LOD	538	385000	0.75	0.019	4.87	0.05	0.78	1.75	0.202	9.12	3.3	40.4	16.25	76	171.4	32.5	7920	B-LOD	13.69	0.78	1.41	119.2	526	174.1
AOLH2_07_1	515	10.2	B-LOD	3300	379000	1.78	0.065	12.2	0.22	4.79	11.9	1.17	73.6	24.5	285.1	105.1	444	769	134.7	8200	B-LOD	72.8	4.11	14.6	1257	2800	927
AOLH2_07_2	65	4.4	B-LOD	176.6	374000	0.72	B-LOD	4.53	0.01	0.099	0.31	0.063	1.53	0.702	9.51	4.63	27.4	87.8	18.2	8800	B-LOD	8.89	0.51	1.07	95.5	385	120.3
AOLH2_07_4	144	6.9	B-LOD	382	331000	0.74	0.017	5.57	0.02	0.37	1.3	0.083	6.12	2.29	27.6	11.8	55.4	152	26.5	9630	0.97	24.8	1.5	1.87	131	971	321
AOLH2_07_5	313	5.5	B-LOD	1351	443000	0.94	0.019	8.85	0.08	2.48	4.9	0.44	29.3	9.8	115.5	44.9	200	397	77.5	10530	2.7	57.9	3.38	4.89	429	2310	727
AOLH2_07_7	103	4.9	19	231	343000	0.81	0.018	5.37	0.01	0.168	0.4	0.041	2.81	1.09	14.3	6.8	35.9	108.5	21.9	8320	B-LOD	22.9	1.27	1.17	87.8	1020	305
AOLH2_07_8	255	6.9	B-LOD	759	369000	0.86	B-LOD	6.8	0.06	1.03	2.71	0.147	14.2	5.27	60.2	23	105.3	207	44.4	7940	B-LOD	29.6	1.58	3.38	265	1197	371
AOLH2_07_9	141	3.88	B-LOD	378	377000	0.74	0.0012	5.36	0.03	0.33	0.87	0.084	4.95	2.26	27.2	11.4	55.8	137.8	30.2	8890	B-LOD	15.76	0.837	1.69	140	647	203
AOLH2_07_11	283	19.7	58	1050	343000	0.77	0.062	5.73	0.26	3.77	5.7	0.66	26.9	9	97	34.6	147	272	49.7	6200	B-LOD	12.3	0.777	1.88	149	543	164
AOLH2_07_12	75	5.68	B-LOD	180	356000	0.63	B-LOD	4.84	0.00	0.057	0.192	0.036	1.95	0.78	10.7	4.99	25.6	80.3	17.5	8660	0.91	18.1	1	0.868	70.6	833	243
AOLH2_07_15	236	8.8	99	649	378000	1.34	0.072	8.94	0.17	2.07	2.55	0.38	10.4	3.52	45	18.7	92.6	209.7	42	9760	B-LOD	45.4	2.44	3.61	294	1787	578
AOLH2_07_18	92	5.4	B-LOD	175.7	384000	0.67	0.013	4.29	B-LOD	0.084	0.23	0.033	1.47	0.538	9.43	4.43	25.6	85	16.04	10590	B-LOD	5.95	0.383	1.36	114.3	210	77.3
AOLH2_07_20	166	B-LOD	271	414	477000	0.82	0.063	6.54	0.03	0.46	0.77	0.12	4.6	1.61	25.5	12.8	64.5	165.3	30.7	13020	1.9	41.3	2.45	1.9	160.3	1500	542
AOLH2_07_21	450	13.9	34	1291	393000	1.26	0.024	9.87	0.08	2.13	4.65	0.47	23.7	7.11	102.1	39.1	170.8	323	47.7	8640	1.8	53.5	2.99	10.76	878	1875	666
AOLH2_07_22	132	4.1	B-LOD	305	383000	0.81	0.014	5.06	0.01	0.23	0.36	0.106	3.18	1.011	17.8	8.26	46.6	135.2	25.8	8240	B-LOD	14.78	0.731	1.68	131.6	541	193
AOLH2_07_24	75	3.27	B-LOD	137	334000	0.65	B-LOD	3.19	B-LOD	0.134	0.26	B-LOD	1.02	0.446	8.2	3.79	22	74.7	12	7860	B-LOD	8.65	0.42	0.772	60.2	335	120
AOLH2_07_25	87	4.1	B-LOD	166	401000	0.74	B-LOD	4.25	0.01	0.079	0.33	0.035	1.62	0.526	10.4	5.14	28.9	94.9	15.7	10610	B-LOD	9.1	0.501	1.05	83.8	346	128.1
AOLH2_07_26	92	15.1	19	1200	321000	1.17	0.043	8.6	0.05	1.26	3.44	0.72	22.2	6.9	97	36.6	164	358	48.6	6780	B-LOD	7.61	0.406	0.733	52.4	281	98.7
AOLH2_07_28	63	4.4	B-LOD	192	394000	0.67	0.017	4.52	B-LOD	0.147	0.39	0.041	1.92	0.75	12.5	5.67	31.7	111.8	18.5	10020	B-LOD	10.37	0.491	1.2	93.8	416	147
AOLH2_07_30	63	3.6	B-LOD	140	327000	0.53	B-LOD	3.87	0.00	0.073	0.155	0.038	0.97	0.452	7.98	3.58	21	73	14.04	8600	B-LOD	6.17	0.318	0.967	82.6	249	84.3
AOOJA04_1	271	3.53	17	1197	377000	1.9	0.05	11.9	0.07	1.36	3.13	0.393	20.8	8.01	100.1	40.5	188	411	78.4	8590	B-LOD	27.5	1.45	1.95	157	1140	376
AOOJA04_2	464	4.63	116	2620	390000	2.09	0.074	17.8	0.17	3.47	8.85	1.34	53.5	19.7	244	94.8	413	858	140.6	7750	2.2	20.4	1.82	3.4	196	794	261

Anexo C, continuación

Sample/ Grain	P31 (ppm)	Ti49 (ppm)	Fe57 (ppm)	Y89 (ppm)	Zr90 (ppm)	Nb93 (ppm)	La139 (ppm)	Ce140 (ppm)	Pr141 (ppm)	Nd146 (ppm)	Sm147 (ppm)	Eu153 (ppm)	Gd157 (ppm)	Tb159 (ppm)	Dy163 (ppm)	Ho165 (ppm)	Er166 (ppm)	Yb172 (ppm)	Lu175 (ppm)	Hf178 (ppm)	Pb204 (ppm)	Pb206 (ppm)	Pb207 (ppm)	Pb208 (ppm)	Th232 (ppm)	U235 (ppm)	U238 (ppm)
AOOJA04_3	281	3.07	B-LOD	1348	378000	1.95	0.02	14.6	0.05	1.44	4.62	0.395	24.1	9.5	118.7	47	213	466	79.6	9210	B-LOD	19.5	1.14	2.07	164	854	276
AOOJA04_4	126	2.42	33	280	426000	1.36	0.023	4.89	B-LOD	0.075	0.34	0.069	2.89	1.23	18	8	47.5	143	30.2	12570	B-LOD	12.6	0.72	1.15	95.5	515	169
AOOJA04_5	453	4.9	B-LOD	1930	383000	3.04	0.008	20.7	0.13	1.91	5.54	0.82	36.8	13.9	180	69.4	308	685	110.1	8490	B-LOD	23.3	1.22	2.35	209	1008	321
AOOJA04_6	537	3.9	119	1213	391000	5.69	0.43	8.61	0.24	1.49	1.73	0.364	8.5	3.38	62.4	33.8	202	654	134	8810	B-LOD	34.4	2.22	3.73	236	1360	439
AOOJA04_7	374	4.17	22	1881	373000	2.34	0.013	16.43	0.11	1.87	5.22	0.705	35.1	12.81	166.1	65.2	293	595	106.7	8140	B-LOD	25.4	1.5	2.39	193.4	1038	339
AOOJA04_10	293	4.14	B-LOD	997	389000	1.9	0.013	9.58	0.02	0.69	2.25	0.235	15.44	5.91	80.8	33.4	156.6	342	67	9050	B-LOD	21.1	1.13	1.54	127.3	860	276
AOOJA04_11	309	7.2	74	1149	364000	2.34	0.204	13.7	0.15	1.87	2.96	0.68	19.5	7.3	95.4	38	173	388	71.3	8460	B-LOD	19.2	1.22	3.08	270	810	271
AOOJA04_12	213	5.1	40	850	381000	1.23	0.053	8.45	0.06	0.72	2.39	0.287	14.4	5.63	71.6	28.4	133.9	294	56.3	9000	1.7	12.95	0.82	1.78	138.4	501	162
AOOJA04_14	372	B-LOD	B-LOD	1410	408000	3.09	0.045	17.8	0.04	0.74	2.72	0.29	20.2	8	111	47.6	221	514	96	10690	B-LOD	33.2	1.7	2.13	186	1444	467
AOOJA04_17	300	2.71	B-LOD	1539	391000	1.62	B-LOD	13.82	0.08	1.52	4.36	0.55	28.1	10.77	136	53.8	237.7	509	86.1	9970	B-LOD	19.3	0.97	1.79	150.9	793	248
AOOJA04_18	194	2.94	B-LOD	584	392000	1.32	B-LOD	7.53	0.02	0.35	1.14	0.158	7.8	3.41	45.6	19.6	92	214	42.6	10160	2.2	11.12	0.646	1.46	121.3	442	142.1
AOOJA04_20	217	1.9	B-LOD	1129	393000	1.49	0.032	10.69	0.07	1.16	3.73	0.354	20.2	7.33	93.9	36.6	170	365	69.5	10270	B-LOD	18.7	1.08	1.64	141.1	809	263
AOOJA04_21	178	3.89	B-LOD	486	395000	1.04	B-LOD	6.45	0.02	0.28	0.98	0.112	7.7	3.09	41.4	16.4	76.5	188	34.4	10300	B-LOD	11.28	0.65	1.51	120.5	467	144.4
AOOJA04_22	407	3.64	B-LOD	2221	409000	2.22	B-LOD	16.91	0.11	2.48	6.36	0.79	42.6	15.88	198.8	78.8	342	685	122.2	8920	B-LOD	20.9	1.22	1.89	171.6	855	286
AOOJA04_23	54	1.5	B-LOD	83.5	374000	0.79	B-LOD	2.36	B-LOD	0.03	0.126	0.038	0.85	0.303	4.69	2.7	14.9	61.7	15.1	9810	B-LOD	5.65	0.328	0.422	36	242	76
AOOJA04_25	335	2.21	B-LOD	1280	383000	2.67	0.02	14.9	0.05	0.94	2.87	0.381	19.7	8.05	106	43.1	198	439	82.2	9270	B-LOD	34.8	1.79	2.58	204	1430	448
AOOJA04_26	321	4.8	B-LOD	1607	391000	1.63	0.022	11.23	0.10	1.77	5.42	0.72	32.9	12.02	148	58.4	250	516	91.5	8890	B-LOD	13.44	0.82	1.6	129.8	550	174.8
AOOJA04_28	511	5.11	B-LOD	2650	397000	2.41	0.64	22	0.69	6.81	11.2	1.96	57.3	21	257	97.7	425	829	147	8220	B-LOD	25.4	1.48	2.64	215	1029	334
AOOJA04_30	135	5.6	B-LOD	620	389000	0.7	B-LOD	6.27	0.04	0.83	1.8	0.293	11.4	4.05	50.4	21	98	222	47.4	9900	B-LOD	10.96	0.616	2.66	222	450	145.3
AOOJA04_31	221	7.1	93	818	402000	2.15	0.048	14.18	0.04	0.75	2.15	0.33	14.1	5.81	72.9	29	134	302	55.4	10110	B-LOD	18.66	1.24	4.9	414	791	252
AOOJA04_34	275	2.87	19	960	388000	2.16	B-LOD	13.1	B-LOD	0.59	1.9	0.245	15.3	5.55	78	32.1	160	386	68.9	9860	B-LOD	17.6	1.16	1.81	143	722	234
AOOJA04_35	246	3.1	B-LOD	840	384000	1.29	0.061	7.4	0.08	0.82	2.26	0.47	15.7	6.1	75	30.2	133	303	54.3	9260	B-LOD	12.3	0.77	1.61	126	496	159
AOOJA04_36	202	6.2	47	755	376000	2.22	0.041	8.66	0.06	0.68	1.69	0.32	11.8	4.69	58	24.8	124	302	61.8	9370	B-LOD	14.9	0.97	2.36	174	553	183
AOOJA04_38	53	2.01	B-LOD	56.1	393000	0.476	B-LOD	1.95	B-LOD	B-LOD	0.17	0.029	0.39	0.209	3.34	1.61	9.65	37.1	9.47	10610	B-LOD	5.25	0.329	0.345	28.5	211	69.3
AORE_05_0	251	9.4	B-LOD	1382	492000	0.75	B-LOD	6.84	0.08	1.84	5.3	0.85	29.3	10.8	124	55.8	225	539	94.4	9280	B-LOD	7.48	0.378	0.82	76.3	307	100.1
AORE_05_1	482	15.3	B-LOD	3110	494000	1.4	0.018	11.56	0.25	4.84	11.1	1.55	63.6	24.4	275	128.3	508	1205	200.5	8560	B-LOD	19.7	0.9	3.12	261	784	264
AORE_05_2	431	7.8	B-LOD	1353	492000	1.3	B-LOD	12.6	0.05	1.39	4.13	0.544	22.2	8.96	106.4	53.7	229	626	113.1	10260	B-LOD	23.9	0.98	2.62	223	912	315

Anexo C, continuación

Sample/ Grain	P31 (ppm)	Ti49 (ppm)	Fe57 (ppm)	Y89 (ppm)	Zr90 (ppm)	Nb93 (ppm)	La139 (ppm)	Ce140 (ppm)	Pr141 (ppm)	Nd146 (ppm)	Sm147 (ppm)	Eu153 (ppm)	Gd157 (ppm)	Tb159 (ppm)	Dy163 (ppm)	Ho165 (ppm)	Er166 (ppm)	Yb172 (ppm)	Lu175 (ppm)	Hf178 (ppm)	Pb204 (ppm)	Pb206 (ppm)	Pb207 (ppm)	Pb208 (ppm)	Th232 (ppm)	U235 (ppm)	U238 (ppm)
AORE_05_3	477	11.1	B-LOD	2850	496000	1.65	0.042	13.09	0.17	4.52	9.2	1.38	50.9	19.7	244	116.6	464	1149	197.2	8800	B-LOD	25.8	1.09	3.73	326	1002	344
AORE_05_4	324	9.4	B-LOD	1348	508000	1	B-LOD	7.15	0.04	1.29	3.97	0.52	23.9	9.18	108.3	52.7	218	548	103.6	10010	3.4	10.66	0.48	1.09	89.8	415	138.4
AORE_05_5	475	10.6	B-LOD	3670	478000	1.78	0.047	11.81	0.30	5.03	9.85	1.24	52.6	21.4	270	142.2	599	1395	254	8920	1.6	26.2	1.14	3.11	268	1027	347
AORE_05_6	385	9.1	B-LOD	1931	461000	1.12	B-LOD	10.52	0.13	2.29	6.08	0.87	32.6	12.82	159.7	73.8	302	709	124.7	9820	2.5	17.87	0.729	2.31	193.9	715	237.7
AORE_05_7	327	6.8	B-LOD	2175	459000	0.91	0.0022	10.01	0.16	2.94	8.3	1	43.6	15.36	182.1	82.8	339	754	132.6	9260	B-LOD	15.53	0.619	1.98	171.9	602	205.6
AORE_05_8	381	9.4	B-LOD	2610	450000	1.33	B-LOD	12.48	0.23	4.23	9.07	1.2	47.9	17.29	215	96.6	412	892	159.2	9420	B-LOD	21.8	0.911	3.14	262	868	288
AORE_05_9	498	9.4	B-LOD	2220	449000	1.65	0.033	15.04	0.16	2.4	7.01	0.9	36	15.02	182.5	82.6	359	820	134.1	9350	B-LOD	26.6	1.31	3.82	332	1081	348
AORE_05_10	324	9.9	B-LOD	2010	410000	0.77	0.0043	9.01	0.05	1.99	5.62	0.75	38.3	13.04	165	69.9	309	602	108.4	9310	B-LOD	13.69	0.81	1.78	153.4	518	172
AORE_05_11	381	9	B-LOD	1205	434000	1.13	B-LOD	9.91	0.01	0.92	2.63	0.36	19.3	7.33	94.2	42.3	196.2	425	77.3	10580	B-LOD	13.57	0.63	1.38	123.6	540	173.3
AORE_05_12	352	9.2	B-LOD	1839	423000	0.9	B-LOD	7.69	0.16	2.92	7	1.11	33.8	12.2	150.8	65.2	293	604	103	8850	B-LOD	12.84	0.711	1.51	128.7	504	166.7
AORE_05_15	511	10.7	B-LOD	1466	401000	1.1	B-LOD	11.68	0.06	1.38	4.11	0.66	24	9.72	124	48.9	242	516	89.8	8760	B-LOD	18.73	1.13	3.3	284	778	253
AORE_05_16	328	4.7	B-LOD	1098	394000	1.15	B-LOD	12.17	0.04	0.96	2.43	0.222	17	6.87	92	37.7	183.7	421	71.9	11330	B-LOD	17.18	0.881	1.7	140	710	231
AORE_05_17	427	10	B-LOD	1851	381000	1.04	0.013	9.96	0.15	2.63	5.93	0.75	32.2	12.94	153.2	64.3	300	627	103.3	8200	B-LOD	15.33	0.88	2.14	179.8	685	217
AORE_05_19	362	9.1	B-LOD	2260	400000	1.08	0.026	9.91	0.16	3.49	6.91	0.95	42.2	15.69	193	78.1	379	738	125.8	9670	B-LOD	18.9	0.94	2.52	213	797	262
AORE_05_20	305	7.1	B-LOD	1838	379000	0.75	B-LOD	7.69	0.18	2.5	5.87	0.84	35.9	14	164.6	66.4	296	558	99.3	8980	0.3	10.98	0.49	1.39	128.8	447	149.1
AORE_05_21	348	6.6	B-LOD	1830	379000	0.9	B-LOD	9.31	0.17	3.15	6.35	0.86	36.1	13.32	164.7	66.8	298	605	101.5	9050	1.4	13.59	0.71	1.71	151.1	551	181.8
AORE_05_22	465	7.7	B-LOD	2790	386000	1.54	0.0036	14.18	0.24	4.09	9	1.09	50.9	19.2	243	100.4	470	914	153.5	8750	B-LOD	28.2	1.54	4.53	388	1209	393
AORE_05_23	333	9.3	B-LOD	1760	375000	0.75	B-LOD	7.04	0.12	2.53	5.89	0.95	36.5	13.37	163	63.4	281	550	91.4	8540	B-LOD	8.89	0.51	1.19	107.7	383	126.4
AORE_05_24	309	10.8	15	1866	394000	0.82	0.023	7.61	0.17	2.77	5.75	0.98	35.7	13.85	166.5	68.2	303	581	103.1	8830	B-LOD	12.7	0.751	1.52	129.8	497	171
AORE_05_25	432	12.3	B-LOD	2382	404000	0.99	B-LOD	6.95	0.15	3.41	6.62	1.04	43	16.96	207.5	83.4	388	709	125.3	8400	B-LOD	13.17	0.79	1.91	160.5	531	179.5
AORE_05_26	292	5.6	B-LOD	943	345000	0.85	B-LOD	8.26	0.03	0.98	2.08	0.332	16.3	6.14	77.2	33.8	154	345	59.4	8420	B-LOD	11.7	0.65	1.26	105.4	478	162
AORE_02_0	261	7.1	47	1221	386000	0.78	0.188	9.89	0.09	0.93	2.63	0.35	19.4	9.2	100.9	41.3	188	383	83.4	10190	B-LOD	9.62	0.6	1.23	93.9	398	116.9
AORE_02_1	219	7.6	B-LOD	1080	365000	0.66	B-LOD	6.45	0.19	2.05	3.7	0.59	22.8	9.2	97	38.8	162	367	69.6	7350	B-LOD	7.6	0.39	0.83	71.2	318	102
AORE_02_3	247	6.2	B-LOD	1375	422000	0.7	B-LOD	8.74	0.09	1.11	3.71	0.51	26.3	11.46	118.3	48.4	214.4	417	99.7	10500	1.4	8.07	0.424	1.021	89.1	352	106.3
AORE_02_4	419	5.55	B-LOD	2238	404000	0.97	B-LOD	18.28	0.16	2.41	6.77	0.79	41.5	19.09	198.6	79.6	360	761	167.4	11660	B-LOD	27.9	1.5	3.37	290	1225	356
AORE_02_5	356	7.3	B-LOD	1870	393000	0.83	0.019	11.12	0.21	2.23	6.1	0.82	36.1	15.85	166.7	65.5	292	584	129	8980	B-LOD	12.06	0.64	1.63	136	550	157.1
AORE_02_6	404	8	B-LOD	1930	401000	0.87	0.095	10.65	0.16	2.89	6.28	0.78	35.6	15.21	164.4	66.1	300	600	136.3	9160	B-LOD	12.73	0.661	1.67	145	587	166.8

Anexo C, continuación

Sample/ Grain	P31 (ppm)	Ti49 (ppm)	Fe57 (ppm)	Y89 (ppm)	Zr90 (ppm)	Nb93 (ppm)	La139 (ppm)	Ce140 (ppm)	Pr141 (ppm)	Nd146 (ppm)	Sm147 (ppm)	Eu153 (ppm)	Gd157 (ppm)	Tb159 (ppm)	Dy163 (ppm)	Ho165 (ppm)	Er166 (ppm)	Yb172 (ppm)	Lu175 (ppm)	Hf178 (ppm)	Pb204 (ppm)	Pb206 (ppm)	Pb207 (ppm)	Pb208 (ppm)	Th232 (ppm)	U235 (ppm)	U238 (ppm)
AORE_02_7	257	12	23	677	397000	0.88	0.047	8.51	0.05	0.66	1.61	0.22	10.7	5.64	58.7	23.6	107.3	267	54.7	8870	B-LOD	6.68	0.312	0.69	50.6	339	90.7
AORE_02_8	353	9.8	B-LOD	2145	405000	0.97	B-LOD	11.05	0.19	2.82	6.48	0.944	39.6	17.29	186.8	73.6	328.3	643	142.2	9220	B-LOD	12.82	0.701	1.83	150.5	581	167.8
AORE_02_9	356	4.1	B-LOD	2030	382000	1.01	B-LOD	16.8	0.14	2.85	6.99	0.69	39.1	17.3	179	72.4	334	711	148	10640	B-LOD	25.5	1.49	3.2	267	1240	341
AORE_02_10	420	7.7	B-LOD	2053	416600	1.1	B-LOD	10.52	0.16	3	6.47	0.85	37.6	15.42	178.3	70	324.7	632	138.6	10330	B-LOD	15.77	0.83	1.91	173.4	689	202.9
AORE_02_13	416	7.7	B-LOD	1852	401000	0.98	0.005	11.12	0.14	2.99	5.66	0.77	35.5	13.52	159.8	63.5	286	614	114.5	10020	B-LOD	14.3	0.78	1.82	151.6	702	197
AORE_02_14	328	9.1	B-LOD	1870	393000	0.91	0.029	8.55	0.18	2.64	5.99	0.91	39.6	14.4	167	65.4	292	589	111	8700	B-LOD	11.3	0.62	1.52	128	493	145
AORE_02_15	278	4.6	B-LOD	970	411000	0.65	B-LOD	4.71	B-LOD	0.36	1.93	0.32	17.3	6.49	82.4	33.7	151	305	58.5	10690	B-LOD	7.02	0.39	0.82	57.3	260	81.5
AORE_02_16	222	4.6	B-LOD	508	409000	0.83	B-LOD	4	B-LOD	0.26	1.13	0.146	7.3	3.12	41.3	17.5	82.9	198	35.1	10750	B-LOD	4.25	0.285	0.351	27.7	167	58
AORE_02_17	460	13.2	69	2624	403000	1.42	0.074	7.6	0.25	3.52	8.95	1.29	51.9	18.23	233.8	92.4	403	764	130.3	8190	B-LOD	13.15	0.91	2.28	175.5	491	173.9
AORE_02_19	443	8.7	34	2530	397000	1.16	0.138	10.9	0.22	3.47	8.4	0.82	45.7	16.1	214	85.9	392	756	134	9450	B-LOD	20.7	1.25	3.19	246	743	259
AORE_02_20	385	6.9	B-LOD	1768	406000	0.84	B-LOD	8.4	0.10	2.71	6.28	0.64	34.8	11.83	155.5	61.5	279	551	94.3	10380	B-LOD	14.64	0.77	B-LOD	146.1	517	181
AORE_02_21	226	8	B-LOD	1028	415000	0.67	B-LOD	5.35	0.03	1.15	2.89	0.42	19.4	6.75	89.1	35	161	333	55.4	9730	B-LOD	5.88	0.394	B-LOD	54.2	213	76.8
AORE_02_22	425	10.3	B-LOD	2270	405000	1.11	0.022	8.14	0.25	3.85	7.2	1.37	44	15.7	206	80.9	351	739	107	8400	B-LOD	13	0.76	1.81	151	489	174
AORE_02_23	283	6.5	B-LOD	1418	377000	0.71	B-LOD	7.29	0.06	1.52	4.42	0.461	24.8	9.22	123.7	48.2	217	461	72	9370	B-LOD	11.08	0.66	1.45	115.6	432	150.1
AORE_02_24	617	10.8	B-LOD	2510	417000	1.71	B-LOD	16.4	0.20	2.74	6.6	0.98	43.8	16.27	214.9	86.1	395	816	134.6	9050	B-LOD	23.4	1.31	3.7	316	895	310
AORE_04_0	609	11.5	98	1507	450300	1.63	1.92	13.14	0.81	4.87	4.31	0.96	29.1	10.03	124.2	50.7	234.6	477	95.3	10810	B-LOD	18.2	1.08	2.01	173	728	237
AORE_04_1	456	10.7	28	1093	407000	1.17	0.196	7.52	0.08	1.44	3.3	0.68	17.3	7.09	92.8	37.4	171	402	71.5	8080	B-LOD	10.76	0.68	1.05	86.7	447	144
AORE_04_2	501	14.7	45	1772	406000	1.26	0.11	7.29	0.18	2.2	4.98	1.27	35	12.59	153.1	59.9	279	525	105.1	7950	3.5	12.96	0.75	1.82	158.6	498	161
AORE_04_3	670	14.5	B-LOD	1737	455000	2.01	0.81	11.54	0.46	4	4.7	1.23	32.5	11.5	153.3	57.8	266	510	107.8	9370	B-LOD	14.77	0.76	1.89	179.3	624	193.2
AORE_04_4	335	12.5	B-LOD	1496	407000	1.32	0.088	7.79	0.13	1.24	3.82	0.7	25.3	10.14	124.4	50.3	226.4	460	95	8320	1.2	13.7	0.81	1.5	128	573	175
AORE_04_5	599	8.9	300	2780	415000	1.82	1	14.5	0.66	6.4	10.7	1.78	64.3	22.5	258	98.6	446	823	149.5	8520	2.5	20.1	1.71	3.23	239	830	270
AORE_04_7	471	16.1	29	1708	411000	1.67	0.018	8.56	0.10	2.04	4.44	1.14	31.5	11.43	146.9	59.8	271	536	102.8	8080	1.6	15.32	0.89	2.25	172	597	179.5
AORE_04_8	440	13.5	B-LOD	1955	415000	1.55	0.02	7.24	0.17	2.23	5.9	1.2	37.5	13.85	178	67.4	299	599	115.3	8070	B-LOD	11.02	0.68	1.25	107.5	461	138.8
AORE_04_9	232	B-LOD	B-LOD	592	409000	1.42	B-LOD	5.7	B-LOD	0.64	1.02	0.32	6.5	3.16	43.3	19.1	92.4	241	49.9	12050	B-LOD	11.84	0.49	0.89	76.7	468	147.9
AORE_04_10	399	10.2	29	1850	402000	2.04	0.039	11.56	0.15	2.45	6	1.11	39.6	13.8	171	66.3	288	568	97.4	7970	2.2	16.3	0.95	2.72	189	592	202.2
AORE_04_11	513	7.6	21	1626	398000	2.32	0.36	12.36	0.21	2.47	3.57	1.02	27.3	10.77	138.9	55.9	254	520	93.1	8270	3	24.1	1.23	3.61	305	902	315
AORE_04_12	636	11.5	B-LOD	2590	401000	1.44	0.6	12.49	0.38	4.97	10.1	1.96	60.6	20.6	249.7	92.8	405	755	132.9	7650	2.3	14.24	0.88	1.95	163.2	512	177.1

Anexo C, continuación

Sample/ Grain	P31 (ppm)	Ti49 (ppm)	Fe57 (ppm)	Y89 (ppm)	Zr90 (ppm)	Nb93 (ppm)	La139 (ppm)	Ce140 (ppm)	Pr141 (ppm)	Nd146 (ppm)	Sm147 (ppm)	Eu153 (ppm)	Gd157 (ppm)	Tb159 (ppm)	Dy163 (ppm)	Ho165 (ppm)	Er166 (ppm)	Yb172 (ppm)	Lu175 (ppm)	Hf178 (ppm)	Pb204 (ppm)	Pb206 (ppm)	Pb207 (ppm)	Pb208 (ppm)	Th232 (ppm)	U235 (ppm)	U238 (ppm)
AORE_04_14	514	14	B-LOD	1677	404000	2	B-LOD	7.91	0.07	1.47	4.19	1.01	27.5	10.48	133.7	56.8	268	585	105.9	7400	B-LOD	11.63	0.59	1.08	82.1	405	146.2
AORE_04_15	459	13.8	B-LOD	1673	400000	1.7	0.061	7.52	0.16	1.77	3.58	0.96	26.9	9.88	130.8	56.2	266.5	535	107	7860	B-LOD	11.67	0.66	1.13	84.7	370	138.1
AORE_04_17	309	3.6	B-LOD	795	404500	2.11	0.029	11.5	B-LOD	0.97	2.26	0.38	10.5	4.21	56.5	26	128.7	339	73.2	9330	B-LOD	22.6	1.26	2.38	181.6	694	279
AORE_04_18	510	10.2	43	1280	403000	0.97	0.28	6.6	0.15	1	3.37	0.48	23.1	7.9	106	40.6	194	398	71.6	8400	B-LOD	11	0.73	1.14	96	351	141
AORE_04_19	467	13.2	33	1680	428400	1.32	B-LOD	6.77	0.13	1.86	4.57	0.9	30.1	10.33	136	55.1	259.1	516	98.8	8630	2.5	11.47	0.68	1.33	105.2	343	137.7
AORE_04_21	520	6.7	B-LOD	2490	392000	2.04	0.6	13.2	0.41	4.2	8.1	1.39	54.6	19.1	242	92.1	406	813	130	8160	B-LOD	22.5	1.41	2.82	233	731	303
AOAL_03_0	450	12.5	B-LOD	1390	547000	1.38	B-LOD	12.1	0.10	2.75	7.1	1.13	48.5	14.2	200	76.4	383	679	117	11990	2.1	13.5	0.84	2.04	199	537	242
AOAL_03_1	647	4.7	190	2220	496000	2.66	0.113	31	0.19	3.7	10.8	0.73	60	18.9	302	115	659	1200	192	11900	B-LOD	88	5.71	5.57	515	3530	1630
AOAL_03_3	394	10.2	B-LOD	2379	563000	1.19	0.009	12.99	0.35	7.66	15.9	2.17	91.7	25.9	360	128.8	709	1130	181.9	12330	1.39	16.62	1.15	2.53	250	633	300
AOAL_03_5	649	10.5	35	4040	528000	2.16	0.041	20.5	0.47	11.3	23.2	3.5	140	42.9	536	197	971	1592	252	10960	B-LOD	26.2	1.62	4.85	450	980	418
AOAL_03_6	560	7	B-LOD	3260	460000	2.24	B-LOD	28.6	0.32	7.9	16.5	2.22	104.5	32.9	426	156	772	1370	200	9580	B-LOD	38.4	2	5.56	533	1470	626
AOAL_03_8	309	12.4	B-LOD	1790	471000	1.03	B-LOD	9.5	0.18	4.5	10.7	1.5	56.3	16.7	212	74.8	353	623	100	9410	B-LOD	9.57	0.435	1.25	113.3	352	137.6
AOAL_03_9	332	5.3	27	1540	457000	1.24	B-LOD	13.54	0.17	2.74	5.38	0.73	38.5	12.9	163	62.1	304	559	95.6	10210	B-LOD	14.4	0.81	1.74	134.9	508	195
AOAL_03_10	679	15.6	B-LOD	4720	482000	2.22	0.061	18.5	0.45	7.8	19.6	2.57	116.8	40.2	476	177.5	772	1313	223.3	9750	B-LOD	25.2	1.2	4.57	382	925	340
AOAL_03_11	316	14.4	B-LOD	2077	428000	1.02	B-LOD	7.1	0.18	3.86	8.42	1.4	49.1	17.01	189.3	71	313	535	94.2	8150	0.99	8.24	0.5	1.23	101.5	305	109.1
AOAL_03_12	630	10.6	34	4290	383000	2.29	0.053	23.1	0.33	7.16	15.2	1.74	90.9	32.6	388	145	621	1055	182	7400	B-LOD	27.7	1.73	4.77	413	1055	358
AOAL_03_15	418	14.2	B-LOD	1140	379000	1.21	0.014	7.13	0.05	1.19	3.55	0.45	19.3	7.01	96.8	37.3	168	343	62	7280	B-LOD	10.91	0.7	1.08	93.9	431	141
AOAL_03_16	408	9.6	B-LOD	2420	367000	1.42	B-LOD	9.14	0.29	3.89	8.6	1.34	50	17.4	222	84.1	345	660	107	7260	B-LOD	14.3	0.79	2.09	175	600	190
AOAL_03_17	420	9.9	B-LOD	1760	383000	1.08	0.053	7.4	0.19	2.05	6.4	0.99	39.5	13.2	165	61.9	274	526	88	7950	B-LOD	10.8	0.71	1.45	112	463	143
AOAL_03_18	315	5.1	B-LOD	920	367000	1.89	B-LOD	11.9	0.01	0.54	1.58	0.172	14	4.97	70.1	29.7	147	363	64.8	9150	B-LOD	53.1	2.91	1.97	152	2160	677
AOAL_03_19	309	11.4	116	1410	399000	0.98	B-LOD	6.92	0.11	1.56	4.75	0.78	29.7	9.75	127	47.4	209	405	70.8	9030	B-LOD	17.7	0.88	1.06	83.7	730	236
AOAL_03_21	455	11.6	46	3050	422000	1.43	0.044	9.93	0.27	4.53	10.4	1.51	70	22.7	270	101.5	436	761	133.1	7780	B-LOD	14.6	0.83	2.15	192	576	187
AOAL_03_22	341	4.83	B-LOD	1530	371000	1.45	0.042	14.64	0.09	1.28	4.39	0.441	28.4	9.87	136	50.6	236	476	76.8	7790	B-LOD	19.2	1.22	2.05	154	747	242
AOAL_03_24	343	4.9	130	1250	381000	1.6	0.023	10	0.10	1.21	3.78	0.51	24.3	8.7	118.9	44.5	202	414	67	7950	B-LOD	13.3	0.77	1.52	106	546	175
AOAL_03_26	557	7.5	55	2310	383000	2.66	0.028	27.2	0.09	2.34	5.79	0.69	44.6	16	199	77.1	355	637	114.3	7420	B-LOD	37.9	2.21	5.82	481	1482	482
AOAL_03_27	342	6.6	43	1334	411000	1.65	0.033	9.13	0.08	1.26	3.39	0.51	22.6	7.87	105.6	42.7	207	423	79.9	8230	B-LOD	42.1	2.38	1.53	123.2	1655	537
AOAL_04_0	278	14.1	17	723	366000	1.03	0.022	4.71	0.05	0.98	2.61	0.383	13.4	4.8	55.2	21.9	96.8	203	37.8	8350	B-LOD	4.58	0.276	0.637	48.7	195	60.8

Anexo C, continuación

Sample/ Grain	P31 (ppm)	Ti49 (ppm)	Fe57 (ppm)	Y89 (ppm)	Zr90 (ppm)	Nb93 (ppm)	La139 (ppm)	Ce140 (ppm)	Pr141 (ppm)	Nd146 (ppm)	Sm147 (ppm)	Eu153 (ppm)	Gd157 (ppm)	Tb159 (ppm)	Dy163 (ppm)	Ho165 (ppm)	Er166 (ppm)	Yb172 (ppm)	Lu175 (ppm)	Hf178 (ppm)	Pb204 (ppm)	Pb206 (ppm)	Pb207 (ppm)	Pb208 (ppm)	Th232 (ppm)	U235 (ppm)	U238 (ppm)
AOAL_04_1	282	14.1	B-LOD	1193	379000	0.89	B-LOD	4.56	0.10	1.78	3.98	0.68	24	8.03	93.5	36	154.2	290	55.6	7380	B-LOD	4.92	0.276	0.655	53.3	196	64.5
AOAL_04_3	343	13.3	57	1289	348000	1.37	0.257	6.46	0.17	1.85	4.03	0.6	21.5	7.75	93.5	37.8	166.5	349	61.7	7100	1.8	8.17	0.49	1.012	81.8	311	104.1
AOAL_04_5	417	13.6	B-LOD	1082	397000	1.54	0.01	6.98	0.06	0.99	2.71	0.47	15.8	6.54	80	34	151.9	355	63.6	8400	B-LOD	9.83	0.58	1.09	82.7	366	124.9
AOAL_04_7	330	14.9	B-LOD	1447	356000	0.92	0.064	6.07	0.13	2.24	4.62	0.71	27	9.15	109.1	42	181	352	65.7	7310	2	6.78	0.31	1.06	91.5	260	87
AOAL_04_8	311	11.7	B-LOD	1409	371000	1.37	0.086	8.13	0.11	1.85	3.91	0.78	27.6	9.5	107.2	42.4	185.6	368	69	9270	B-LOD	11.38	0.594	1.74	146.3	441	146.1
AOAL_04_9	416	10.4	B-LOD	1138	322000	1.15	B-LOD	8.82	0.04	1.22	3.36	0.39	18.7	6.51	77.9	33.1	145	306	56.2	6300	1.3	11.2	0.63	1.64	130	448	146
AOAL_04_12	536	13.9	B-LOD	2610	431000	1.68	0.022	9.77	0.25	3.82	8.9	1.31	54.7	19.3	222	88.2	370	714	127.3	8880	B-LOD	14.28	0.75	2.01	177.5	537	180.3
AOAL_04_13	409	16.4	B-LOD	2078	396000	1.26	0.021	8.24	0.17	3.13	6.39	1.06	40.9	14.17	172.3	64	271	531	93.1	7300	B-LOD	10.47	0.557	1.61	130.7	410	135.2
AOAL_04_14	242	14.5	B-LOD	1237	345000	0.74	0.011	4.57	0.09	1.52	4.45	0.7	24.5	8.32	102.9	38.6	165.7	315	57.2	6520	B-LOD	4.93	0.241	0.705	56.9	190	62.4
AOAL_04_15	557	10.5	55	3000	466000	3.12	B-LOD	22.08	0.26	3.36	9.46	2.04	62.5	22.77	309	114.1	507	886	167.7	9790	B-LOD	29.2	1.61	5.24	463	1104	361.2
AOAL_04_18	449	17.9	B-LOD	1252	461000	1.31	0.14	8.25	0.15	1.54	3.89	0.66	23.4	8.55	116.8	46	208.8	435	81.3	9810	B-LOD	13.02	0.57	1.57	144.9	471	154.5
AOAL_04_19	271	14.3	B-LOD	650	412000	0.78	B-LOD	5.28	0.04	0.44	1.56	0.346	12.1	4.21	58.7	22.9	105.9	214	42	8400	B-LOD	5.97	0.252	0.555	45.5	209	70.5
AOAL_04_20	290	13	B-LOD	677	400000	0.97	B-LOD	6.41	0.04	0.9	1.98	0.36	12.2	4.65	62.6	24.3	110.8	257	45.2	9300	B-LOD	10.24	0.56	1	68.1	417	123.9
AOAL_04_22	447	9.4	B-LOD	1816	407000	2.28	0.006	14.16	0.10	1.39	4.21	1.12	31.3	11.98	168.1	64	288	586	102.9	8410	B-LOD	22.1	1.21	3.76	304	835	268
AOAL_04_23	1077	6.9	34	4270	395000	4.23	0.18	29.6	0.18	3.61	10	2.34	83	30.9	400	153	669	1192	207	7590	B-LOD	39.3	2.16	5.87	490	1500	473
AOAL_04_26	440	10.6	B-LOD	1149	448000	1.39	B-LOD	7.94	0.06	1.06	3.38	0.46	21.4	7.45	101.3	37.8	180	361	70.7	10960	B-LOD	12.2	0.57	1.48	113	494	142.8
AOAL_04_27	353	10.3	B-LOD	2570	373000	1.54	B-LOD	9.42	0.18	4.02	6.89	1.65	57.1	19.1	237	88.4	386	709	127.1	7220	0.9	14.06	0.651	2.2	183	580	178
AOAL_04_28	320	10.6	60	1104	399000	1.21	0.068	7.65	0.07	0.78	2.39	0.58	18.8	6.45	89.1	36.2	171.7	348	66.9	7920	B-LOD	9.8	0.48	0.89	76.9	370	119.5
AOAL_04_29	265	10.2	28	939	368000	1.37	0.198	9	0.12	1.58	2.56	0.517	16.4	5.97	77.7	30.72	135.7	281	49.7	9670	B-LOD	11.31	0.74	1.85	139.8	422	135.4
AOAL_04_30	341	15	B-LOD	1374	415000	0.99	0.035	7.22	0.17	2.48	5.7	0.85	29.2	10.71	124.4	47	205	403	72.4	8560	B-LOD	8.51	0.51	1.04	83.7	313	108.5
AOAL_04_31	328	11	B-LOD	824	423000	1.04	B-LOD	5.45	0.02	0.76	1.97	0.46	14.2	5.27	68.3	27.3	126.3	277	50.4	8530	B-LOD	6.73	B-LOD	0.687	53.9	276	92
AOAL_04_33	359	11.1	B-LOD	1475	395500	1.6	B-LOD	7.39	0.06	0.94	3.78	0.66	24	8.86	118.2	47.1	223	466	85.2	7350	B-LOD	11.11	0.667	1.3	105.2	422	148.8
AOAL_04_34	414	15.5	40	2203	419000	1.22	0.159	9.37	0.28	3.92	9.6	1.48	52	16.62	204.3	75	320	639	106.2	8400	B-LOD	12.54	0.69	1.9	145.1	474	162.5
AOAL_04_35	422	13.3	B-LOD	1601	412000	1.33	0.053	7.74	0.12	2.16	4.21	1.03	28.5	10.45	132.6	52.5	245	510	91	7960	B-LOD	11.99	0.724	1.48	113	462	155.5
AOAL_04_36	545	8.9	283	2140	415500	3.12	1.56	23.3	0.61	4.7	7.8	1.2	42.9	14.2	172	66.9	300	569	111.1	12900	B-LOD	24.6	1.76	4.18	339	970	312
AOLH_09_1	338	8.9	B-LOD	1480	414000	2.02	B-LOD	13.7	0.06	1.15	3.2	0.55	23.6	9.9	125	52	240	533	93	10300	B-LOD	17.9	1.01	3.02	210	667	233
AOLH_09_2	388	8.2	B-LOD	1663	432000	1.43	0.007	20.7	0.13	2.39	5.26	0.87	31.9	11.96	145.7	61.5	281	598	98.4	10780	B-LOD	24	1.51	3.43	254	979	316

Anexo C, continuación

Sample/ Grain	P31 (ppm)	Ti49 (ppm)	Fe57 (ppm)	Y89 (ppm)	Zr90 (ppm)	Nb93 (ppm)	La139 (ppm)	Ce140 (ppm)	Pr141 (ppm)	Nd146 (ppm)	Sm147 (ppm)	Eu153 (ppm)	Gd157 (ppm)	Tb159 (ppm)	Dy163 (ppm)	Ho165 (ppm)	Er166 (ppm)	Yb172 (ppm)	Lu175 (ppm)	Hf178 (ppm)	Pb204 (ppm)	Pb206 (ppm)	Pb207 (ppm)	Pb208 (ppm)	Th232 (ppm)	U235 (ppm)	U238 (ppm)
AOLH_09_4	602	B-LOD	B-LOD	4660	427000	2.45	B-LOD	26.4	0.44	8.09	17.1	3.77	115.5	42.5	494	189.6	798	1409	249	8870	B-LOD	34.6	1.91	5.62	481	1365	454
AOLH_09_5	659	16	138	3900	425000	3.24	0.25	49.7	0.38	7.5	12.5	3.44	88.5	30.5	364	146	620	1200	210	8730	4.3	27.5	1.82	6.9	600	1120	369
AOLH_09_6	214	5.4	55	618	413000	1.52	0.14	13.2	0.06	0.4	1.22	0.239	8.5	3.57	46.1	20.7	105	263	49.2	9640	B-LOD	14.2	0.83	1.64	123.1	558	193
AOLH_09_7	510	9.6	B-LOD	3680	432000	1.73	B-LOD	21.1	0.37	7.38	15.8	3.11	96.6	33.2	366	144.7	598	1029	183	8530	B-LOD	26.5	1.59	4.12	346	1090	349
AOLH_09_9	311	9.2	34	1650	417000	1.17	0.041	15.8	0.12	2.78	5.89	1.42	36.1	13.16	147	58.3	248	515	87.8	7700	B-LOD	10.4	0.67	1.83	143.7	394	137.1
AOLH_09_10	492	5.4	B-LOD	4070	406000	2.02	0.022	20.83	0.36	6.24	15.4	3.19	95.4	34.6	390	152	621	1135	193.9	7980	B-LOD	25.8	1.39	4.15	347	1039	340
AOLH_09_12	695	8.5	B-LOD	4110	384000	2.53	0.053	45.4	0.31	4.98	13.7	3.45	89.8	31.6	372	145	617	1171	198	7790	B-LOD	25.1	1.44	5.82	487	1008	334
AOLH_09_13	577	7.5	B-LOD	3910	380000	1.9	0.02	19.8	0.35	6.75	17.2	3.69	96	33.4	377	142.3	579	1125	185.4	7120	1.6	22.2	1.21	3.49	295	918	292
AOLH_09_14	669	7.3	B-LOD	4550	400000	3.67	0.043	34.9	0.42	6.54	18.5	3.57	111.2	38.9	463	176	702	1308	221	8080	B-LOD	37.4	2.08	6.64	557	1484	489
AOLH_09_15	473	4.2	360	1260	397000	2.97	0.049	11.41	0.04	0.67	1.16	0.23	10.6	5.02	78.5	36.6	194	480	90.3	9170	B-LOD	34.7	2.12	7.4	600	1340	443
AOLH_09_16	578	20.4	66	2380	405000	3.96	0.28	52.2	0.22	2.79	6.8	1.14	44.5	15.67	205	80.9	374	833	142	9290	B-LOD	29	1.71	7.27	575	1159	383
AOLH_09_17	817	15.3	B-LOD	5630	394000	4.02	0.056	38	0.47	8.72	26	5.34	155.6	47.3	571	204.7	883	1753	280	7800	B-LOD	42.8	2.35	9.15	772	1608	546
AOLH_09_18	286	4.2	B-LOD	826	383000	1.56	B-LOD	17.2	0.06	1.03	2.82	0.48	16.8	5.39	69.3	27.9	135	344	56.3	10090	B-LOD	23.5	1.2	1.98	164	928	303
AOLH_09_19	720	6.4	39	5660	417000	3	0.017	31.6	0.45	10.3	23.5	4.64	156.3	48.7	578	209.4	907	1753	289	9070	B-LOD	36.6	2.15	7.48	580	1488	478
AOLH_09_20	459	11.1	B-LOD	2220	404000	1.33	B-LOD	19.4	0.14	2.73	7.4	1.62	45.8	16.3	206	79	361	774	132.3	8750	B-LOD	13.4	0.68	2.81	216	480	171.9
AOLH_09_21	568	6.7	B-LOD	3480	405000	2.78	0.015	32.7	0.15	4.13	9.8	2.55	75.5	24.9	320	124	548	1150	197	9150	B-LOD	23.7	1.24	5.56	440	916	310
AOLH_09_23	262	5.1	77	948	402000	1.62	0.256	12.41	0.18	1.91	2.75	0.57	19.1	6.41	78.7	32.2	154.4	356	66.1	12480	B-LOD	15.18	1.01	2.72	189	558	193
AOLH_09_25	497	11.1	B-LOD	2680	417000	1.46	B-LOD	21.2	0.16	3.6	8.5	1.98	57.9	19.93	241.1	92.4	425	897	156.2	8120	B-LOD	15.37	0.88	3.46	258	570	196
AOLH_09_26	464	9.1	106	3350	445000	1.62	0.024	16.06	0.28	6.1	13.4	2.85	76.9	26.1	318	119.5	542	1032	190.4	10120	B-LOD	20.95	1.23	3.67	286	796	274
AOLH_09_27	262	6.3	B-LOD	1370	360000	1.23	0.0045	15.2	0.11	1.83	4.17	1.21	28.6	10.1	124	46.6	217	494	88	8130	B-LOD	13	0.68	2.17	179	471	168
RETA2_2	314	15.3	B-LOD	1338	527000	0.73	B-LOD	6	0.11	2.17	5.11	0.595	25.1	8.84	121	45.7	205.2	356	72.8	11540	B-LOD	6.06	0.265	0.615	59.6	240	79.6
RETA2_3	172	6.04	B-LOD	460	530000	0.72	B-LOD	5.27	B-LOD	0.22	0.63	0.063	4.81	1.97	33.8	14.83	74.8	153.8	34.1	15320	B-LOD	4.63	0.228	0.298	27.4	187	60.9
RETA2_4	280	10.3	B-LOD	780	557000	0.51	B-LOD	3.66	0.03	0.95	2.23	0.36	10.1	3.6	59.5	26.4	124.3	240	55.2	12400	B-LOD	3.26	0.184	0.222	24.04	131	40.5
RETA2_5	197	9.2	B-LOD	672	571000	0.77	0.014	4.61	0.01	0.41	1.29	0.283	9.34	3.55	54.7	23.41	108.5	217.2	49.6	13050	B-LOD	3.25	0.154	0.209	24.42	120	41.4
RETA2_6	451	13	B-LOD	1630	542000	1.29	B-LOD	14.32	0.11	1.57	4.81	0.4	23.9	9.23	133.8	54.8	253	498	101.1	12380	B-LOD	14.49	0.697	1.8	181.4	598	193
RETA2_7	467	10.7	B-LOD	1840	520000	2.16	B-LOD	16.2	0.06	1.62	4	0.79	25.2	9.85	151.1	61.1	286	659	110.7	11030	B-LOD	14.53	0.75	1.75	153	625	209
RETA2_12	264	8.6	B-LOD	1721	545000	0.74	B-LOD	8.58	0.07	1.91	5.66	1.27	39.5	13.99	156	59.4	268	562	95.1	11790	B-LOD	5.59	0.29	0.64	60.5	222	75.7

Anexo C, continuación

Sample/ Grain	P31 (ppm)	Ti49 (ppm)	Fe57 (ppm)	Y89 (ppm)	Zr90 (ppm)	Nb93 (ppm)	La139 (ppm)	Ce140 (ppm)	Pr141 (ppm)	Nd146 (ppm)	Sm147 (ppm)	Eu153 (ppm)	Gd157 (ppm)	Tb159 (ppm)	Dy163 (ppm)	Ho165 (ppm)	Er166 (ppm)	Yb172 (ppm)	Lu175 (ppm)	Hf178 (ppm)	Pb204 (ppm)	Pb206 (ppm)	Pb207 (ppm)	Pb208 (ppm)	Th232 (ppm)	U235 (ppm)	U238 (ppm)
RETA2_13	294	14.3	B-LOD	1102	532000	0.654	0.0021	5.77	0.10	1.73	4.11	0.623	25.5	9.02	97.8	37.8	167.1	372.7	61.7	11300	B-LOD	4.15	0.27	0.435	42	162	55.7
RETA2_14	470	11.8	31	1683	530000	1.59	0.067	8.11	0.03	1.06	2.96	0.78	26.2	11.13	137.5	57.8	273	625	113.9	11190	B-LOD	10.33	0.56	0.925	86.3	412	132.6
RETA2_15	346	10.2	B-LOD	1016	531000	0.81	B-LOD	5.17	0.05	0.58	2.06	0.76	18.2	7.23	83	35.1	172	414	83.8	11030	B-LOD	5.63	0.389	0.415	35.6	220	73
RETA2_16	331	9.4	B-LOD	921	529000	1.04	B-LOD	7.41	0.01	0.48	2.2	0.38	15.4	6.03	74.5	31.6	148.4	361	65.3	11610	B-LOD	5.55	0.403	0.376	40.5	243	75.6
RETA2_17	425	12.7	B-LOD	3078	529000	0.99	0.029	8.06	0.22	4.55	8.83	2.12	60	21.79	259.7	105.3	464	937	163	10190	B-LOD	11.27	0.599	1.48	137.5	470	152.5
RETA2_19	265	9	B-LOD	905	555000	0.77	B-LOD	5.3	0.04	1.1	2.69	0.6	17.1	5.96	76.1	31.2	149.3	335	66.1	11600	B-LOD	4.58	0.295	0.355	34.3	194	62.4
RETA2_20	420	15.6	B-LOD	1076	519000	0.75	0.0041	6.8	0.08	1.79	3.48	0.5	19.2	7.43	91.8	35.5	162.3	341	63.7	10290	B-LOD	5.72	0.308	0.639	54.9	240	78.8
RETA2_21	431	11.4	B-LOD	3160	508000	1.19	0.046	11.58	0.22	4.31	9.38	2.04	61.6	23.2	274	107.9	466	931	156.9	9640	B-LOD	11.02	0.625	1.58	146.3	466	151.5
RETA2_22	343	10.1	B-LOD	1296	510000	1.02	0.018	7.61	0.02	0.93	2.88	0.76	20.9	7.95	104.9	45.7	216.4	473	92.6	10180	B-LOD	8.86	0.492	0.899	74.1	338	116
RETA2_23	273	9.1	B-LOD	829	501000	0.82	0.007	6.66	0.03	0.44	1.72	0.253	11.4	5.21	65.6	27.3	126.3	294	56	12140	B-LOD	5.1	0.247	0.457	38.5	193	73
RETA2_24	356	11.7	B-LOD	2442	465000	0.95	0.004	8.84	0.19	3.56	7.6	1.86	47.4	16.31	215	83.1	361	766	126.3	8890	B-LOD	8.99	0.52	1	98.9	370	126
RETA2_25	491	9.7	B-LOD	2430	539000	2.2	0.065	16.22	0.18	2.79	5.82	1.48	44.8	15.76	214.1	83	378	791	150.4	10730	B-LOD	16.42	0.92	2.27	223.2	667	212.8
RETA2_27	296	8	B-LOD	1023	515000	1.08	B-LOD	7.6	0.02	0.75	2.28	0.4	15.81	6.08	84.2	34.9	165.3	382	70.5	11400	B-LOD	5.57	0.292	0.455	42.8	228	76.3
RETA2_28	304	14.6	B-LOD	1195	505000	0.7	B-LOD	6.46	0.13	2.16	4.56	0.83	25.4	8.4	106.4	40.2	177.7	381.9	62.6	10170	B-LOD	4.1	0.22	0.52	43.8	166	56.2
RETA2_29	466	11.2	B-LOD	2331	507000	1.01	B-LOD	8.96	0.16	3.28	6.72	1.02	44.1	14.77	199.8	79.3	359	741	129	10950	B-LOD	9.66	0.517	1.33	116.2	390	128.6
RETA2_31	265	8	B-LOD	773	500000	0.539	B-LOD	3.81	0.02	0.68	1.39	0.473	12.7	4.51	64	25.88	123.1	288.9	53.1	10070	B-LOD	3.49	0.173	0.261	23.32	131.1	45.7
RETA2_32	297	9.6	B-LOD	1661	508000	0.81	B-LOD	6.02	0.06	1.31	4.8	0.82	31.7	10.55	139.7	56.5	252	508	99.7	10170	B-LOD	6.75	0.31	0.72	64.7	257	83.6
RETA2_33	236	9.6	B-LOD	631	497000	0.57	B-LOD	4.47	0.01	0.59	1.64	0.259	10.9	3.9	52.6	21.5	101	250.4	43.9	10580	B-LOD	3.74	0.238	0.248	25.2	161	49
RETA2_34	427	10.3	35	1657	488000	1.43	0.0043	8.84	0.07	1.2	3.13	0.73	23.4	8.69	123.4	55.2	268.1	621	114.3	9800	B-LOD	11.32	0.68	1.08	95.5	425	147.3
AOIN_02_1	452	22.7	126	4040	442000	2.63	0.014	13.24	0.25	4.16	13	2.64	98.3	32.2	383	143.9	616	1146	197.1	9570	B-LOD	19.19	0.92	5.48	469	804	262.6
AOIN_02_2	159	22.4	B-LOD	1419	410600	0.93	B-LOD	4.88	0.08	1.79	4.62	0.86	28.7	9.71	118.9	47.4	213.2	459	84.4	9640	B-LOD	7.01	0.346	1.1	88.1	277	85.4
AOIN_02_3	427	19.4	B-LOD	3110	425000	1.82	0.048	10.22	0.22	3.71	9.6	1.6	66.3	23.5	279	104.4	471	868	159.7	9890	B-LOD	16.08	0.82	4.82	392	685	204.9
AOIN_02_4	330	18.1	B-LOD	2525	416000	1.34	B-LOD	10.16	0.11	3.64	7.31	0.9	45.6	17.01	207.1	82.3	379	767	135.2	10590	B-LOD	20.09	1.12	3.87	315	792	254.7
AOIN_02_5	373	24.5	820	4810	406000	4.99	0.046	19.4	0.21	5.16	19.6	3.29	121.5	39	444	162	723	1383	252	11170	B-LOD	32.3	1.96	15.61	1243	1338	404
AOIN_02_6	591	16.2	B-LOD	3930	421000	2.86	B-LOD	21.57	0.18	4.52	12.7	1.6	86.5	30	345	132.5	560	1088	191.8	11250	B-LOD	35.7	1.81	9.27	708	1416	437
AOIN_02_8	378	22.1	48	1848	429000	1.96	0.022	14.26	0.10	2.51	4.82	0.8	33.8	12.09	152.3	60.1	268	576	103.4	10330	B-LOD	19.9	1.2	6.65	598	847	266
AOIN_02_9	317	15.2	77	1995	431000	1.08	B-LOD	8.49	0.12	2.72	5.25	1	39	13.34	166.3	64.6	289	553	105.6	10730	B-LOD	13.1	1.26	4.18	293	470	157

Anexo C, continuación

Sample/ Grain	P31 (ppm)	Ti49 (ppm)	Fe57 (ppm)	Y89 (ppm)	Zr90 (ppm)	Nb93 (ppm)	La139 (ppm)	Ce140 (ppm)	Pr141 (ppm)	Nd146 (ppm)	Sm147 (ppm)	Eu153 (ppm)	Gd157 (ppm)	Tb159 (ppm)	Dy163 (ppm)	Ho165 (ppm)	Er166 (ppm)	Yb172 (ppm)	Lu175 (ppm)	Hf178 (ppm)	Pb204 (ppm)	Pb206 (ppm)	Pb207 (ppm)	Pb208 (ppm)	Th232 (ppm)	U235 (ppm)	U238 (ppm)
AOIN_02_10	376	25.8	B-LOD	1483	427000	2.49	0.0022	8.02	0.03	1.27	3.92	0.702	22.4	8.66	109.5	47.6	233.2	553	107.7	9800	B-LOD	12.82	0.768	1.88	149.6	516	168.7
AOIN_02_11	207	19.3	B-LOD	1435	431000	0.91	B-LOD	5.5	0.13	1.69	4.56	1.1	29.2	10.83	127	50.6	218	472	79.1	9930	B-LOD	6.73	0.374	1.41	113.2	261	84.4
AOIN_02_12	622	21.8	B-LOD	3540	429000	2.81	B-LOD	15.61	0.24	4.15	10.23	1.41	69.3	24.8	314	124.7	551	1077	186	10840	B-LOD	25.2	1.41	6.53	531	994	324
AOIN_02_13	178	19.8	B-LOD	1771	420000	1.16	B-LOD	6.26	0.11	2.63	7.06	1.04	36.2	12.53	153	58.6	255	542	90.4	9780	B-LOD	8.43	0.48	1.6	136.4	347	114.6
AOIN_02_14	526	22.2	B-LOD	3880	415000	3.1	0.115	17.5	0.29	5.19	13.2	2.41	89.7	31.6	368	137.9	577	1120	188.4	9180	B-LOD	24.6	1.31	9.88	773	978	308
AOIN_02_15	364	22.6	B-LOD	2238	391000	2.12	B-LOD	12.76	0.13	2.34	6.62	1.13	43.7	16.03	193.4	78.2	338	714	121.3	9420	B-LOD	16.41	0.919	4.43	353	682	213.5
AOIN_02_16	373	20.9	B-LOD	2799	427000	1.66	B-LOD	9.69	0.17	3	9.7	1.83	64.1	21.7	258	97.1	426	824	147	9600	B-LOD	13.61	0.68	3.44	287	538	174.5
AOIN_02_17	159	29.5	B-LOD	1376	406000	0.93	0.0036	4.31	0.13	2.48	4.54	0.73	26.2	9.46	114.6	44.8	198.2	418	75.6	8990	B-LOD	10.02	0.565	2.91	244	377	130.1
AOIN_02_18	415	17.7	124	1870	459100	0.94	B-LOD	8.88	0.12	1.9	5.2	0.67	35	12.83	154.3	61.4	272	511	96.7	12930	B-LOD	15.64	0.95	6.01	509	637	208
AOIN_02_19	322	21.9	B-LOD	1270	425800	1.74	B-LOD	10.52	0.06	1.38	3.34	0.511	22.8	8.21	104.2	41.5	186.3	399.4	73.1	10550	B-LOD	14.39	0.749	2.31	186.2	563	179.7
AOIN_02_20	932	14.5	B-LOD	4390	421000	2.62	B-LOD	22.8	0.33	5.9	14.9	1.44	84.9	29.6	379	144.6	636	1100	199.4	11880	1.7	54.7	2.89	22.9	1810	2040	700
AOIN_02_21	442	27.8	B-LOD	2622	410000	3.45	0.011	17.3	0.11	2.85	7.78	0.87	47.7	17.79	217.4	86.9	388.5	820	148.1	9880	1.5	32.6	1.68	7.78	612	1290	403
AOIN_02_22	444	13.2	112	2280	410000	2.18	0.016	10.38	0.12	3.01	7.5	0.98	43.5	15.5	185	73.4	337	713	136.8	10870	B-LOD	25.3	1.43	6.2	530	975	303
AOIN_02_23	238	14	B-LOD	1062	418000	1.11	B-LOD	6.3	0.03	0.85	4.02	0.572	22.9	7.67	92.6	35.9	157.1	365	61.9	7980	B-LOD	6.19	0.303	1.12	82	253	81.4
AOIN_02_24	485	17.9	B-LOD	3060	392000	2.34	B-LOD	16.1	0.13	3.93	12.15	1.87	68.4	23.54	276	103.7	443	883	147.8	10020	B-LOD	18.69	1.1	5.63	470	731	242.7
AOIN_02_25	372	20.5	B-LOD	1237	393000	1.52	B-LOD	9.58	0.03	1.48	4.05	0.67	24	8.19	104.4	41.5	191	436	80.1	8980	B-LOD	14.62	0.718	3.8	345	591	191
RRJP_01_0	298	5.1	B-LOD	1058	404000	0.58	0.004	7.19	0.06	1.37	3.09	1.01	17.5	6.45	78.2	34	170.9	460	94.8	9200	B-LOD	8.73	0.344	0.884	79.2	342	115.6
RRJP_01_1	322	6.2	B-LOD	1319	434000	1.57	0.033	12	0.10	1.64	3.52	1.28	20.7	7.75	99.7	43	212	560	112.9	8940	B-LOD	13.3	0.71	1.54	139	541	174
RRJP_01_3	242	5.7	B-LOD	1233	422700	0.92	B-LOD	8.06	0.10	1.52	2.77	1.12	20.8	7.18	91.7	39.84	198.4	523	109.8	8770	0.69	8.18	0.522	0.839	74.1	304	106.3
RRJP_01_5	262	5.1	B-LOD	878	433000	0.83	B-LOD	7.92	0.04	0.81	2.64	0.68	10.21	4.72	60.7	26.9	142	399	79.7	8670	B-LOD	8.62	0.42	0.74	69.7	361	121.6
RRJP_01_6	391	5.3	B-LOD	1458	421000	1.65	0.074	9.58	0.05	1.36	3.58	1.11	23.1	8.72	110.6	48.7	242	555	113.7	9030	B-LOD	8.18	0.49	0.96	77.3	308	106.3
RRJP_01_7	282	5.2	B-LOD	783	401000	1	B-LOD	7.41	0.04	0.67	1.46	0.64	11.5	4.15	56.2	24.7	134.4	360	75.9	8570	B-LOD	7.24	0.406	0.608	50.3	288	97.1
RRJP_01_8	187	9.3	B-LOD	840	408000	0.9	0.028	6.53	0.09	1.25	1.9	0.7	13.1	4.9	66.3	28	137.2	377	75.5	8750	B-LOD	6.19	0.357	0.652	51	285	83.5
RRJP_01_10	369	6.9	B-LOD	1809	415000	2.08	B-LOD	15.68	0.08	1.86	4.67	1.48	28.4	10.19	137.4	60.6	299	787	161.5	9280	B-LOD	16.5	1.01	2.06	171	726	239
RRJP_01_11	272	6.5	B-LOD	1309	407000	1.5	0.037	12.47	0.05	1.49	3.09	1.05	18.6	6.72	95.1	41	212	580	121.1	9180	B-LOD	13.43	0.59	1.45	131.8	539	177.8
RRJP_01_12	383	6.7	B-LOD	1437	414000	1.49	0.24	12.62	0.15	2.13	3.95	1.32	23.9	8.73	117	47	228	548	108.9	8310	B-LOD	8.8	0.442	1.28	98.8	375	124.9
RRJP_01_13	271	3.5	B-LOD	618	419000	0.98	0.03	6.96	0.04	0.32	1.05	0.45	7.6	3.21	42.5	19.3	95.6	289	66.1	9300	B-LOD	7.03	0.269	0.727	58.4	287	93

Anexo C, continuación

Sample/ Grain	P31 (ppm)	Ti49 (ppm)	Fe57 (ppm)	Y89 (ppm)	Zr90 (ppm)	Nb93 (ppm)	La139 (ppm)	Ce140 (ppm)	Pr141 (ppm)	Nd146 (ppm)	Sm147 (ppm)	Eu153 (ppm)	Gd157 (ppm)	Tb159 (ppm)	Dy163 (ppm)	Ho165 (ppm)	Er166 (ppm)	Yb172 (ppm)	Lu175 (ppm)	Hf178 (ppm)	Pb204 (ppm)	Pb206 (ppm)	Pb207 (ppm)	Pb208 (ppm)	Th232 (ppm)	U235 (ppm)	U238 (ppm)
RRJP_01_14	422	8.6	B-LOD	2234	411000	1.7	B-LOD	17	0.18	3.29	7.22	2.36	44.4	15.67	203	79.6	357	819	152.7	8490	B-LOD	11.18	0.525	1.72	146.1	475	154.8
RRJP_01_15	412	8.7	B-LOD	2240	410000	1.19	B-LOD	13.8	0.15	2.88	7.3	2.05	46.4	17.4	213	80.5	364	779	142	8870	B-LOD	9.31	0.404	1.29	122	418	129
RRJP_01_16	275	5.9	B-LOD	1054	427900	1.86	B-LOD	10.55	0.02	0.43	1.9	0.565	12.34	5.18	73.2	31.8	172.1	474	104.7	9510	B-LOD	10.99	0.568	1.135	100.4	449	151.2
RRJP_01_17	260	4.2	B-LOD	752	427300	1.16	B-LOD	7.89	0.01	0.37	1.32	0.55	9.2	3.81	52.6	24.2	123.4	361	77.3	9480	B-LOD	8.89	0.47	0.85	68.1	350	116.8
RRJP_01_19	269	5.9	B-LOD	976	431000	0.77	0.054	6.5	0.08	1.12	3.13	0.81	14.9	5.67	77.9	32.2	157.6	410	91.7	9130	B-LOD	6.42	0.402	0.517	55.5	275	85
RRJP_01_20	359	4.8	B-LOD	824	397000	1.22	0.46	8.87	0.12	1.32	1.47	0.64	10.15	4.26	59.5	25.9	136.6	386	82	9030	B-LOD	9.01	0.456	0.755	68.2	379	123.8
RRJP_01_23	237	5.7	B-LOD	680	416000	0.88	0.021	6.28	0.01	0.45	1.48	0.508	9.7	4.08	54.6	22.7	112.5	286	52.1	9260	B-LOD	4.64	0.257	0.346	34.1	178	60.5
RRJP_01_24	246	5.3	B-LOD	1150	405000	1.01	B-LOD	7.8	0.09	1.64	3.11	1.27	19.1	6.73	95.1	39.9	190.6	464	103.4	8680	B-LOD	8.41	0.277	0.94	79.3	320	107.5
RRJP_01_25	208	5.5	B-LOD	809	413000	0.65	0.049	7.9	0.10	1.08	2.15	0.82	14.1	5.02	62.9	26.6	128	323	65.8	9130	B-LOD	4.93	0.286	0.65	51.6	192	66.6
RRJP_01_26	298	6.3	B-LOD	916	428000	0.823	B-LOD	8	0.05	0.94	2.31	0.82	11.9	5.12	66.6	28.8	150	435	90.8	9090	B-LOD	9.51	0.432	0.94	80.2	379	128.2
RRJP_01_27	221	6.6	B-LOD	987	396000	1.1	B-LOD	9.16	0.06	0.89	2.17	0.77	15.4	5.27	74	30.7	155.3	411	89.4	9010	B-LOD	9.84	0.474	1.073	99.1	387	130.8
RRJP_01_28	327	7.3	B-LOD	1232	392000	1.1	B-LOD	8.82	0.04	1.32	3.62	0.69	20.7	7.19	101.2	40.2	199.8	462	95.1	8830	B-LOD	7.15	0.354	0.72	65	284	97.7
RRJP_01_29	246	8.8	B-LOD	955	401000	0.81	B-LOD	6.28	B-LOD	0.84	2.81	0.87	18.4	6.33	78.7	32.1	155.2	413	79.9	8240	B-LOD	5.39	0.293	0.482	49.6	222	77
RRJP_01_30	409	7.4	B-LOD	1583	420000	1.06	B-LOD	9.31	0.11	2.15	4.58	1.29	27.9	10.08	134.8	55.2	260	576	107.1	8240	B-LOD	7.27	0.391	0.94	81.1	278	102.8
RRJP_01_31	255	6.3	B-LOD	851	410000	1.18	0.026	8.67	0.03	0.73	1.81	0.67	11	4.31	60.5	27.3	142.4	408	86.8	8510	B-LOD	9.93	0.462	0.98	83.7	400	132.2
RRJP_01_32	311	7.93	B-LOD	1380	414000	0.77	B-LOD	7.91	0.07	1.75	3.98	0.99	25.9	9.18	121.4	49	222	495	93.1	9140	B-LOD	6.18	0.313	0.738	65.2	249	83
RRJP_01_33	214	5.8	B-LOD	688	420000	1.12	0.025	6.29	0.03	0.59	1.15	0.404	8.9	3.54	46	21.2	116.2	338	73.4	8920	B-LOD	6.04	0.29	0.451	42.8	255	84.7
RRJP_01_34	214	4.6	B-LOD	873	426000	1.37	B-LOD	9.04	0.07	1.03	2.37	1.04	14.2	5.02	66.3	27.9	138.1	351	76.4	9590	B-LOD	17.7	1.04	1.26	113.3	688	235